


1-1-2017

# Development Of Nanostructured Austempered Ductile Cast Iron

Saranya Panneerselvam  
*Wayne State University,*

Follow this and additional works at: [https://digitalcommons.wayne.edu/oa\\_dissertations](https://digitalcommons.wayne.edu/oa_dissertations)

 Part of the [Materials Science and Engineering Commons](#), and the [Nanoscience and Nanotechnology Commons](#)

---

## Recommended Citation

Panneerselvam, Saranya, "Development Of Nanostructured Austempered Ductile Cast Iron" (2017). *Wayne State University Dissertations*. 1856.  
[https://digitalcommons.wayne.edu/oa\\_dissertations/1856](https://digitalcommons.wayne.edu/oa_dissertations/1856)

This Open Access Dissertation is brought to you for free and open access by DigitalCommons@WayneState. It has been accepted for inclusion in Wayne State University Dissertations by an authorized administrator of DigitalCommons@WayneState.

**DEVELOPMENT OF NANOSTRUCTURED AUSTEMPERED DUCTILE CAST IRON**

by

**SARANYA PANNEERSELVAM**

**DISSERTATION**

Submitted to the Graduate School

of Wayne State University,

Detroit, Michigan

in partial fulfillment of the requirements

for the degree of

**DOCTOR OF PHILOSOPHY**

2017

Major: MATERIALS SCIENCE AND  
ENGINEERING

Approved By:

---

Advisor

Date

---

---

---

## ACKNOWLEDGEMENTS

I would like to express my deep gratitude to my advisor Dr. Susil Putatunda for giving me the opportunity to work on this research project. His exceptional guidance, continuous encouragement and financial support all these years helped me in completing my Ph. D thesis. My sincere thanks to my co-advisor Dr. James Boileau whose valuable suggestions and guidance helped me in improving the quality of my Ph.D. thesis. I would also like to acknowledge and thank my committee members Dr. Howard William Matthew and Dr. Steven O Salley for agreeing to be on my dissertation committee, their valuable time serving on my committee and for their valuable suggestions.

My special thanks to Dr. Zhi Mei from Lumigen Instrumentation Center, Department of Chemistry, Wayne State University, for assisting me with SEM and TEM imaging. I also thank the Metallurgy department at Focus Hope Industries, Detroit for allowing me to use their equipments for research.

I would like to express my gratitude to my former labmates Dr. Codrick Martis, Dr. Varun Nagarajan for their encouragement and great friendship. I would like to thank my current labmates Dr. to be Mohamed Alshwigi, Shashank Nellikuppam and Sagar Bajaj in the Fatigue Research Lab at Wayne State University for their help and support.

Words can do no justice to the unconditional support and affection rendered by my parents, my siblings and my in-laws throughout my graduate studies. I would like to extend my warmest regards and love to my husband Bharath Palanisamy, without him I would not have had the chance to pursue and complete Ph.D. Special thanks to my beloved daughter Arya for being such a good baby girl and for always cheering me up.

## TABLE OF CONTENTS

ACKNOWLEDGEMENTS .....	ii
LIST OF TABLES .....	ix
LIST OF FIGURES.....	xi
CHAPTER 1. INTRODUCTION .....	1
CHAPTER 2. LITERATURE REVIEW.....	4
2.1 Cast irons.....	4
2.1.1 Gray cast iron .....	5
2.1.2 White cast iron .....	6
2.1.3 Malleable cast iron .....	6
2.1.4 Ductile cast iron .....	8
2.2 Austempered ductile cast iron (ADI) .....	8
2.3 Chemical composition of ADI .....	9
2.4 Processing of ADI.....	10
2.5 Microstructure of ADI.....	12
2.5.1 Bainite in ADI .....	12
2.5.2 Upper bainite .....	12
2.5.3 Lower bainite.....	13
2.5.4 Austenite.....	14
2.5.5 Martensite.....	14
2.6 Nucleation and growth process of bainite .....	14
2.7 Mechanical properties of ADI.....	16
2.8 Fracture toughness of ADI .....	17

2.9 Intercritical austenitizing.....	17
2.10 Two-step austempering.....	20
2.11 Cryogenic processing.....	21
2.12 Stability of austenite.....	21
2.13 Nanostructured ADI.....	22
CHAPTER 3. OBJECTIVES.....	25
CHAPTER 4. EXPERIMENTAL PROCEDURE.....	26
4.1 Material.....	26
4.2 Heat treatment.....	27
4.2.1 Conventional austempering.....	27
4.2.2 Cryogenic processing.....	28
4.2.3 Intercritical austempering.....	29
4.2.4 Plastic deformation and single step austempering.....	30
4.2.5 Plastic deformation and two- step austempering.....	31
4.3 Microstructural analysis.....	33
4.4 Fracture toughness testing.....	35
4.5 Tensile testing.....	36
4.6 Hardness measurement.....	37
4.7 Transmission Electron Microscopy(TEM).....	37
CHAPTER 5. RESULTS AND DISCUSSIONS- MICROSTRUCTURE.....	38
5.1 Microstructure of the as-cast ductile iron.....	38
5.1.1 Microstructures of conventionally austempered ductile cast iron samples.....	38
5.1.2 Microstructures of cryogenically treated ADI samples.....	40

5.1.3 Microstructures of intercritically austempered ADI samples (constant $T_A= 680^\circ\text{F}$ ) .....	42
5.1.4 Microstructures of intercritically austempered ADI samples (constant $T_\gamma= 1520^\circ\text{F}$ ) .....	46
5.1.5 Microstructure of plastically deformed, conventional ADI .....	47
5.1.6 Microstructure of plastically deformed, intercritically austempered ductile cast iron.....	48
5.1.7 Microstructures of the plastic deformed, two-step austempered ductile cast iron .....	49
5.1.8 Microstructure of ductile iron plastically deformed at different strain rate .....	53
5.2 Lath size measurements .....	54
5.2.1 Lath size measurements of conventional ADI .....	55
5.2.2 Lath size measurements of cryogenically treated ADI .....	57
5.2.3 Lath size measurements of intercritically austenitized ADI .....	59
5.2.4 Lath size measurements of the plastically deformed ADI .....	62
5.2.5 Lath size measurements of plastic deformed ADI with respect to strain rate .....	70
5.3 Ferritic cell size .....	71
5.3.1 Ferritic cell sizes of conventional and cryogenically treated ADI.....	71
5.3.2 Ferritic cell size of conventional ADI with respect to plastic deformation .....	73
5.3.3 Ferritic cell size of intercritical ADI with respect to plastic deformation.....	74
CHAPTER 6. TRANSMISSION ELECTRON MICROSCOPY .....	78
CHAPTER 7. AUSTENITE AND ITS STABILITY .....	97
7.1 Volume fraction of austenite and its carbon content.....	97
7.1.1 Variation in the volume fraction of austenite and its carbon content in conventional ADI .....	97

7.1.2 Variation in the volume fraction of austenite and its carbon content in intercritically austenitized ADI (with constant $T_A$ ) .....	99
7.1.3 Variation in the volume fraction of austenite and its carbon content in intercritical ADI (with constant $T_\gamma$ ) .....	101
7.1.4 Variation in the volume fraction of austenite and its carbon content in conventional ADI with respect to plastic deformation .....	103
7.1.5 Variation in the volume fraction of austenite and its carbon content in intercritical ADI with respect to plastic deformation .....	105
7.2 Stability of austenite .....	107
7.2.1 Thermal Stability of austenite .....	107
7.2.2 Influence of cryogenic treatment on the mechanical stability of austenite .....	109
7.2.2.1 Strain induced transformation .....	110
7.2.2.2 Stress-induced deformation .....	111
7.2.2.3 Analytical Model for the Crack Growth Process .....	113
CHAPTER 8. MICROSTRUCTURE-PROPERTY RELATIONSHIP .....	119
8.1 Mechanical properties and fracture toughness of conventional and cryogenically treated ADI .....	119
8.1.1 Fractographs of the conventional ADI .....	121
8.1.2 Fractographs of the cryogenically treated ADI .....	123
8.1.3 Influence of width of different phases on the yield strength of conventional ADI .....	125
8.1.4 Influence of ferritic cell size and austenite volume fraction on the yield strength of conventional ADI .....	127
8.1.5 Influence of width of different phases on the fracture toughness of conventional ADI .....	128

8.1.6 Influence of width of different phases on the yield strength of cryogenically treated ADI.....	129
8.1.7 Influence of ferritic cell size and austenite volume fraction on the yield strength of cryogenically treated ADI.....	131
8.1.8 Influence of width of different phases on the fracture toughness of cryogenically treated ADI .....	132
8.2 Mechanical properties and fracture toughness of intercritically austenitized ADI .....	133
8.2.1 Fractographs of the intercritical ADI .....	135
8.2.2 Influence of width of different phases on the yield strength of intercritical ADI (contant $T_A$ ).....	139
8.2.3 Influence of ferritic cell size and austenite volume fraction on the yield strength of cryogenically treated ADI (contant $T_A$ ).....	140
8.2.4 Influence of width of different phases on the fracture toughness of intercritical ADI (contant $T_A$ ).....	141
8.2.5 Influence of width of different phases on the yield strength of intercritical ADI (contant $T_\gamma$ ) .....	142
8.2.6 Influence of austenite volume fraction and ferritic cell size on the yield strength of intercritical ADI (contant $T_\gamma$ ).....	144
8.2.7 Influence of width of different phases on the fracture toughness of intercritical ADI (contant $T_\gamma$ ) .....	145
8.3 Mechanical properties of plastically deformed ADI- single step austempering .....	146
8.3.1 Influence of width of different phases on the yield strength of plastically deformed ADI- single step austempering .....	147
8.3.2 Influence of ferritic cell size and austenite volume fraction on the yield strength of plastically deformed ADI: $T_\gamma=1700^\circ\text{F}$ and single step austempering.....	148
8.3.3 Influence of width of different phases on the yield strength of plastically deformed ADI-: $T_\gamma=1520^\circ\text{F}$ and single step austempering.....	150



8.3.4 Influence of ferritic cell size and austenite volume fraction on the yield strength of plastically deformed ADI-: $T_{\gamma}=1520^{\circ}\text{F}$ and single step austempering.....	151
8.4 Mechanical properties of plastically deformed ADI- two-step austempering .....	152
8.4.1 Influence of width of bainitic ferrite on the yield strength of plastically deformed ADI-: two step austempering.....	154
8.4.2 Influence of width of retained austenite on the yield strength of plastically deformed ADI-: two step austempering .....	155
8.4.3 Influence of width of proeutectoid ferrite on the yield strength of plastically deformed ADI-: two step austempering.....	156
8.4.4 Influence of ferritic cell size on the yield strength of plastically deformed ADI-: two step austempering .....	157
8.4.5 Influence of austenite volume fraction on the yield strength of plastically deformed ADI-: two step austempering .....	158
8.5 Comparison of yield strength with respect to the heat treatment.....	159
8.6 Comparison of ultimate tensile strength with respect to the heat treatment .....	160
CHAPTER 9. OBSERVATIONS .....	162
CHAPTER 10. CONCLUSIONS.....	165
CHAPTER 11. FUTURE WORK.....	166
APPENDIX -MICROSTRUCTURES OF ADI .....	167
REFERENCES .....	182
ABSTRACT.....	197
AUTOBIOGRAPHICAL STATEMENT.....	199

## LIST OF TABLES

Table 1: Chemical composition of ductile cast iron .....	26
Table 2: Lath size measurement of phases with respect to conventional austempering.....	55
Table 3: Lath size measurement of phases with respect to cryogenic processing .....	57
Table 4: Lath size measurement of phases with respect to intercritical austempering .....	59
Table 5: Lath size measurement of phases with respect to intercritical austempering .....	61
Table 6: Lath size measurements of different phases in plastically deformed ADI with respect to single step austempering .....	63
Table 7: Lath size measurements of different phases in plastically deformed ADI with respect to two-step austempering (samples austenitized at $T_\gamma$ as shown for 3 hours, $T_{A1}= 500^\circ\text{F}$ for 15 minutes, $T_{A2}$ at temperatures shown for 2.5 hours).....	64
Table 8: Comparison of lath size measurements .....	70
Table 9: Lath size measurements of different phases in plastically deformed ADI with respect to two-step austempering temperature.....	71
Table 10: Ferritic cell size of the ADI with respect to cryogenic treatment.....	72
Table 11: Ferritic cell size of the ADI with respect to the plastic deformation and single/two-step austempering temperatures.....	73
Table 12: Ferritic cell size of the intercritically austenitized ADI with respect to the plastic deformation, single/two-step austempering temperatures and strain rates .....	75
Table 13: Ferritic cell size of the intercritically austenitized ADI with respect to the plastic deformation, single/two-step austempering temperatures.....	76
Table 14: Summary of ADI samples analyzed with TEM.....	78
Table.15: Indexing details of diffraction pattern of ferrite phase (Conventional ADI, $T_\gamma=1700^\circ\text{F}$ for 3 hours, $T_A=725^\circ\text{F}$ for 3 hours).....	81
Table.16: Indexing details of diffraction pattern of ferrite phase (Conventional ADI, $T_\gamma=1700^\circ\text{F}$ , $T_A=725^\circ\text{F}$ ).....	82

Table.17: Indexing details of diffraction pattern of ferrite phase (Plastically deformed ADI, $T_{\gamma}=1700^{\circ}\text{F}$ , $T_D= 1700^{\circ}\text{F}$ , $T_A=725^{\circ}\text{F}$ ) .....	86
Table.18: Indexing details of diffraction pattern of austenite phase (Plastically deformed ADI, $T_{\gamma}=1700^{\circ}\text{F}$ , $T_D= 1700^{\circ}\text{F}$ , $T_A=725^{\circ}\text{F}$ ) .....	86
Table.19: Indexing details of diffraction pattern of ferrite phase (Plastically deformed, two-step austempered ADI, $T_{\gamma}=1700^{\circ}\text{F}$ , $T_D= 1700^{\circ}\text{F}$ , $T_{A1}=500^{\circ}\text{F}$ , $T_{A2}= 725^{\circ}\text{F}$ ).....	89
Table 20: Indexing details of diffraction pattern of ferrite phase (Plastically deformed, two-step austempered ADI, ( $T_{\gamma}=1520^{\circ}\text{F}$ , $T_D= 1520^{\circ}\text{F}$ , $T_{A1}=500^{\circ}\text{F}$ , $T_{A2}= 600^{\circ}\text{F}$ ).....	91
Table.21: Indexing details of diffraction pattern of ferrite phase (Plastically deformed, two-step austempered ADI, ( $T_{\gamma}=1472^{\circ}\text{F}$ , $T_D= 1472^{\circ}\text{F}$ , $T_{A1}=500^{\circ}\text{F}$ , $T_{A2}= 680^{\circ}\text{F}$ ).....	93
Table.22: Indexing details of diffraction pattern of ferrite phase (Plastically deformed, two-step austempered ADI, ( $T_{\gamma}=1520^{\circ}\text{F}$ , $T_D= 1520^{\circ}\text{F}$ , strain rate= 10mm/min, $T_{A1}=500^{\circ}\text{F}$ , $T_{A2}= 680^{\circ}\text{F}$ ).....	95
Table 23: The Volume Fraction of Austenite in the ADI as a Function of Cryogenic Treatment .....	108
Table 24: The Volume Fraction of Austenite in the ADI as a Function of Cryogenic Treatment and Testing .....	110
Table 25: The Volume Fraction of Austenite in the ADI as a Function of Cryogenic Treatment and Testing .....	112
Table 26: Mechanical Properties of ADI with respect to cryogenic treatment.....	119
Table 27: Fracture toughness and Hardness of ADI with respect to cryogenic treatment .....	120
Table 28: The Mechanical Properties of the ADI as a Function of intercritical austenitizing and Austempering Temperature. ....	133
Table 29: The Fracture toughness and Hardness of the ADI as a Function of Intercritical austenitizing and Austempering Temperature. ....	135
Table 30: The Mechanical Properties of the ADI as a Function of austenitization temperature, plastic deformation and Austempering Temperature. ....	146
Table 31: The Mechanical Properties of the ADI as a Function of austenitization temperature, plastic deformation and two- step austempering. ....	153

## LIST OF FIGURES

Figure.1: Carbon and silicon content in cast iron compared to steel .....	5
Figure.2:Optical photomicrographs of cast irons (a)Gray cast iron (500X), (b)White cast iron (400X), (c)Malleable cast iron (150X), and (d) ductile cast iron (200X) .....	7
Figure.3: Comparison of mechanical properties of various types of ductile cast iron .....	9
Figure.4:Isothermal transformation diagram for unalloyed ductile cast iron together with time temperature transformation (TTT) curve .....	11
Figure.5: Difference between ausferrite in ductile iron and bainite in steel [34].....	13
Figure.6: Schematic representation of upper bainite and lower bainite.....	14
Figure.7: $T_0$ curve construction on the Fe-C Phase diagram using free energy of austenite and ferrite .....	15
Figure.8: A schematic diagram of intercritical austenitization process .....	18
Figure.9: Plastic deformation of austenite grain. ....	24
Figure.10: Schematic Diagram of the conventional austempering heat treatment .....	27
Figure. 11: Schematic Diagram of the cryogenic heat treatment process.....	28
Figure.12: Schematic diagram of intercritical austempering process .....	29
Figure.13: Schematic Diagram of heat treatment involving (a) plastic deformation and single step conventional austempering process (b) plastic deformation and single step intercritical austempering process .....	30
Figure.14: Schematic diagram of heat treatment involving (a) plastic deformation and single step conventional austempering process (a) plastic deformation and single step intercritical austempering process .....	32
Figure.15: Compact tension sample dimensions (inches).....	35
Figure.16: Cylindrical tensile sample dimensions (mm). ....	36
Figure.17: As-cast microstructure of ductile cast iron (a) Optical microscope image (Mag 200x) b) Optical microscope image (Mag 1000x).....	38
Figure.18(a): Optical and SEM micrograph of ADI, $T_\gamma=1700^\circ\text{F}$ , $T_A=500^\circ\text{F}$ .....	39

Figure.18(b): Optical and SEM micrograph of ADI, $T_{\gamma}=1700^{\circ}\text{F}$ , $T_A=725^{\circ}\text{F}$ .....	39
Figure.19(a): Optical and SEM micrograph of cryogenically treated ADI, $T_{\gamma}=1700^{\circ}\text{F}$ , $T_A=500^{\circ}\text{F}$ .....	41
Figure.19(b): Optical and SEM micrograph of cryogenically treated ADI, $T_{\gamma}=1700^{\circ}\text{F}$ , $T_A=725^{\circ}\text{F}$ .....	41
Figure.20(a): Optical and SEM micrograph of intercritically austempered ductile cast iron, $T_{\gamma}=1520^{\circ}\text{F}$ , $T_A=680^{\circ}\text{F}$ .....	43
Figure.20(b): Optical and SEM micrograph of intercritically austempered ductile cast iron, $T_{\gamma}=1472^{\circ}\text{F}$ , $T_A=680^{\circ}\text{F}$ .....	43
Figure.20(c): Optical and SEM micrograph of intercritically austempered ductile cast iron, $T_{\gamma}=1436^{\circ}\text{F}$ , $T_A=680^{\circ}\text{F}$ .....	44
Figure.20(d): Optical and SEM micrograph of intercritically austempered ductile cast iron, $T_{\gamma}=1418^{\circ}\text{F}$ , $T_A=680^{\circ}\text{F}$ .....	44
Figure.21: Volume fraction of proeutectoid ferrite as a function of austenitizing temperatures .....	45
Figure.22: Volume fraction of ausferrite as a function of austenitizing temperatures .....	46
Figure.23: Optical and SEM micrograph of intercritically austempered ductile cast iron, $T_{\gamma}=1520^{\circ}\text{F}$ , $T_A=725^{\circ}\text{F}$ .....	47
Figure.24: Optical and SEM micrograph of plastically deformed ADI, $T_{\gamma}=1700^{\circ}\text{F}$ , $T_D=1700^{\circ}\text{F}$ , $T_A=725^{\circ}\text{F}$ .....	48
Figure.25: Optical and SEM micrograph of plastically deformed ADI, $T_{\gamma}=1520^{\circ}\text{F}$ , $T_D=1520^{\circ}\text{F}$ , $T_A=725^{\circ}\text{F}$ .....	49
Figure.26: Optical and SEM micrograph of plastically deformed, two step austempered ADI, $T_{\gamma}=1700^{\circ}\text{F}$ , $T_D=1700^{\circ}\text{F}$ , $T_{A1}=500^{\circ}\text{F}$ , $T_{A2}=550^{\circ}\text{F}$ .....	50
Figure.27: Optical and SEM micrograph of plastically deformed, two step austempered ADI, $T_{\gamma}=1520^{\circ}\text{F}$ , $T_D=1520^{\circ}\text{F}$ , $T_{A1}=500^{\circ}\text{F}$ , $T_{A2}=550^{\circ}\text{F}$ .....	51
Figure.28: Optical and SEM micrograph of plastically deformed, two step austempered ADI, $T_{\gamma}=1472^{\circ}\text{F}$ , $T_D=1472^{\circ}\text{F}$ , $T_{A1}=500^{\circ}\text{F}$ , $T_{A2}=550^{\circ}\text{F}$ .....	52

Figure.29: Optical and SEM micrograph of plastically deformed, two step austempered ADI, $T_{\gamma}=1436^{\circ}\text{F}$ , $T_D=1436^{\circ}\text{F}$ , $T_{A1}=500^{\circ}\text{F}$ , $T_{A2}=550^{\circ}\text{F}$ .....	52
Figure.30: Optical and SEM micrograph of plastically deformed, two step austempered ADI, $T_{\gamma}=1520^{\circ}\text{F}$ , $T_D=1520^{\circ}\text{F}$ , strain rate = 0.5mm/min, $T_A=550^{\circ}\text{F}$ .....	54
Figure.31: Variation of the width of bainitic ferrite (BF) and width of films of retained austenite (RA) with respect to austempering temperature in conventional ADI .....	56
Figure.32: Variation of the width of bainitic ferrite (BF) and width of films of retained austenite (RA) with respect to austempering temperature in cryogenically treated ADI .....	58
Figure.33: Variation of the width of bainitic ferrite (BF), width of films of retained austenite (RA) of ADI with respect to austempering temperature from data in Table 4. .....	60
Figure.34: Variation of the width of bainitic ferrite (BF), width of films of retained austenite (RA) of ADI with respect to intercritical austenitizing temperature from data in Table 5.....	61
Figure.36: Variation in the width of retained austenite in the ADI samples austenitized and plastically deformed at $1700^{\circ}\text{F}$ with respect to single step and two-step austempering. ....	66
Figure.37: Variation in the width of bainitic ferrite (BF) in the ADI samples austenitized and plastically deformed at $1520^{\circ}\text{F}$ with respect to single step and two-step austempering .....	67
Figure.38: Variation in the width of films of retained austenite (RA) in ADI samples austenitized and plastically deformed at $1520^{\circ}\text{F}$ with respect to single step and two- step austempering.....	68
Figure.39: Variation in the width of (a) bainitic ferrite (BF), (b) films of retained austenite (RA) with respect to intercritical austenitization at $1472^{\circ}\text{F}$ and $1436^{\circ}\text{F}$ in plastically deformed ADI.....	69
Figure.40: TEM micrographs of conventional ADI a) Bright Field image b) Dark field image .....	79

Figure.41.: TEM micrographs of ductile cast iron conventionally austempered at 725°F (a) Indexed diffraction pattern for bainitic ferrite phase (b) Indexed diffraction pattern for austenite .....	80
Figure.42: X-ray diffraction pattern of conventional ductile cast iron ( $T_{\gamma}=1700^{\circ}\text{F}$ for 3 hours, $T_A=725^{\circ}\text{F}$ for 3 hours).....	80
Figure.43: TEM micrographs showing Bright field image of plastically deformed ADI ( $T_{\gamma}=1700^{\circ}\text{F}$ , $T_D=1700^{\circ}\text{F}$ , $T_A=725^{\circ}\text{F}$ ).....	82
Figure.44: TEM micrographs of plastically deformed ADI ( $T_{\gamma}=1700^{\circ}\text{F}$ , $T_D=1700^{\circ}\text{F}$ , $T_A=725^{\circ}\text{F}$ ) (a) Dark Field image showing ferrite phase b) Dark field image showing austenite phase .....	83
Figure.45: Indexed diffraction of (a)ferrite phase (b) austenite phase of plastically deformed ADI ( $T_{\gamma}=1700^{\circ}\text{F}$ , $T_D=1700^{\circ}\text{F}$ , $T_A=725^{\circ}\text{F}$ ).....	84
Figure.46: X-ray diffraction pattern of ductile cast iron plastically deformed ADI.....	84
Figure.47: Changes in diffraction pattern with respect to grain size .....	85
Figure.48: TEM micrographs of plastically deformed, two-step austempered ADI ( $T_{\gamma}=1700^{\circ}\text{F}$ , $T_D=1700^{\circ}\text{F}$ , $T_{A1}=500^{\circ}\text{F}$ , $T_{A2}=725^{\circ}\text{F}$ ), a) Bright Field image b) Dark field image .....	87
Figure.49: TEM micrographs of plastically deformed, two-step austempered ADI ( $T_{\gamma}=1700^{\circ}\text{F}$ , $T_D=1700^{\circ}\text{F}$ , $T_{A1}=500^{\circ}\text{F}$ , $T_{A2}=725^{\circ}\text{F}$ ), (a) indexed SAED pattern (b) X-ray diffraction profile.....	88
Figure.50: TEM micrographs of ductile cast iron intercritically austenitized, plastically deformed, two-step austempered ADI ( $T_{\gamma}=1520^{\circ}\text{F}$ , $T_D=1520^{\circ}\text{F}$ , $T_{A1}=500^{\circ}\text{F}$ , $T_{A2}=600^{\circ}\text{F}$ , (a) Bright Field image, (b) and (c) Dark field image (d) SAED Pattern.....	90
Figure.51: X-ray diffraction pattern of ductile cast iron plastically deformed ADI , ( $T_{\gamma}=1520^{\circ}\text{F}$ , $T_D=1520^{\circ}\text{F}$ , $T_{A1}=500^{\circ}\text{F}$ , $T_{A2}=600^{\circ}\text{F}$ ).....	91
Figure.52: TEM micrographs of ductile cast iron intercritically austenitized, plastically deformed, two-step austempered ADI ( $T_{\gamma}=1472^{\circ}\text{F}$ , $T_D=1472^{\circ}\text{F}$ , $T_{A1}=500^{\circ}\text{F}$ , $T_{A2}=680^{\circ}\text{F}$ ), (a) Bright Field image, (b)Dark field image.....	92
Figure.53: TEM micrographs of ductile cast iron intercritically austenitized, plastically deformed, two-step austempered ADI ( $T_{\gamma}=1472^{\circ}\text{F}$ , $T_D=1472^{\circ}\text{F}$ , $T_{A1}=500^{\circ}\text{F}$ , $T_{A2}=680^{\circ}\text{F}$ , (a) Indexed SAED Pattern and (b) X-ray diffraction profile .....	93

Figure.54: TEM micrographs of ductile cast iron intercritically austenitized, plastically deformed at higher strain rate, two-step austempered ADI $T_{\gamma}=1520^{\circ}\text{F}$ , $T_D=1520^{\circ}\text{F}$ , strain rate= 10mm/min $T_{A1}=500^{\circ}\text{F}$ , $T_{A2}=550^{\circ}\text{F}$ a) Bright Field image, (b) Dark field image.....	94
Figure.55: TEM micrographs of ductile cast iron intercritically austenitized, plastically deformed at higher strain rate, two-step austempered ADI $T_{\gamma}=1520^{\circ}\text{F}$ , $T_D=1520^{\circ}\text{F}$ , strain rate= 10mm/min, $T_{A1}=500^{\circ}\text{F}$ , $T_{A2}=550^{\circ}\text{F}$ (a) SAED Pattern (b) X-ray diffraction profile.....	95
Figure.56: Effect of conventional austempering on the volume fraction of austenite ( $T_{\gamma}=1700^{\circ}\text{F}$ , $T_A$ as shown).....	98
Figure.57: Volume fraction of austenitic carbon with respect to conventional austempering temperature ( $T_{\gamma}=1700^{\circ}\text{F}$ , $T_A$ as shown).....	99
Figure.58: Influence of intercritical austenitizing temperatures on the volume fraction of austenite ( $T_{\gamma}$ as shown, $T_A=680^{\circ}\text{F}$ ).....	100
Figure.59: Influence of intercritical austenitizing temperatures on the carbon content of austenite ( $T_{\gamma}$ as shown, $T_A=680^{\circ}\text{F}$ ).....	101
Figure.60: Influence of austempering temperatures on the volume fraction of austenite in the intercritical ADI ( $T_{\gamma}=1520^{\circ}\text{F}$ , $T_A$ as shown).....	102
Figure.61: Influence of austempering temperatures on the carbon content austenite in the intercritical ADI ( $T_{\gamma}=1520^{\circ}\text{F}$ , $T_A$ as shown).....	103
Figure.62: Influence of austempering temperatures on the volume fraction of austenite in the plastically deformed ADI ( $T_{\gamma}=1700^{\circ}\text{F}$ , $T_A$ as shown).....	104
Figure.63: Influence of austempering temperatures on the volume fraction of austenitic carbon in the plastically deformed ADI ( $T_{\gamma}=1700^{\circ}\text{F}$ , $T_A$ as shown).....	104
Figure.64: Influence of intercritical austenitization on the volume fraction of austenite in the plastically deformed ADI ( $T_{\gamma}=1520^{\circ}\text{F}$ , $T_A$ as shown).....	105
Figure.65: Influence of intercritical austenitization on the volume fraction of austenitic carbon in the plastically deformed ADI ( $T_{\gamma}=1520^{\circ}\text{F}$ , $T_A$ as shown).....	106
Figure.66: Influence of intercritical austenitization on the volume fraction of austenite with respect to plastically deformation and two step austempering.....	107



Figure.67: Area ahead of the Crack Tip.....	115
Figure.68: Area ahead of the Crack Tip during loading.....	116
Figure.69: Effective crack length.....	117
Figure.70: SEM fractographs of conventional ADI (CT) specimen, (a) $T_{\gamma}=1700^{\circ}\text{F}$ , $T_A=500^{\circ}\text{F}$ , (b) $T_{\gamma}=1700^{\circ}\text{F}$ , $T_A=550^{\circ}\text{F}$ (c) $T_{\gamma}=1700^{\circ}\text{F}$ , $T_A=700^{\circ}\text{F}$ , (d) $T_{\gamma}=1700^{\circ}\text{F}$ , $T_A=725^{\circ}\text{F}$ , (e) $T_{\gamma}=1700^{\circ}\text{F}$ , $T_A=750^{\circ}\text{F}$ , DF- Dimpled ductile fracture, TC- Transgranular cleavage fracture, QC-Quasi cleavage .....	122
Figure.71: SEM fractographs of cryogenically treated ADI (CT) specimen (a) $T_{\gamma}=1700^{\circ}\text{F}$ , $T_A=500^{\circ}\text{F}$ , (b) $T_{\gamma}=1700^{\circ}\text{F}$ , $T_A=550^{\circ}\text{F}$ (c) $T_{\gamma}=1700^{\circ}\text{F}$ , $T_A=700^{\circ}\text{F}$ , (d) $T_{\gamma}=1700^{\circ}\text{F}$ , $T_A=725^{\circ}\text{F}$ , (e) $T_{\gamma}=1700^{\circ}\text{F}$ , $T_A=750^{\circ}\text{F}$ , DF- Dimpled ductile fracture, TC- Transgranular cleavage fracture, QC-Quasi cleavage fracture .....	124
Figure.72: Influence of the width of (a) bainitic ferrite lath, (b)films of retained austenite and (c) islands of retained austenite on the yield strength of conventional ADI( $T_{\gamma}= 1700^{\circ}\text{F}$ , $T_A$ as shown) .....	126
Figure.73: Influence of the width of (a)ferritic cell size, (b)volume fraction of austenite on the yield strength of conventional ADI ( $T_{\gamma}= 1700^{\circ}\text{F}$ , $T_A$ as shown) ...	127
Figure.74: Influence of the width of (a) BF-bainitic ferrite lath, RA-films of retained austenite and (b) IRA- islands of retained austenite on the fracture toughness of conventional ADI( $T_{\gamma}= 1700^{\circ}\text{F}$ , $T_A$ as shown).....	128
Figure.75: Influence of the width of (a)bainitic ferrite, (b) films of retained austenite and (c) islands of retained austenite on the yield strength of the cryogenically treated ADI ( $T_{\gamma}= 1700^{\circ}\text{F}$ , $T_A$ as shown) .....	130
Figure.76: Influence of the width of (a)ferritic cell size, (b)volume fraction of austenite on the yield strength of the cryogenically treated ADI ( $T_{\gamma}= 1700^{\circ}\text{F}$ , $T_A$ as shown) .....	131
Figure.77: Influence of the width of (a) BF-bainitic ferrite lath, RA-films of retained austenite and (b) IRA- islands of retained austenite on the fracture toughness of cryogenically treated ADI ( $T_{\gamma}= 1700^{\circ}\text{F}$ , $T_A$ as shown).....	132
Figure.78: SEM fractographs of intercritical ADI (CT) specimen (a) $1535^{\circ}\text{F}$ - $680^{\circ}\text{F}$ , (b) $1472^{\circ}\text{F}$ - $680^{\circ}\text{F}$ , (c) $T_{\gamma}=1436^{\circ}\text{F}$ , $T_A=680^{\circ}\text{F}$ , (d) $T_{\gamma}=1418^{\circ}\text{F}$ , $T_A=680^{\circ}\text{F}$ , DF- Dimpled ductile fracture, TC- Transgranular cleavage fracture.....	136

Figure.79: SEM fractographs of intercriticalADI (CT) °F, (a) $T_{\gamma}=1520^{\circ}\text{F}$ , $T_A=725^{\circ}\text{F}$ and (b) $T_{\gamma}=1520^{\circ}\text{F}$ , $T_A=680^{\circ}\text{F}$ , (c) $T_{\gamma}=1520^{\circ}\text{F}$ , $T_A=600^{\circ}\text{F}$ , (d) $T_{\gamma}=1520^{\circ}\text{F}$ , $T_A=550^{\circ}\text{F}$ , respectively, DF- Dimpled ductile fracture, TC- Transgranular cleavage fracture.....	138
Figure.80: Influence of the width of (a)bainitic ferrite, (b) films of retained austenite and (c) islands of retained austenite on the yield strength of intercritical ADI ( $T_{\gamma}$ as shown, constant $T_A=680^{\circ}\text{F}$ ) .....	139
Figure.81 : Influence of the width of (a) ferritic cell size, (b)volume fraction of austenite on the yield strength of intercritical ADI ( $T_{\gamma}$ as shown, constant $T_A=680^{\circ}\text{F}$ ).....	141
Figure.82: Influence of the width of (a)ferritic cell size, (b)volume fraction of austenite on the yield strength of intercritical ADI ( $T_{\gamma}$ as shown, constant $T_A=680^{\circ}\text{F}$ ).....	142
Figure.83: Influence of the width of (a)bainitic ferrite, (b) films of retained austenite and (c) islands of retained austenite on the yield strength of intercritical ADI ( $T_{\gamma}= 1520^{\circ}\text{F}$ , $T_A$ as shown) .....	143
Figure.84: Influence of the (a) volume fraction of austenite, (b) ferritic cell size on the yield strength of intercritical ADI ( $T_{\gamma}= 1520^{\circ}\text{F}$ , $T_A$ as shown).....	144
Figure.85: Influence of the width of (a)BF-bainitic ferrite, RA-films of retained austenite, (b) proeutectoid ferrite on the fracture toughness of intercritical ADI ( $T_{\gamma}= 1520^{\circ}\text{F}$ , $T_A$ as shown) .....	145
Figure.86: Influence of the width of (a)bainitic ferrite, (b) films of retained austenite and (c) islands of retained austenite on the yield strength of plastically deformed ADI, ( $T_{\gamma}=1700^{\circ}\text{F}$ , $T_D=1700^{\circ}\text{F}$ , $T_A$ as shown).....	148
Figure.87: Influence of (a) ferritic cell size, (b)volume fraction of austenite on the yield strength of plastically deformed ADI, ( $T_{\gamma}=1700^{\circ}\text{F}$ , $T_D=1700^{\circ}\text{F}$ , $T_A$ as shown).....	149
Figure.88: Influence of the width of (a)bainitic ferrite, (b) films of retained austenite and (c) islands of retained austenite on the yield strength of plastically deformed ADI, ( $T_{\gamma}=1520^{\circ}\text{F}$ , $T_D=1520^{\circ}\text{F}$ , $T_A$ as shown).....	150
Figure.89: Influence of (a) ferritic cell size, (b)volume fraction of austenite on the yield strength of plastically deformed ADI, ( $T_{\gamma}=1520^{\circ}\text{F}$ , $T_D=1520^{\circ}\text{F}$ , $T_A$ as shown).....	151
Figure.90: Comparison of the effect of width of the bainitic ferrite on the yield strength of the plastically deformed, two-step austempered ADI with respect to the austenitization temperature. ....	154

Figure.91: Comparison of the effect of width of the films of retained austenite on the yield strength of the plastically deformed, two-step austempered ADI with respect to the austenitization temperature.....	155
Figure.92: Comparison of the effect of width of the proeutectoid ferrite on the yield strength of the plastically deformed, two-step austempered ADI with respect to the austenitization temperature.....	156
Figure.93 Comparison of the ferritic cell size to the yield strength of plastically deformed, two-step austempered ADI with respect to the austenitization temperature .....	157
Figure.94: Comparison of the volume fraction of austenite to the yield strength of plastically deformed, two-step austempered ADI with respect to the austenitization temperature. ....	158
Figure.95: Comparison of yield strength of ADI with respect to the heat treatment.....	159
Figure.96: Comparison of ultimate tensile strength of ADI with respect to the heat treatment. .	161
Figure.A.1: Optical and SEM micrograph of ADI, $T_{\gamma}=1700^{\circ}\text{F}$ , $T_A=550^{\circ}\text{F}$ .....	167
Figure.A.2: Optical and SEM micrograph of ADI, $T_{\gamma}=1700^{\circ}\text{F}$ , $T_A=700^{\circ}\text{F}$ .....	167
Figure.A.3: Optical and SEM micrograph of ADI, $T_{\gamma}=1700^{\circ}\text{F}$ , $T_A=750^{\circ}\text{F}$ .....	168
Figure.A.4: Optical and SEM micrograph of cryogenically treated ADI, $T_{\gamma}=1700^{\circ}\text{F}$ , $T_A=550^{\circ}\text{F}$ .....	168
Figure.A.5: Optical and SEM micrograph of cryogenically treated ADI, $T_{\gamma}=1700^{\circ}\text{F}$ , $T_A=700^{\circ}\text{F}$ .....	169
Figure.A.6: Optical and SEM micrograph of cryogenically treated ADI, $T_{\gamma}=1700^{\circ}\text{F}$ , $T_A=750^{\circ}\text{F}$ .....	169
Figure.A.7: Optical and SEM micrograph of intercritically austempered ductile cast iron, $T_{\gamma}=1520^{\circ}\text{F}$ , $T_A=680^{\circ}\text{F}$ .....	170
Figure.A.8: Optical and SEM micrograph of intercritically austempered ductile cast iron, $T_{\gamma}=1520^{\circ}\text{F}$ , $T_A=600^{\circ}\text{F}$ .....	170
Figure.A.9: Optical and SEM micrograph of intercritically austempered ductile cast iron, $T_{\gamma}=1520^{\circ}\text{F}$ , $T_A=550^{\circ}\text{F}$ .....	171

Figure.A.10: Optical and SEM micrograph of plastically deformed ADI, $T_{\gamma}=1700^{\circ}\text{F}$ , $T_D=1700^{\circ}\text{F}$ , $T_A=680^{\circ}\text{F}$ .....	171
Figure.A.11: Optical and SEM micrograph of plastically deformed ADI, $T_{\gamma}=1700^{\circ}\text{F}$ , $T_D=1700^{\circ}\text{F}$ , $T_A=600^{\circ}\text{F}$ .....	172
Figure.A.12: Optical and SEM micrograph of plastically deformed ADI, $T_{\gamma}=1700^{\circ}\text{F}$ , $T_D=1700^{\circ}\text{F}$ , $T_A=550^{\circ}\text{F}$ .....	172
Figure.A.13: Optical and SEM micrograph of plastically deformed ADI, $T_{\gamma}=1520^{\circ}\text{F}$ , $T_D=1520^{\circ}\text{F}$ , $T_A=680^{\circ}\text{F}$ .....	173
Figure.A.14: Optical and SEM micrograph of plastically deformed ADI, $T_{\gamma}=1520^{\circ}\text{F}$ , $T_D=1520^{\circ}\text{F}$ , $T_A=600^{\circ}\text{F}$ .....	173
Figure.A.15: Optical and SEM micrograph of plastically deformed ADI, $T_{\gamma}=1520^{\circ}\text{F}$ , $T_D=1700^{\circ}\text{F}$ , $T_A=550^{\circ}\text{F}$ .....	174
Figure.A.16: Optical and SEM micrograph of plastically deformed, two step austempered ADI, $T_{\gamma}=1700^{\circ}\text{F}$ , $T_D=1700^{\circ}\text{F}$ , $T_{A1}=500^{\circ}\text{F}$ , $T_{A2}=725^{\circ}\text{F}$ .....	174
Figure.A.17: Optical and SEM micrograph of plastically deformed, two step austempered ADI, $T_{\gamma}=1700^{\circ}\text{F}$ , $T_D=1700^{\circ}\text{F}$ , $T_{A1}=500^{\circ}\text{F}$ , $T_{A2}=680^{\circ}\text{F}$ .....	175
Figure.A.18: Optical and SEM micrograph of plastically deformed, two step austempered ADI, $T_{\gamma}=1700^{\circ}\text{F}$ , $T_D=1700^{\circ}\text{F}$ , $T_{A1}=500^{\circ}\text{F}$ , $T_{A2}=600^{\circ}\text{F}$ .....	175
Figure.A.19: Optical and SEM micrograph of plastically deformed, two step austempered ADI, $T_{\gamma}=1520^{\circ}\text{F}$ , $T_D=1520^{\circ}\text{F}$ , $T_{A1}=500^{\circ}\text{F}$ , $T_{A2}=725^{\circ}\text{F}$ .....	176
Figure.A.20: Optical and SEM micrograph of plastically deformed, two step austempered ADI, $T_{\gamma}=1520^{\circ}\text{F}$ , $T_D=1520^{\circ}\text{F}$ , $T_{A1}=500^{\circ}\text{F}$ , $T_{A2}=680^{\circ}\text{F}$ .....	176
Figure.A.21: Optical and SEM micrograph of plastically deformed, two step austempered ADI, $T_{\gamma}=1520^{\circ}\text{F}$ , $T_D=1520^{\circ}\text{F}$ , $T_{A1}=500^{\circ}\text{F}$ , $T_{A2}=600^{\circ}\text{F}$ .....	177
Figure.A.22: Optical and SEM micrograph of plastically deformed, two step austempered ADI, $T_{\gamma}=1472^{\circ}\text{F}$ , $T_D=1472^{\circ}\text{F}$ , $T_{A1}=500^{\circ}\text{F}$ , $T_{A2}=725^{\circ}\text{F}$ .....	177
Figure.A.23: Optical and SEM micrograph of plastically deformed, two step austempered ADI, $T_{\gamma}=1472^{\circ}\text{F}$ , $T_D=1472^{\circ}\text{F}$ , $T_{A1}=500^{\circ}\text{F}$ , $T_{A2}=680^{\circ}\text{F}$ .....	178

Figure.A.24: Optical and SEM micrograph of plastically deformed, two step austempered ADI, $T_{\gamma}=1472^{\circ}\text{F}$ , $T_{\text{D}}=1472^{\circ}\text{F}$ , $T_{\text{A1}}=500^{\circ}\text{F}$ , $T_{\text{A2}}=600^{\circ}\text{F}$ .....	178
Figure.A.25: Optical and SEM micrograph of plastically deformed, two step austempered ADI, $T_{\gamma}=1436^{\circ}\text{F}$ , $T_{\text{D}}=1436^{\circ}\text{F}$ , $T_{\text{A1}}=500^{\circ}\text{F}$ , $T_{\text{A2}}=725^{\circ}\text{F}$ .....	179
Figure.A.26: Optical and SEM micrograph of plastically deformed, two step austempered ADI, $T_{\gamma}=1436^{\circ}\text{F}$ , $T_{\text{D}}=1436^{\circ}\text{F}$ , $T_{\text{A1}}=500^{\circ}\text{F}$ , $T_{\text{A2}}=680^{\circ}\text{F}$ .....	179
Figure.A.27: Optical and SEM micrograph of plastically deformed, two step austempered ADI, $T_{\gamma}=1436^{\circ}\text{F}$ , $T_{\text{D}}=1436^{\circ}\text{F}$ , $T_{\text{A1}}=500^{\circ}\text{F}$ , $T_{\text{A2}}=600^{\circ}\text{F}$ .....	180
Figure.A.28: Optical and SEM micrograph of plastically deformed, two step austempered ADI, $T_{\gamma}=1520^{\circ}\text{F}$ , $T_{\text{D}}=1520^{\circ}\text{F}$ , strain rate = 10mm/min, $T_{\text{A}}=550^{\circ}\text{F}$	180
Figure.A.29: Optical and SEM micrograph of plastically deformed, two step austempered ADI, $T_{\gamma}=1520^{\circ}\text{F}$ , $T_{\text{D}}=1520^{\circ}\text{F}$ , strain rate = 0.5mm/min, $T_{\text{A1}}=500^{\circ}\text{F}$ , $T_{\text{A2}}=550^{\circ}\text{F}$ .....	181
Figure.A.30: Optical and SEM micrograph of plastically deformed, two step austempered ADI, $T_{\gamma}=1520^{\circ}\text{F}$ , $T_{\text{D}}=1520^{\circ}\text{F}$ , strain rate = 10mm/min, $T_{\text{A1}}=500^{\circ}\text{F}$ , $T_{\text{A2}}=550^{\circ}\text{F}$ .....	181

## CHAPTER 1. INTRODUCTION

Austempered Ductile Cast Iron (ADI) has emerged as a major engineering material in recent years despite the vigorous energetic promotion of newer materials and alloys because of its exceptional combination of properties including high strength, good fracture toughness [1-3], good fatigue strength and excellent wear resistance [4-5] with good ductility [6-7]. Austempered ductile iron is an alloyed and heat treated ductile cast iron. Another advantage of ADI is that, it has low production costs due to its good castability, excellent machinability and shorter heat treatment processing cycles. The chemical composition and the heat treatment parameters determine the properties of the ADI. In order to take complete advantage of the engineering properties of ADI, the chemical composition and heat treatment parameters must be optimized [8]. ADI compete favorably with steel and aluminium castings and has been extensively used as a structural component in wide variety of industrial applications such as automotive, defense, agricultural, railways, mining, and construction [9].

The current demand for vehicle weight reduction, improved fuel economy, while maintaining the crash performance, requires innovative processing, for the creation of unique microstructures in the materials. While ADI has good mechanical properties, studies show that, with respect to toughness properties, the ADI ratings are certainly not the best. The bending strength of ADI is lower than that of the carburized alloy steel [10], the machining of thick section parts is difficult in the commercially available ADI due to its poor machinability. One of the way to improve the properties such as strength and toughness is by refining the grain size to a nanoscale range.

Nanostructured materials are the crystals with sizes less than 100nm. Those materials with the grain size  $>100\text{nm}$  but  $< 500\text{nm}$  are referred to as ultra-fine- grained materials [11-13]. The

grain boundary of the nanostructured materials accounts for about 50% of its total volume. The nanostructured materials are gaining importance in recent because of its attractive physical and chemical properties than the coarse-grained materials.

While a significant number of nanostructured materials has been developed in recent years, the application of nanotechnology in bulk structural materials like iron and steel has been rather limited. The literature details the development of nanostructured materials on steel and nonferrous alloys [14-22]. However, only limited investigations [23] have been carried out to produce nanostructured ADI.

Ductile cast iron is relatively inexpensive and has lower density than steel. The ADI components are 10% lighter than forged steel and the overall production costs of ADI is 30-40% lower than the forged steel [24]. Considering the good combination of strength and toughness in ADI, it is believed that nanostructured ADI will be a potential substitute for structural materials in many critical applications where forged or wrought steels are being used.

The relation between grain size and strength is often expressed in terms of the Hall-Petch equation [25,26]

$$\sigma_y = \sigma_0 + k/d^{1/2} \quad (1.1)$$

where  $\sigma_y$  is the yield stress,  $\sigma_0$  is a materials constant,  $k_y$  is the strengthening coefficient and  $d$  is the average grain diameter. This equation shows that the reduction in grain size will significantly improve the strength and mechanical properties of the ADI. Thus, the reduction in the prior austenite grain size favors the improvement in mechanical properties of ADI.

The primary focus of this investigation was thus, to develop nanostructured austempered ductile cast iron. In this investigation, a unique heat treatment cycle has been proposed to create ADI with nanostructured grains with ausferritic structures in it. High temperature plastic

deformation will result in the refinement of the coarse grain into the nanometer regime. It was hypothesized that, by the deformation and refinement of the austenite grains, it will be possible to produce nanostructured carbide free ferrite and high carbon austenite, referred to as ausferrite in ADI.

The ductility of ADI generally diminishes as the grain size is reduced. However, the ductility of the ADI can be compensated to some extent by the producing proeutectoid ferrite in the microstructure of ADI along with the ausferrite by a process called intercritical austempering. It was also hypothesized that size of the austenite-ferrite lath spatial arrangement can be reduced by the two-step austempering process.

While the mechanism of transformation and microstructural features are well observed in ADI, the uncertainty regarding the stability of austenite remains a debate. Thus, the secondary objective of this investigation is to determine the thermal and mechanical stability of austenite. The cryogenic treatment allowed for the examination of the thermal and mechanical stability of the high-carbon austenite ( $\gamma_{HC}$ ) in the ADI. This investigation also examined the microstructure and mechanical properties of ADI subjected to cryogenic processing. Finally, the co-relation between the microstructure and mechanical properties ADI has been established in this investigation.



## CHAPTER 2. LITERATURE REVIEW

### 2.1 Cast irons

Cast irons are a class of ferrous alloy with the carbon contents above 2.14 wt% and silicon content ranging between 1 to 3%. Cast iron, in practice, often contains 3 to 4.5 wt% carbon, and, in addition, other alloying elements. Cast irons offer a wide range of properties [27] including strength, ductility, machinability, hardness, damping capacity, thermal conductivity, castability, wear resistance and corrosion resistance together with low cost. The chemical composition and the cooling rate determine the form that the graphite takes in cast irons. As the cooling rate increases, the tendency to form graphite decreases, whereas the increase in the concentration of carbon or silicon promotes graphitization in cast irons. The combined effect of elements such as carbon, silicon and phosphorous can be represented by a term called carbon equivalent (C.E)

$$\text{C.E} = \%C + 0.33(\%Si + \%P) \quad (2.1)$$

C.E determines how close the given analysis is to that of the eutectic composition (C.E=4.3) for specific cooling rates [28]. The carbon and silicon content of the different types of cast iron is compared to that of the steel in Figure 1. Historically, cast iron was divided into two categories namely white cast iron and gray cast iron based on their fractured surface. With the advent of metallography, other classifications based on the microstructural features were established. The most common types of cast irons include white cast iron, gray cast iron, malleable cast iron and ductile cast iron.

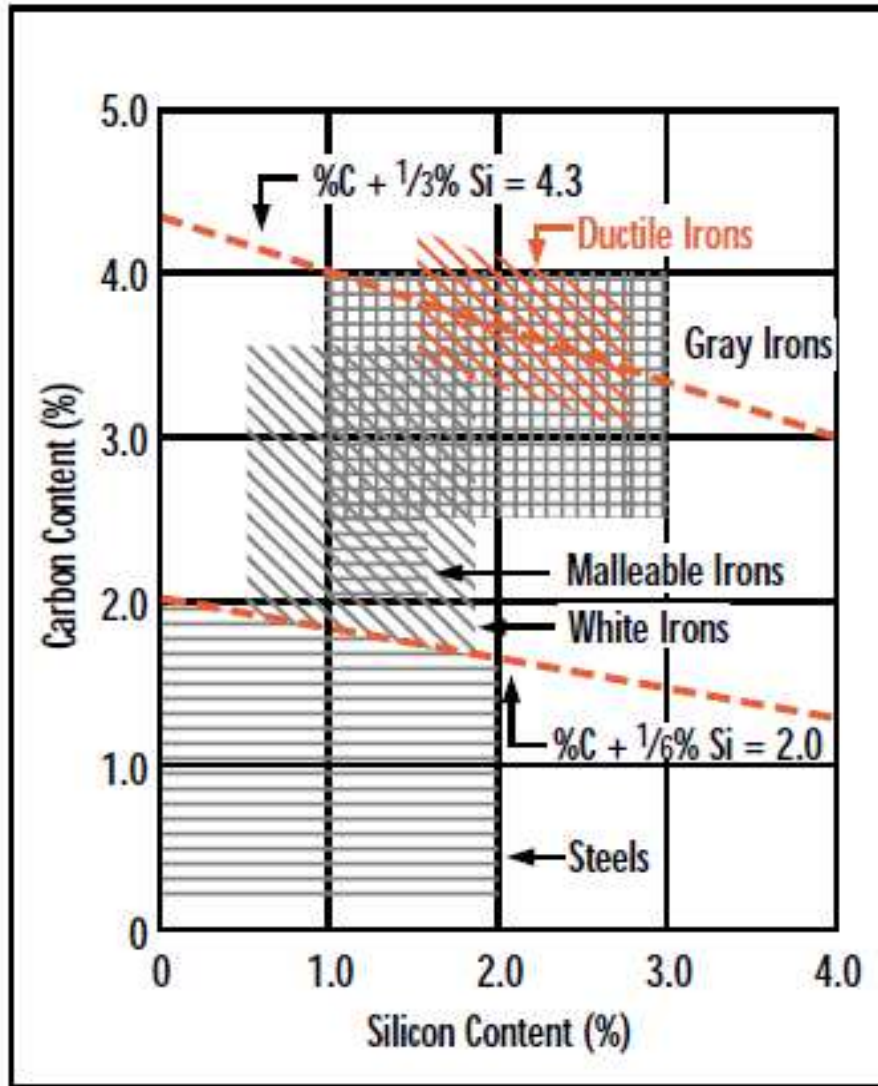


Figure.1: Carbon and silicon content in cast iron compared to steel [29]

### 2.1.1 Gray cast iron

The carbon and silicon content of gray cast iron vary between 2.5 to 4wt% and 1 to 3wt% respectively. During solidification, the graphite occurs in the form of flakes in these types of cast iron. The fractured surface of the gray cast iron takes on a gray appearance, because the fracture occurs along the graphite flakes. The microstructure of the gray cast iron consists of graphite flakes surrounded by ferrite or pearlite matrix as shown in the Figure 2(a). Gray cast iron exhibits

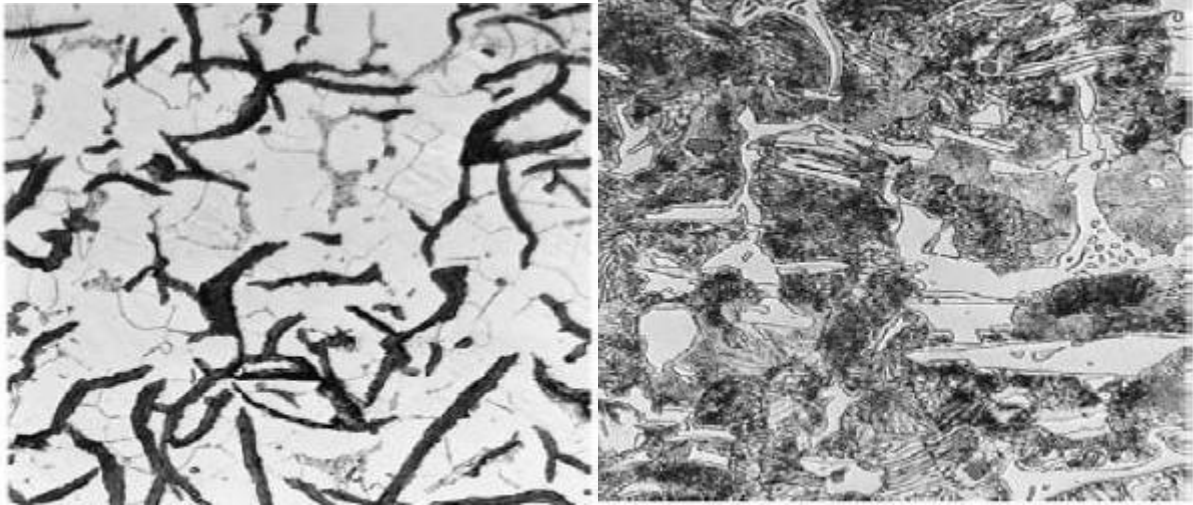
high damping capacity, high thermal conductivity, high wear resistance, moderate strength and low ductility. Gray cast iron is used in applications such as transmission cases, brake rotors, cylinders and liners [27-31].

### **2.1.2 White cast iron**

When the C.E is below than the eutectic value, specifically due to lower silicon content or due to rapid cooling rates, most of the carbon are present in the form of cementite rather than graphite. In this type of cast iron, the fracture occurs along the iron carbide plates and exhibits white crystalline appearance, hence termed as white cast iron. The microstructure of the white cast iron consists of cementite and pearlite, which is a ferrite-cementite layered structure as shown in the Figure 2(b). White iron is extremely hard and brittle. White cast iron is used in applications that requires hard and wear or abrasion resistance such as the roller mills, grinding mills, shell liners and bearing surfaces [27-31].

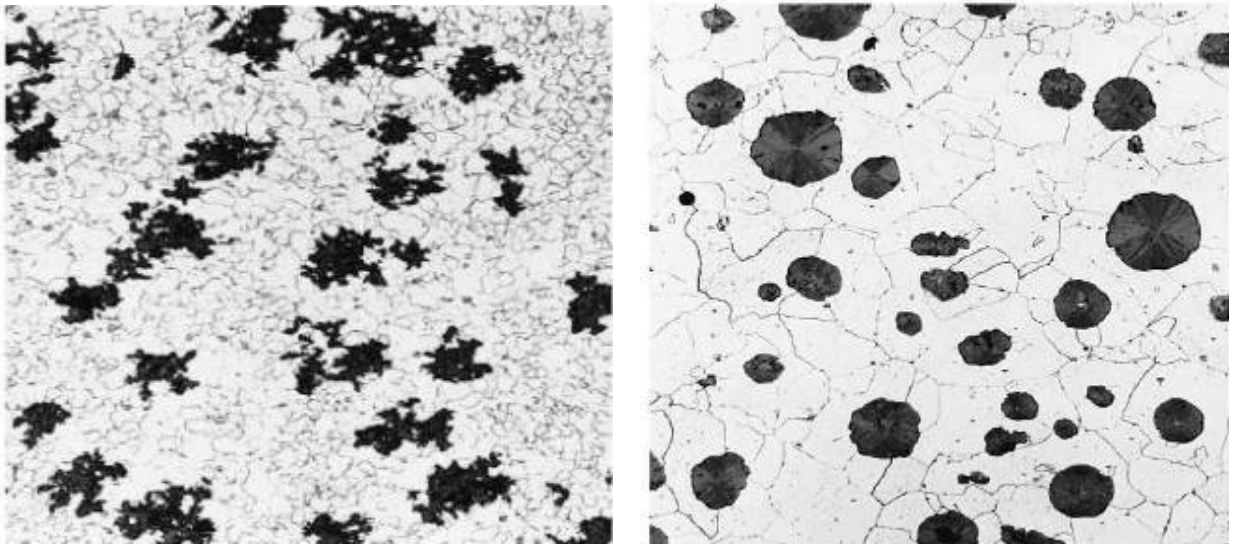
### **2.1.3 Malleable cast iron**

Malleable cast iron is the heat treated white cast iron. Prolonged high temperature annealing (between 800-900°C) of the white cast iron in a neutral atmosphere induces the decomposition of cementite into graphite. The graphite exists in the form of clusters or rosettes as shown in the Figure 2(c). The resulting microstructure of the malleable cast iron consists of graphite distributed in the pearlite or ferrite matrix depending on the cooling rate. Malleable cast iron has relatively high strength from 280 MPa to 800 MPa and good elongation from 2 to 18%. Some of the applications of malleable cast iron includes connecting rods, transmission gears, pipe fittings etc. [27-31].



(a)

(b)



(c)

(d)

Figure.2:Optical photomicrographs of cast irons (a)Gray cast iron (500X), (b)White cast iron (400X), (c)Malleable cast iron (150X), and (d) ductile cast iron (200X) [28]

#### **2.1.4 Ductile cast iron**

When alloying elements like magnesium or cerium is added to the gray cast iron, graphite flakes, which are the weakest structural features, takes the shape of nodules and imparts ductility to the material. The distinctive characteristic of ductile cast iron is the presence of graphite nodules in the microstructure matrix. The graphite nodule imparts ductility to the material, almost 5 to 20% greater than gray cast iron and hence the name 'ductile cast iron'. The graphite nodules in the ductile iron must be as spherical as possible, else they act as stress raisers. The control of the graphite shape is important in nodular cast iron. The percent nodularity can be calculated per the ASTM standard E2567[32]. The nodularity of 80% can be easily achieved in ductile iron [8]. Ductile cast iron is also referred to as nodular or spheroidal graphite irons..

The mechanical properties of the ductile cast iron are determined by the matrix which may be ferrite or pearlite or mixture of both depending on the heat treatment as shown in the Figure 2(d). To facilitate the dissolution of carbon into austenite during the heat treatment, it is recommended to have a pearlite as cast structure in ductile cast iron [27]. The ductile cast iron is extensively processed by various heat treatments such as annealing, stress relieving, hardening, normalizing and austempering. Typical applications of ductile cast iron include valves, gears and other automotive components[27-31].

#### **2.2 Austempered ductile cast iron (ADI)**

Austempered ductile cast iron is the most recent addition to the ductile iron family. Austempering is an isothermal heat treatment process in which the ductile cast iron is heat treated in the bainitic transformation range usually 260-400°C (500-750°F) after austenitization in the temperature range of 871-982°C (1600-1800°F). Austempering process is extensively used in ductile iron to obtain superior mechanical properties [33,34]. This results in austempered ductile

cast iron (ADI) with an exceptional combination of strength, toughness and wear resistance. ADI exhibits higher strength, good machinability, impact values much higher than pearlitic grades and comparable to that of ferritic grades. The comparison of mechanical properties [29] in Figure 3 shows that the strength of the ADI is much higher than gray iron or the quenched and tempered ductile iron.

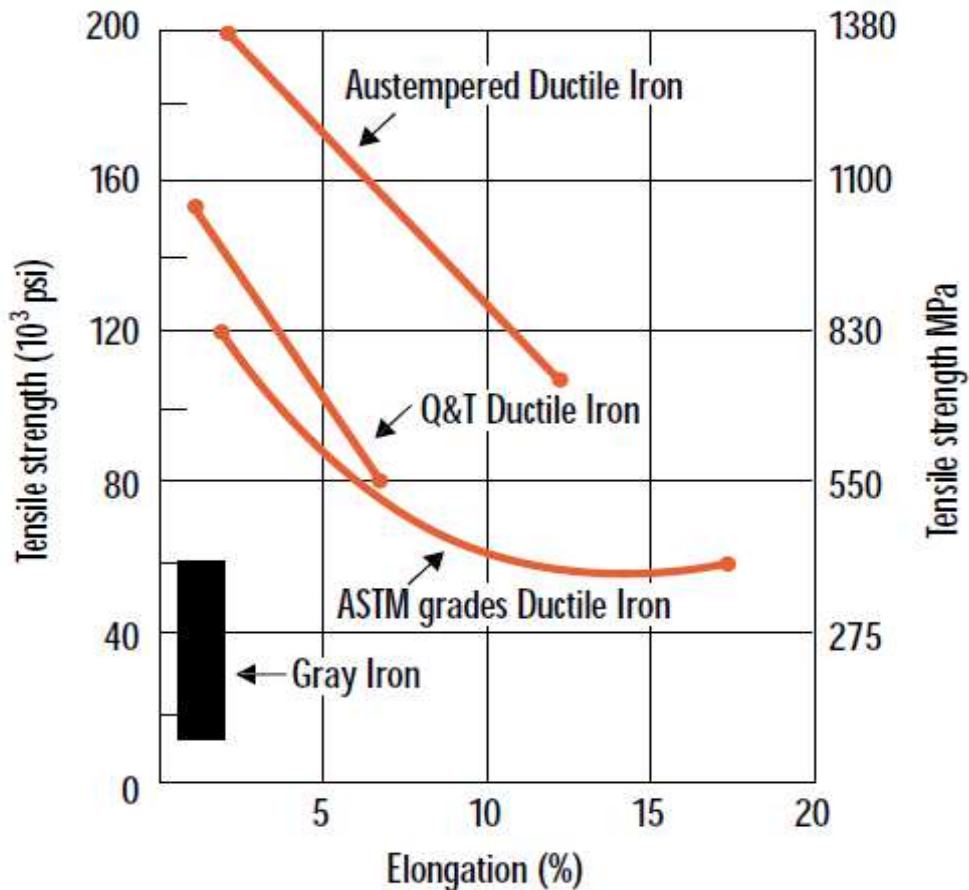


Figure.3: Comparison of mechanical properties of various types of ductile cast iron [29]

### 2.3 Chemical composition of ADI

The chemical composition of ADI is very important factor in determining the mechanical properties. Adequate control of chemical composition determines the optimum properties of ductile iron castings. Alloying elements like Mn, Mo, Ni and Cu are added to the ductile cast iron

mainly to increase the hardenability of the material, to avoid pearlite nose at the CCT curve [6]. The average concentration of manganese can be varied between 0.25 to 0.5wt % to prevent the segregation of manganese along the cell boundaries, which may result in heterogenous hardenability [35,36]. Molybdenum is the most potent hardenability enhancer in ADI. However, like Mn, Mo also segregates along the cell boundary and serve as the nucleation site or the propagation path for the cracks. Thus, the concentration of molybdenum is usually limited to a minimum up to 0.2% and should be used in combination with Ni or Cu. The addition of Ni/Cu shortens the time required to complete austempering process. The Ni concentration may vary between 0.5 to 3.5 wt % and the Cu concentration may vary from 0.5 to 1.0 wt%. The carbon and silicon contents in ductile iron must be adjusted per the section size [36].

#### **2.4 Processing of ADI**

Melting, casting and heat treatment of ductile cast iron alloyed with elements such as Ni, Mo and Cu are the three major steps involved in the processing of ADI. Heat treatment is performed in ductile iron to improve the strength, toughness, ductility and increase the machinability by controlling the microstructure. The heat treatment of ADI involves three steps: 1) Austenitizing, 2) Quenching and 3) Austempering. The final properties of ADI depend on all the three heat treatment cycles.

During austenitizing, the ductile iron casting is heated to a temperature ranging between 1600°F-1800°F. The casting is held at this temperature for 1-2 hours. The rate of austenitizing has very little effect on the final properties of the material. The alloy addition, segregation of alloying elements and the section size should be considered for optimizing the austenitization temperature and time [37]. During this process, the matrix microstructure of the ductile iron is completely transformed to face center cubic (FCC) austenitic ( $\gamma$ ) phase saturated with carbon [37].

After austenitizing, the ductile cast iron is quenched in a molten salt bath to avoid surface oxidation. The rate of quenching must be high enough to avoid the formation of pearlite as shown in the isothermal transformation diagram in Figure 4. The molten salt bath is maintained in the austempering temperature range of 500°F to 750°F. The temperature and time of austempering have major effect on the final properties of the material.

Austempering is an isothermal heat treatment process and involves two stages [38-40]. During the first stage, the austenite ( $\gamma$ ) is decomposed into ferrite ( $\alpha$ ) and high carbon austenite ( $\gamma_{HC}$ ):

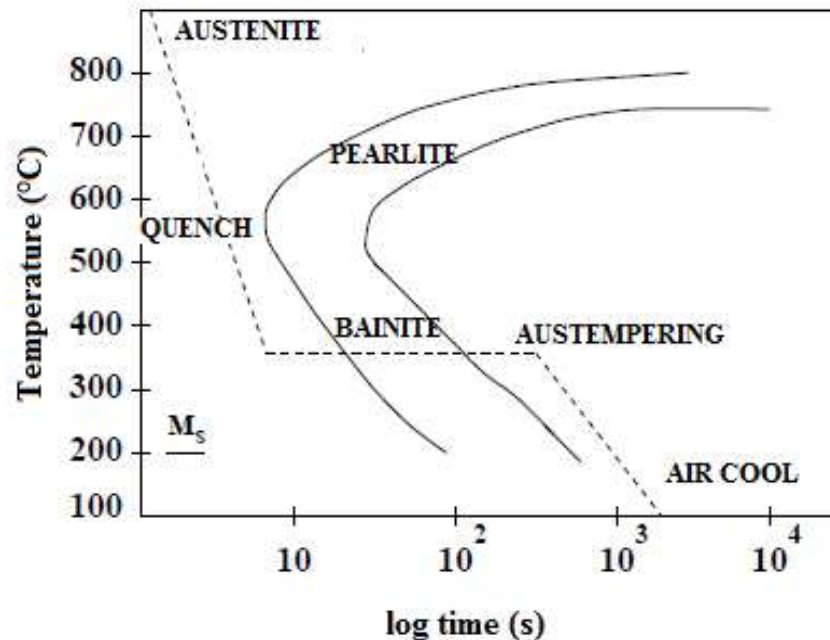


Figure.4: Isothermal transformation diagram for unalloyed ductile cast iron together with time temperature transformation (TTT) curve

The ductile iron is held at the austempering temperature for a sufficient time to yield a microstructure whose matrix is mostly ausferrite and free of pearlite and martensite. If the ductile



cast iron casting is held at the austempering temperature for too long, undesirable second stage occurs in which the high carbon austenite can further decompose into ferrite and carbide:



$\varepsilon$  carbide is undesirable and must be avoided, otherwise, it will make the material brittle. The period between the completion of the first reaction and the onset of the second reaction is called the "process window". In general, addition of alloying elements such as Ni, Mo and Cu will significantly enlarge the process window in ductile cast iron and thus helps in achieving optimum combination of strength and ductility in ADI.

## 2.5 Microstructure of ADI

Austempering of ductile cast iron produces a unique microstructure consisting of predominantly bainitic ferrite, high carbon austenite with graphite nodules dispersed in it. Other constituents of the microstructure may include martensite and carbides.

### 2.5.1 Bainite in ADI

Bainite is formed at isothermal transformation temperature range of 260 to 400°C (500 to 750°F), which is below the pearlitic transformation temperature but above the martensitic start temperature. In this isothermal transformation temperature range, the bainite occur in two different forms, namely upper and lower bainite.

### 2.5.2 Upper bainite

When the ductile iron is austempered in the upper bainitic temperature range above 600°F and up to 750°F, coarser carbide free ferrite and retained austenite along with graphite nodules occur in the microstructure. The resulting microstructure with carbide free ferrite and high carbon austenite ( $\alpha + \gamma_{\text{HC}}$ ) is referred to as 'ausferrite' [41-43]. This structure is different from those of bainite in steel as shown in the Figure 5. The formation of cementite phase as in the bainitic

reaction of steel is generally suppressed in ADI or high silicon steels due to the presence of high concentration of Si and C content.

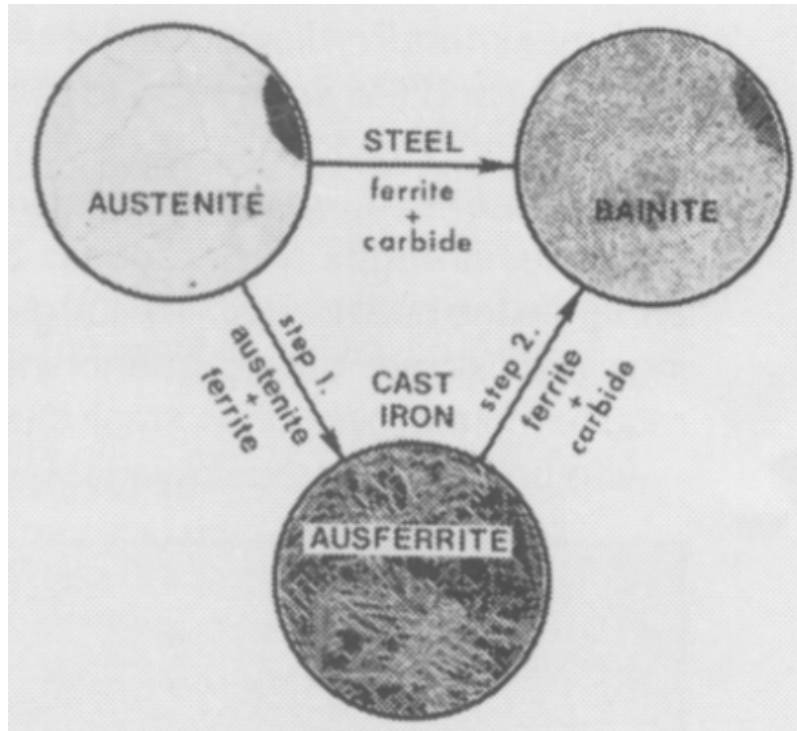


Figure.5: Difference between ausferrite in ductile iron and bainite in steel [34]

Additionally, carbon rejected from the ferrite does not form carbide in ADI because of the high concentration of Si. Instead the carbon enters the solid solution and enriches the austenite. When the austenite is sufficiently saturated with carbon, the martensite start temperature is moved below the room temperature resulting in stable austenite in ADI.

### 2.5.3 Lower bainite

Austempering of ductile cast iron in the lower bainitic temperature range of 500°F to 600°F results in the microstructure consisting of fine needle shaped bainitic ferrite and austenite along with graphite nodules. The major difference between the upper and lower bainite is that the carbide precipitates within the bainitic ferrite plates as represented in the Figure 6. However, in

ADI and high silicon steels, the carbide may occur in different forms such as carbides or other transition carbides [41-46].

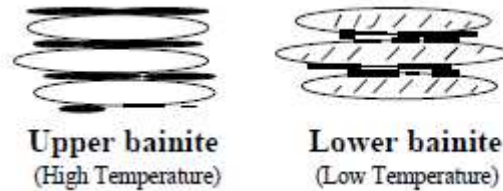


Figure.6: Schematic representation of upper bainite and lower bainite

#### 2.5.4 Austenite

Austenite is the gamma phase iron with a face centered cubic structure. The face centered cubic structure of austenite allows dissolution of high proportion of carbon in it [41]. Austenite is generally evident at temperatures above  $723^{\circ}\text{C}$  depending on the carbon content. The volume fraction of austenite and its carbon content mainly depends on the austenitizing temperature. During isothermal transformation process, bainitic ferrite nucleates at the grain boundary by enriching and saturating the austenite with carbon. When the austenite is sufficiently saturated with carbon, the diffusion of carbon ahead of ferrite becomes difficult and the growth of ferrite is arrested. After the course of isothermal transformation, remaining austenite can be retained at room temperatures and they occur as slivers between the ferritic needles [41-46].

#### 2.5.5 Martensite

A portion of the high carbon austenite may transform into martensite up on cooling to room temperature or under conditions of suitable stress or strain.

#### 2.6 Nucleation and growth process of bainite

The bainitic transformation occur at the interfaces, where the transformation of austenite to ferrite takes place by the nucleation and instantaneous growth of bainitic subunits.

The transformation progresses with the formation of aggregates of subunits called sheaves.

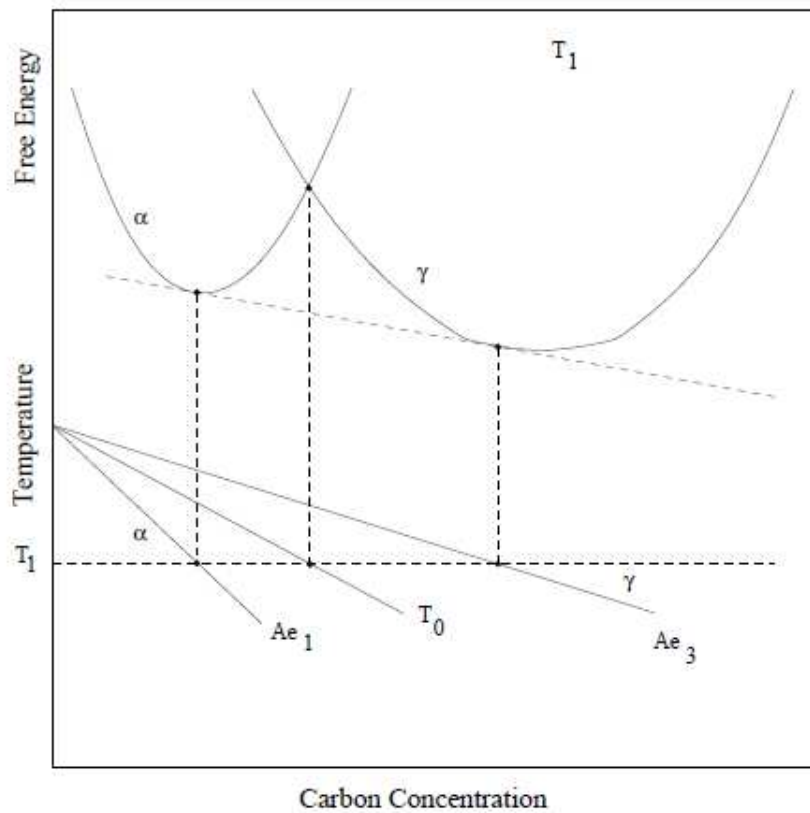


Figure.7:  $T_0$  curve construction on the Fe-C Phase diagram using free energy of austenite and ferrite

Review of the existing literatures shows that growth of bainite occur by diffusionless phenomena [45,46]. A thermodynamic model [47] for the phase transformation in steels, introduced by Zener shows that the growth of bainite occur by diffusionless phenomena in which the carbon is partitioned into the residual austenite after growth. Films of carbon enriched retained austenite gets trapped between the bainitic subunits. As the subunit of bainite continue to nucleate at the grain boundaries, the austenite becomes enriched and saturated with carbon. The next subunit must grow from the carbon enriched austenite. Figure 7 shows the equilibrium carbon concentration  $Ae_1$  and  $Ae_3$  curves of ferrite and austenite respectively. The growth of the new subunit is arrested when the austenite is completely saturated with carbon or when the carbon

concentration of austenite reaches  $T_0$  curve, the diffusionless transformation is thermodynamically unfavorable and remains untransformed. The remaining austenite can be retained to room temperature.

## **2.7 Mechanical properties of ADI**

Mechanical properties of ADI are dependent on various interlinked factors such as the chemical composition, austenitizing and austempering temperatures and times, as cast microstructure, microstructural features after the heat treatment.

The microstructural features prior to the heat treatment significantly influences the properties of the ADI. The prior pearlitic structure increases the toughness of ADI with respect to the holding time as longer holding time is necessary to decompose the relatively stable carbides around the eutectic cell boundaries [48].

Austempering temperature plays a significant role in defining the mechanical properties of ADI. At lower austempering temperatures near 500°F, fine acicular ferritic structure along with a smaller volume fraction of austenite provides high tensile strength up to 1600 MPa (260 Ksi) and hardness of about 60HRC. However, limited ductility with only 1% elongation and poor machinability is obtained at this lower austempering temperatures. At higher austempering temperatures near 725°F, a typical ausferritic structure consisting of coarser ferrite and higher volume fraction of austenite (up to 40%) provides substantial improvement in ductility with elongation of up to 14% and good machinability with relatively lower hardness value and limited strength in the range of 800MPa to 1200MPa [49]. Greatest amount of high carbon austenite provides maximum ductility to the material [50]. Thus, the mechanical properties of ADI are dependent on the fineness of ferrite and austenite in the ausferritic structure and the carbon content of austenite [49-52]. Recent studies [49] shows that the mechanism of strengthening of

ferrite is caused by strain hardening and the austenite strengthening is obtained by the solution hardening and grain refining.

The machinability of the ADI can be improved when the microstructure of ADI contains a considerable amount of ferrite in the matrix. Numerous studies [53-56] are being undertaken to develop dual phase matrix containing ferritic-ausferritic structures to enhance the machinability properties of ADI to compete with forged steels.

## **2.8 Fracture toughness of ADI**

The fracture toughness of the ADI is strongly dependent on its microstructural features such as the morphology of ausferritic structure, retained austenite and the carbon content of austenite [1,2, 57-60]. Studies [2,57,58] have shown that the following relationship is valid for the fracture toughness of ADI.

$$K_{IC}^2 = \sigma_y (X_\gamma C_\gamma)^{1/2} \quad (2.5)$$

where  $K_{IC}$  is the fracture toughness,  $\sigma_y$  is the yield strength,  $X_\gamma$  is the volume fraction of austenite,  $C_\gamma$  is the carbon content of austenite. Other researchers have shown that the yield strength of ADI is dependent on the ferritic cell size and width of the ferrite [1, 58-60]. The maximum fracture toughness of  $66\text{MPa}\sqrt{\text{m}}$  is obtained in conventional ADI with finer ferritic structure when the ADI is austempered at lower austempering temperatures [61-62]. In conventional austempered ductile iron [63-64]. Improvement in the fracture toughness is possible by reducing the ferrite particle size, stabilizing the retained austenite content and by increasing the carbon content of austenite which will increase the strain hardening ability in ADI.

## **2.9 Intercritical austenitizing**

A review of the literature indicates that the ductility of most nanostructured materials is low compared to the conventional microcrystalline counterparts [65-67]. The limitation of

conventional ADI includes the absence of proeutectoid ferrite in the microstructure as well as the predetermined amount of transformed ferrite content in the process window range. Intercritical austempering will produce dual matrix structure consisting of ausferrite (bainitic ferrite and high carbon austenite) and proeutectoid ferrite in the matrix. This material will exhibit much greater ductility than the conventional austempered or quenched and tempered ductile iron [65-67]. This can be achieved by austempering the ductile iron from the intercritical austenitizing temperature range as represented in Figure 8.

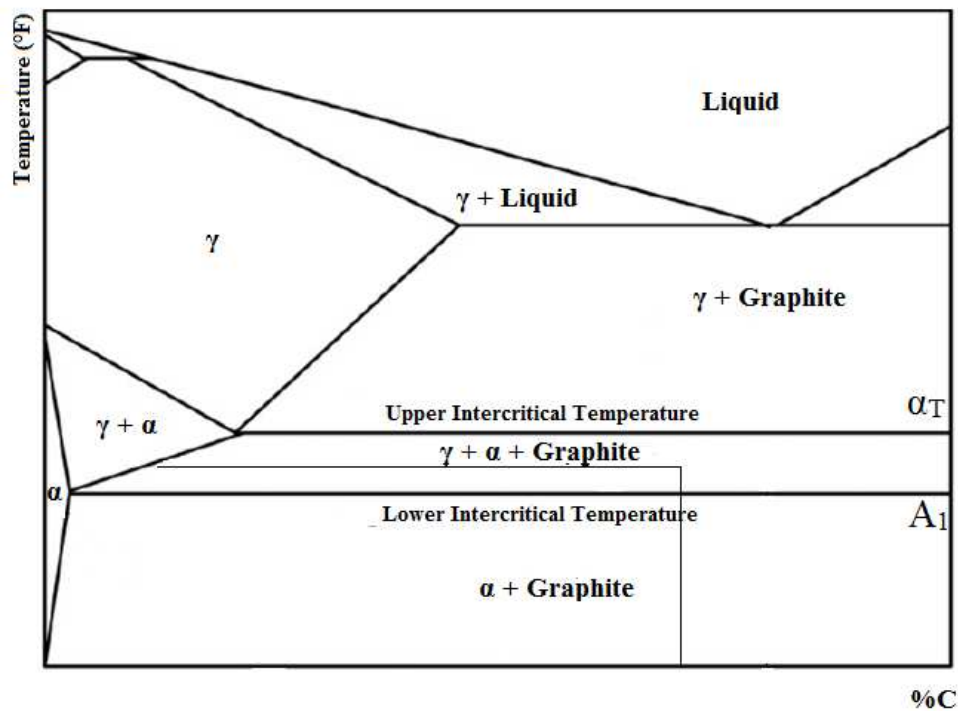


Figure.8: A schematic diagram of intercritical austenitization process

During intercritical austempering, ductile cast iron is austenitized in the temperature range between  $A_1$  and  $\alpha$  trans ( $\alpha_T$ ) where the austenite, ferrite and graphite ( $\alpha + \gamma + \text{graphite}$ ) co-exist [68-70], and then austempered. This will produce a microstructure consisting of bainitic ferrite and high carbon austenite together with proeutectoid ferrite. As predicted by the lever rule [71],

the holding in the intercritical austenitizing region determines the austenite carbon content before austempering as well as controls the volume fractions of austenite and proeutectoid ferrite based on the intercritical austenitizing temperature [72].

Ductile iron with dual matrix structure (DMS) was introduced in the early 1980's [73]. The DMS ductile iron consisted of ferrite as soft phase and either bainite or martensite as the hard phase. Existing literature shows that [74], the mechanical properties of ADI with DMS consisting of ferrite-bainite has better mechanical properties than the ferrite-martensite combination. It is also shown that the Stage 1 austempering reaction can be accelerated by lowering the austenitization temperature, resulting in mechanical properties that satisfies the ASTM standard [75-77].

Austenitizing the low alloyed ductile iron in the ( $\alpha+\gamma$ ) range, stabilizes the austenite phase by diffusing the austenite forming elements into the austenite phase, thereby improving its strength and toughness properties. This austenite is less likely to transform into martensite while cooling to room temperature or up on application of stress [78]. Rouns et al. [79] showed that for a given austempering temperature, the volume fraction of the untransformed austenite decreases with the decrease in austenitizing temperature. At lower austempering temperatures, the transforming percentage of ferrite from the austenite is higher in ADI when austenitized in the intercritical region [80]. The volume fractions of the proeutectoid ferrite and austenite, in turn will influence the tensile strength and ductility. Hence, these parameters can be successfully optimized by choosing the critical combinations of intercritical austenitizing and austempering temperatures. Amount of ferrite present can be varied from 5% to 85% by the intercritical austempering process. The intercritically austempered ADI with approximately 75% ausferrite exhibits best combination of strength and ductility compared with pearlitic grades [81]. Kobayashi et al. [82] attempted to



improve the strength and toughness by austempering the ADI from ( $\alpha+\gamma$ ) range. This intercritical austenitizing significantly improved crack propagation resistance in the Ni and Mg alloyed iron.

Tensile stress of about 1.15GPa with up to 16% elongation can be achieved by the intercritical austempering process [83-86]. The strength and hardness of this material is comparable to that of the pearlitic grades and much higher than the ferritic grades. The ductility of intercritically austempered ADI is four times higher than the pearlitic grades but like that of the ferritic grades adequate for most applications [69]. The intercritical austempered ADI finds applications such as suspension parts [87], which requires a good combination of strength and ductility.

### **2.10 Two-step austempering**

Two-step austempering process involves quenching the material from the austenitizing temperature to a lower austempering temperature to create larger supercooling to facilitate more ferrite nucleation. The transformation of austenite to ferrite by the isothermal treatment occur by nucleation and growth process [88-90]. Nucleation depends on supercooling and the high carbon content can be achieved by higher austempering temperature. Once the nucleation is complete, the material is then heated to a higher austempering temperature thus promoting growth of ferrite by faster diffusion of carbon and thus increasing the carbon content of austenite. [91-93].

Putatunda [91] proposed the two step austempering process in which the ADI samples were quenched to a low temperature range between 260°C and 375°C, at which the samples were held for 5 minutes and then held to a time of 2 hours austempering, at which the temperature was raised by 14°C/h. Another variant of the two-step processing proposed by Yang et al [92], consists of quenching at low austempering temperature for 5 minutes and then holding for 2 hours by increasing the austempering temperature 30°C higher than the first austempering temperature.

Existing literatures [91-94] reports that the ADI austempered by two-step austempering process produced higher strength and toughness than those ADI austempered by single step austempering process. The morphology of the ferrite, austenite and the carbon content of austenite play a major role in determining the mechanical properties of ADI. Two-step austempering will reduce the overall time for the processing of ADI, produces very fine grain ausferritic structure and simultaneously results in significant improvement the strength and toughness of ADI [91-94].

### **2.11 Cryogenic processing**

Cryogenic processing is a heat treatment in which the work piece is subjected to temperatures below  $-190^{\circ}\text{C}$ . Cryogenic processing is gaining significant interest in recent years as it results in improved mechanical properties in ADI as reported in several investigators [95-98].

Cryogenic treatment promotes the transformation of the residual austenite to martensite [96], therefore, wear resistance of the ADI is significantly improved by the cryogenic treatment [98,99]. Conventional cryogenic processing involves several steps such as (a) Ramp down, (b) hold, (c) Ramp up and (d) Tempering. During ramp down stage the material is slowly cooled down from an ambient temperature to a temperature ranging between  $-80$  to  $-155^{\circ}\text{C}$ . This slow cooling prevents the temperature gradient and thus allows the stresses to be minimum. Then the material is held at the subzero temperature for a predetermined time and then ramped up to the ambient temperature followed by tempering at a slightly elevated temperature.

Cryogenic processing is applied to components such as brake rotors, gun barrels, racing motor components, cutting tools, tool steels, landing gear systems, turbine blades etc.

### **2.12 Stability of austenite**

Control of the heat treatment process mainly to produce the appropriate amount of austenite is important in determining the grade of ADI [97]. The amount and the stability of

austenite in ADI determine the final properties of the ADI castings [96]. The presence of mechanically unstable austenite aids the hardening process during manufacturing [99,100].

Several published studies [96,100-104] have reported that the austenite is not mechanically stable and transforms to martensite by transformation induced plasticity (TRIP) phenomena. Such unstable austenite that transforms into martensite by the transformation induced plasticity (TRIP) phenomena results in excellent combination of strength and elongation in steels [103-104]. Cryogenic treatment results in conversion of unstable retained austenite to martensite without any mechanical tests in ADI [95].

Several other literatures [105,106] have reported no such transformations in ADI. The stability of the austenite also depends on the graphite nodularity. Greater stability of the austenite can be achieved by the higher fraction of graphite nodules in the microstructure of ADI [107]. Austenite stability is also affected by the austempering time. Shorter austempering times lead to the complete transformation of thermally unstable austenite to martensite up on cooling to room temperature. However, longer austempering time will lead to the increase in volume fraction of ferrite, while further transformation within the processing window range, will stabilize the austenite [108].

### **2.13 Nanostructured ADI**

A review of the existing research shows that nanostructured materials produce better physical and chemical properties owing to their large number of crystallite interfaces. Nanostructuring of metals and alloys has been used in recent years to improve the mechanical properties of bulk materials [21].

During the last decade, number of studies have been carried out to produce ultra-fine grained metallic alloys with enhanced properties such as high strength, superplastic properties

than the coarse-grained materials [109]. However, the nano crystallinity affects the ductility of the material and hinders the use of these materials in structural applications. This lack of ductility is not due to the brittleness but due to the lack of strain hardening [110, 111].

Nieman et al [112] performed the first mechanical test on nano crystalline metals. Further literatures focused on the development of nanostructured materials in nonferrous alloys and steel [12-22, 113]. By now, nanostructures have been obtained in various pure metals, alloys and steels by the application of severe plastic deformation techniques. Plastic deformation is permanent deformation produced by the application of sufficient stress or strain beyond the elastic limit of the material. Plastic deformation has a significant effect on the microstructure and improvement of properties in a material. Several authors have tried to reduce the grain size by various plastic deformation techniques including equal channel angular pressing, torsion straining, multiple forging, alloying, repetitive corrugation and straightening [113-116]. There are several disadvantages associated with the above-mentioned plastic deformation techniques such as contamination, micro porosity resulting in brittleness of the material.

Refinement of the microstructure by transformation, rather than deformation lead to combination of increased strength, toughness and hardening of larger sections [117]. In steels with high carbon and silicon content, it is possible to produce high strength and toughness by isothermal transformation, inducing carbide free bainitic structures and high carbon austenite, both in the nanoscale dimensions [20, 52].

Characteristics of ADI including the non-homogenous chemical composition in the micro regions, thickness of the specimen, presence of graphite has a significant effect on the heat treatment process. Therefore, it is difficult to obtain ferritic structures in the submicron range with characteristics like that of a nano bainitic steel [20,52]. Only, a very few investigations have been

carried out recently on the development of ultra-fine ADI. Azevedo et al [118] achieved refinement in austenite grain boundary by a process of rapid austenitization of prior martensitic structures. A recent study carried out by D. Myska et al. [23, 108] proposed that longer isothermal transformation time at lower ausferritic transformation temperature range, resulted in significant refinement of ferrite plates in less than 100nm range.

In ADI used in this study, it is hypothesized to produce nano grains by the deformation of the austenite grains. During high temperature plastic deformation in ADI, deformation energy produces simultaneous deformation and recrystallization of austenite grains. As the austenite grain deform, austenite grain boundaries give more nucleation sites for the growth of finer ferrite as shown in the Figure 9.

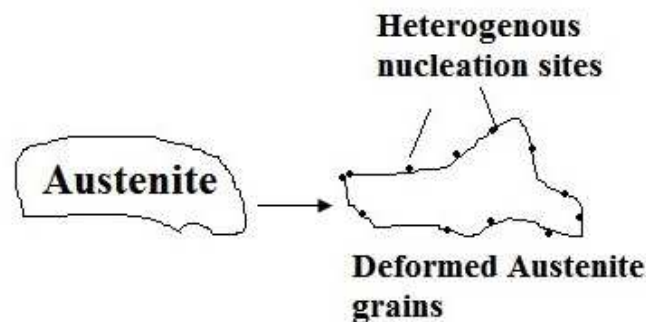


Figure.9: Plastic deformation of austenite grain.

During austempering or isothermal transformation, more ferrite nucleates at a shorter time. Therefore, it is also hypothesized that austenitization followed by the high temperature plastic deformation will result in much shorter time for austempering than the conventional austempering process.

### **CHAPTER 3. OBJECTIVES**

The objectives of this investigation are as follows

- To develop a nanostructured austempered ductile cast iron.
- To examine the effect of conventional austempering, cryogenic processing, intercritical austempering and plastic deformation on the microstructure, lath size, ferritic cell size and mechanical properties of the ductile cast iron.
- To investigate the thermal and mechanical stability of austenite.
- To establish the correlation between the microstructure and mechanical properties of ADI.

## CHAPTER 4. EXPERIMENTAL PROCEDURE

### 4.1 Material

A low alloyed ductile cast iron with the chemical composition detailed in Table 1 is used in this study. The material was originally cast in the form of KEEL blocks per ASTM standard A-536[119]. The KEEL blocks measured 7.9"X 3.0"X4.0". From these cast blocks, cylindrical tensile samples and compact tension sample blanks for fracture toughness tests were prepared as per ASTM standards E-8 [120] and E-399 [121], respectively.

Table 1: Chemical composition of ductile cast iron

Element	Wt%
C	3.44
S	0.008
P	0.016
Si	2.46
Mn	0.08
Cr	0.05
Cu	0.52
Ni	1.03
Mo	<0.01
V	0.017
Al	0.018
Ti	0.010
Mg	0.043
Ce	0.013

## 4.2 Heat treatment

After fabrication, the cylindrical tensile samples and compact tension blanks were divided into 4 sets (A, B, C, D and E) and heat treated as follows.

### 4.2.1 Conventional austempering

The first set of samples (A) were initially austenitized at 927°C (1700°F) for 2 hours and then quenched and austempered in a molten salt bath. Figure 10 shows the schematic diagram of the conventional heat treatment performed in this study.

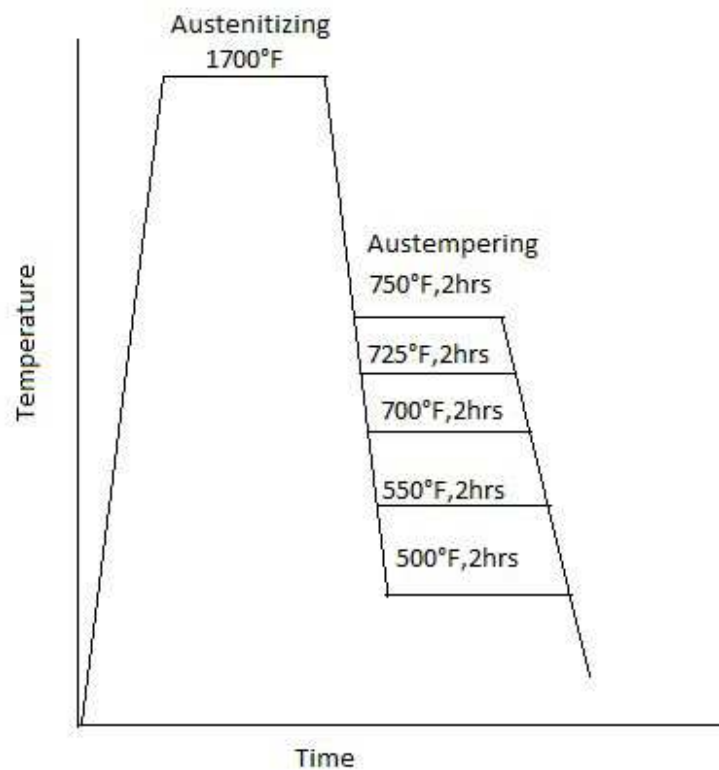


Figure.10: Schematic Diagram of the conventional austempering heat treatment



The austempering temperatures were chosen in such a way that specific samples had either an upper or lower bainitic microstructure. As the demarcation between upper and lower bainitic temperature is 600°F, the lower bainitic temperature range of 500°F and 550°F was chosen for specific samples and to ensure specific samples had upper bainitic microstructure, an upper bainitic temperature range of 700°F, 725°F and 750°F were also chosen.

#### 4.2.2 Cryogenic processing

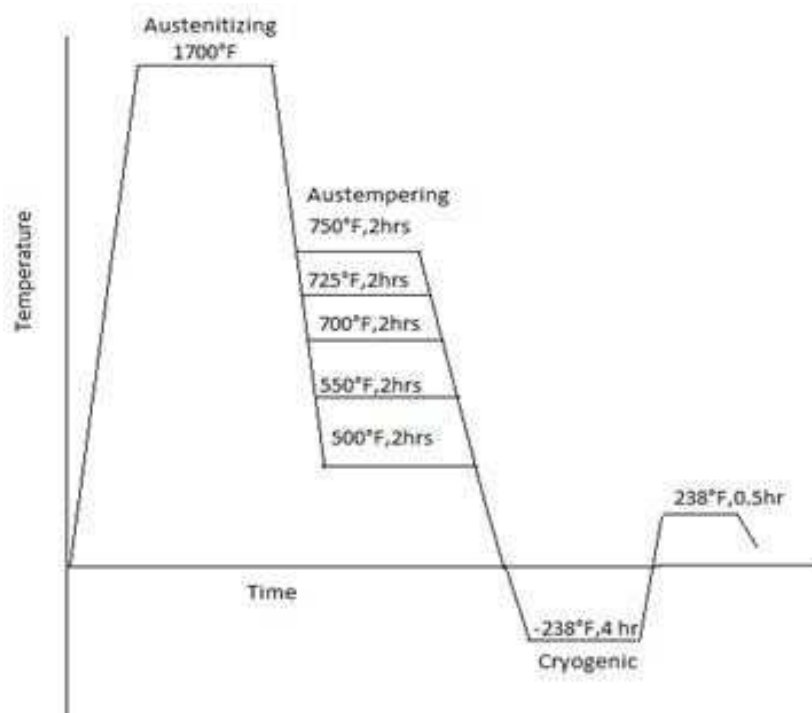


Figure. 11: Schematic Diagram of the cryogenic heat treatment process

The austempered samples from the each of the first set were divided into two groups (A1 and A2); one group from each is set aside. The second group of the samples (A2) were then cryogenically treated by cooling them from ambient to -238°F (-150°C) over the course of eight hours as shown in the Figure 11. The samples were held at -238°F(-150°C) for four hours before allowing them to rise to ambient temperature again over the course of eight hours. All the cryogenically-treated samples were then tempered at +238°F (+150°C) for half an hour.

### 4.2.3 Intercritical austempering

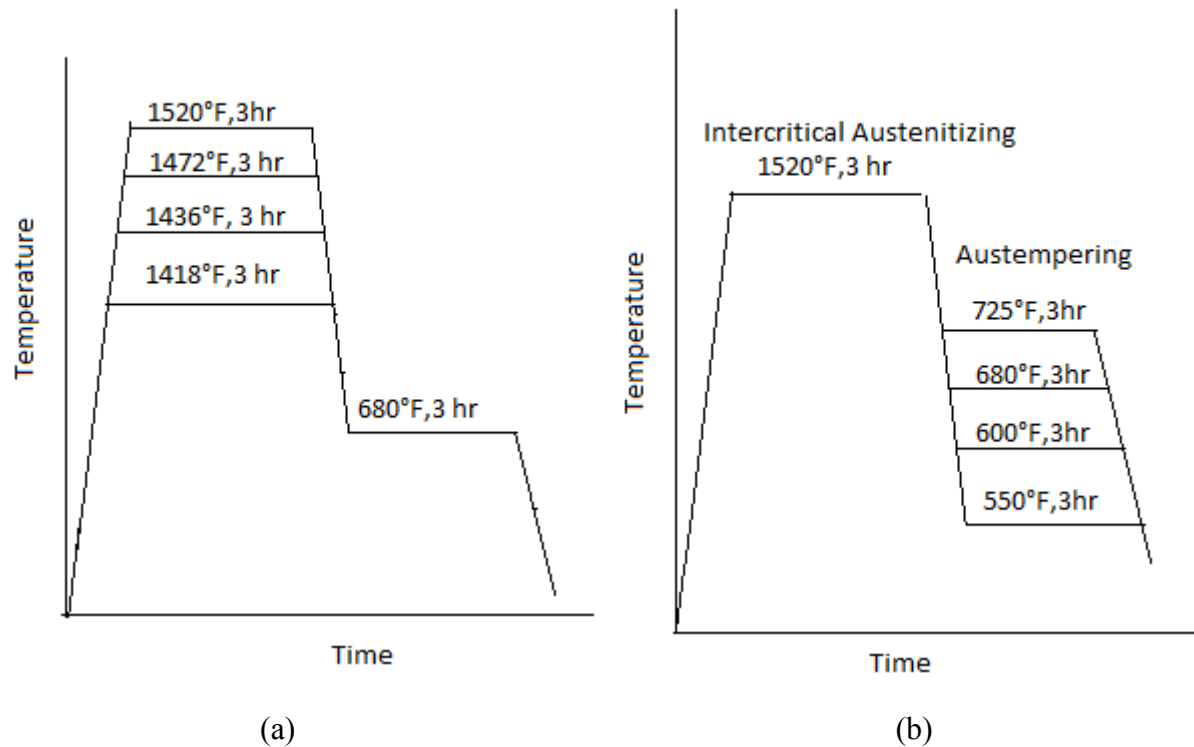


Figure.12: Schematic diagram of intercritical austempering process

An equation [97] developed by the Ductile Iron Society was used to predict the upper intercritical temperature (UCT) and lower intercritical temperature (LCT). Based on the chemical composition of the ductile iron used in this study, it was determined to be 1520°F and 1404°F respectively. The second set of samples (B) were divided into four groups (B1, B2, B3, B4) and intercritically austenitized at temperatures between  $A_1$  and  $\alpha_T$  at 1520°F, 1472°F, 1436°F, 1418°F and then quenched and austempered for 3 hours in a molten salt bath maintained at 680°F as shown in the Figure 12(a). To determine the effect of austempering temperatures with respect to intercritical austenitization, several austempering temperatures (725°F, 680°F, 600°F, 550°F) were chosen for the same intercritical austenitizing temperature (1520°F) as shown in Figure 12(b).

#### 4.2.4 Plastic deformation and single step austempering

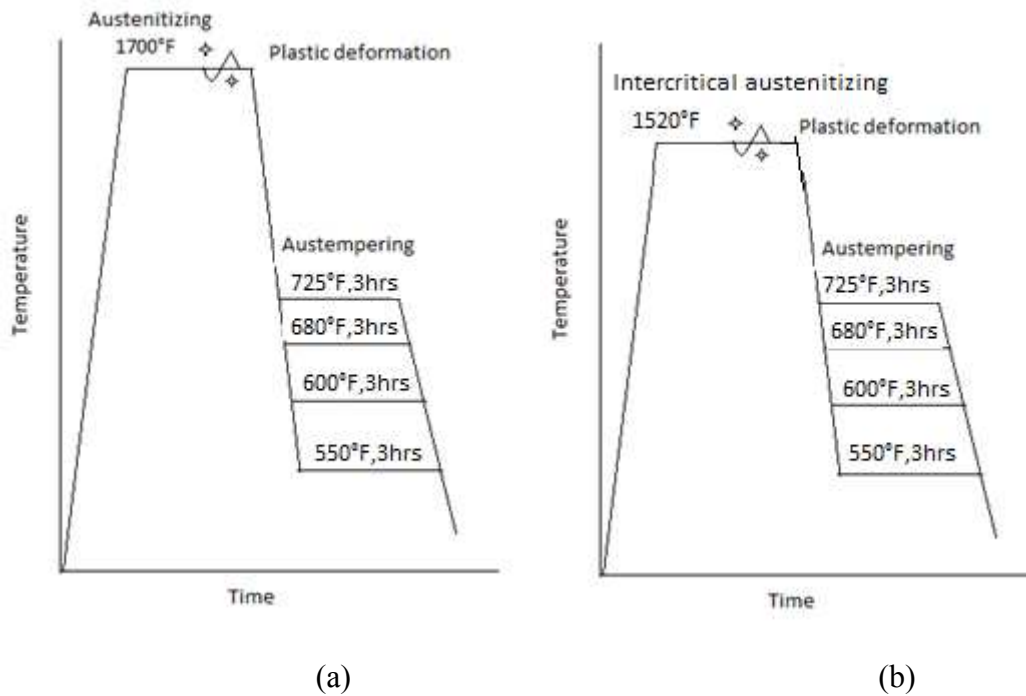


Figure.13: Schematic Diagram of heat treatment involving (a) plastic deformation and single step conventional austempering process (b) plastic deformation and single step intercritical austempering process

Third set of samples (C) consisted of only cylindrical tensile specimens and was divided into two groups (C1 and C2). The first group of cylindrical tensile samples (C1) were conventionally austenitized at 1700°F for 3 hours in a furnace attached to the Instron Universal Testing Machine. The samples were then plastically deformed beyond the yield strength at a strain rate of 5 mm/min at the same conventional austenitizing temperature of 1700°F. Immediately following the plastic deformation, the samples were quenched in a molten salt bath maintained at specific austempering temperatures of 550°F, 600°F, 680°F, and 725°F for 3 hours and then air cooled to room temperature as shown in Figure 13(a).

The upper intercritical temperature of 1520°F was chosen for the austenitization of the second group of cylindrical tensile samples (C2). The samples were intercritically austenitized at 1520°F for 3 hours and then plastically deformed beyond the yield strength at strain rate of 5 mm/min at the intercritical temperature of 1520°F, followed by austempering in a molten salt bath maintained at a specific austempering temperatures of 550°F, 600°F, 680°F, and 725°F as shown in Figure 13(b).

#### **4.2.5 Plastic deformation and two- step austempering**

Fourth set of samples (D) were divided into 2 groups (D1 and D2) and consisted of only cylindrical tensile samples. Different austenitizing temperature including the conventional austenitizing temperature of 1700°F and intercritical temperatures of 1520°F, 1472°F, 1436°F, 1418°F were chosen.

After austenitizing, the cylindrical tensile samples were plastically deformed at a strain rate of 5mm/min beyond the yield strength and then the samples were initially quenched in a molten salt bath maintained at 500°F and while being kept in the salt bath for about 15 minutes, the temperature of the salt bath was increased to the following austempering temperatures for specific samples i.e. 725°F,680°F,600°F and 550°F and the samples remained in the salt bath for 3 hours. The samples were then air cooled to room temperature as illustrated in the Figure 14.

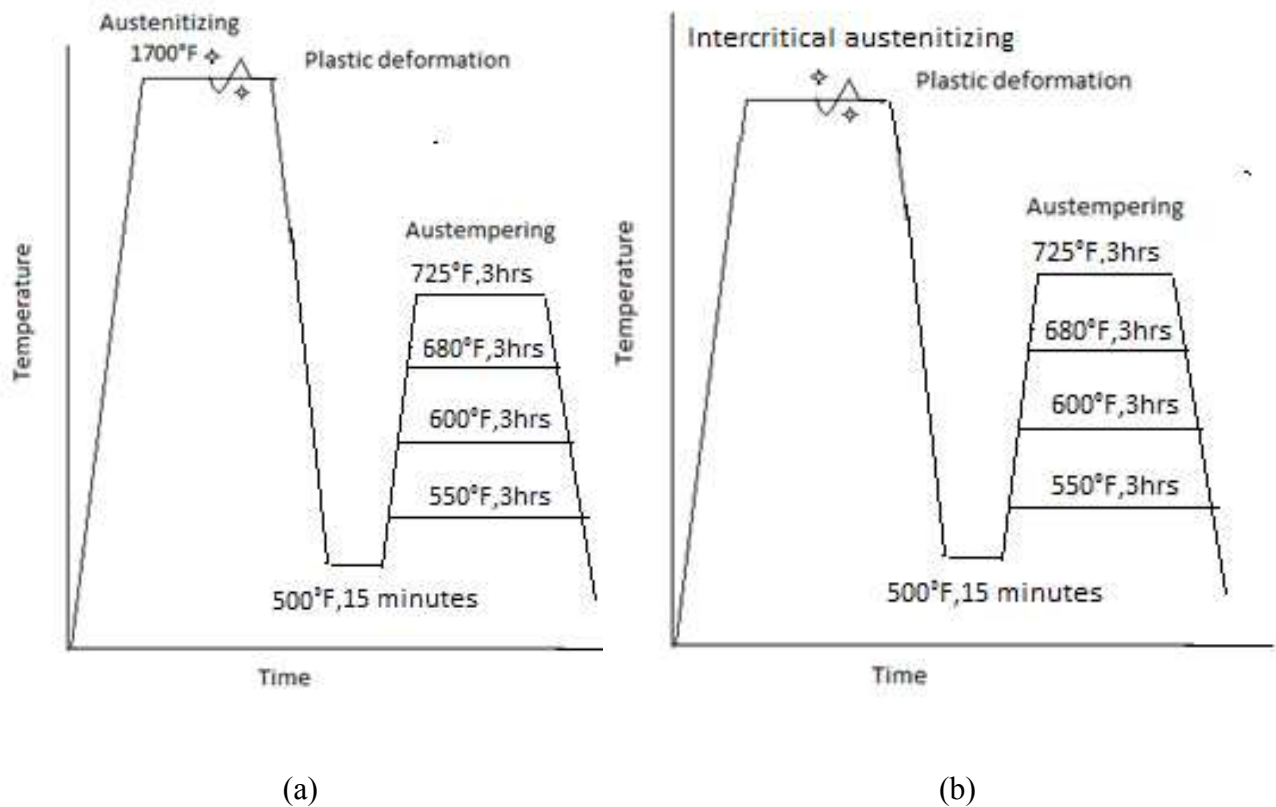


Figure.14: Schematic diagram of heat treatment involving (a) plastic deformation and single step conventional austempering process (a) plastic deformation and single step intercritical austempering process

#### 4.2.6 Plastic deformation at different strain rates

Fifth set of samples (E) consisted of only cylindrical tensile samples. These samples were initially austenitized at upper intercritical temperature of 1520°F, followed by plastic deformation beyond the yield strength at two different strain rates of 0.5mm/min and 10mm/min, Specific samples from each of the strain rate was austempered by single step conventional austempering process in which the samples were quenched in the molten salt bath maintained at 550°F. Similarly, some samples were processed by two-step austempering process in which the samples were initially quenched in a molten salt bath maintained at 500°F and while being maintained in the salt bath for about 15 minutes, the temperature of the salt bath was raised to 550°F and then

the samples remained in the salt bath for 3 hours. After austempering, all the samples were air cooled to room temperature.

### **4.3 Microstructural analysis**

Metallographic samples were cut from each of the heat-treated samples. These samples were mounted in a phenolic resin using hot compression mounting equipment and polished in accordance with standard procedures; silicon carbide abrasive discs of varying grit size 180 -2400 were used to grind the sample surface. Final cloth polishing with suspended alumina powder resulted in a scratch free polished surface; all samples were etched with a 5% Nital. The microstructures of all the samples were examined by optical microscopy and photographed. The microstructures were also examined using a JEOL JSM-6510LV-LGS scanning electron microscope.

The volume fraction of the proeutectoid ferrite and ausferrite in the intercritically austenitized ADI samples was determined by point counting in accordance with ASTM standard E-562 [122].

The fractured surface of all the heat-treated ADI samples was examined by JEOL JSM 6510 LV LGS scanning electron microscope to determine the mode of fracture.

X-ray diffraction (XRD) analysis was performed to estimate the overall amount of retained austenite and the carbon content of austenite in the heat-treated ADI samples. The thermal and mechanical stability of the austenite was also analyzed by the XRD data. To examine whether any TRIP effects (austenite to martensite transformation) occurs in ADI, the samples were cut from the crack tip region of fracture toughness specimens. The fractured surface of the specimen is polished and examined with XRD. The analysis estimated the volume fraction of austenite in the austempered, cryogenically-treated, and mechanically-deformed samples. The

volume fraction of retained austenite and carbon content of austenite were determined using a procedure of Rundman and Klug [123].

XRD was conducted using monochromatic copper  $K_{\alpha}$  radiation at 30 kV and 10 mA with the Bruker Phaser II diffractometer. An angular  $2\theta$  range from  $42^{\circ}$ - $46^{\circ}$  and  $72^{\circ}$ - $92^{\circ}$  was chosen to obtain specific diffraction pattern for the austenite and ferrite peaks. The profiles were then analyzed using a Jade 5® software and Diffraction Eva software to obtain the peak positions and the integrated intensities for the  $\{1\ 1\ 1\}$  and  $\{2\ 2\ 0\}$  planes of FCC austenite as well as the  $\{1\ 1\ 0\}$  and  $\{2\ 1\ 1\}$  planes of BCC ferrite. The volume fractions of ferrite ( $X_{\alpha}$ ) and austenite ( $X_{\gamma}$ ) were determined by the direct comparison method using the integrated intensities of the above planes. The intensity ratios are given by the following equation [124]:

$$\frac{I_{\gamma(hkl)}}{I_{\alpha(hkl)}} = \frac{R_{\gamma(hkl)}}{R_{\alpha(hkl)}} \cdot \frac{X_{\gamma(hkl)}}{X_{\alpha(hkl)}} \quad (4.1)$$

where  $I_{\gamma(hkl)}$  is the integrated intensity from a given (hkl) plane from the  $\gamma$  phase and  $I_{\alpha(hkl)}$  is the integrated intensity from a given (hkl) plane from the  $\alpha$  phase;  $X_{\gamma}$  and  $X_{\alpha}$  is the volume fraction of austenite and ferrite respectively;  $R_{\gamma(hkl)}$  and  $R_{\alpha(hkl)}$  are given by the following equation for respective (hkl) peak:

$$R = 1/v^2 [F^2 \cdot p \cdot LP] e^{-2m} \quad (4.2)$$

where  $v$  is the atomic volume of the unit cell;  $F$  is the structure factor;  $p$  is the multiplicity factor;  $LP$  is the Lorentz-Polarization factor and  $e^{-2m}$  is the temperature factor.

The lattice parameter “ $a_{\gamma}$ ” of austenite increases linearly with interstitial carbon atoms. Therefore, the carbon content of austenite was determined from the following equation [125]:

$$a_{\gamma} = 0.3548 + 0.0044 C_{\gamma} \quad (4.3)$$

where  $a_\gamma$  is the lattice parameter of austenite in nm and  $C_\gamma$  is the carbon content of austenite in wt%. The  $\{1\ 1\ 1\}$  and  $\{2\ 2\ 0\}$  planes of austenite were used to estimate the lattice parameter. The ferrite particle sizes ( $d$ ) were determined using the well-known Scherrer equation [124].

$$d = \frac{0.9\lambda}{\beta \cos\theta} \quad (4.4)$$

where  $\lambda$  is the wavelength,  $\beta$  is the breadth of ferrite peak at half height in radians and  $\theta$  is the Bragg angle.

#### 4.4 Fracture toughness testing

After machining to the specified thickness of 0.745 inch (18.9mm) and dimensions as shown in the Figure 15, the compact tension (CT) samples were ground and polished through 600 grid emery paper; a minimum of four compact tension specimens per heat treatment were tested as per ASTM standard E-399 [121].

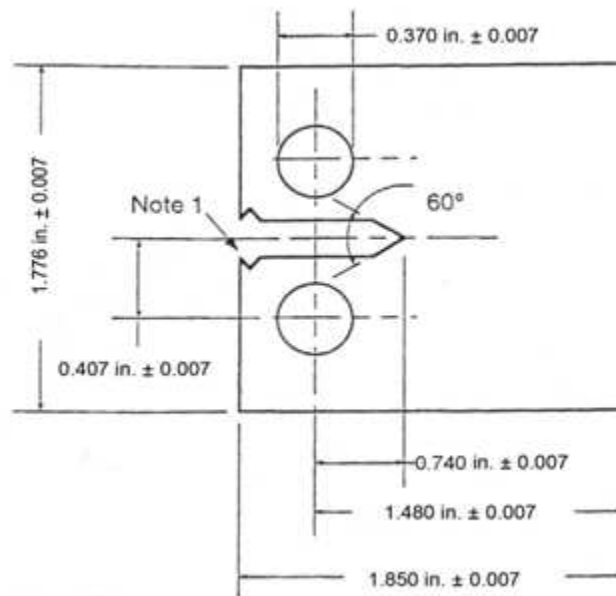


Figure.15: Compact tension sample dimensions (inches).



Fatigue pre-cracking was carried out on all the compact tension samples to obtain a 2-mm sharp crack front using a  $\Delta K$  level of  $20\text{MPa}\sqrt{\text{m}}$  with a load ratio of  $R=0.10$ . The pre-cracked samples were then loaded in tension using a MTS testing machine. The clip gauge was placed in the knife-edge attachment to obtain load versus displacement plots. Using the 5% secant deviation technique,  $P_Q$  values were determined. Using the standard stress intensity factor calibration function for the compact tension specimens,  $K_Q$  values were calculated using the  $P_Q$  values. Since all the  $K_Q$  values satisfied the requirements for a valid  $K_{IC}$  test as per ASTM E-399 [121], the  $K_Q$  values are also valid  $K_{IC}$  values.

#### 4.5 Tensile testing

Cylindrical tensile samples with the dimension shown in the Figure 16 were machined from the KEEL blocks as per ASTM standards E-8 [120].

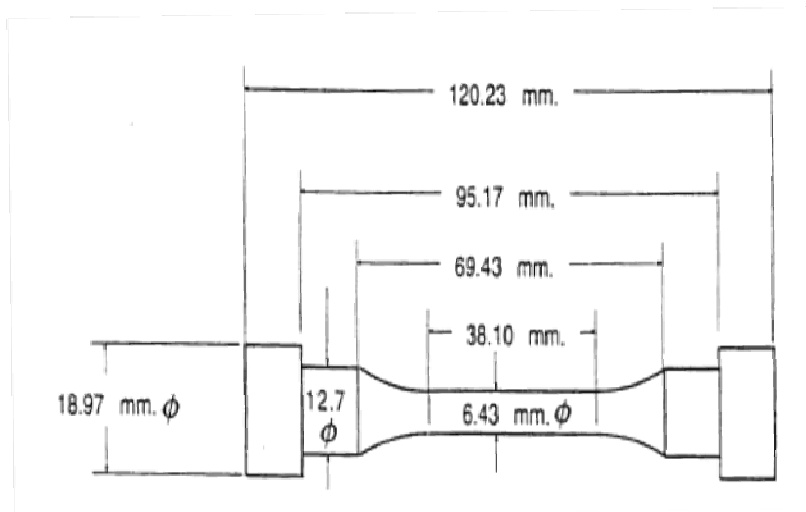


Figure.16: Cylindrical tensile sample dimensions (mm).

Tensile tests were performed on a servo-hydraulic MTS system at a constant strain rate of  $4 \times 10^{-4} \text{ s}^{-1}$ . Load versus displacement plots were used to calculate the 0.2% yield strength, ultimate tensile strength, % elongation, and strain hardening exponent values. Since all the

samples are isotropic and homogeneous properties exists in the material, the mechanical properties measured were not dependent on the sample reference orientation or loading direction. Average values of these samples are reported here and the statistical analysis was carried out on the obtained data using student t-test with a confidence interval set at 95%.

#### **4.6 Hardness measurement**

A Rockwell Type Hardness tester with 150 Kg load was used to measure the hardness of the ductile iron as cast and of all austempered samples per ASTM E-18 standard [126].

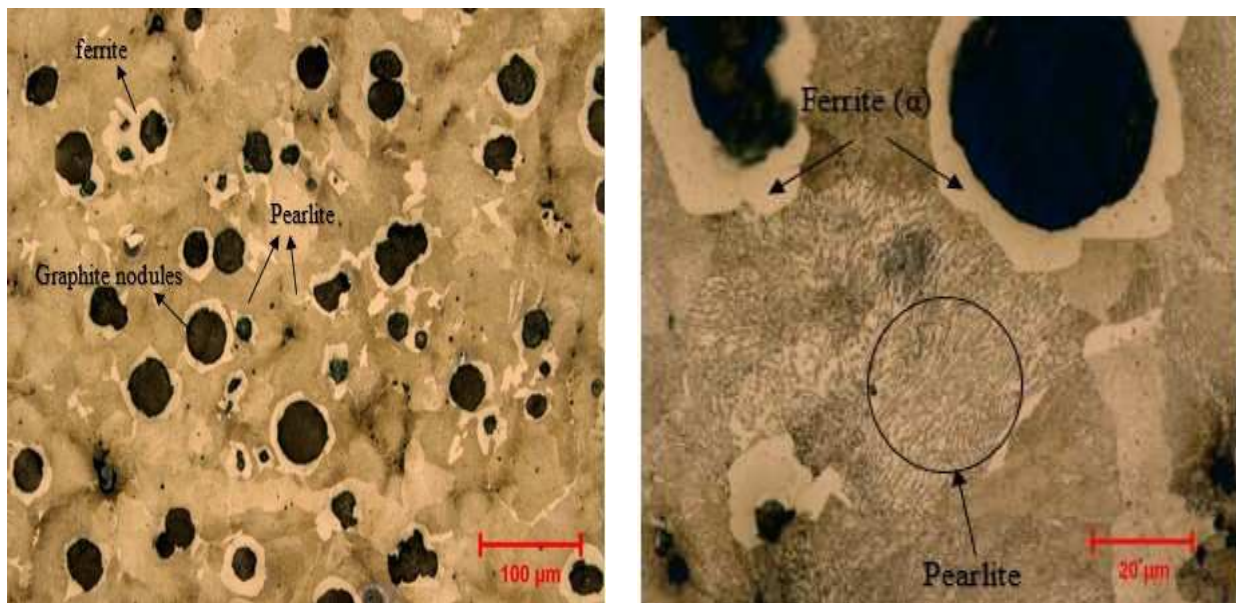
#### **4.7 Transmission Electron Microscopy(TEM)**

TEM analysis was carried out to confirm the presence of nanostructure in ADI and to identify the phases by indexing the diffraction patterns. Thin samples were cut from the gauge length of the heat treated cylindrical tensile samples using a precision diamond wafering cutter. These samples were then mechanically polished to 0.1mm thickness using a 180-grit silicon carbide paper. Final polishing was done using a cloth and 0.05 $\mu$ m alumina powder solution and thickness of the samples were reduced to about 70 $\mu$ m. Discs of 3mm diameter samples were then punched from these sections. The 3mm discs were then ion beam thinned using a dual gun ion beam milling machine, initially under 9° inclination angle and ion gun voltage of 5kV until perforation is visible for time ranging from 3 to 5 hours depending on the initial thickness of the sample. After perforation, the ion gun voltage is reduced to 3 kV and the inclination angle is set to 6° for about 20 minutes. These samples were then examined near the perforated area using a JEOL 2010 (LaB6 Filament Gun) transmission electron microscope at an accelerating voltage of 200kV.

## CHAPTER 5. RESULTS AND DISCUSSIONS- MICROSTRUCTURE

### 5.1 Microstructure of the as-cast ductile iron

The microstructure of the as-cast ductile cast iron is illustrated in Figure 17. The optical microstructure of ductile cast iron shows lamellar pearlite with alternating layers of ferrite and cementite. The as-cast microstructure consisted of dispersed graphite nodules surrounded by ferrite in the form of typical bull's eye structure. The ferrite phase is also referred to as proeutectoid ferrite. The graphite nodules in the as cast structure appears to be well rounded with 85% nodularity. Figure10 (b) is the magnified image of the lamellar pearlite phase showing alternating layer of ferrite ( $\alpha$ ) and cementite( $Fe_3C$ ).



(a)

(b)

Figure.17: As-cast microstructure of ductile cast iron (a) Optical microscope image (Mag 200x)

b) Optical microscope image (Mag 1000x)

#### 5.1.1 Microstructures of conventionally austempered ductile cast iron samples

Figure 18(a) and (b) shows the typical microstructure of the conventional ADI austenitized at 1700°F and austempered at lower and upper bainitic temperatures of 500°F and

725°F respectively. APPENDIX details individual micrograph for each austempering temperatures.

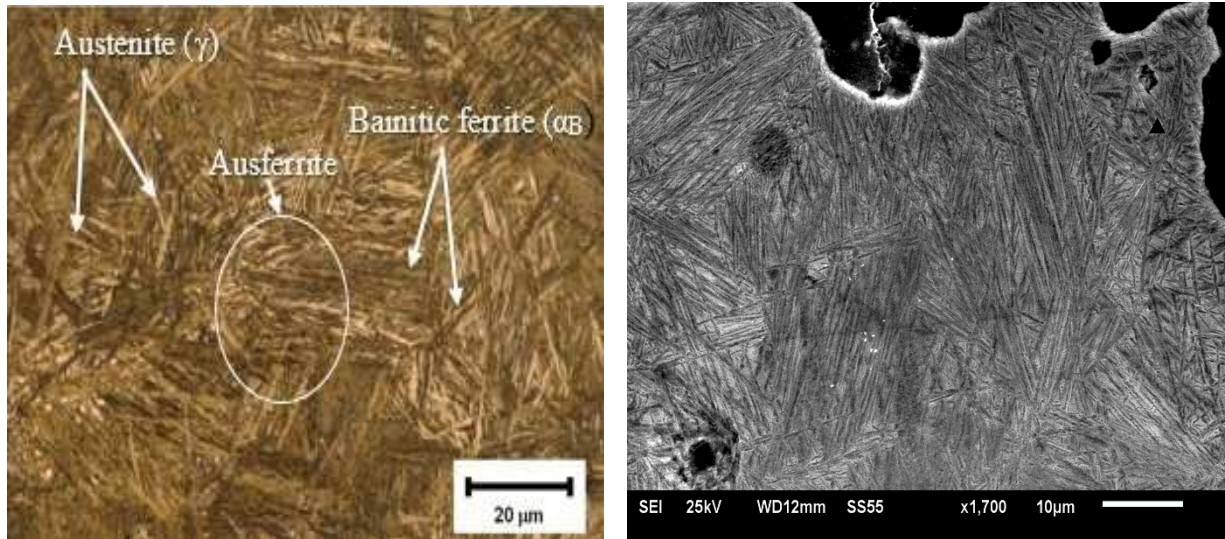


Figure.18(a): Optical and SEM micrograph of ADI,  $T_\gamma=1700^\circ\text{F}$ ,  $T_A=500^\circ\text{F}$

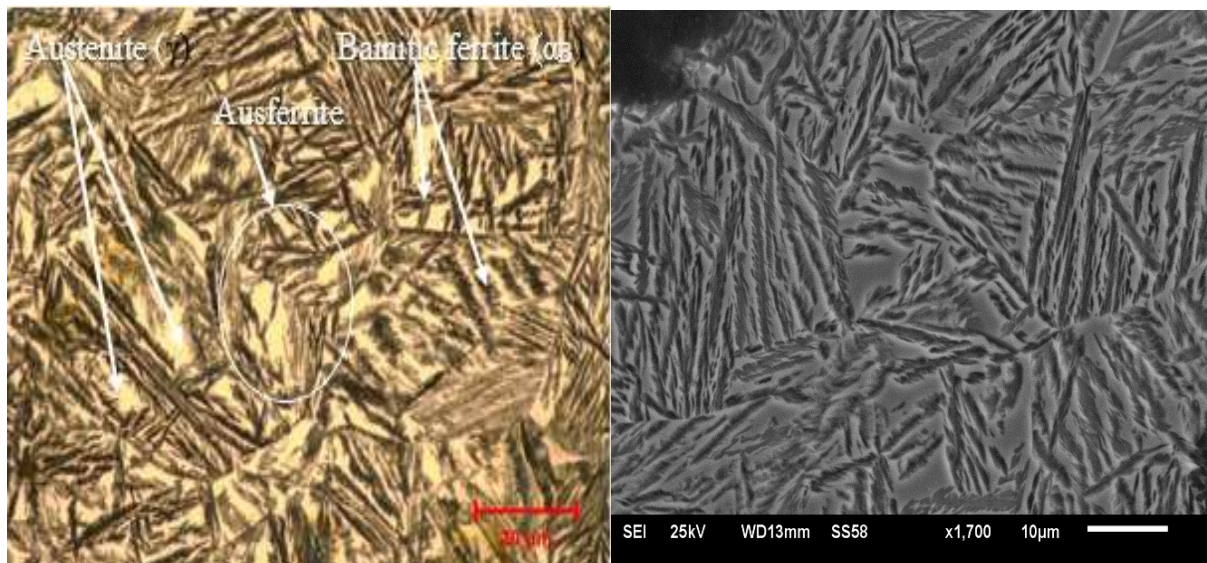


Figure.18(b): Optical and SEM micrograph of ADI,  $T_\gamma=1700^\circ\text{F}$ ,  $T_A=725^\circ\text{F}$

The ductile cast iron samples were initially austenitized at 1700°F and then quenched and austempered in a molten salt bath maintained at specific temperatures of 500°F, 550°F, 700°F, 725°F and 750°F. Scanning Electron Microscopy (SEM) image shows the morphology of the different phases at different austempering temperatures.

The microstructure of the conventionally austempered ductile cast iron consists of a ausferritic matrix with the dispersed graphite nodules. The ausferritic phase consists of bainitic ferrite ( $\alpha_B$ ) and high carbon austenite ( $\gamma$ ). Typical ausferritic microstructure structures consisting dark needles of bainitic ferrite and the austenite distributed as white phases in between the bainitic needles were observed. The bainitic ferrite is separated by thin layers of austenite. The coarseness of the ferrite increases with the increase in austempering temperature because the growth rate of ferrite is higher due to the higher energy supplied at higher austempering temperatures. Lower austempering temperature of 500°F and 550°F, resulted in very fine bainitic ferrite whereas the samples austempered at the upper bainitic temperature regions of 700°F, 725°F and 750°F resulted in the coarse bainitic ferrite structures.

### **5.1.2 Microstructures of cryogenically treated ADI samples**

Figure 19(a)-(b) shows the typical microstructures of the cryogenically treated austempered ductile cast iron samples with respect to the austempering temperatures. APPENDIX details the individual micrograph for each condition. Cryogenic treatment was subjected to the previously austempered ductile cast iron samples. The corresponding SEM image shows the morphology of the cryogenically treated ADI.



Figure.19(a): Optical and SEM micrograph of cryogenically treated ADI,  $T_{\gamma}=1700^{\circ}\text{F}$ ,  $T_A=500^{\circ}\text{F}$

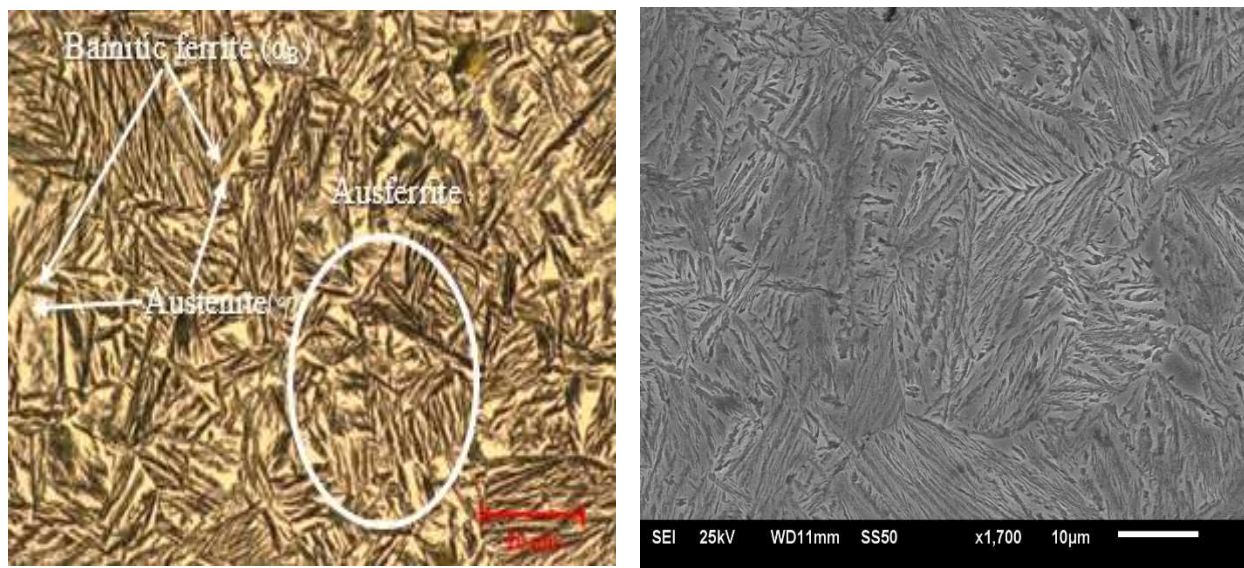


Figure.19(b): Optical and SEM micrograph of cryogenically treated ADI,  $T_{\gamma}=1700^{\circ}\text{F}$ ,  $T_A=725^{\circ}\text{F}$

The microstructure of the cryogenically treated ADI samples consists of ausferritic microstructure in which dark bainitic ferrite is dispersed in the white austenite phase along with graphite nodules. Cryogenic processing does not significantly alter the microstructure of the austempered ductile iron. The influence of austempering temperature still exists in the samples and the coarseness of these samples varies similar to that of the conventional ADI samples.

### **5.1.3 Microstructures of intercritically austempered ADI samples (constant $T_A= 680^\circ\text{F}$ )**

Optical micrographs of the samples intercritically austenitized at  $1520^\circ\text{F}$ ,  $1472^\circ\text{F}$ ,  $1436^\circ\text{F}$  and  $1418^\circ\text{F}$  and austempered at  $680^\circ\text{F}$  are shown in the Figures 20(a)- (d). The corresponding high magnification micrographs obtained from the scanning electron microscope shows of the morphology of the phases. The intercritically austempered ductile iron shows a mixed microstructure consisting of proeutectoid ferrite and ausferrite. One of the unique feature of intercritical austempering compared with conventional austempering is that the amount of ausferrite and proeutectoid ferrite varies significantly with the increase in austenitizing temperature. The coarser ausferritic matrix along with a small amount of pro-eutectoid ferrite is observed in these intercritically austempered ADI samples austempered at  $680^\circ\text{F}$ . Even though, unalloyed ductile cast iron is used in this study, appreciable amount of Ni, Si, Cu were present and they segregated around the graphite nodules and hence ferrite was found in the areas surrounding the graphite nodules of the intercritically austempered samples.

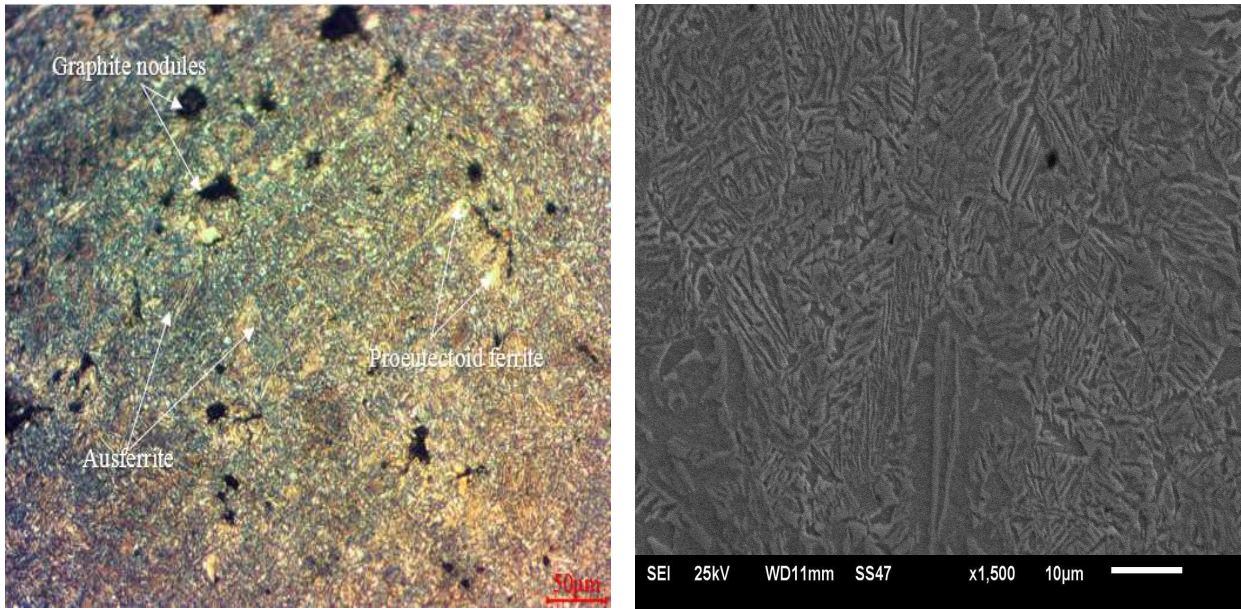


Figure.20(a): Optical and SEM micrograph of intercritically austempered ductile cast iron,

$$T_{\gamma}=1520^{\circ}\text{F}, T_{\text{A}}=680^{\circ}\text{F}$$

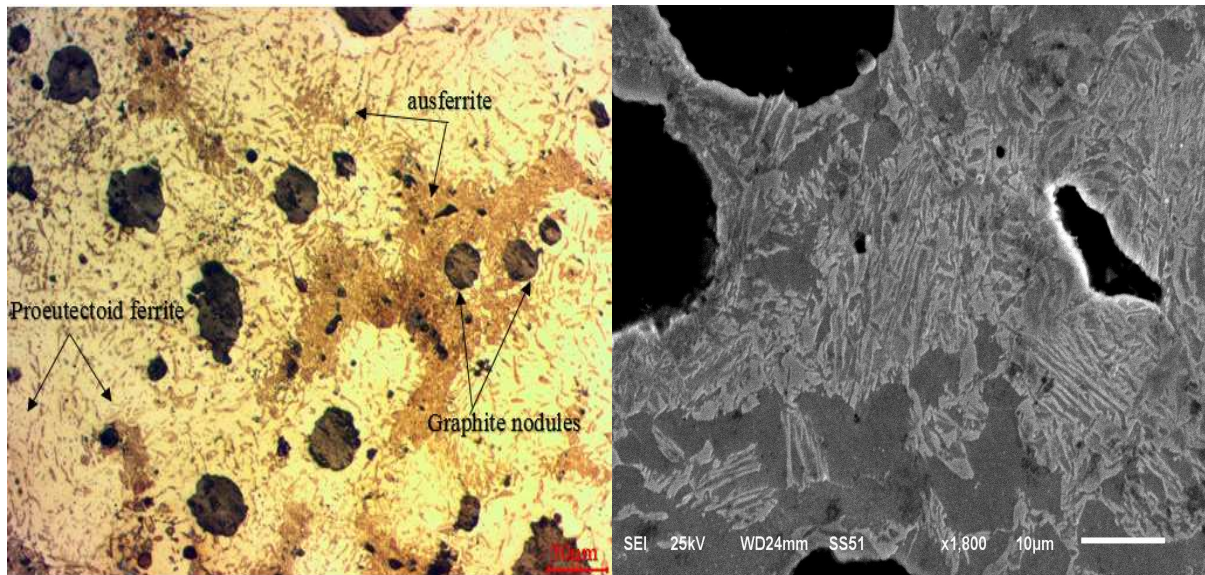


Figure.20(b): Optical and SEM micrograph of intercritically austempered ductile cast iron,

$$T_{\gamma}=1472^{\circ}\text{F}, T_{\text{A}}=680^{\circ}\text{F}$$



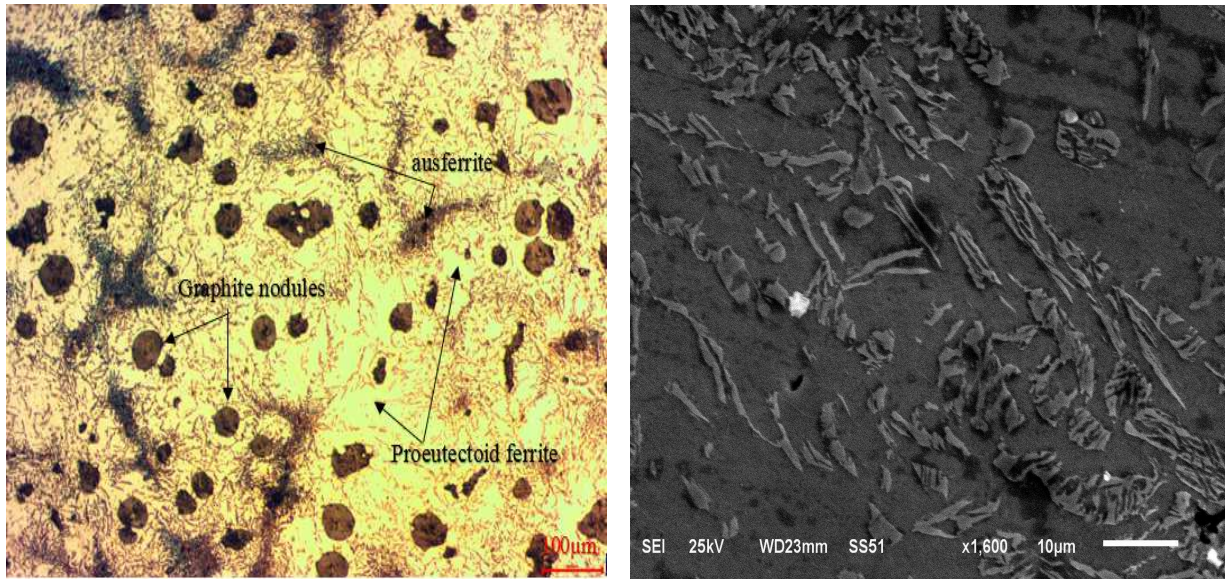


Figure.20(c): Optical and SEM micrograph of intercritically austempered ductile cast iron,

$T_{\gamma}=1436^{\circ}\text{F}$ ,  $T_{\text{A}}=680^{\circ}\text{F}$

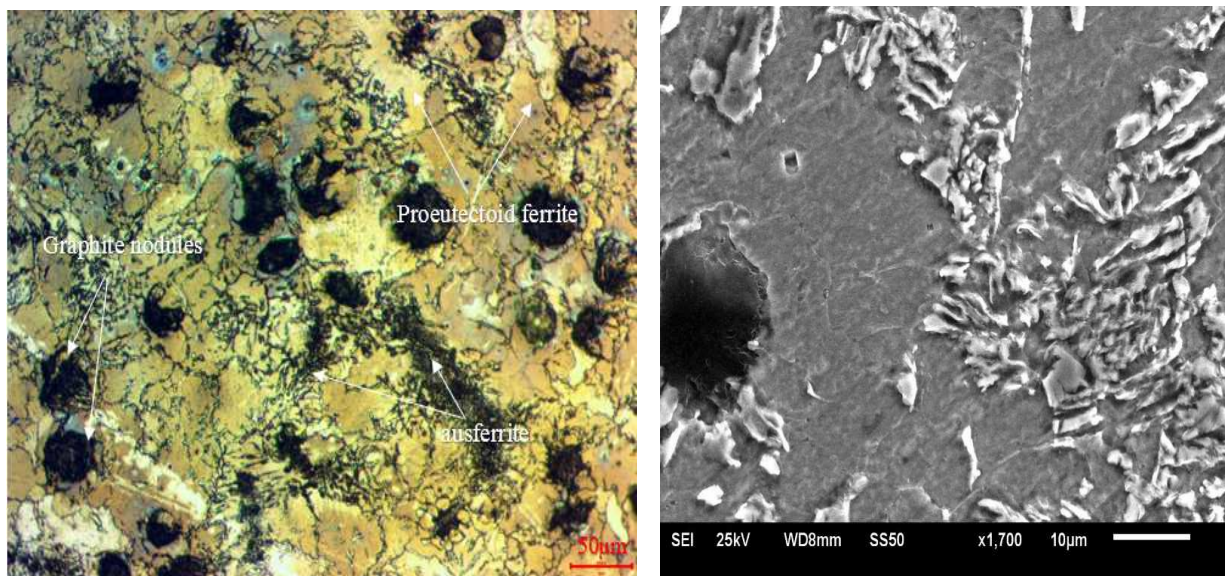


Figure.20(d): Optical and SEM micrograph of intercritically austempered ductile cast iron,

$T_{\gamma}=1418^{\circ}\text{F}$ ,  $T_{\text{A}}=680^{\circ}\text{F}$

The influence of austenitizing temperatures on the volume fractions of proeutectoid ferrite and ausferrite is represented in the Figures 21 and 22 respectively. Volume fraction of proeutectoid ferrite and ausferrite were point counted as per ASTM E562 standard [122]. During intercritical austempering where the ductile iron is heated in the intercritical temperature region where ferrite and austenite ( $\alpha+\gamma$ ) coexist, the pearlitic phase of the as cast ductile cast iron is converted into the austenite phase. Isothermal transformation at 680°F converts this austenite phase into ausferritic phase. The amount of proeutectoid ferrite that remains is dependent on the intercritical austenitizing temperature. The volume fraction of proeutectoid ferrite is lower at higher intercritical austenitization temperature, because pearlite and a large portion of ferrite is converted into austenite at higher austenitization temperatures. On the other hand, the ausferrite volume fraction increases as the austenitizing temperature is increased from 1418°F to 1520°F as predicted by the Lever rule [28,72].

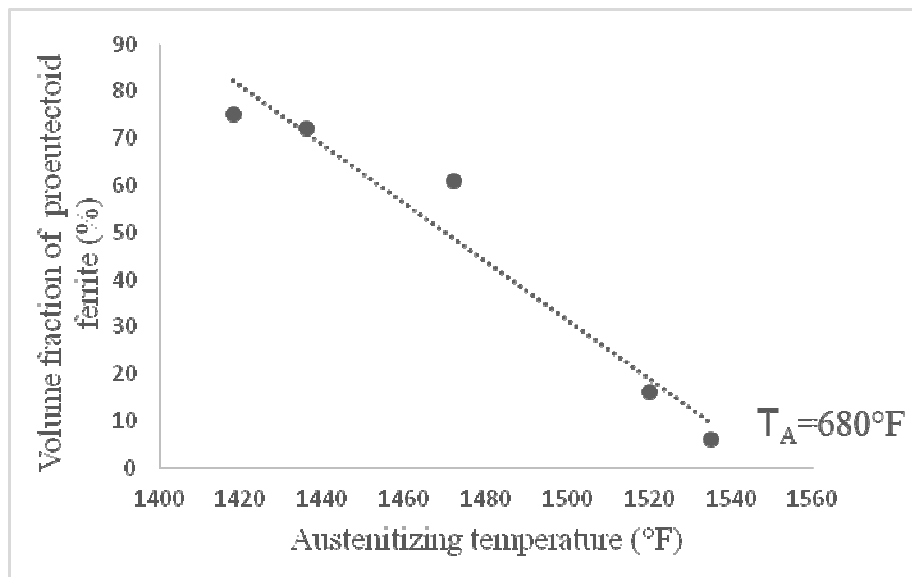


Figure.21: Volume fraction of proeutectoid ferrite as a function of austenitizing temperatures

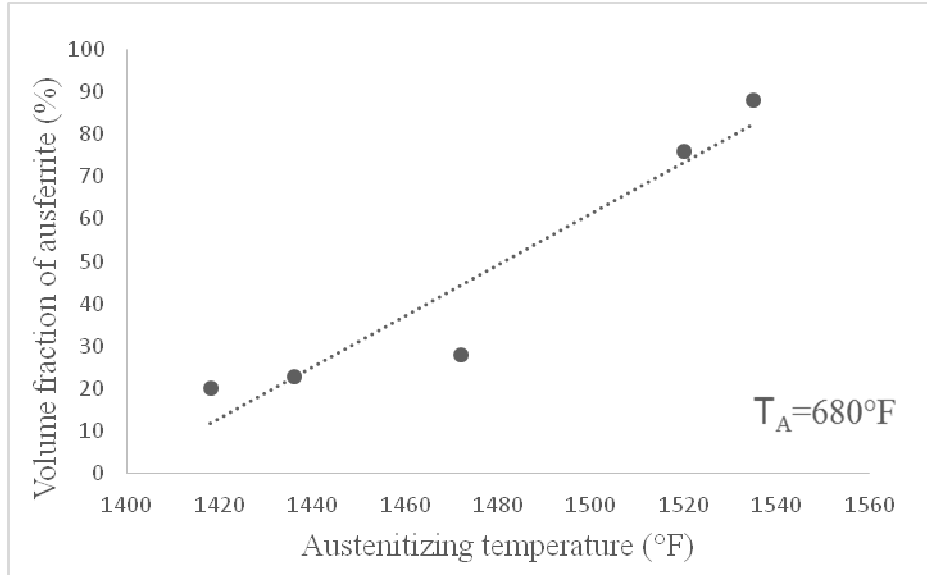


Figure.22: Volume fraction of ausferrite as a function of austenitizing temperatures

#### 5.1.4 Microstructures of intercritically austempered ADI samples (constant $T_{\gamma}=1520^{\circ}\text{F}$ )

To determine the effect of austempering temperature on the intercritically austenitized ADI, some of the samples were quenched at different austempering temperatures as shown, for the same austenitizing temperature of  $1520^{\circ}\text{F}$ . Typical optical microstructures and the corresponding high magnification SEM Micrograph (example:  $T_{\gamma}=1520^{\circ}\text{F}$ ,  $T_{\text{A}}=725^{\circ}\text{F}$ ) of the ADI is shown in the Figures 23. APPENDIX details the individual micrograph for other austempering temperatures ( $680^{\circ}\text{F}$ ,  $600^{\circ}\text{F}$  and  $550^{\circ}\text{F}$ ). Higher austempering temperatures of  $725^{\circ}\text{F}$  and  $680^{\circ}\text{F}$  in the ADI samples austenitized at upper intercritical austenitization temperature of  $1520^{\circ}\text{F}$  produced coarser ausferritic structure in the microstructure matrix. At lower austempering temperatures of  $550^{\circ}\text{F}$  and  $600^{\circ}\text{F}$ , due to large super cooling, more ferrite is nucleated, however, the grain growth of ferrite is low because of the lower diffusion rate of carbon out into the surrounding austenite, resulting in finer ferritic structures. The analysis of the microstructure shows that the austenite occurred as slivers between the ferritic needles. The width of the

austenite slivers reduced with the decrease in austempering temperature. Only small amount of proeutectoid ferrite was retained at this upper intercritical austenitization temperature of 1520°F.

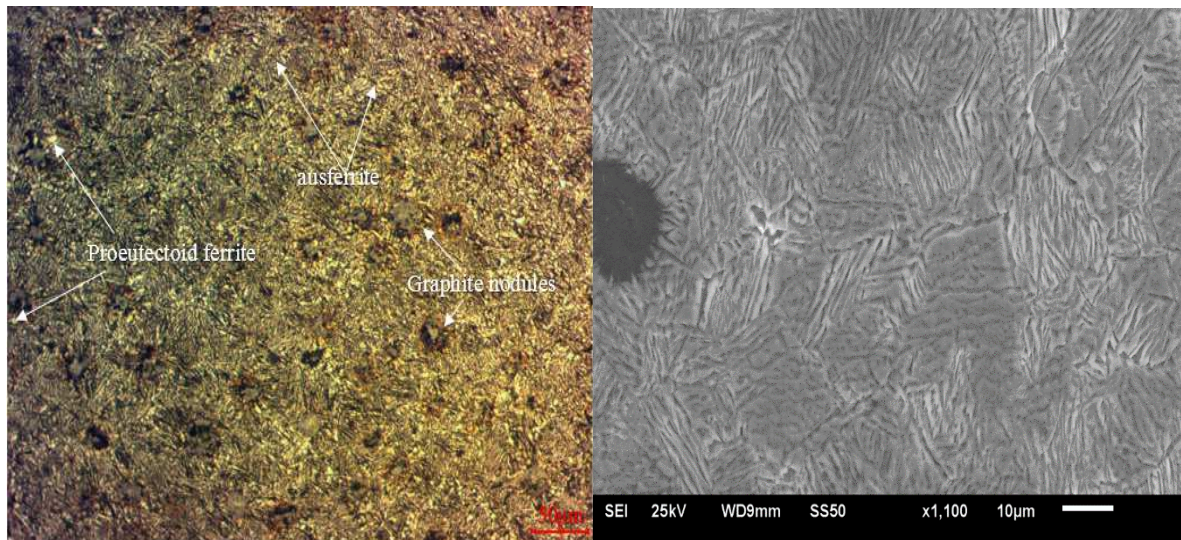


Figure.23: Optical and SEM micrograph of intercritically austempered ductile cast iron,  
 $T_{\gamma}=1520^{\circ}\text{F}$ ,  $T_A=725^{\circ}\text{F}$

### 5.1.5 Microstructure of plastically deformed, conventional ADI

Figures 24 shows the typical optical and the corresponding high magnification SEM image of the plastically deformed and conventionally austempered ductile iron samples. Individual micrographs for each austempering temperature is detailed in APPENDIX. The samples were initially austenitized at 1700°F for 3 hours, followed by plastic deformation at 1700°F and subsequent quenching in the salt bath maintained at specific austempering temperatures for 3 hours and then air cooled to room temperature. Plastic deformation significantly reduced the width of bainitic ferrite of the ADI samples. The effect of austempering temperatures was mainly observed in the volume fraction and the coarseness of bainitic ferrite and austenite. Higher austempering temperatures produced coarser ausferritic structures as the higher austempering temperatures limits the nucleation of bainitic ferrite. Higher austempering temperatures also produced bulky retained austenite in the microstructure. On the other hand,

since nucleation depends on super cooling, lower austempering temperature produced finer and higher volume fraction of bainitic ferrite and less volume fraction of retained austenite. It is also observed that the high temperature plastic deformation did not affect the nodularity of the graphite.

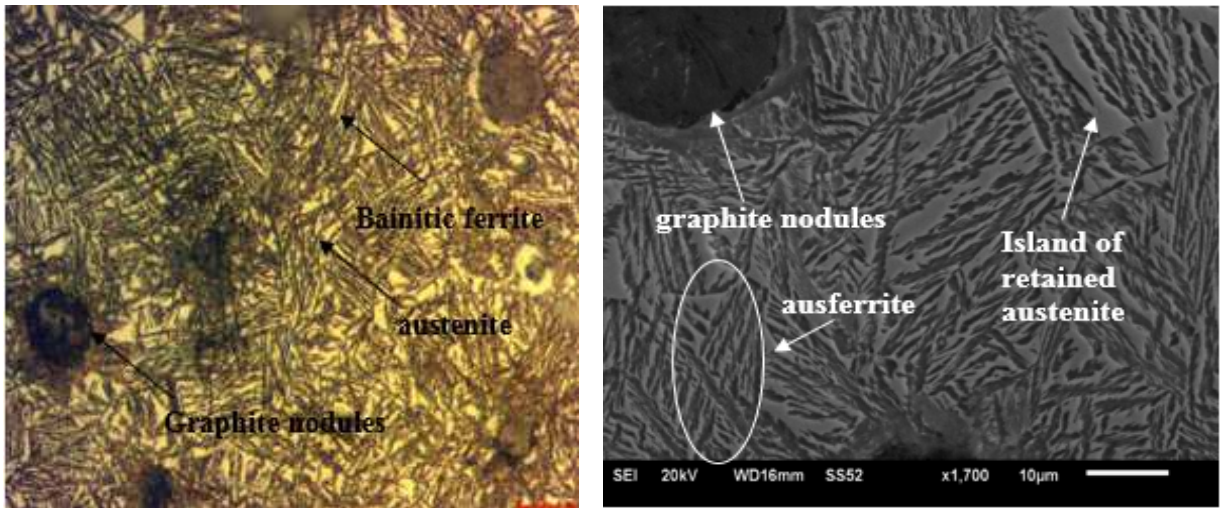


Figure.24: Optical and SEM micrograph of plastically deformed ADI,  $T_{\gamma}=1700^{\circ}\text{F}$ ,  $T_{\text{D}}=1700^{\circ}\text{F}$ ,  
 $T_{\text{A}}=725^{\circ}\text{F}$

### 5.1.6 Microstructure of plastically deformed, intercritically austempered ductile cast iron

Figure 25 shows the typical optical micrograph and the corresponding SEM micrograph of the ductile iron samples, intercritically austenitized for 3 hours at the upper intercritical temperature of  $1520^{\circ}\text{F}$ , followed by plastic deformation at the same intercritical temperature before quenching into the salt bath maintained at specific austempering temperatures (example:  $T_{\text{A}}=725^{\circ}\text{F}$ ). Optical and SEM micrographs of the each austempering temperature is detailed in the APPENDIX. The microstructure of these samples consists of bainitic ferrite, austenite and proeutectoid ferrite along with dispersed graphite nodules. The ausferritic structures were distributed uniformly either as a continuous or network of ausferritic structure along the eutectic cell boundary. Plastic deformation of the ductile iron samples at the intercritical temperature of

1520°F, refined the width of bainitic ferrite, compared to the conventional austempering without plastic deformation, irrespective of the austempering temperatures. The effect of austempering temperature was observed in the volume fractions of ferrite and austenite. Larger undercooling produced finer bainitic ferrite structures at lower austempering temperatures of 550°F and 600°F. At higher austempering temperature of 725°F and 680°F, reduced nucleation of austenite led to the coarser feather like ausferritic structures.

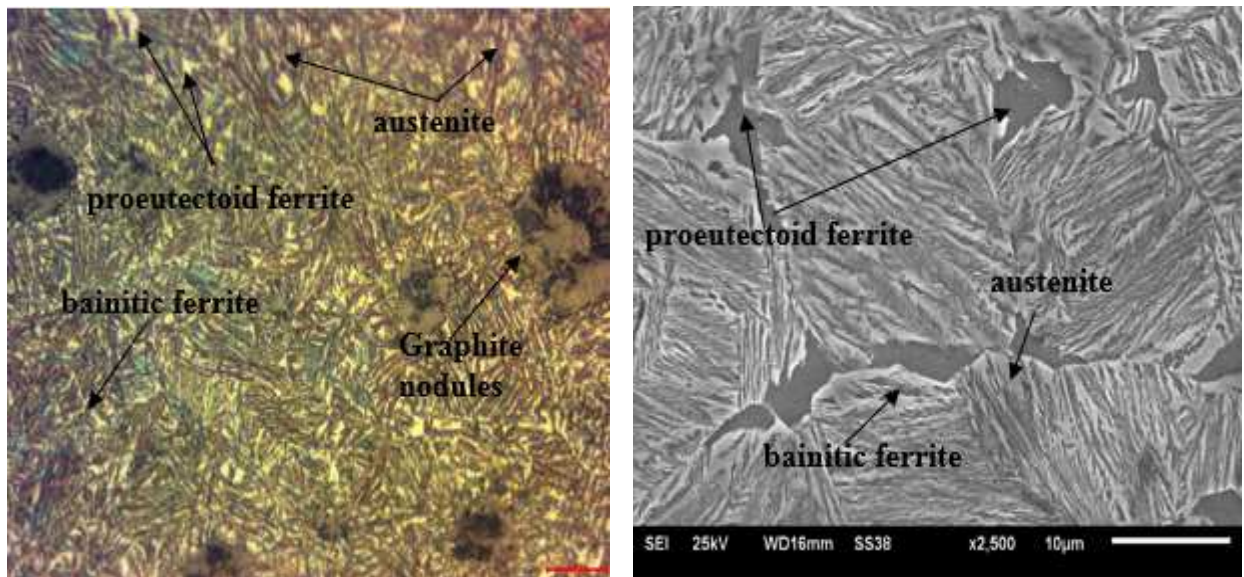


Figure.25: Optical and SEM micrograph of plastically deformed ADI,  $T_{\gamma}=1520^{\circ}\text{F}$ ,  $T_D=1520^{\circ}\text{F}$ ,  
 $T_A=725^{\circ}\text{F}$

### 5.1.7 Microstructures of the plastic deformed, two-step austempered ductile cast iron

Figures 26 shows the typical microstructure of the ductile iron samples conventionally austenitized at 1700°F, plastically deformed at 1700°F and then austempered by two-step austempering process. In all these samples, the first austempering temperature was maintained at 500°F and the second austempering temperature was raised to 550°F, 600°F, 680°F and 725°F for specific samples.

Figure 27-29 shows typical microstructures of the ductile iron samples intercritically austenitized at 1520°F, 1472°F and 1436 °F plastically deformed at corresponding austenitizing temperature and then austempered by two-step austempering process. The individual micrographs for each austempering temperature is reported in the APPENDIX.

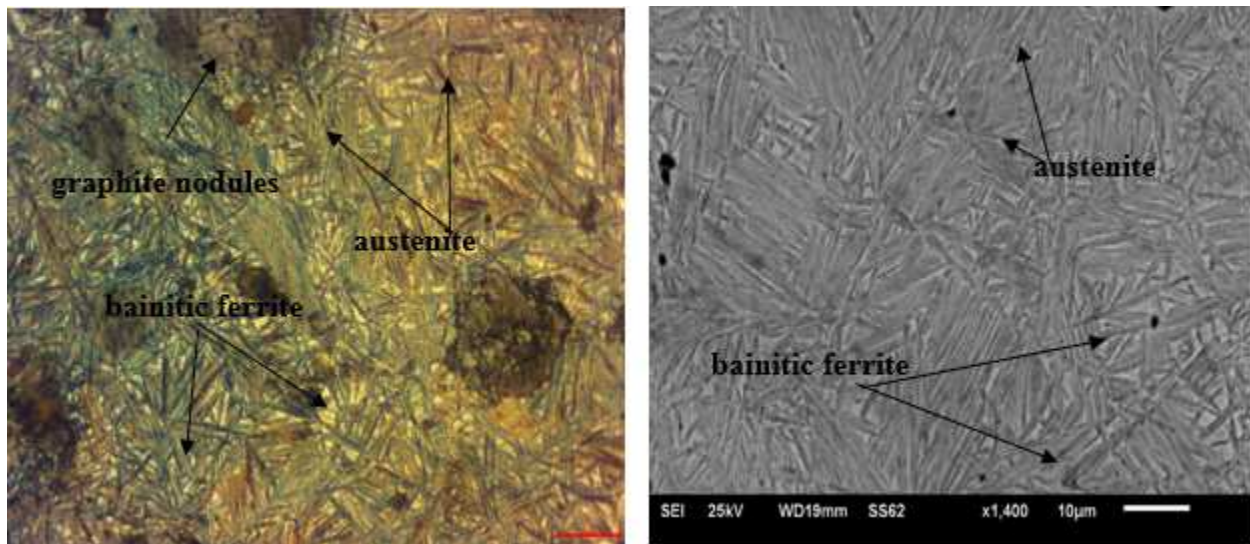


Figure.26: Optical and SEM micrograph of plastically deformed, two step austempered ADI,  
 $T_{\gamma}=1700^{\circ}\text{F}$ ,  $T_D=1700^{\circ}\text{F}$ ,  $T_{A1}=500^{\circ}\text{F}$ ,  $T_{A2}=550^{\circ}\text{F}$

After plastic deformation, during recrystallization at the bainitic temperature range, the austenite grain boundaries provide more nucleation sites for the growth of ferrite. During the two-step austempering process, the ductile cast iron samples were initially quenched to a lower temperature of 500°F which facilitates higher super cooling and hence greater ferrite nucleation. As the austempering temperature is raised to the second austempering temperature mainly influenced the coarseness of bainitic ferrite and high carbon austenite in the microstructure matrix. Lower austempering temperature of 550°F and 600°F resulted in finer ferritic structures than those austempered at higher austempering temperatures of 680°F and 725°F.

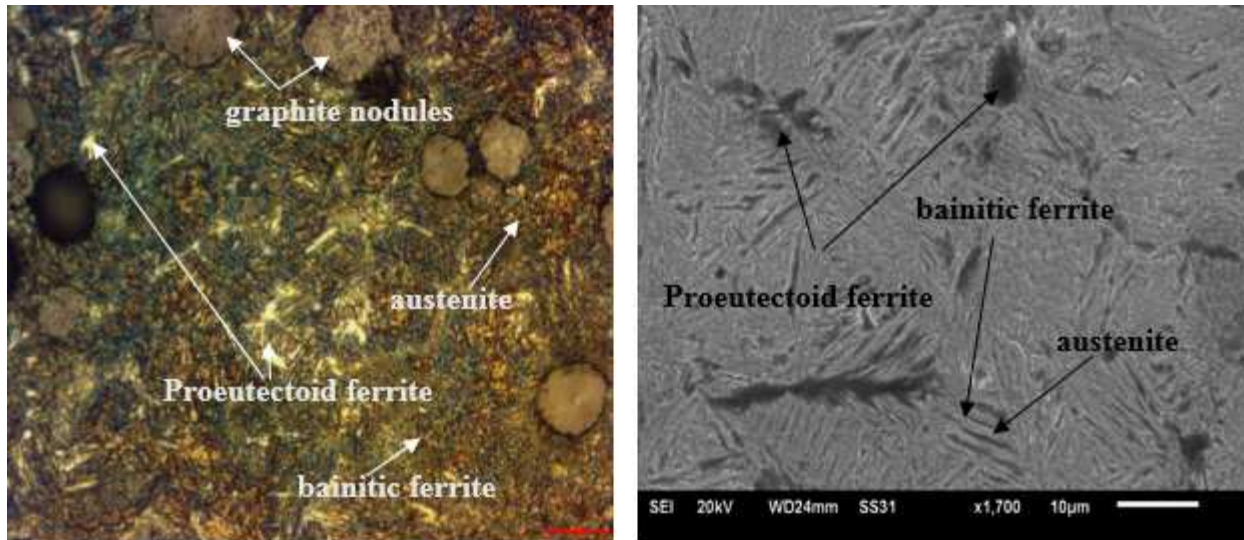


Figure.27: Optical and SEM micrograph of plastically deformed, two step austempered ADI,  
 $T_{\gamma}=1520^{\circ}\text{F}$ ,  $T_D=1520^{\circ}\text{F}$ ,  $T_{A1}=500^{\circ}\text{F}$ ,  $T_{A2}=550^{\circ}\text{F}$

In the intercritically austenitized and plastically deformed samples, the volume fraction of ausferritic phases increased whereas the volume fraction of proeutectoid ferrite decreased with the increase in austenitizing temperature as predicted by the Lever rule [28,72]. Even though low alloyed ductile cast iron is used in this study, appreciable amount of Si, Ni, Mn were present that segregated around the graphite nodules during solidification to stabilize the ferrite present in the microstructure matrix. As the austenitizing temperature is reduced, the ausferritic structures were observed along the grain boundaries. The proeutectoid ferrite appears around the graphite nodules irrespective of the austempering temperatures in these intercritically austempered ductile iron samples. The nodularity of the graphite is not affected by this heat treatment process



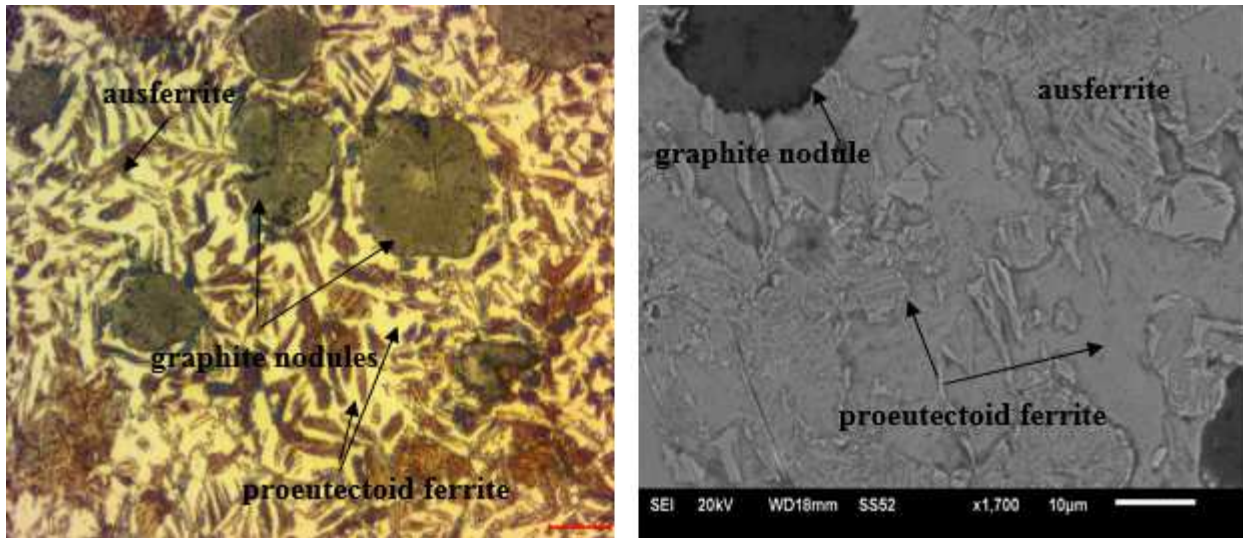


Figure.28: Optical and SEM micrograph of plastically deformed, two step austempered ADI,

$$T_{\gamma}=1472^{\circ}\text{F}, T_{\text{D}}=1472^{\circ}\text{F}, T_{\text{A1}}=500^{\circ}\text{F}, T_{\text{A2}}=550^{\circ}\text{F}$$

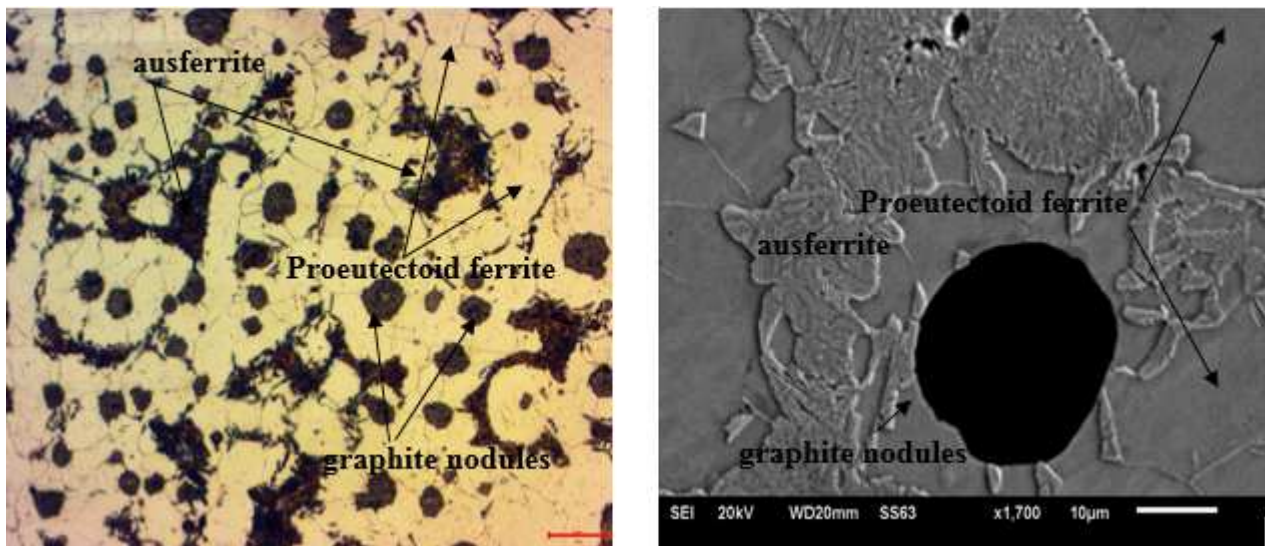


Figure.29: Optical and SEM micrograph of plastically deformed, two step austempered ADI,

$$T_{\gamma}=1436^{\circ}\text{F}, T_{\text{D}}=1436^{\circ}\text{F}, T_{\text{A1}}=500^{\circ}\text{F}, T_{\text{A2}}=550^{\circ}\text{F}$$

In summary, the coarseness of the ausferrite increased with the increase in austempering temperature. The combination of simultaneous austenitizing and high temperature plastic deformation and the greater super cooling in two step austempering process resulted in finer ausferritic structure in the microstructure matrix irrespective of the austenitizing and

austempering temperatures. This unique heat treatment resulted in refinement of the bainitic ferrite and austenite. Due to Si segregation around the graphite nodules, the rate of formation of ferrite was interrupted and these ausferritic structures were absent near the areas surrounding the graphite nodules.

#### **5.1.8 Microstructure of ductile iron plastically deformed at different strain rate**

Plastic deformation of the ductile iron was carried out at two different strain rate of 0.5mm/min and 10mm/min respectively, at the intercritical austenitizing temperature of 1520°F followed by either single step austempering at  $T_A=550^\circ\text{F}$  or two step austempering process in which the first austempering temperature was maintained at 500°F for 15 minutes and the second austempering temperature was raised to 550°F and maintained for about 3 hours.

All these samples resulted in a microstructure consisting of bainitic ferrite and high carbon austenite along with the graphite nodules irrespective of the strain rate. A typical microstructure and the corresponding SEM micrograph, obtained from this unique heat treatment process is shown in the Figure 30. The individual micrographs for each condition is reported in the APPENDIX. Very low amount of proeutectoid ferrite was observed in these samples. The high temperature deformation at strain rates of 0.5mm/min and 10mm/min significantly reduced the width of the bainitic ferrite and austenite in ADI. The ultra-fine grained structures in the range of nanoscale was obtained by this unique heat treatment process.

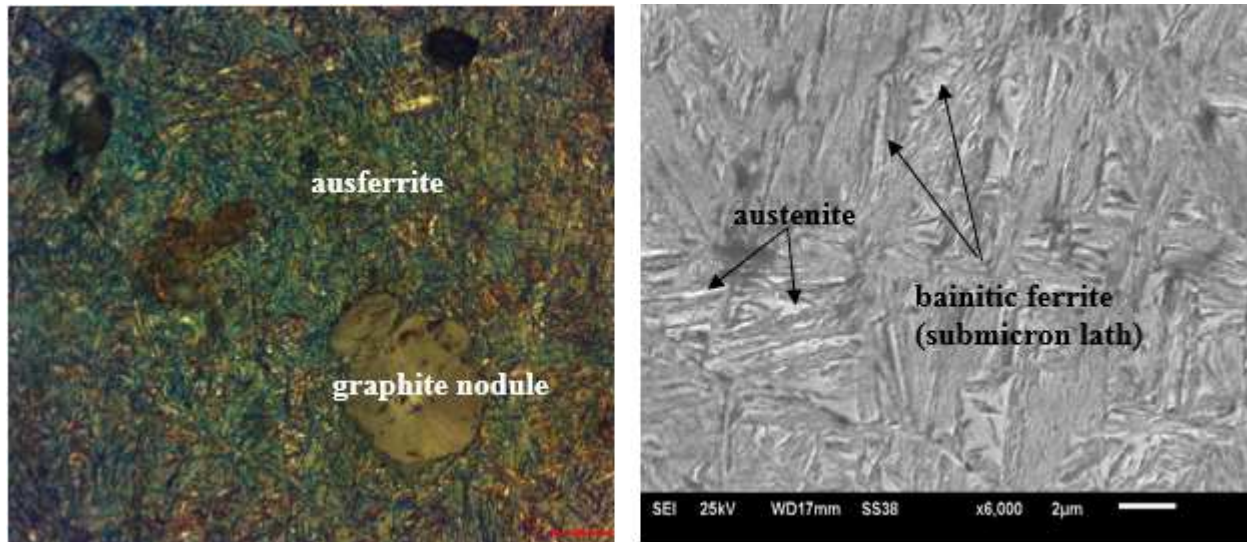


Figure.30: Optical and SEM micrograph of plastically deformed, two step austempered ADI,  $T_{\gamma}=1520^{\circ}\text{F}$ ,  $T_D=1520^{\circ}\text{F}$ , strain rate = 0.5mm/min,  $T_A=550^{\circ}\text{F}$

## 5.2 Lath size measurements

Lath size measurements was carried out to determine the variation in the width of bainitic ferrite, austenite and the proeutectoid ferrite as a function of heat treatment. TEM observation (discussed later in this chapter) shows that the grain size of the ADI has been greatly reduced by the unique heat treatment process combining both plastic deformation and austempering. An attempt has been made to measure the individual lath sizes of bainitic ferrite, inter lath austenite, islands of retained austenite and proeutectoid ferrite. The width of the phases was measured from the high magnification SEM images corresponding to different areas of the microstructure. Image pro plus 6 software was used for this purpose. The lath size measurements were made perpendicular to the longitudinal axis. Approximately 100 measurements of each phases were made for every ADI sample and the average values are reported here.

### 5.2.1 Lath size measurements of conventional ADI

Table 2 reports the measured lath sizes of bainitic ferrite, retained austenite and islands of retained austenite with respect to the conventional austempering. The width of the bainitic ferrite and the films of retained austenite reduces significantly from 750°F to 550°F. The islands of the retained austenite were present predominantly in the conventionally austempered ADI at all austempering temperatures except 500°F. Statistically, there is no significant difference in the width of the islands of retained austenite in the conventional ADI. The presence of islands of retained austenite promotes enhanced ductility to the ADI.

Table 2: Lath size measurement of phases with respect to conventional austempering (samples austenitized for 3 hours at 1700°F and austempered for 2 hours for temperatures shown)

<b>Austempering temperature (°F)</b>	<b>width of bainitic ferrite lath (μm)</b>	<b>width of films of retained austenite (μm)</b>	<b>width of islands of retained austenite (μm)</b>
750°F	1.128 ± 0.429	0.677 ± 0.220	3.307 ± 1.760
725°F	0.835 ± 0.274	0.614 ± 0.194	2.276 ± 0.590
700°F	0.385 ± 0.177	0.327 ± 0.207	1.901 ± 0.770
550°F	0.294 ± 0.093	0.261 ± 0.090	2.791 ± 0.770
500°F	0.207 ± 0.053	0.206 ± 0.055	-

Figure 31 shows the variation in the width of the different phases with respect to austempering temperature in conventional ADI. The width of the bainitic ferrite and the austenite is not proportional to the austempering temperature. As the austempering temperature increases

above 700°F, greater growth of bainitic ferrite structure is observed than the growth at lower austempering temperatures. At lower bainitic temperatures, only bainitic ferrite and retained austenite exist because ausferrite does not form at lower austempering temperatures. Comparatively, the lath size of the austenite and the bainitic ferrite was identical at lower bainitic austempering temperatures up to 550°F. At upper bainitic temperatures, where the ausferritic structures form, the width of is bainitic ferrite is larger than the retained austenite structures. As expected, the standard conventional austempering process did not produce any nanoscale bainitic ferrite in ADI.

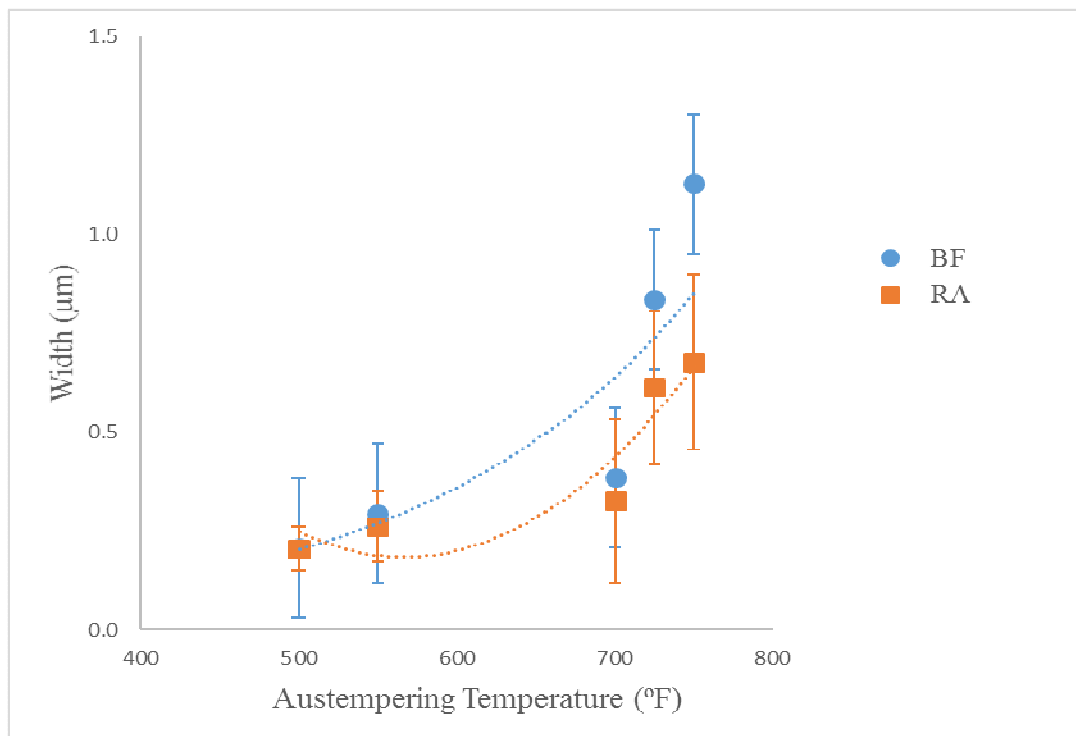


Figure.31: Variation of the width of bainitic ferrite (BF) and width of films of retained austenite (RA) with respect to austempering temperature in conventional ADI

### 5.2.2 Lath size measurements of cryogenically treated ADI

Table 3 reports the measured width sizes of different phases in ADI with respect to the cryogenic treatment. Islands of retained austenite was observed only in the cryogenically treated ADI samples austempered at upper bainitic temperature range. Figure 32 shows the variation of the width of bainitic ferrite, retained austenite and the islands of retained austenite with respect to the cryogenic treatment.

Table 3: Lath size measurement of phases with respect to cryogenic processing  
(samples austenitized for 3 hours at 1700°F and austempered for 2 hours for temperatures shown followed by cryogenic processing)

<b>Austempering temperature (°F)</b>	<b>width of bainitic ferrite lath (μm)</b>	<b>width of films of retained austenite (μm)</b>	<b>width of islands of retained austenite (μm)</b>
750°F	0.756 ± 0.306	0.865 ± 0.372	2.891 ± 0.816
725°F	0.436 ± 0.224	0.443 ± 0.187	2.368 ± 0.897
700°F	0.331 ± 0.132	0.422 ± 0.326	1.746 ± 0.824
550°F	0.296 ± 0.119	0.305 ± 0.309	-
500°F	0.181 ± 0.055	0.217 ± 0.072	-

Due to the thermal instability of austenite, some portion of austenite is transformed to martensite. Cryogenic treatment significantly reduced the width of the bainitic ferrite (or newly formed martensite) and films of retained austenite of the ADI austempered at upper bainitic temperatures of 725°F and 750°F. However, no significant reduction in the width of bainitic

ferrite or austenite was observed in the cryogenically treated ADI austempered at lower austempering temperatures of 700°F, 550°F and 500°F. As shown in the Figure 32, width of the bainitic ferrite and austenite is mostly proportional to temperature up to 725°F. Beyond 725°F, perhaps there occurs an additional mechanism that activates the increase in the width of austenite and bainitic ferrite structures. Compared to conventional austempering, approximately 33% and 48% reduction in the width of bainitic ferrite was observed in cryogenic treated ADI austempered at upper bainitic temperatures of 750°F and 725°F respectively. Approximately, only 12-14% reduction in the width of bainitic ferrite was observed in cryogenically treated ADI austempered at lower bainitic temperatures. In summary, cryogenic processing alone is insufficient to produce nanoscale ausferritic structure in ADI.

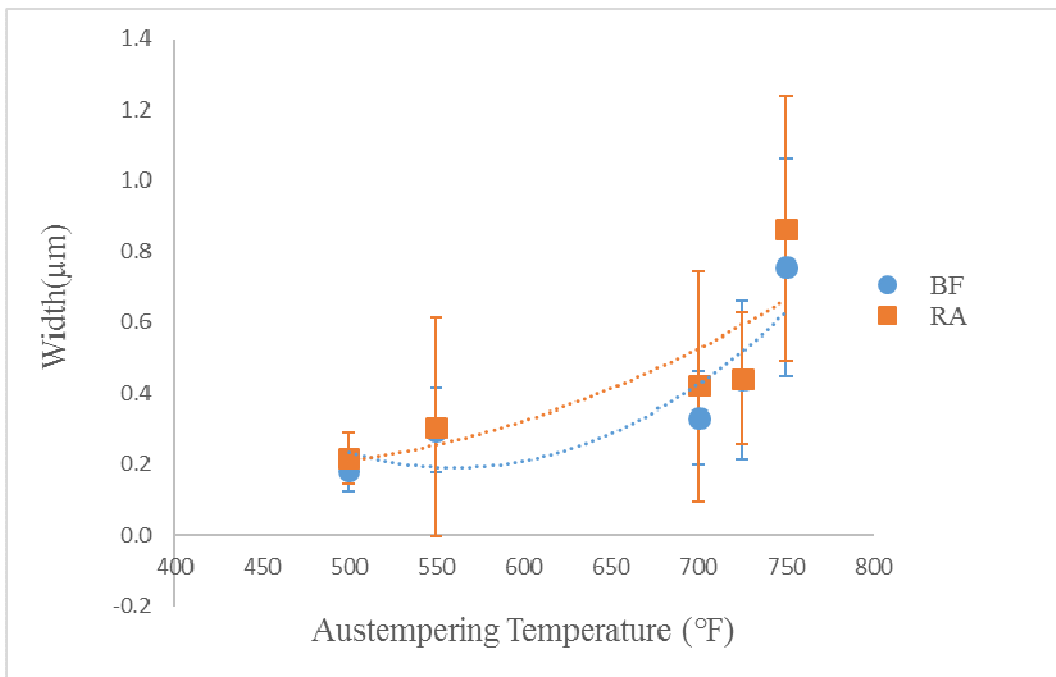


Figure.32: Variation of the width of bainitic ferrite (BF) and width of films of retained austenite (RA) with respect to austempering temperature in cryogenically treated ADI

### 5.2.3 Lath size measurements of intercritically austenitized ADI

Table 4 reports the measured width of the bainitic ferrite lath and films of retained austenite of ADI intercritically austenitized at 1520°F with respect to austempering temperature.

Table 4: Lath size measurement of phases with respect to intercritical austempering (samples austenitized for 3 hours at 1520°F and austempered for 3 hours for temperatures shown)

$T_{\gamma}$ (°F)	$T_A$ (°F)	width of bainitic ferrite lath ( $\mu\text{m}$ )	width of films of retained austenite) ( $\mu\text{m}$ )	width of islands of retained austenite ( $\mu\text{m}$ )	width of proeutectoid ferrite ( $\mu\text{m}$ )
1520°F	725°F	$0.582 \pm 0.233$	$0.360 \pm 0.135$	$1.287 \pm 0.310$	$1.2 \pm 0.4$
	680°F	$0.426 \pm 0.158$	$0.360 \pm 0.154$	-	$3.9 \pm 3.0$
	600°F	$0.399 \pm 0.163$	$0.315 \pm 0.119$	-	$2.6 \pm 1.0$
	550°F	$0.333 \pm 0.195$	$0.190 \pm 0.054$	-	$0.6 \pm 0.2$

In the ADI samples, intercritically austenitized at upper intercritical temperature of 1520°F, the average width of bainitic ferrite is higher than the retained austenite at all the austempering temperatures as shown in the Figure 33. The width of the austenite and ferrite laths was finer at lower austempering temperature of 550°F. The coarseness of both the austenite and ferrite laths was observed as the austempering temperature increases from 550°F to 725°F in the intercritically austenitized ADI. Islands of retained austenite was present only at higher austempering temperature of 725°F in the ADI austenitized at upper intercritical austenitizing temperature of 1520°F.



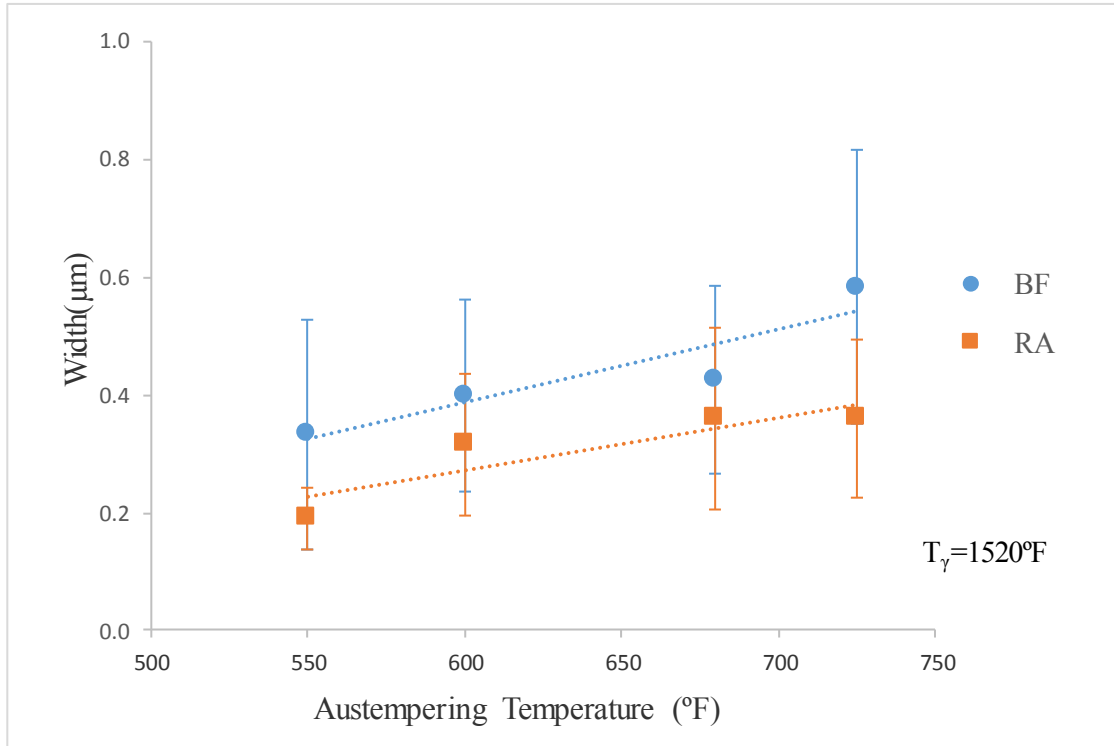


Figure.33: Variation of the width of bainitic ferrite (BF), width of films of retained austenite (RA) of ADI with respect to austempering temperature from data in Table 4.

Table 5 details the measured width of the bainitic ferrite lath and films of retained austenite with respect to the austenitizing temperature for the austempering temperature of 680°F. The width of the proeutectoid ferrite was higher for the samples austenitized at lower intercritical temperature of 1418°F. The average width of the proeutectoid ferrite increased approximately up to 96% between the upper and lower intercritical temperatures of 1520°F and 1418°F respectively.

Figure 34 shows the dependence of the width of bainitic ferrite lath and the films of retained austenite laths with respect to intercritical austenitization temperatures. Minor effects on the width of the bainitic ferrite, austenite was observed as the austenitizing temperature was lowered from 1520°F to 1436°F.

Table 5: Lath size measurement of phases with respect to intercritical austempering  
(samples austenitized for 3 hours for temperatures shown and austempered for 3 hours for 680°F)

$T_\gamma$ (°F)	width of bainitic ferrite lath ( $\mu\text{m}$ )	width of films of retained austenite) ( $\mu\text{m}$ )	width of proeutectoid ferrite ( $\mu\text{m}$ )
1520°F	$0.426 \pm 0.158$	$0.360 \pm 0.154$	$3.9 \pm 3.0$
1472°F	$0.478 \pm 0.176$	$0.485 \pm 0.274$	$8.2 \pm 6.6$
1436 °F	$0.352 \pm 0.133$	$0.350 \pm 0.126$	$10.6 \pm 8.2$
1418°F	$0.689 \pm 0.204$	$0.844 \pm 0.309$	$88.4 \pm 50$

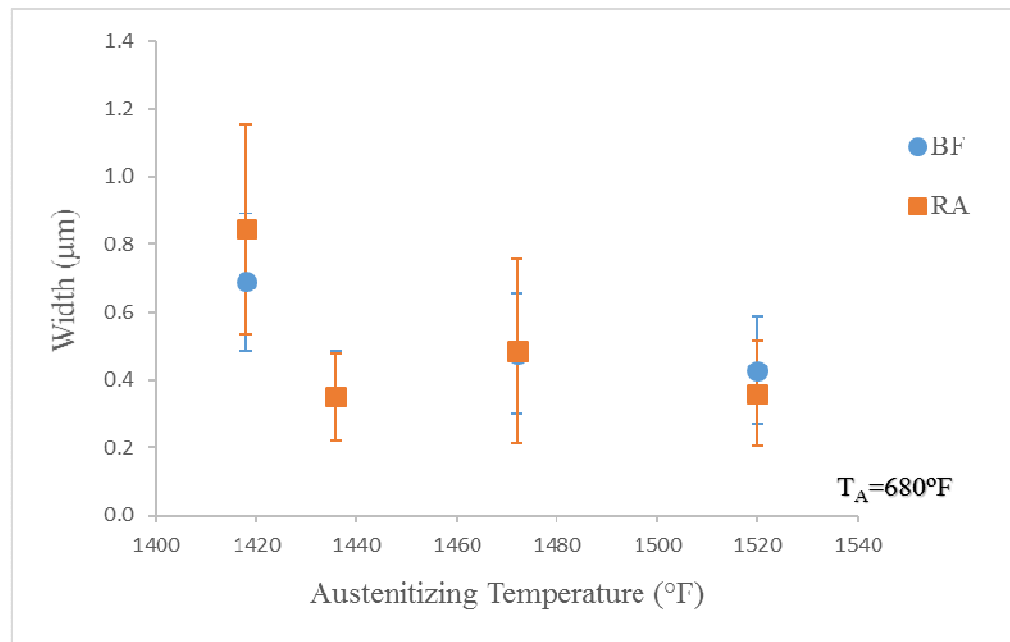


Figure.34: Variation of the width of bainitic ferrite (BF), width of films of retained austenite (RA) of ADI with respect to intercritical austenitizing temperature from data in Table 5.

The width of the bainitic ferrite and austenite was higher for the samples austenitized at lower intercritical temperature of 1418°F. Islands of retained austenite was not observed in these samples. No significant variation was observed between the ferritic and austenite lath sizes of the conventional and intercritically austenitized ADI. Thus, it appears that intercritical austenitizing alone is not sufficient to produce nanostructured ADI.

#### **5.2.4 Lath size measurements of the plastically deformed ADI**

Table 6 reports the lath size of the different phases observed in the plastically deformed ADI with respect to austenitizing temperature and austempering temperature. In these samples, the width of the bainitic ferrite lath decreases significantly as the austempering temperature decreases from 725°F to 550°F. Approximately 35% reduction in the width of bainitic ferrite and austenite was observed in the plastically deformed ADI austempered at lower bainitic temperatures when compared to the conventionally austempered ADI. In these samples austenitized and plastically deformed at 1700°F, below the austempering temperature of 725°F, the bainitic ferrite is refined, therefore the change in temperature is not proportional to the change in the width of bainitic ferrite structures. This indicates that there exists an optimum temperature to control the growth of bainitic ferrite structures. However, no significant difference was observed in the lath sizes of bainitic ferrite and austenite between the traditional and the plastically deformed ADI at upper bainitic temperature ranges of 680°F and 725°F.

In the ADI samples, austenitized and deformed at the upper intercritical temperature of 1520°F, significant reduction in the width of bainitic ferrite was observed at lower austempering temperatures of 550°F and 600°F. This reduction in width was approximately 35 to 55% when compared to the traditional ADI. However, only 2% reduction in the width of bainitic ferrite lath was observed at the higher austempering temperature of 725°F. Austempering temperature did not

significantly influence the width of proeutectoid ferrite in the ADI samples intercritically austenitized and plastically deformed at upper intercritical temperature of 1520°F.

Table 6: Lath size measurements of different phases in plastically deformed ADI with respect to single step austempering

(samples austenitized for 3 hours at  $T_{\gamma}$  as shown, plastically deformed at corresponding  $T_{\gamma}$  s and austempered for 3 hours for temperatures shown)

$T_{\gamma}$ (°F)	$T_A$ (°F)	width of bainitic ferrite lath ( $\mu\text{m}$ )	width of films of retained austenite) ( $\mu\text{m}$ )	width of islands of retained austenite( $\mu\text{m}$ )	width of proeutectoid ferrite( $\mu\text{m}$ )
1700°F	725°F	$0.769 \pm 0.265$	$0.634 \pm 0.234$	$3.289 \pm 1.353$	-
	680°F	$0.421 \pm 0.157$	$0.321 \pm 0.147$	$1.781 \pm 0.381$	-
	600 °F	$0.204 \pm 0.058$	$0.197 + 0.066$	-	-
	550°F	$0.192 \pm 0.049$	$0.208 \pm 0.053$	-	-
1520°F	725°F	$0.575 \pm 0.194$	$0.407 \pm 0.155$	-	$1.484 \pm 0.463$
	680°F	$0.276 \pm 0.099$	$0.278 \pm 0.157$	-	$4.611 \pm 1.640$
	600 °F	$0.219 \pm 0.061$	$0.198 \pm 0.060$	-	$2.290 \pm 0.581$
	550°F	$0.156 \pm 0.049$	$0.209 \pm 0.605$	-	$2.450 \pm 1.570$

Table 7 compares the width of various phases with respect to austenitizing temperature and two-step austempering in the plastically deformed ADI.

Table 7: Lath size measurements of different phases in plastically deformed ADI with respect to two-step austempering (samples austenitized at  $T_{\gamma}$  as shown for 3 hours,  $T_{A1} = 500^{\circ}\text{F}$  for 15 minutes,  $T_{A2}$  at temperatures shown for 3 hours)

$T_{\gamma}$ ( $^{\circ}\text{F}$ )	$T_{A2}$ ( $^{\circ}\text{F}$ )	width of bainitic ferrite lath ( $\mu\text{m}$ )	width of films of retained austenite) ( $\mu\text{m}$ )	width of islands of retained austenite( $\mu\text{m}$ )	width of proeutectoid ferrite ( $\mu\text{m}$ )
1700 $^{\circ}\text{F}$	725 $^{\circ}\text{F}$	$0.283 \pm 0.105$	$0.297 \pm 0.114$	$2.235 \pm 1.143$	
	680 $^{\circ}\text{F}$	$0.276 \pm 0.234$	$0.285 \pm 0.173$	$2.540 \pm 1.110$	
	600 $^{\circ}\text{F}$	$0.204 \pm 0.068$	$0.211 \pm 0.062$	$1.767 \pm 0.866$	
	550 $^{\circ}\text{F}$	$0.210 \pm 0.058$	$0.283 \pm 0.105$	-	
1520 $^{\circ}\text{F}$	725 $^{\circ}\text{F}$	$0.248 \pm 0.082$	$0.238 \pm 0.060$	-	$1.325 \pm 0.277$
	680 $^{\circ}\text{F}$	$0.222 \pm 0.061$	$0.272 \pm 0.074$	-	$2.903 \pm 1.609$
	600 $^{\circ}\text{F}$	$0.184 \pm 0.049$	$0.179 \pm 0.049$	-	$0.841 \pm 0.523$
	550 $^{\circ}\text{F}$	$0.290 \pm 0.088$	$0.218 \pm 0.067$	-	$1.896 \pm 0.820$
1472 $^{\circ}\text{F}$	725 $^{\circ}\text{F}$	$0.168 \pm 0.041$	$0.154 \pm 0.034$	-	$7.371 \pm 6.976$
	680 $^{\circ}\text{F}$	$0.168 \pm 0.033$	$0.177 \pm 0.063$	-	$6.006 \pm 5.150$
	600 $^{\circ}\text{F}$	$0.175 \pm 0.020$	$0.168 \pm 0.040$	-	$8.256 \pm 5.387$
	550 $^{\circ}\text{F}$	$0.202 \pm 0.054$	$0.176 \pm 0.036$	-	$4.458 \pm 1.753$
1436 $^{\circ}\text{F}$	725 $^{\circ}\text{F}$	$0.176 \pm 0.045$	$0.167 \pm 0.030$	-	$7.017 \pm 7.101$
	680 $^{\circ}\text{F}$	$0.205 \pm 0.041$	$0.188 \pm 0.040$	-	$12.046 \pm 6.192$
	600 $^{\circ}\text{F}$	$0.164 \pm 0.038$	$0.179 \pm 0.050$	-	$16.315 \pm 10.796$
	550 $^{\circ}\text{F}$	$0.174 \pm 0.036$	$0.220 \pm 0.044$	-	$28.867 \pm 14.817$

Islands of retained austenite was observed only in the conventionally austenitized ADI austempered in the higher austempering temperatures. The width of the proeutectoid ferrite significantly increased as the intercritical austenitization temperature varied from 1520°F to 1436°F. Statistically, no significant effect of austempering temperature on the width of the proeutectoid ferrite was observed.

Figure 35 compares the variation of width of bainitic ferrite of the ADI samples austenitized and plastically deformed at 1700°F with respect to single step and two-step austempering.

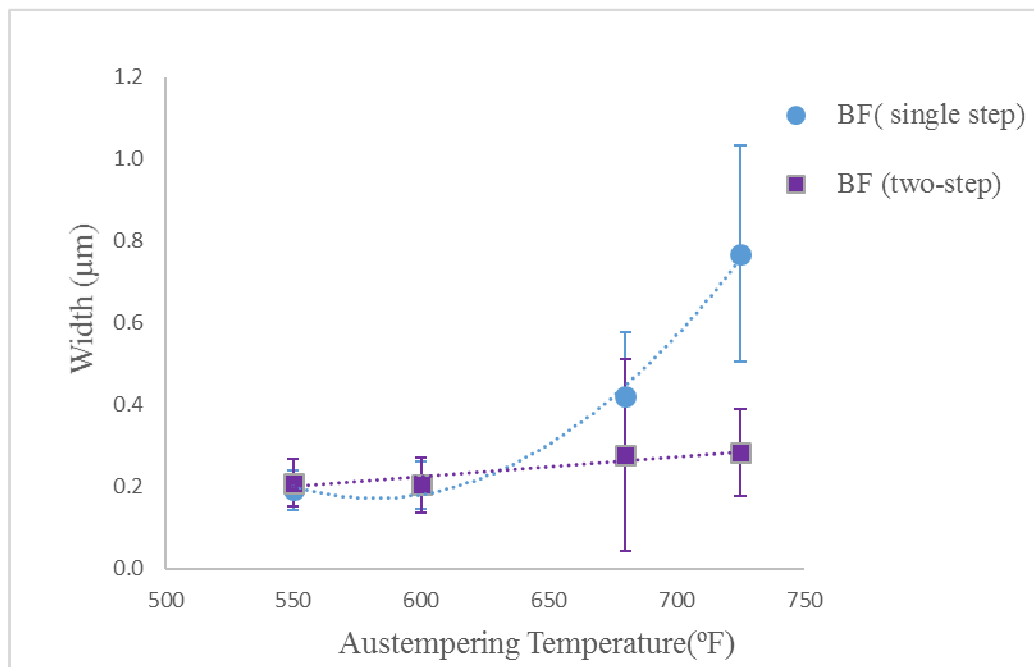


Figure.35: Variation in the width of bainitic ferrite in the ADI samples austenitized and plastically deformed at 1700°F with respect to single step and two-step austempering

The two step austempering along with the plastic deformation has significantly reduced the lath size of the bainitic ferrite in ADI samples austempered in the upper bainitic temperature range of 680°F and 725°F. However, no significant difference in the lath sizes was observed in the samples austempered at lower bainitic temperature range of 550°F and 600°F. When the

difference between the first and second austempering temperature is large during two-step austempering, the resultant bainitic ferrite structure is significantly smaller than the single step austempered ADI. Thus, it appears that the transformation of austenite to ferrite occur predominantly by nucleation rather than growth process. Figure 36 compares the variation of width of films of retained austenite in the ADI samples austenitized and plastically deformed at 1700°F with respect to single step and two-step austempering. The effect of two-step austempering in refining the width of austenite was observed ion the ADI samples austempered at upper austempering temperatures of 700°F and 725°F. However, no significant difference in the width of the retained austenite was observed in the ADI samples as the austempering temperatures varied from 700°F to 550°F.

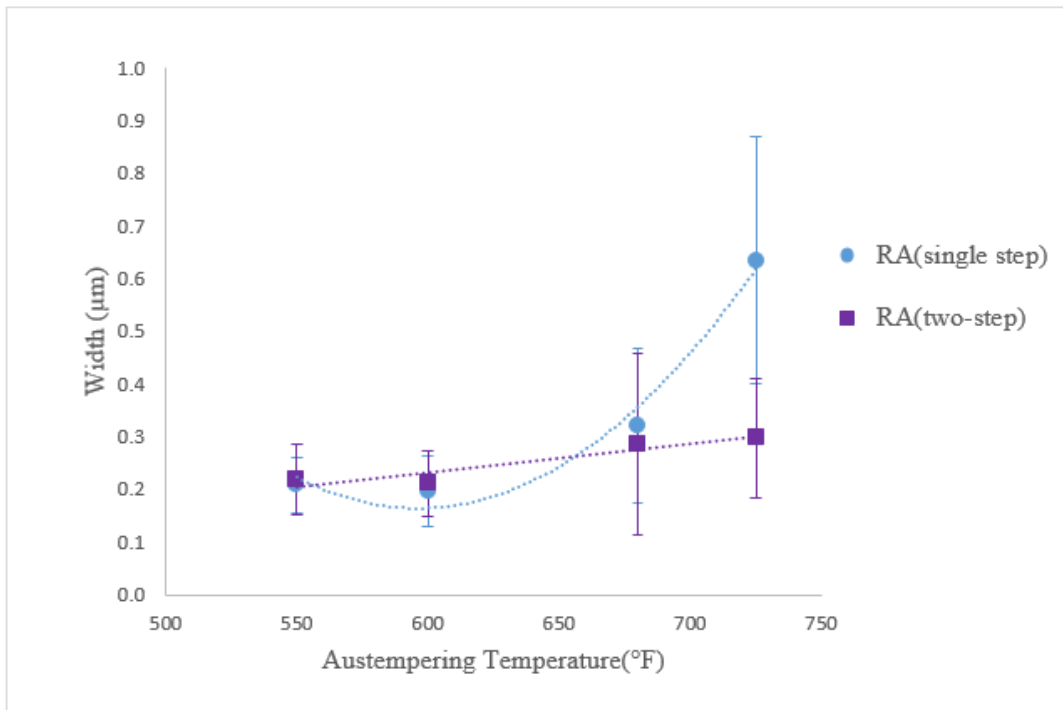


Figure.36: Variation in the width of retained austenite in the ADI samples austenitized and plastically deformed at 1700°F with respect to single step and two-step austempering.

Figure 37 shows the variation of width of bainitic ferrite in the ADI samples intercritically austenitized and plastically deformed at 1520°F with respect to single step and two step austempering. The reduction in the width of the bainitic ferrite lath with respect to two-step austempering is more noticeable in ADI as the austempering temperatures vary from 600°F to 725°F.

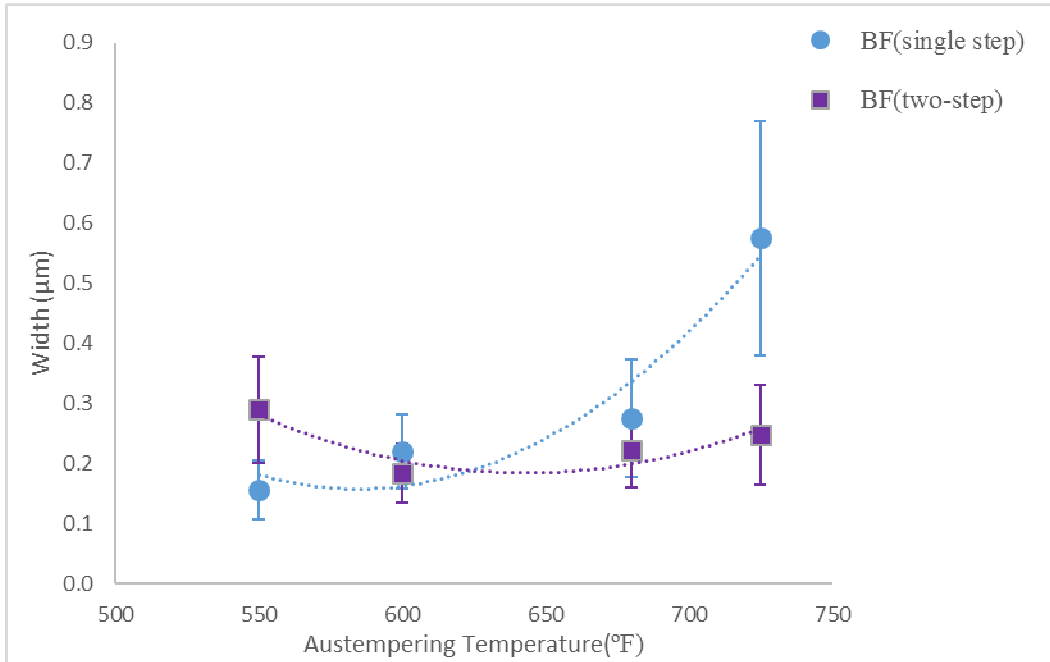


Figure.37: Variation in the width of bainitic ferrite (BF) in the ADI samples austenitized and plastically deformed at 1520°F with respect to single step and two-step austempering

Figure 38 shows the variation of width of films of retained austenite in the ADI samples intercritically austenitized and plastically deformed at 1520°F with respect to single step and two step austempering. Statistically, no significant difference was observed in the width of films of retained austenite between the single-step and two-step austempered ADI samples.



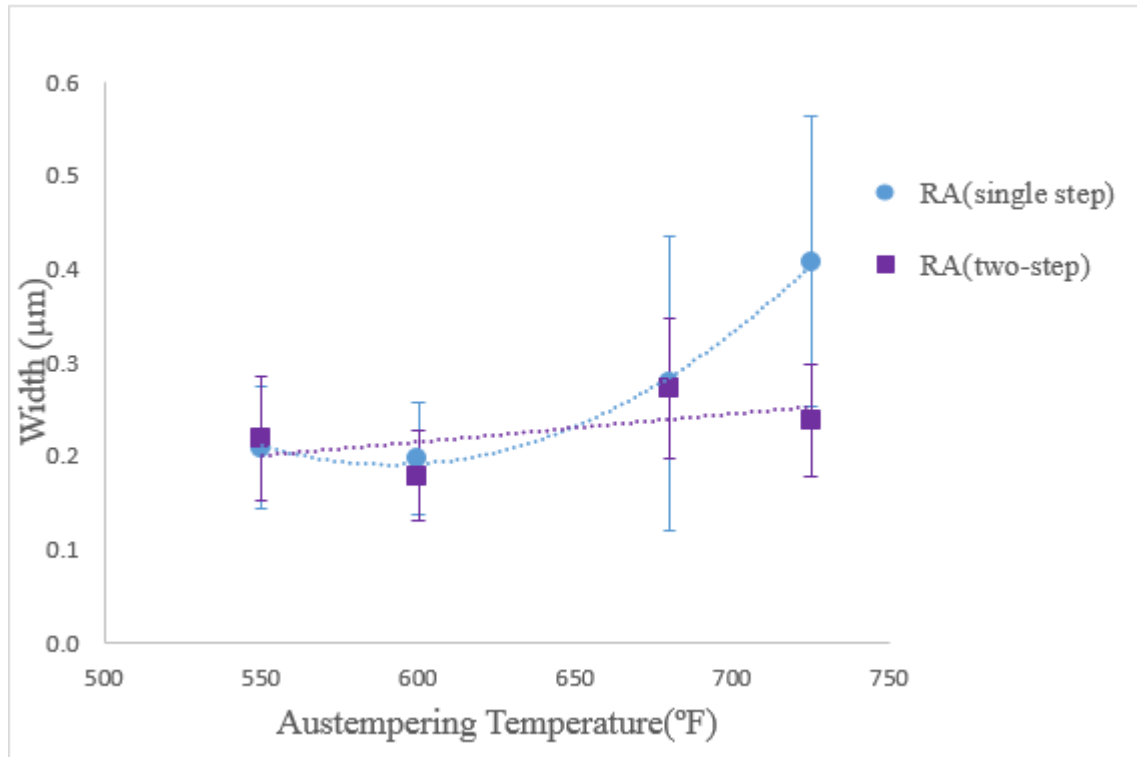


Figure.38: Variation in the width of films of retained austenite (RA) in ADI samples austenitized and plastically deformed at 1520°F with respect to single step and two-step austempering

Figure 39 shows the variation of width of bainitic ferrite and austenite with respect to plastic deformation in the two step austempered ADI samples. The samples were intercritically austenitized at 1472°F and 1436°F respectively. Statistically, no significant difference in the width of bainitic ferrite or austenite was observed in these intercritically austenitized, plastically deformed ADI samples. Approximately 80% reduction in the average width of the bainitic ferrite and retained austenite laths was observed in the ADI austempered at upper bainitic temperature of 725°F, whereas approximately only 40 % reduction in bainitic ferrite was observed in lower bainitic temperature austempered ADI with respect to plastic deformation in the ADI austenitized at lower intercritical temperatures of 1472°F and 1436°F austenitized followed by two-step austempered ADI when compared to traditionally austempered ADI samples.

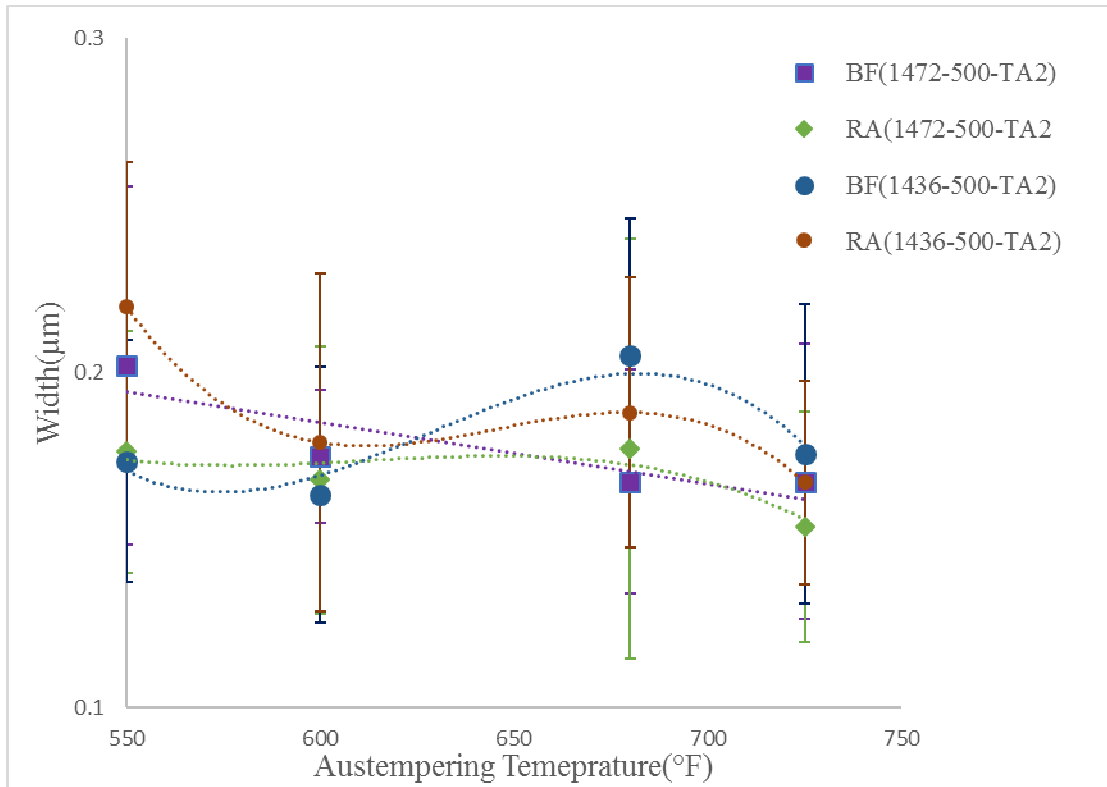


Figure.39: Variation in the width of (a) bainitic ferrite (BF), (b) films of retained austenite (RA) with respect to intercritical austenitization at 1472°F and 1436°F in plastically deformed ADI

High temperature plastic deformation followed by two -step austempering makes the ADI more robust to variations in austenitizing temperature and austempering temperature in terms of width of bainitic ferritic lath, films of retained austenite and width of the proeutectoid ferrite.

Table 8 compares the lath size measurements of the bainitic ferrite and the films of retained austenite with respect to the heat treatment and plastic deformation. The average width of the bainitic ferrite reduces with the application of high temperature plastic deformation to the ductile iron samples. The plastically deformed samples austempered by two-step austempering process resulted in slightly higher width of bainitic ferrite structures at lower bainitic temperature of 550°F compared to single step austempering with plastic deformation. During two-step austempering process, the samples were initially quenched to a lower austempering temperature of

500°F to facilitate greater ferrite nucleation. As the temperature is raised to the second austempering temperature, mainly the growth of the bainitic ferrite occurred. Thus, two-step austempering process resulted in the increase in average width of bainitic ferrite structures at lower bainitic temperatures.

Table 8: Comparison of lath size measurements

<b>T<sub>γ</sub></b> <b>(°F)</b>	<b>Plastic deformation</b>	<b>T<sub>A1</sub></b> <b>(°F)</b>	<b>T<sub>A2</sub></b> <b>(°F)</b>	<b>width of bainitic ferrite lath</b> <b>(μm)</b>	<b>width of films of retained austenite</b> <b>(μm)</b>
1700°F	n/a	550°F	n/a	0.294 ± 0.093	0.261 ± 0.090
	yes	550°F	n/a	0.192 ± 0.049	0.208 ± 0.053
	yes	500°F	550°F	0.210 ± 0.058	0.283 ± 0.105
1520°F	n/a	550°F	n/a	0.333 ± 0.195	0.190 ± 0.054
	yes	550°F	n/a	0.156 ± 0.049	0.209 ± 0.605
	yes	500°F	550°F	0.290 ± 0.088	0.218 ± 0.067

### 5.2.5 Lath size measurements of plastic deformed ADI with respect to strain rate

Table 9 reports the lath sizes of the bainitic ferrite lath and the width of films of retained austenite in the plastically deformed samples with respect to the strain rate and austempering process. The average width of the bainitic ferrite in these ADI samples were in the nanoscale range i.e. approximately less than 100nm. The width of bainitic ferrite and austenite reduced significantly at the strain rates of both 0.5mm/min and 10mm/min in both the single step and two step austempered ADI indicating that the heat treatment process is robust to strain rates. Thus, it appears that the strain rate can be optimized to obtain nanostructured bainitic ferrite in ADI.

Table 9: Lath size measurements of different phases in plastically deformed ADI with respect to two-step austempering temperature

(samples austenitized at  $T_{\gamma}=1520^{\circ}\text{F}$  for 3 hours,  $T_{A1}=500^{\circ}\text{F}$  for 15 minutes,  $T_{A2}=550^{\circ}\text{F}$  for 2.5 hours)

$T_{\gamma}$ ( $^{\circ}\text{F}$ )	$T_{A1}$ ( $^{\circ}\text{F}$ )	$T_{A2}$ ( $^{\circ}\text{F}$ )	strain rate(mm/min)	width of bainitic ferrite lath ( $\mu\text{m}$ )	width of films of retained austenite ( $\mu\text{m}$ )
1520 $^{\circ}\text{F}$	500 $^{\circ}\text{F}$	n/a	0.5	$0.127 \pm 0.023$	$0.130 \pm 0.022$
		550 $^{\circ}\text{F}$		$0.128 \pm 0.027$	$0.130 \pm 0.024$
		n/a	10	$0.114 \pm 0.015$	$0.120 \pm 0.063$
		550 $^{\circ}\text{F}$		$0.116 \pm 0.020$	$0.119 \pm 0.020$

In summary, the development of nanostructured bainitic ferrite can be achieved by the additional mechanical processing along with the austempering process. This additional energy, obtained from the high temperature plastic deformation process will enhance the nucleation rate, resulting in more nucleation sites for the growth of bainitic ferrite. During the growth process, the width of the bainitic ferrite lath is very much lower as they can grow only a small distance before they impinge on each other resulting in a refined microstructure.

### 5.3 Ferritic cell size

Ferritic cell size (d) is the measure of mean free path for dislocation motion. Individual laths have numerous ferritic cells present in it. The ferritic cell size of the ADI samples was calculated from the XRD data using the Scherrer equation [125].

#### 5.3.1 Ferritic cell sizes of conventional and cryogenically treated ADI

Table 10 compares the ferritic cell size of the ADI samples with and without cryogenic treatments.

Table 10: Ferritic cell size of the ADI with respect to cryogenic treatment.

(samples not given plastic deformation)

Austenitizing temperature (°F)	Austempering temperature (°F)	Cryogenic treatment	Ferritic cell size (nm)
1700°F	750°F	No	27 ± 3.2
		Yes	22.1 ± 4.6
	725°F	No	26 ± 8.5
		Yes	23.6 ± 2.7
	700°F	No	24.3 ± 3.3
		Yes	23.6 ± 5.5
	550°F	No	19.7 ± 2.6
		Yes	20.3 ± 1.7
	500°F	No	17.5 ± 4.0
		Yes	14.7 ± 1.9

A comparison of data in Table 10 shows that, the average ferritic cell size of the ADI reduced after the cryogenic treatment. This reduction in ferritic cell size as observed from the X-ray analysis is due to the transformation of retained austenite to martensitic structure during the cryogenic treatment. It is also interesting to note that the ferritic cell size of the ADI samples reduced as the austempering temperature varied from 750°F to 500°F. Average percentage difference of approximately 35% was observed between the ADI samples austempered at upper and lower bainitic temperatures of 750°F and 500°F respectively. Similarly, a percentage

difference of approximately 33% was observed between the cryogenically treated ADI samples austempered at upper and lower bainitic temperatures of 750°F and 500°F respectively.

### 5.3.2 Ferritic cell size of conventional ADI with respect to plastic deformation

Table 11: Ferritic cell size of the ADI with respect to the plastic deformation and single/two-step austempering temperatures.

<b>Austenitizing temperature (°F)</b>	<b>Austempering temperature (°F)</b>	<b>Plastic deformation at 1700°F</b>	<b>Single step /two step austempering</b>	<b>Ferritic cell size (nm)</b>
1700°F	750°F	No	Single step	27 ± 3.2
	725°F	No	Single step	26 ± 8.5
		Yes	Single step	19.7 ± 5.6
		Yes	Two-step	21.8 ± 1.1
	700°F	No	Single step	24.3± 3.3
	680°F	Yes	Single step	19.5 ± 7.3
		Yes	Two-step	22.1 ± 5.0
	600 °F	Yes	Single step	17.3 ± 5.4
		Yes	Two-step	18.3 ± 5.5
	550°F	No	Single step	19.7 ± 2.6
		Yes	Single step	17.0± 5.7
		Yes	Two-step	18.4 ± 4.9
	500°F	No	Single step	17.5 ± 4.0

Table 11 details the ferritic cell sizes of the ADI samples conventionally austenitized at 1700°F, followed by either traditional austempering or plastic deformation and single step austempering or plastic deformation and two-step austempering.

The average ferritic cell sizes of the conventionally austempered ADI decreases as the austempering temperature decreases from 750 to 500°F. High temperature plastic deformation followed by single step austempering reduced the ferritic cell size of the ADI by approximately 13 to 24%. Statistically, no significant difference was observed between the single step and two step processing in the plastically deformed ADI.

### **5.3.3 Ferritic cell size of intercritical ADI with respect to plastic deformation**

Table 12 details the ferritic cell size of the ADI samples intercritically austenitized at upper intercritical austenitizing temperature of 1520°F with respect to plastic deformation, single/two-step austempering and strain rates. The average ferritic cell size of the ADI samples reduced as the austempering temperature varied from 750°F to 500°F. Plastic deformation resulted in significant reduction in the ferritic cell sizes of the ADI samples austempered in the upper bainitic temperature range of 680°F and 725°F. However, no significant difference was observed in the ADI samples austempered in the lower bainitic temperature range of 600°F and 550°F. It was also observed that two-step austempering did not have any significant effect in reducing the ferritic cell size in the ADI samples intercritically austenitized and plastically deformed at 1520°F.

Some of the ADI samples were plastically deformed at the lower and higher strain rates of 0.5 and 10 mm/min respectively and austempered at lower bainitic temperature of 550°F by single step as well as two-step austempering process. The average ferritic cell sizes of those samples lie within a small range of 17nm to 17.4nm. As mentioned earlier from Table 9, the the heat

treatment process is robust between 0.5 and 10mm/min. Therefore, no effect with the 5mm/min strain rate is expected.

Table 12: Ferritic cell size of the intercritically austenitized ADI with respect to the plastic deformation, single/two-step austempering temperatures and strain rates

<b>Austenitizing temperature (°F)</b>	<b>Austempering temperature (°F)</b>	<b>Plastic deformation at 1520°F</b>	<b>Strain rate (mm/min)</b>	<b>Single step /two step austempering</b>	<b>Ferritic cell size (nm)</b>
1520°F	725°F	No	-	Single step	24 ± 4.2
		Yes	5	Single step	21.9 ± 5.6
		Yes	5	Two-step	19.6 ± 3.4
	680°F	No	5	Single step	24.6 ± 1.8
		Yes	5	Single step	17.1 ± 6.2
		Yes	5	Two-step	17.9 ± 3.4
	600°F	No	5	Single step	18.6 ± 3.0
		Yes	5	Single step	18.8 ± 6.8
		Yes	5	Two-step	16.5 ± 5.4
	550°F	No	5	Single step	16.5 ± 3.3
		Yes	5	Single step	17.0 ± 6.3
		Yes	5	Two-step	19.1 ± 6.7
		Yes	0.5	Single step	17.3 ± 1.6
		Yes	10	Single step	17.4 ± 3.1
		Yes	0.5	Two step	17.1 ± 2.4
		Yes	10	Two step	17 ± 1.9



Table 13 compares the average ferritic cell sizes of the ADI samples intercritically austenitized at lower intercritical austenitization temperature of 1472°F and 1436°F, with respect to plastic deformation and single/two-step austempering temperatures.

Table 13: Ferritic cell size of the intercritically austenitized ADI with respect to the plastic deformation, single/two-step austempering temperatures.

<b>Austenitizing temperature (°F)</b>	<b>Austempering temperature (°F)</b>	<b>Plastic deformation</b>	<b>Single step /two step austempering</b>	<b>Ferritic cell size (nm)</b>
1472°F	725°F	Yes	Two-step	21.5 ± 2.7
	680°F	No	Single step	23.1 ± 1.4
		Yes	Two-step	19.5 ± 3.5
	600°F	Yes	Two-step	18.3 ± 3.5
	550°F	Yes	Two-step	20.0 ± 2.1
1436°F	725°F	Yes	Two-step	26.0± 2.9
	680°F	No	Single step	27.4 ± 0.5
		Yes	Two-step	20.1 ± 1.5
	600°F	Yes	Two-step	21.4 ± 1.3
	550°F	Yes	Two-step	24.1 ± 0.6

Single step austempering was carried out only in the ADI samples austempered at 680°F. Comparatively, plastic deformation and two step austempering reduced the average ferritic cell sizes in these samples. Approximately 15% and 27% reduction in the average ferritic cell sizes was observed after plastic deformation and two-step austempering in these ADI samples

intercritically austenitized at 1472°F and 1436°F respectively. As the austenitization temperature is reduced, the average ferritic cell size of the ADI increased. This can be attributed to the presence of higher volume fraction of proeutectoid ferrite in the ADI samples intercritically austenitized at lower austenitizing temperatures.

In summary, austempering temperature reduces the ferritic cell size. No significant changes were observed in the ferritic cell size with respect to plastic deformation. Bainitic ferrite and austenite laths must be refined heavily to obtain an increased resistance to the dislocation movement. The individual ferritic cell size doesnot yield nanostructured ADI. Thus, the ferritic cell size is not a key factor in determining the nanostructured bainitic ferrite or films of retained austenite in ADI.

## CHAPTER 6. TRANSMISSION ELECTRON MICROSCOPY

Transmission electron Microscopy was carried out to study the microstructure of the austempered ductile cast iron in detail. Among all the heat treated ductile cast iron samples, only 6 samples were used for the TEM analysis. Detailed summary of the samples analyzed with TEM are reported in Table 14.

Table 14: Summary of ADI samples analyzed with TEM

<b>T<sub>γ</sub> (°F)</b>	<b>Plastic deformation</b>	<b>T<sub>A1</sub>(°F)</b>	<b>T<sub>A2</sub> (°F)</b>
1700	n/a	725	n/a
1700	yes	725	n/a
1700	yes	500	600
1700	yes	500	680
1520	yes	500	600
1520 (strain rate: 10mm/min)	yes	500	550

The TEM Micrograph confirmed the presence of nanostructured ausferritic structure in specific heat treated ADI samples which is detailed below. Selected area electron diffraction patterns (SAED) were obtained and indexed to confirm the presence of bainitic ferrite and austenite phases. The SAED were indexed using the following equation

$$d_{hkl} R_{hkl} = \lambda \quad (6.1)$$

where  $d_{hkl}$  is the lattice spacing of the plane,  $R_{hkl}$  is the distance of the spot from the center beam,  $\lambda$  is the wavelength of the electron beam and  $L$  is the camera length. The product  $\lambda L$  is calculated using the standard aluminium sample of known  $d_{hkl}$  lattice spacing for the operating voltage of

200KeV as 117.57Å-pixels. The Digital Micrograph software was used to measure the lattice spacing of the ductile iron samples.

Figure 40 shows the TEM micrographs of the ductile iron sample conventionally austempered at 725°F. The bright field image in Figure 40 (a) and (b) shows the ausferritic structure where the bainitic ferrite appears bright with austenite present in between the bainitic ferrite as thin dark films.

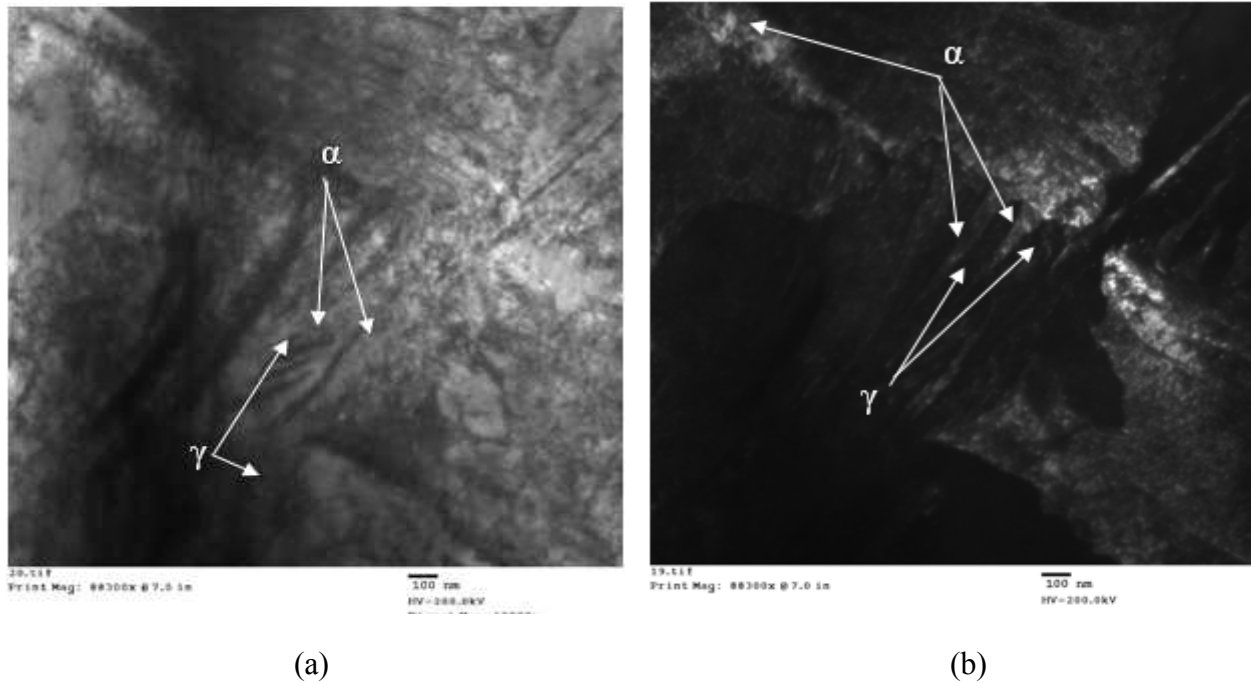
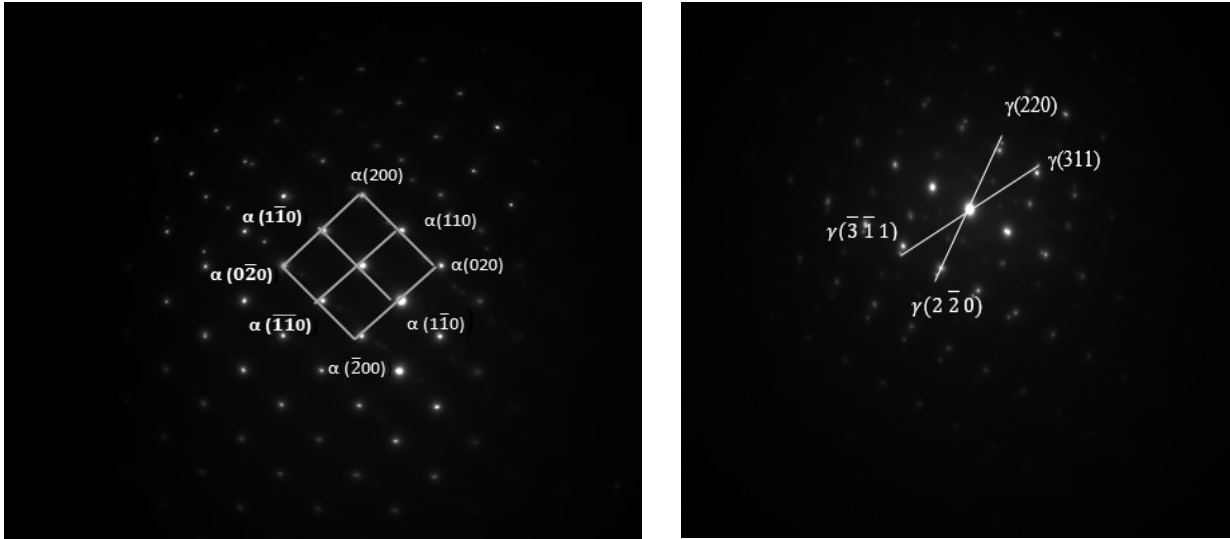


Figure.40: TEM micrographs of conventional ADI a) Bright Field image b) Dark field image

The SAED pattern obtained shows the typical spot diffraction pattern with well-defined spacing and angles in the Figure 41 (a) and (b) and confirms the presence of bainitic ferrite and austenite phases respectively in the microstructure of the conventionally austempered ADI.



(a)

(b)

Figure.41.: TEM micrographs of ductile cast iron conventionally austempered at 725°F (a) Indexed diffraction pattern for bainitic ferrite phase (b) Indexed diffraction pattern for austenite

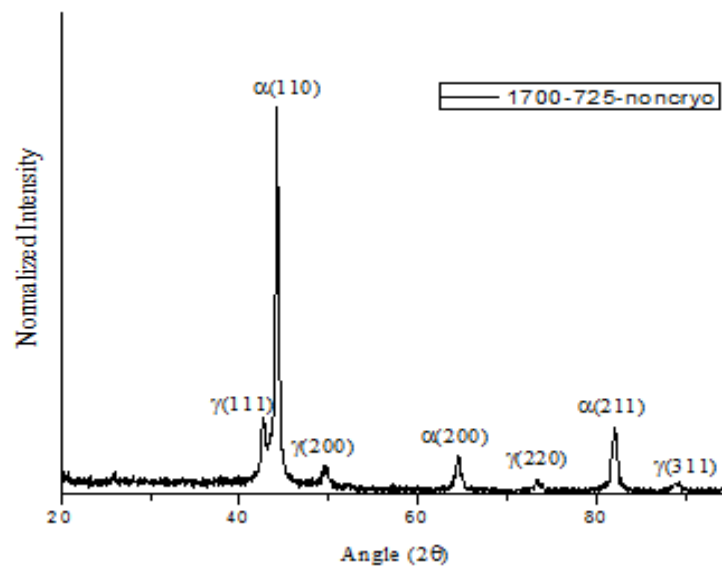


Figure.42: X-ray diffraction pattern of conventional ductile cast iron ( $T_{\gamma}=1700^{\circ}\text{F}$  for 2 hours,  $T_{\text{A}}=725^{\circ}\text{F}$  for 2 hours)

The dark field image obtained from the  $\alpha$  (110) bainitic ferrite reflection shows the coarse bainitic ferrites and retained austenite present in between the bainitic ferrite laths. This is in good

agreement with the X-ray diffraction profile of the conventionally austempered ductile cast iron showing the presence of both the ferrite and austenite phases as shown in the Figure 42. The bainitic ferrite occurs in a sheaf like morphology with some subunits in them. The average width of the bainitic ferrite occurred in the range of 33nm as measured with the image pro software.

The x-ray diffraction pattern was carried out in the  $2\theta$  range of  $20^\circ$  to  $92^\circ$  to obtain the ferrite and austenite peaks. All the conventionally austempered ductile cast iron samples showed similar diffraction pattern consisting of austenite and ferrite peaks. However, the volume fraction of the austenite and ferrite varied with respect to the austempering temperature. The measured d spacing for the obtained diffraction pattern is compared with the calculated d spacing and the percentage difference is reported in Table 15.

Table 16 reports the measured and calculated angle between the diffraction planes. The percentage difference is very low as the measured d spacing and the angle between the diffraction plane is comparable to the theoretical measurements.

Table.15: Indexing details of diffraction pattern of ferrite phase (Conventional ADI,  $T_\gamma=1700^\circ\text{F}$  for 3 hours,  $T_A=725^\circ\text{F}$  for 2 hours)

Spot	Measured d spacing (Å)	(hkl)	Calculated d spacing (Å)	% difference
1	2.081	$\alpha$ (110)	2.029	2.6
2	1.451	$\alpha$ (200)	1.435	1.1
3	2.092	$\alpha$ ( $1\bar{1}0$ )	2.029	3.1
4	1.488	$\alpha$ ( $0\bar{2}0$ )	1.435	3.7

Table.16: Indexing details of diffraction pattern of ferrite phase (Conventional ADI,  $T_{\gamma}=1700^{\circ}\text{F}$ ,  
 $T_A=725^{\circ}\text{F}$ )

Angles	Measured angle ( $^{\circ}$ )	hkl	Calculated angle ( $^{\circ}$ )	% difference
1 $\angle$ 2	44.31	$\alpha(110) \angle \alpha(200)$	45	1.5
2 $\angle$ 3	45	$\alpha(200) \angle \alpha(1\bar{1}0)$	45	0
3 $\angle$ 4	45	$\alpha(1\bar{1}0) \angle \alpha(0\bar{2}0)$	45	0
4 $\angle$ 1	45.67	$\alpha(0\bar{2}0) \angle \alpha(1\bar{1}0)$	45	1.4

Figure 43 shows the TEM micrograph of the ductile cast iron sample conventional austenitized at  $1700^{\circ}\text{F}$ , plastically deformed at  $1700^{\circ}\text{F}$  and austempered at  $725^{\circ}\text{F}$ .



Figure.43: TEM micrographs showing Bright field image of plastically deformed ADI  
( $T_{\gamma}=1700^{\circ}\text{F}$ ,  $T_D=1700^{\circ}\text{F}$ ,  $T_A=725^{\circ}\text{F}$ )

Figure 44 shows the low magnification dark field image of the plastically deformed ADI where the morphology of the ausferritic structure is visible. The dark field image as shown in Figure 44(a) obtained using the bainitic ferrite reflection  $\alpha$  (110) shows the bainitic ferrite structure which occurs as tiny subunits. Similar observation is obtained for the austenite reflection as shown in Figure 44(b).

Plastic deformation significantly refined the grain size of the ADI samples. The length and width of these bainitic ferrite structures are refined by the plastic deformation when compared with the conventional austempered ductile cast iron without plastic deformation.

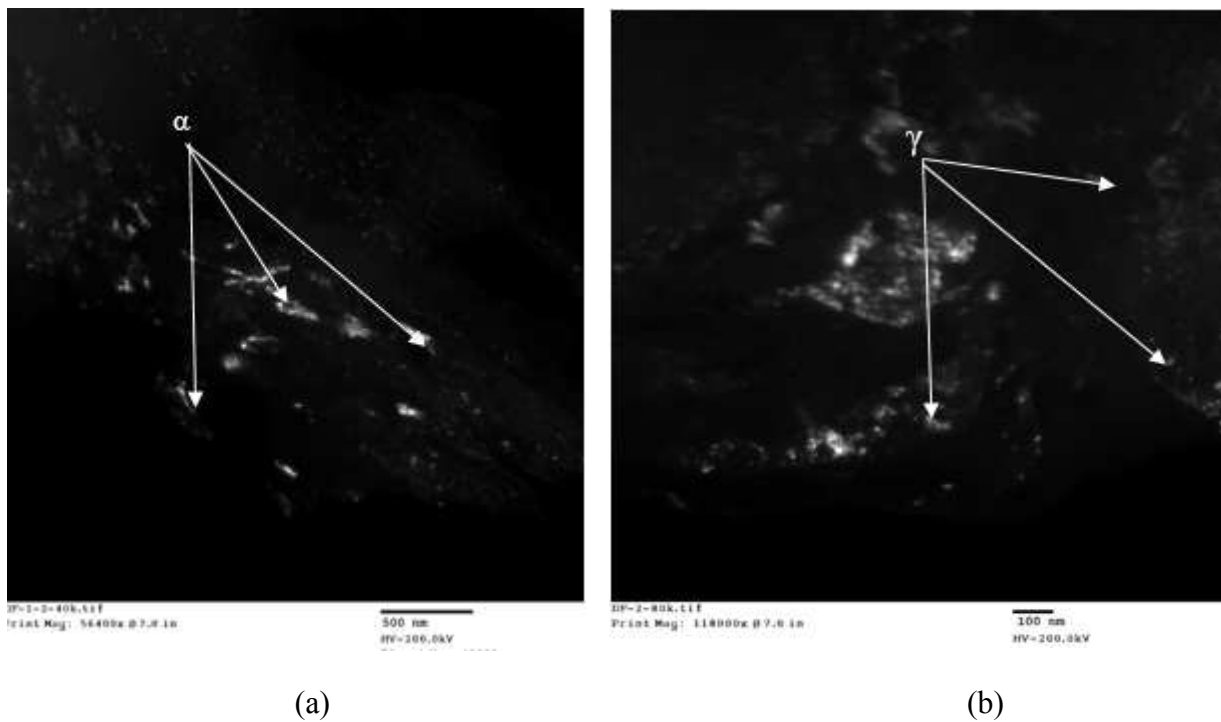
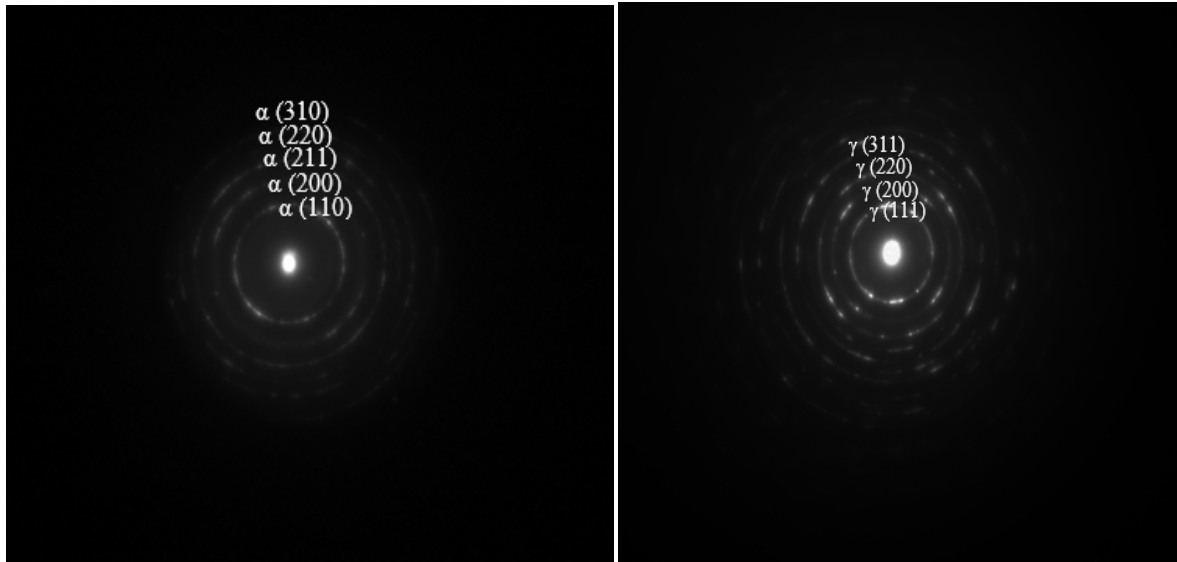


Figure.44: TEM micrographs of plastically deformed ADI ( $T_{\gamma}=1700^{\circ}\text{F}$ ,  $T_D=1700^{\circ}\text{F}$ ,  $T_A=725^{\circ}\text{F}$ )

(a) Dark Field image showing ferrite phase b) Dark field image showing austenite phase





(a)

(b)

Figure.45: Indexed diffraction of (a)ferrite phase (b) austenite phase of plastically deformed ADI

( $T_\gamma=1700^\circ\text{F}$ ,  $T_D= 1700^\circ\text{F}$ ,  $T_A=725^\circ\text{F}$ )

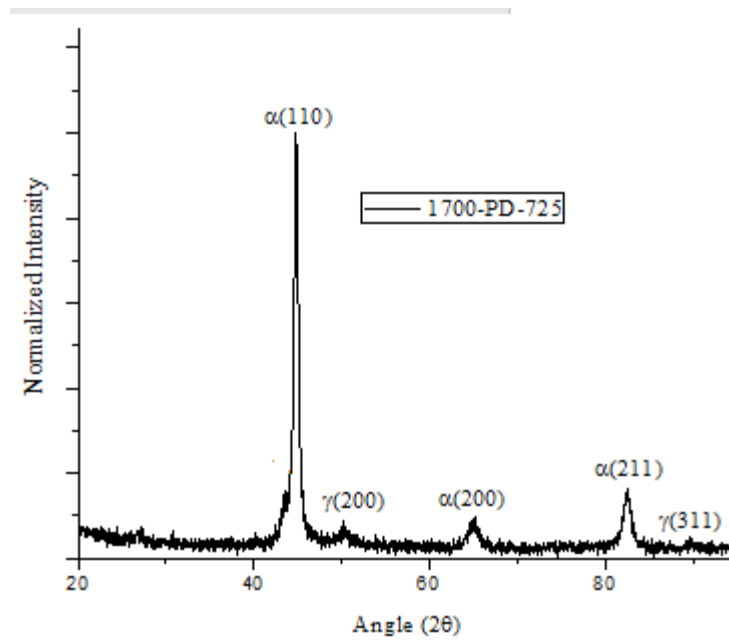


Figure.46: X-ray diffraction pattern of ductile cast iron plastically deformed ADI

( $T_\gamma=1700^\circ\text{F}$ ,  $T_D= 1700^\circ\text{F}$ ,  $T_A=725^\circ\text{F}$ )

The corresponding X-ray diffraction profile is shown in the Figure 46. XRD analysis confirms the presence of both austenite and ferrite phases in this plastically deformed ADI. The  $\gamma$

(111) is not prominent and the  $\gamma$  (220) peak is not present indicating the lower volume fraction of austenite in these plastically deformed samples.

In the conventional austempered ductile cast iron, the selected area electron diffraction (SAED) pattern showed a typical arrangement of the spot pattern along the zone axis, whereas, in the plastically deformed ADI, the ring like SAED pattern is observed as shown in the Figure 45. This continuous rings arise from the very fine grain structures. The diffraction pattern changes from spot to rings (example: Figure 41 and 45) when the refinement of the grains occurs as shown in the Figure 47. The refinement of the grain obviously resulted in the refinement of the crystallites inside the grains. Thus, the plastic deformation of the ADI resulted in ultra-fine nano crystalline bainitic ferrite and austenite.

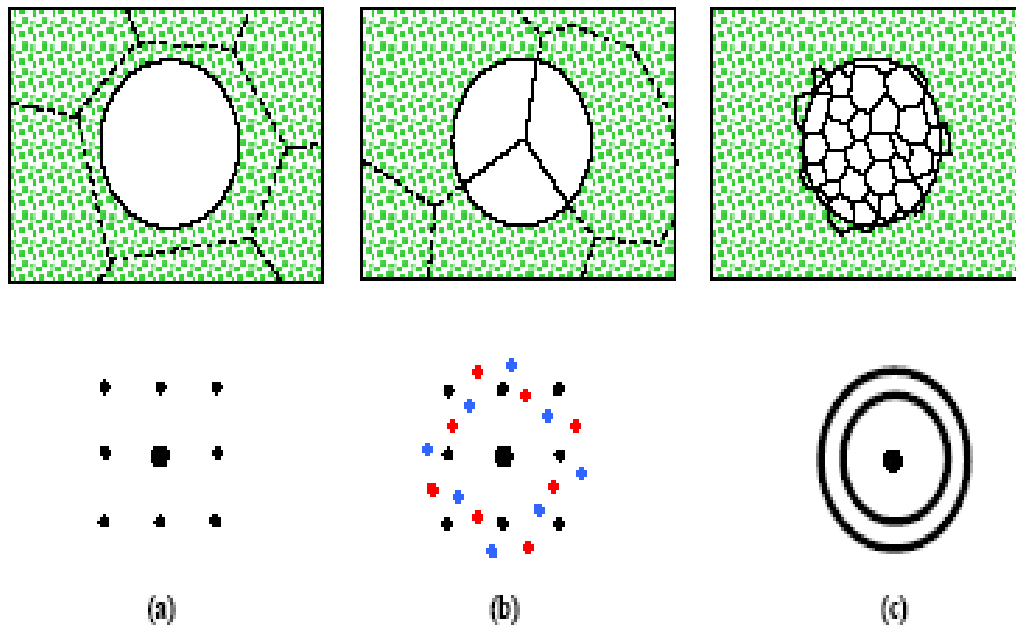


Figure.47: Changes in diffraction pattern with respect to grain size

The percentage difference between the measured and calculated d spacing of the obtained ring pattern for the bainitic ferrite and austenite phase is detailed in Table 17 and Table 18 respectively.

Table.17: Indexing details of diffraction pattern of ferrite phase (Plastically deformed ADI,  $T_{\gamma}=1700^{\circ}\text{F}$ ,  $T_D=1700^{\circ}\text{F}$ ,  $T_A=725^{\circ}\text{F}$ )

Ring	Measured d spacing (Å)	(hkl)	Calculated d spacing (Å)	% difference
1	2.027	$\alpha$ (110)	2.029	0.1
2	1.434	$\alpha$ (200)	1.435	0.1
3	1.170	$\alpha$ (211)	1.172	0.2
4	1.005	$\alpha$ (220)	1.015	1.0
5	0.908	$\alpha$ (310)	0.908	0.0

Table.18: Indexing details of diffraction pattern of austenite phase (Plastically deformed ADI,  $T_{\gamma}=1700^{\circ}\text{F}$ ,  $T_D=1700^{\circ}\text{F}$ ,  $T_A=725^{\circ}\text{F}$ )

Ring	Measured d spacing (Å)	(hkl)	Calculated d spacing (Å)	% difference
1	2.157	$\gamma$ (111)	2.078	3.8
2	1.578	$\gamma$ (200)	1.800	12.3
3	1.251	$\gamma$ (220)	1.272	1.7
4	1.094	$\gamma$ (311)	1.085	0.8

The measured and calculated interatomic distance match well for the bainitic ferrite phase. The interatomic distance of the obtained diffraction pattern for the austenite phase has higher percentage difference than the calculated d spacing. This is due to the the possible overlapping of the ferrite and austenite rings and the weak SAED pattern obtained for this sample which made the location of rings unclear.

Figure 48 shows the TEM micrographs of the ductile iron of the conventionally austenitized, plastically deformed and two-step austempered ADI, ( $T_{\gamma}=1700^{\circ}\text{F}$ ,  $T_D= 1700^{\circ}\text{F}$ ,  $T_{A1}=500^{\circ}\text{F}$ ,  $T_{A2}= 725^{\circ}\text{F}$ ).

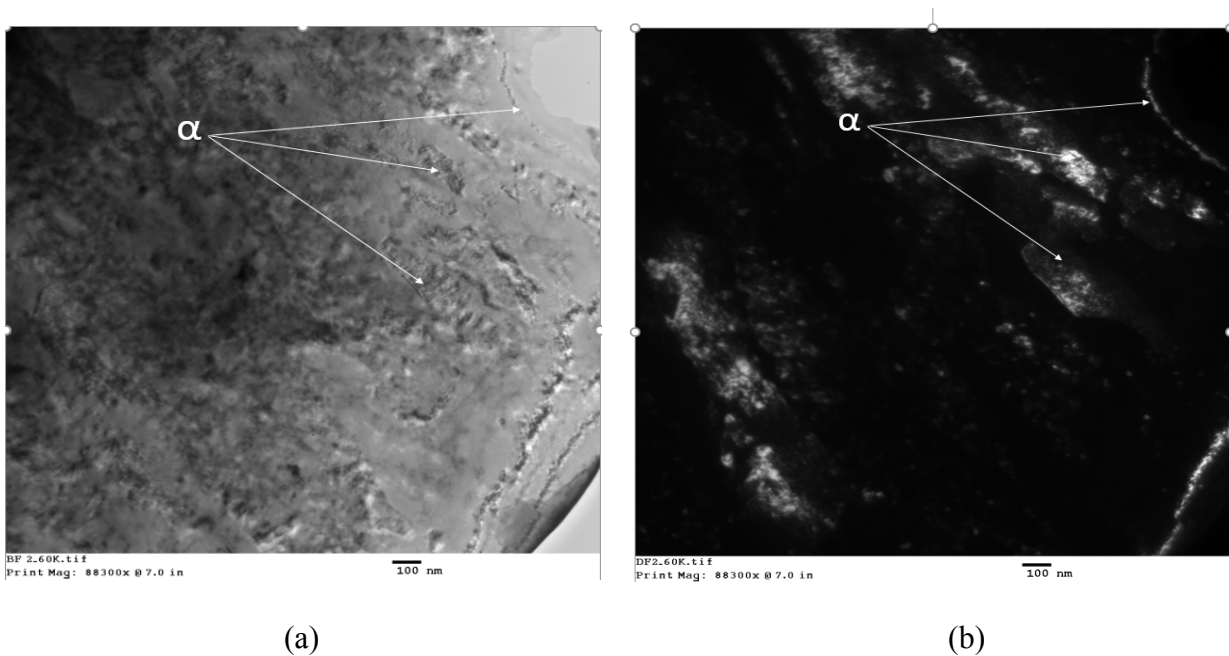


Figure.48: TEM micrographs of plastically deformed, two-step austempered ADI ( $T_{\gamma}=1700^{\circ}\text{F}$ ,  $T_D= 1700^{\circ}\text{F}$ ,  $T_{A1}=500^{\circ}\text{F}$ ,  $T_{A2}= 725^{\circ}\text{F}$ ), a) Bright Field image b) Dark field image

The bright field image in the Figure 48 (a) shows the ausferritic phase in the plastically deformed ADI. The corresponding dark filed image is shown in Figure 48(b). The bainitic ferrite appears as very fine subunits with the films of austenite between them. The SAED pattern of the bainitic ferrite phase is shown in the Figure 49(a). The plastic deformation along with the two-step austempering in this ADI resulted in a ring like diffraction pattern which confirms the

nanoscale grains in this heat-treated ADI. The dark field image from the  $\alpha$  (110) reflection shows the very thin bainitic ferrite structures.

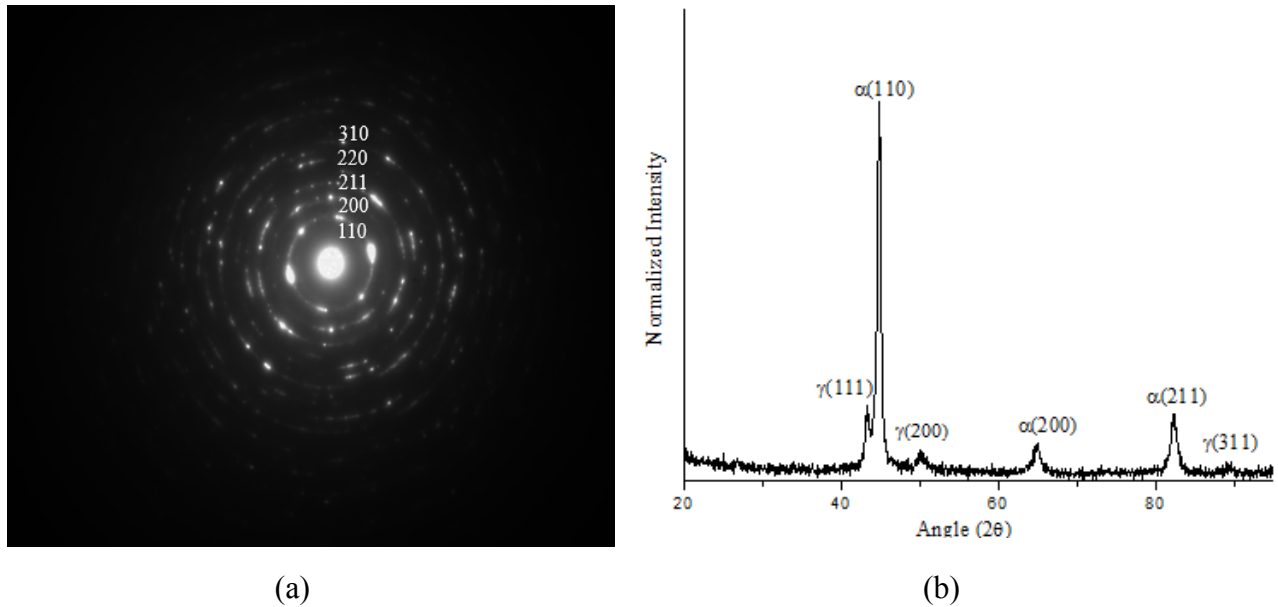


Figure.49: TEM micrographs of plastically deformed, two-step austempered ADI ( $T_{\gamma}=1700^{\circ}\text{F}$ ,  $T_{\text{D}}=1700^{\circ}\text{F}$ ,  $T_{\text{A1}}=500^{\circ}\text{F}$ ,  $T_{\text{A2}}=725^{\circ}\text{F}$ ), (a) indexed SAED pattern (b) X-ray diffraction profile

The corresponding X-ray diffraction pattern is shown in Figure 49(b). Compared to conventional ADI, the  $\gamma$  (220) peak is not present for this sample indicating that the plastic deformation reduced the net amount of austenite present. The SAED pattern for the austenite phase was not observed with TEM analysis for this sample. It is also possible for the overlapping of the ferrite and austenite phases in the ring diffraction pattern of this ADI because of the ultrafine bainitic ferrite and austenite phases present. This could possibly be the reason behind the slight variation in the percentage difference of the measured interatomic distance when compared with the theoretical interatomic distance as detailed in the Table 19.

Table.19: Indexing details of diffraction pattern of ferrite phase (Plastically deformed, two-step austempered ADI,  $T_{\gamma}=1700^{\circ}\text{F}$ ,  $T_{\text{D}}= 1700^{\circ}\text{F}$ ,  $T_{\text{A1}}=500^{\circ}\text{F}$ ,  $T_{\text{A2}}= 725^{\circ}\text{F}$ )

Spot	Measured d spacing ( $\text{\AA}$ )	(hkl)	Calculated d spacing ( $\text{\AA}$ )	% difference
1	2.081	$\alpha$ (110)	2.029	2.5
2	1.547	$\alpha$ (200)	1.435	7.8
3	1.238	$\alpha$ (211)	1.172	5.6
4	1.022	$\alpha$ (220)	1.015	0.8
5	0.933	$\alpha$ (310)	0.908	2.8

Figure 50 shows the TEM micrograph of  $1520^{\circ}\text{F}-500^{\circ}\text{F}-600^{\circ}\text{F}$  sample. The bright field image shows the bainitic ferrite subunits with austenite laths in between them in the nanoscale range. The SAED pattern obtained from this plastically deformed ADI is intermediate which is neither a typical pattern for the polycrystalline material nor the nanocrystalline ring pattern. This is ultimately because there is a significant reduction in the grain size of this ADI with respect to the plastic deformation. The dark field image obtained from the  $\alpha$  (110) bainitic ferrite reflection show the subunits of lath shaped bainitic ferrite however, the length and width of the bainitic ferrite structures are ultrafine unlike the conventional ADI.

The X-ray diffraction profile of the upper intercritical austenitized, plastically deformed, two step austempered ADI in Figure 51, show faint austenite peaks indicating the lesser volume fraction of austenite in these samples. The presence of austenite is also confirmed from the faint reflection spot from the SAED ring pattern. The indexing details are given in the Table 20.

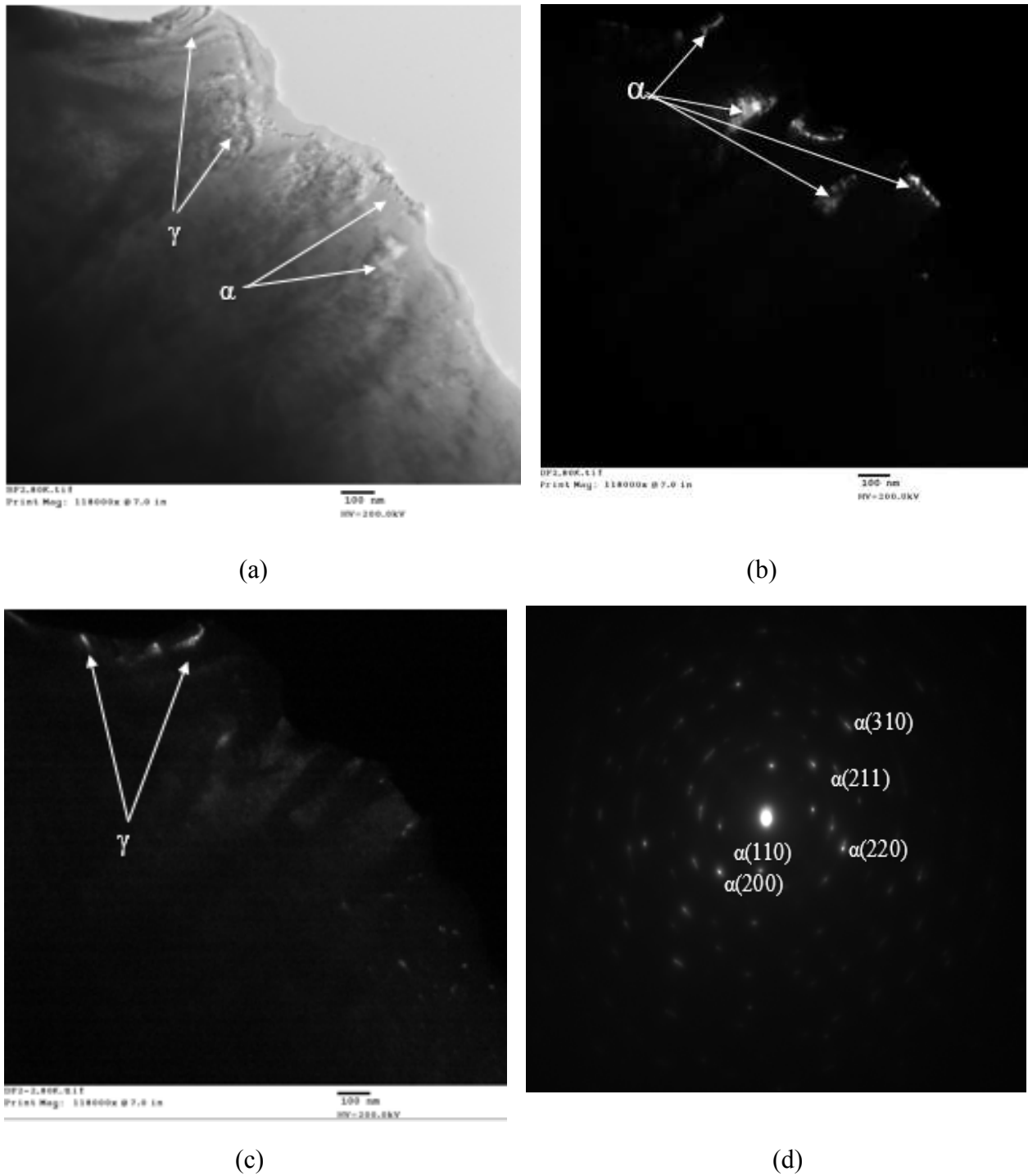


Figure.50: TEM micrographs of ductile cast iron intercritically austenitized, plastically deformed, two-step austempered ADI ( $T_{\gamma}=1520^{\circ}\text{F}$ ,  $T_D=1520^{\circ}\text{F}$ ,  $T_{A1}=500^{\circ}\text{F}$ ,  $T_{A2}=600^{\circ}\text{F}$ , a) Bright Field image, (b) and (c) Dark field image (d) SAED Pattern

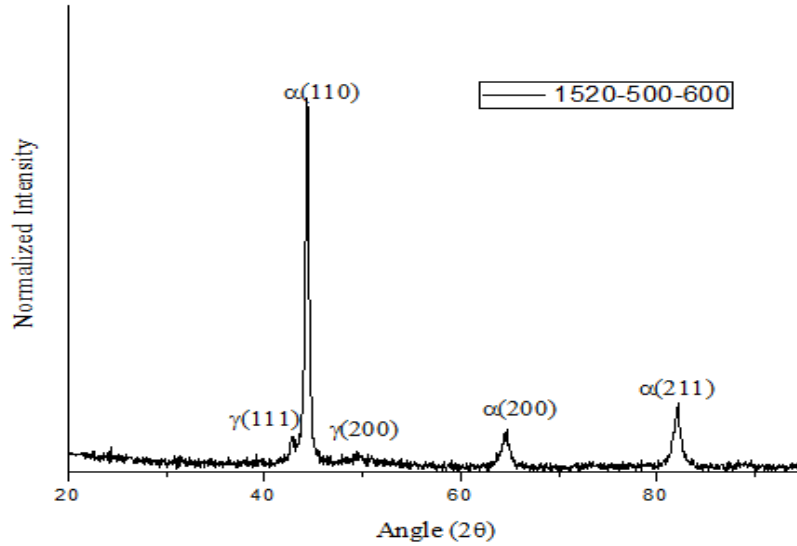


Figure.51: X-ray diffraction pattern of ductile cast iron plastically deformed ADI, ( $T_{\gamma}=1520^{\circ}\text{F}$ ,  $T_D=1520^{\circ}\text{F}$ ,  $T_{A1}=500^{\circ}\text{F}$ ,  $T_{A2}=600^{\circ}\text{F}$ )

Table 20: Indexing details of diffraction pattern of ferrite phase (Plastically deformed, two-step austempered ADI, ( $T_{\gamma}=1520^{\circ}\text{F}$ ,  $T_D=1520^{\circ}\text{F}$ ,  $T_{A1}=500^{\circ}\text{F}$ ,  $T_{A2}=600^{\circ}\text{F}$ )

Ring	Measured d spacing (Å)	(hkl)	Calculated d spacing (Å)	% difference
1	2.038	$\alpha$ (110)	2.029	0.4
2	1.467	$\alpha$ (200)	1.435	2.2
3	1.189	$\alpha$ (211)	1.172	1.5
4	1.053	$\alpha$ (220)	1.015	3.7
5	0.858	$\alpha$ (311)	0.908	5.5



Figure 52 illustrates the TEM micrographs of the intercritically austenitized, plastically deformed, two-step austempered ADI sample ( $T_{\gamma}=1472^{\circ}\text{F}$ ,  $T_D=1472^{\circ}\text{F}$ ,  $T_{A1}=500^{\circ}\text{F}$ ,  $T_{A2}=680^{\circ}\text{F}$ ). Bainitic ferrite in the form of ultrafine nanocrystal morphology is observed in the bright field image in the Figure 52.

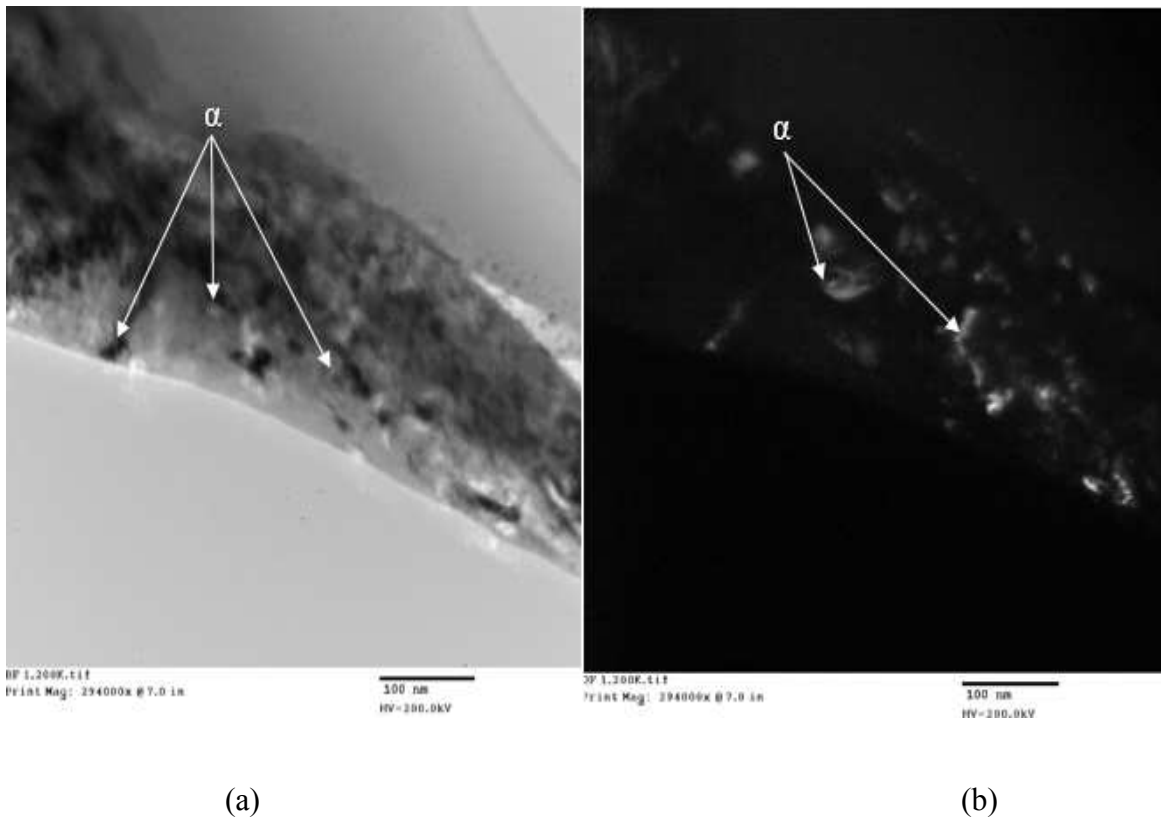


Figure.52: TEM micrographs of ductile cast iron intercritically austenitized, plastically deformed, two-step austempered ADI ( $T_{\gamma}=1472^{\circ}\text{F}$ ,  $T_D=1472^{\circ}\text{F}$ ,  $T_{A1}=500^{\circ}\text{F}$ ,  $T_{A2}=680^{\circ}\text{F}$ ), (a) Bright Field image, (b) Dark field image

The dark field image obtained from the  $\alpha$  (110) reflection shows the ultra-fine bainitic ferrite structures as shown in Figure 52 (b). In Figure 53 (a), the selected area diffraction from the brightfield image shows ring like pattern which confirms the nanostructured bainitic ferrite in this heat-treated ADI. The decrease in the volume fraction of austenite is observed at lower

austenitization temperature of 1472°F which is evident from the X-ray diffraction profile in the Figure 53 (b). The indexing details are reported in Table 21.

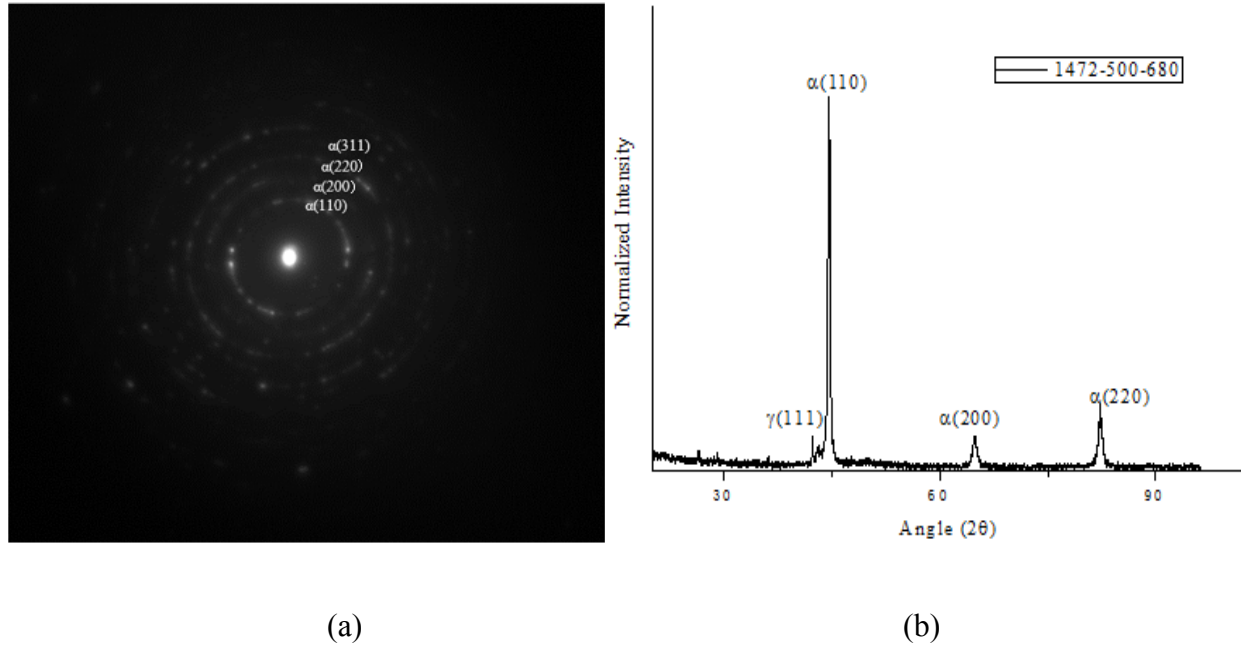


Figure.53: TEM micrographs of ductile cast iron intercritically austenitized, plastically deformed, two-step austempered ADI ( $T_{\gamma}=1472^{\circ}\text{F}$ ,  $T_D=1472^{\circ}\text{F}$ ,  $T_{A1}=500^{\circ}\text{F}$ ,  $T_{A2}=680^{\circ}\text{F}$ , (a) Indexed SAED Pattern and (b) X-ray diffraction profile

Table.21: Indexing details of diffraction pattern of ferrite phase (Plastically deformed, two-step austempered ADI, ( $T_{\gamma}=1472^{\circ}\text{F}$ ,  $T_D=1472^{\circ}\text{F}$ ,  $T_{A1}=500^{\circ}\text{F}$ ,  $T_{A2}=680^{\circ}\text{F}$ )

Spot	Measured d spacing ( $\text{\AA}$ )	(hkl)	Calculated d spacing ( $\text{\AA}$ )	% difference
1	2.027	$\alpha(110)$	2.029	0.1
2	1.434	$\alpha(200)$	1.435	0.1
3	1.170	$\alpha(211)$	1.172	0.2
4	0.992	$\alpha(220)$	1.015	2.2

TEM micrographs of the intercritically austempered, plastically deformed sample at a strain rate of 10mm/min followed by two step austempering, ( $T_{\gamma}=1520^{\circ}\text{F}$ ,  $T_D=1520^{\circ}\text{F}$ , strain rate= 10mm/min,  $T_{A1}=500^{\circ}\text{F}$ ,  $T_{A2}=550^{\circ}\text{F}$ ) is shown in the Figure 54.

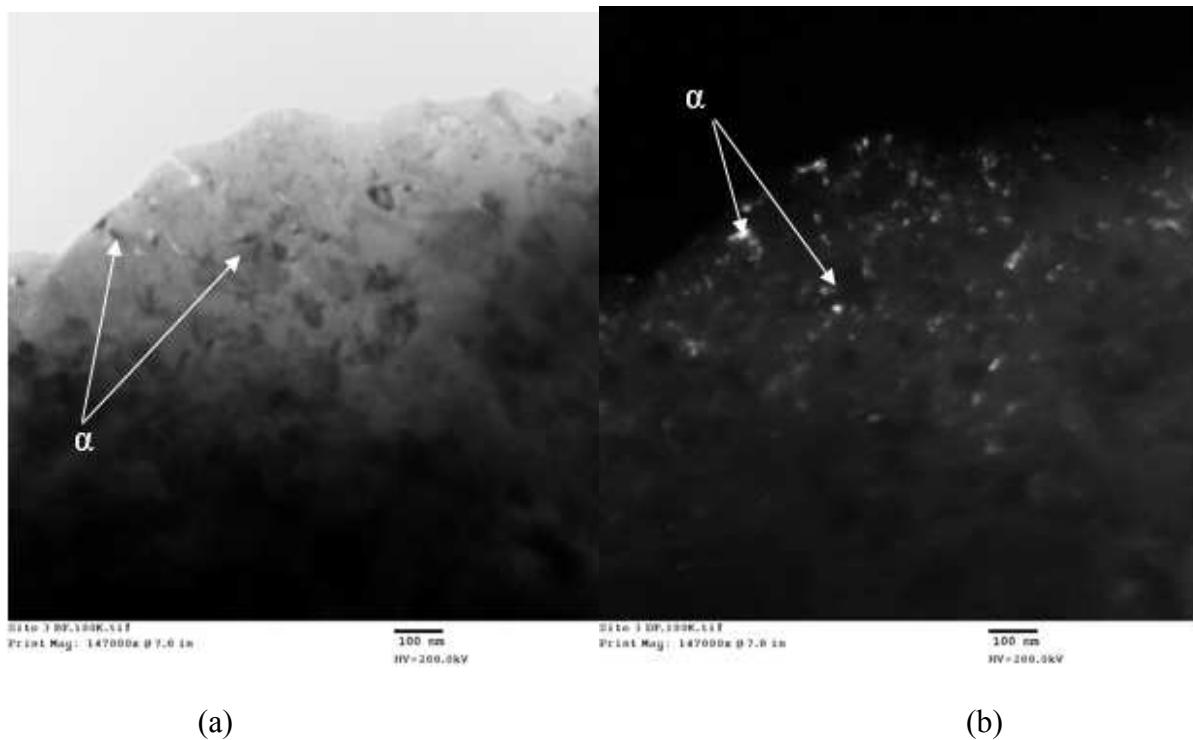


Figure.54: TEM micrographs of ductile cast iron intercritically austenitized, plastically deformed at higher strain rate, two-step austempered ADI  $T_{\gamma}=1520^{\circ}\text{F}$ ,  $T_D=1520^{\circ}\text{F}$ , strain rate= 10mm/min,  $T_{A1}=500^{\circ}\text{F}$ ,  $T_{A2}=550^{\circ}\text{F}$  a) Bright Field image, (b) Dark field image

The bright field image in Figure 54 (a) shows the appearance of bainitic ferrite structures which are in the nanoscale range. Plastic deformation significantly reduced the ferritic cell size in the nanoscale range leading to the ring like SAED pattern as shown in the Figure 55 (a). The diffraction ring corresponding to the austenite phase is not found in the SAED pattern as the volume fraction of austenite is very low for this high strain plastically deformed ADI sample which is evident from the X-ray diffraction profile shown in the Figure 55(b). There were also

traces of  $\text{Fe}_3\text{C}$  carbides observed in these samples from the SAED pattern. The indexing details are reported in the Table 22.

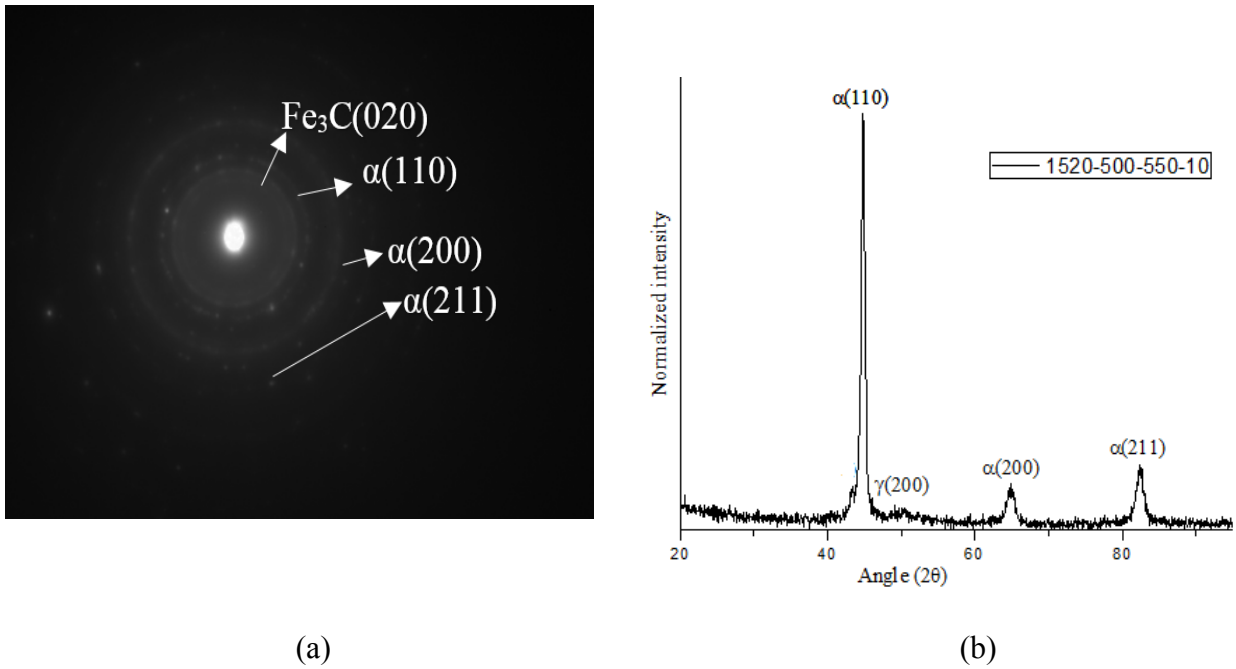


Figure.55: TEM micrographs of ductile cast iron intercritically austenitized, plastically deformed at higher strain rate, two-step austempered ADI  $T_\gamma=1520^\circ\text{F}$ ,  $T_D= 1520^\circ\text{F}$ , strain rate= 10mm/min,  $T_{A1}=500^\circ\text{F}$ ,  $T_{A2}= 550^\circ\text{F}$  (a) SAED Pattern (b) X-ray diffraction profile

Table.22: Indexing details of diffraction pattern of ferrite phase (Plastically deformed, two-step austempered ADI, ( $T_\gamma=1520^\circ\text{F}$ ,  $T_D= 1520^\circ\text{F}$ , strain rate= 10mm/min),  $T_{A1}=500^\circ\text{F}$ ,  $T_{A2}= 550^\circ\text{F}$ )

Ring	Measured d spacing ( $\text{\AA}$ )	(hkl)	Calculated d spacing ( $\text{\AA}$ )	% difference
1	2.501	$\text{Fe}_3\text{C}$ (020)	2.544	1.7
2	2.045	$\alpha$ (110)	2.029	0.8
3	1.470	$\alpha$ (200)	1.435	2.4
4	1.147	$\alpha$ (211)	1.172	2.1

In summary, TEM analysis provided a detailed overview of the ausferritic microstructure in the conventional and plastically deformed ADI. TEM observation clearly shows that the conventional ADI samples resulted in a typical crystalline spot SAED pattern with well-defined spacing and angles. It also confirms the presence of carbide free bainitic ferrite platelets separated by austenite laths. It is also observed that the plastic deformation resulted in the grain refinement in the nanoscale range which is evident from the ring SAED pattern obtained from the plastically deformed ADI samples. At lower austenitization temperatures, the volume fraction of austenite greatly reduced and the TEM observation resulted in a ring pattern for the bainitic ferrite reflections only.

## CHAPTER 7. AUSTENITE AND ITS STABILITY

### 7.1 Volume fraction of austenite and its carbon content

Austenite that do not transform into bainitic ferrite or martensite up on quenching is called retained austenite. By controlling the volume fraction of retained austenite in ADI, the negative influences such as the crack growth, fatigue, excessive dimensional growth can be avoided. The volume fraction of the austenite and its carbon content is important as it determines the strength and ductility of the ADI. The volume fraction of austenite and its carbon content was determined by X-ray diffraction analysis.

#### 7.1.1 Variation in the volume fraction of austenite and its carbon content in conventional ADI

The volume fraction of the austenite was determined by X-ray diffraction analysis. Figure 56 shows the effect of austempering temperatures on the volume fraction of austenite for the conventionally austempered ductile cast iron.

At lower austempering temperatures, the microstructure mainly consists of bainitic ferrite and retained austenite whereas at the upper bainitic temperatures, the microstructure mainly consists of reacted austenite as the ausferrite forms at upper bainitic temperatures. The total volume fractions of austenite (retained and reacted austenite) increases with the increase in austempering temperature.

While the ADI samples austempered at 700°F and 725°F had higher volume fraction of austenite, the samples austempered at 750°F had lower volume fraction of austenite. This is due to the smaller processing window (the period between the end of the first reaction and the onset of second reaction) for the higher austempering temperatures of 750°F. This, in turn, caused the partial decomposition of austenite to ferrite and carbides at this temperature. Moreover, the low

alloyed ductile cast iron is used in this study which had very little Mo% and Ni%. This apparently reduced the process window where the onset of the second reaction occurred resulting in decomposition of austenite into ferrite and carbide in the 750°F austempered samples.

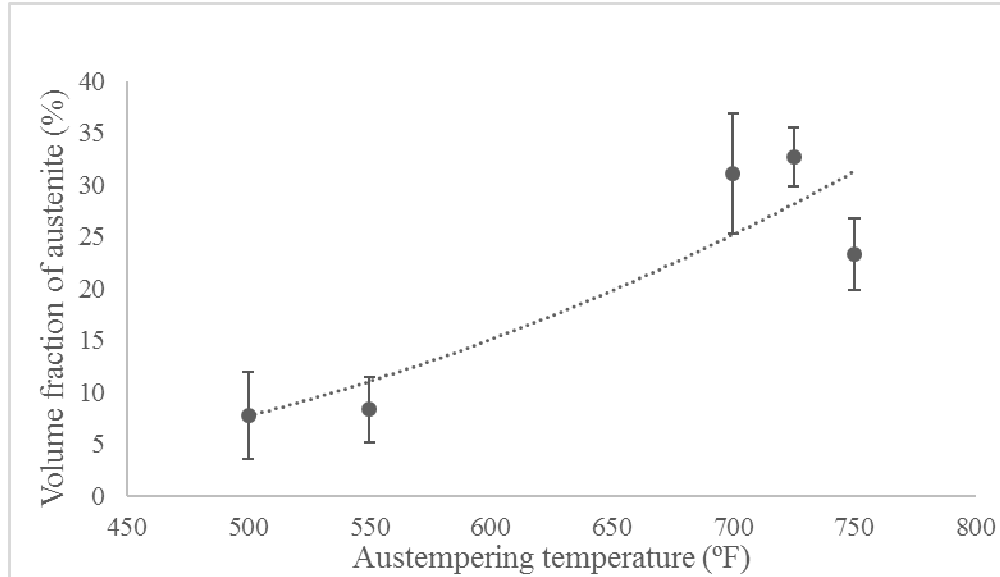


Figure.56: Effect of conventional austempering on the volume fraction of austenite ( $T_{\gamma}=1700^{\circ}\text{F}$ ,  $T_A$  as shown)

Figure 57 shows the austenitic carbon content with respect to the austempering temperature for the conventional ADI. The initial carbon content of austenite before austempering can be estimated by the following equation [127]:

$$C_{\gamma}=(T_{\gamma}/420)-0.17(\%Si)-0.95\% \quad (6.1)$$

where,  $C_{\gamma}$  is the carbon content of the austenite and  $T_{\gamma}$  is the austenitization temperature in  $^{\circ}\text{C}$

The carbon content of the austenite before austempering for the conventional austenitization temperature of  $1700^{\circ}\text{F}$  ( $927^{\circ}\text{C}$ ) for the ductile cast iron used in this study was estimated to be 0.84%. The average amount of dissolved carbon content of the austenite remains in the range of 1.6% for the ADI austempered at higher austempering temperatures. At lower austempering

temperatures of 500°F and 550°F, where only retained austenite exists, austenite carbon content in the range of 0.9% is observed.

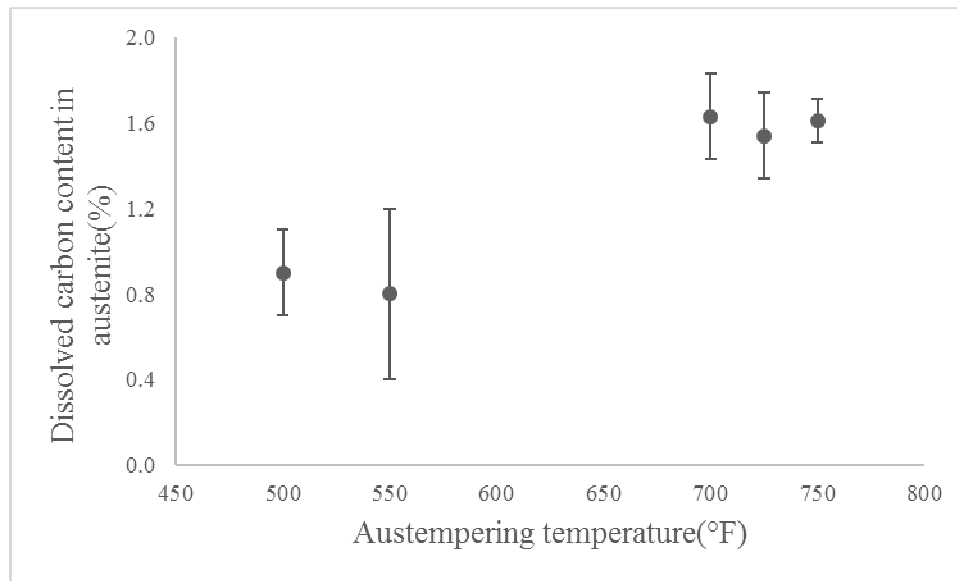


Figure.57: Volume fraction of austenitic carbon with respect to conventional austempering temperature ( $T_{\gamma}=1700^{\circ}\text{F}$ ,  $T_A$  as shown)

### 7.1.2 Variation in the volume fraction of austenite and its carbon content in intercritically austenitized ADI (with constant $T_A$ )

Figure 58 shows the influence of intercritical austenitizing temperatures on the volume fraction of austenite of the ADI austempered at 680°F. The intercritical austenitization of ADI resulted in lower volume fraction of austenite than the volume fraction of austenite obtained from the conventional austempering process.

The amount of the parent phase that transform into austenite phase depends on the austenitization temperature. Thus, the parent austenite volume fraction can be adjusted by varying the austenitization temperature. At lower austenitization temperatures, only a limited transformation of as cast parent phase to the austenite phase occur. Thus, the volume fraction of austenite is very low for the ADI austenitized at lower intercritical austenitizing temperature of



1418°F. With the increase in austenitization temperature from 1418°F to 1520°F, the volume fraction of austenite increases as predicted by the Lever rule.

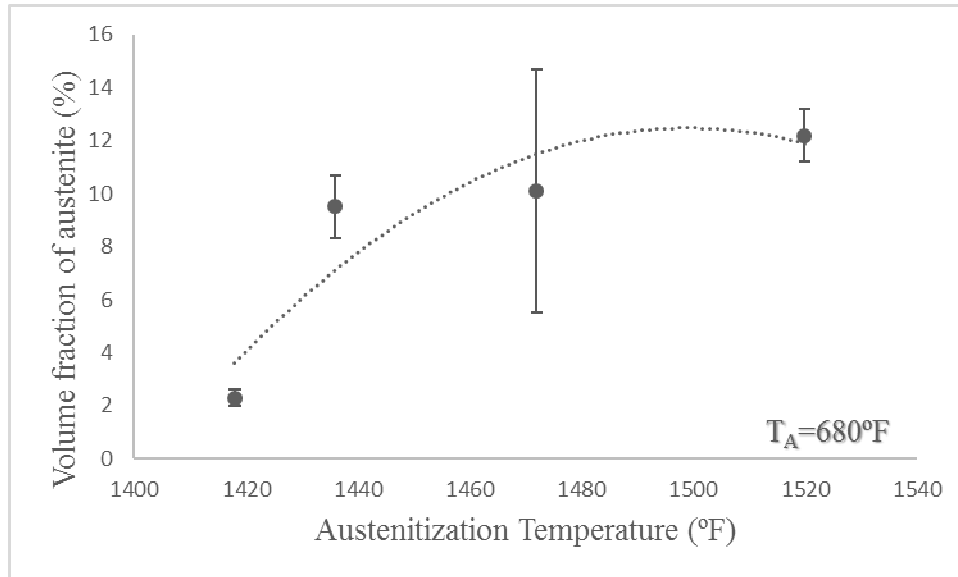


Figure.58: Influence of intercritical austenitizing temperatures on the volume fraction of austenite  
( $T_{\gamma}$  as shown,  $T_A=680^{\circ}\text{F}$ )

The carbon content of the austenite before austempering for the conventional austenitization temperature of 1700°F (927°C) for the ductile cast iron used in this study was estimated to be 0.84% from equation (6.1). Similarly, the carbon content of austenite before austempering for the austenitization temperature of 1520°F, 1472°F, 1436°F and 1418°F were estimated to be 0.60%, 0.54%, 0.49% and 0.46% respectively. The carbon content of austenite prior to austempering influences the stability of high carbon austenite during austempering. The carbon content of the austenite after austempering is calculated to be 2.3%, 2.9%, 2.2% and 1.6% respectively. Thus, there exists a potential to stabilize the high carbon austenite during austempering in intercritically austenitized ductile iron samples.

Figure 59 represents the corresponding carbon content of the austenite calculated from the following equation [125]:

$$a_{\gamma} = 0.3548 + 0.0044 C_{\gamma} \quad (7.2)$$

where  $a_{\gamma}$  is the lattice parameter of austenite in nm and  $C_{\gamma}$  is the carbon in wt%.

Higher the volume fraction of austenite allows the diffusion of more carbon into the austenite during austempering. As the austenitization temperature increases, the carbon content of the austenite also increases for a fixed time. This is in good agreement with the existing literatures [124-125].

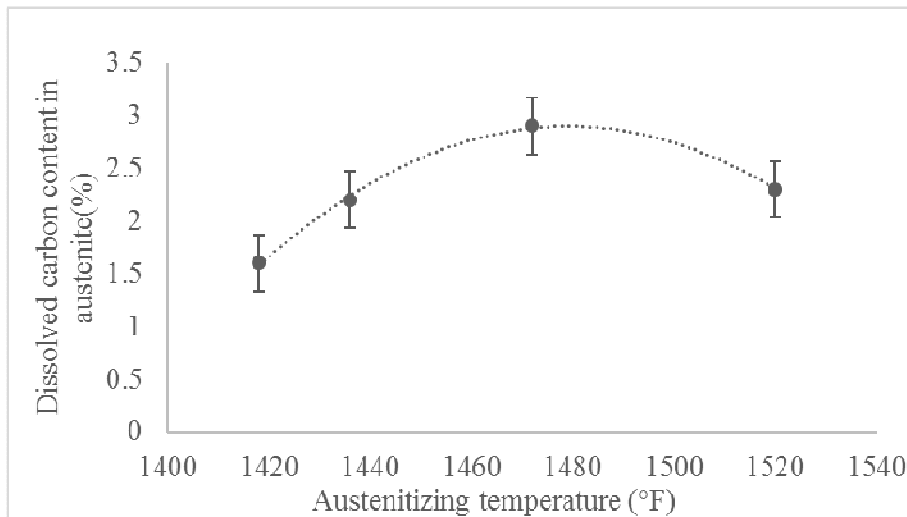


Figure.59: Influence of intercritical austenitizing temperatures on the carbon content of austenite  
( $T_{\gamma}$  as shown,  $T_A=680^{\circ}\text{F}$ )

### 7.1.3 Variation in the volume fraction of austenite and its carbon content in intercritical ADI (with constant $T_{\gamma}$ )

Figure 60 shows the variation in the volume fraction of austenite with respect to austempering temperatures in the ADI intercritically austenitized at the upper intercritical temperature of  $1520^{\circ}\text{F}$  for the austempering temperatures shown.

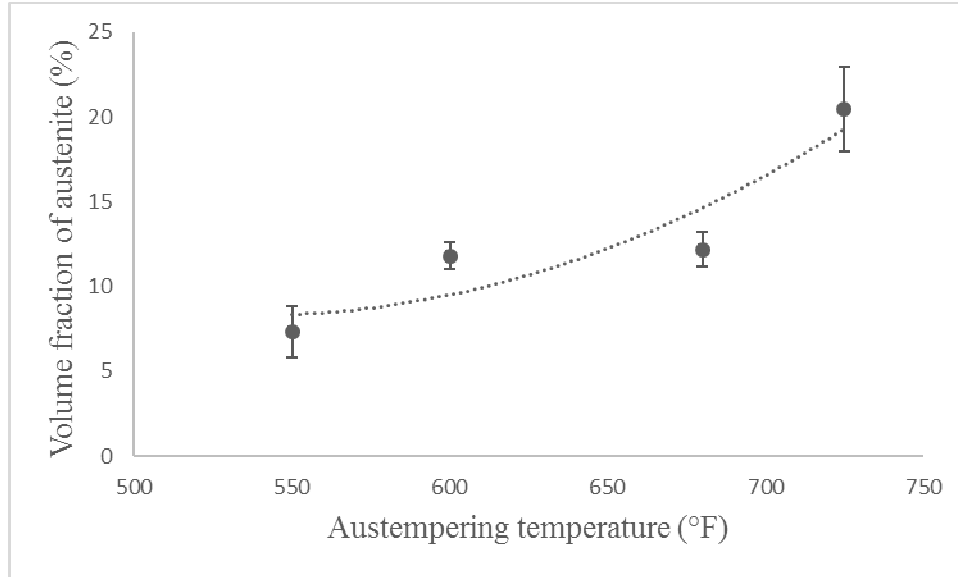


Figure.60: Influence of austempering temperatures on the volume fraction of austenite in the intercritical ADI ( $T_{\gamma} = 1520^{\circ}\text{F}$ ,  $T_A$  as shown)

As the transformation of austenite into ferrite and high carbon austenite depends on the transformation temperature during austempering, the volume fraction of austenite increases as the austempering temperature increased from 550 to 725°F. At lower austempering temperatures, there exists only retained austenite and lower bainite, as the ausferrite form only at upper bainitic temperatures. The volume fraction of the total reacted as well as retained austenite increases with the austempering temperature. At lower austempering temperatures, the growth rate of ferrite is lower, the diffusion rate of carbon into the austenite is also slower, which results in lower volume fraction of austenite at lower austempering temperatures. As the austempering temperature is increased, the volume fraction of austenite increases. This is because at higher austempering temperatures, the rate of diffusion of carbon into the austenite is faster and the growth rate of ferrite is also rapid.

Figure 61 shows the variation of the carbon content of austenite in ADI intercritically austenitized at 1520°F with respect to the austempering temperature. The carbon content of the reacted and retained austenite is unchanged and nominally 2.0%.

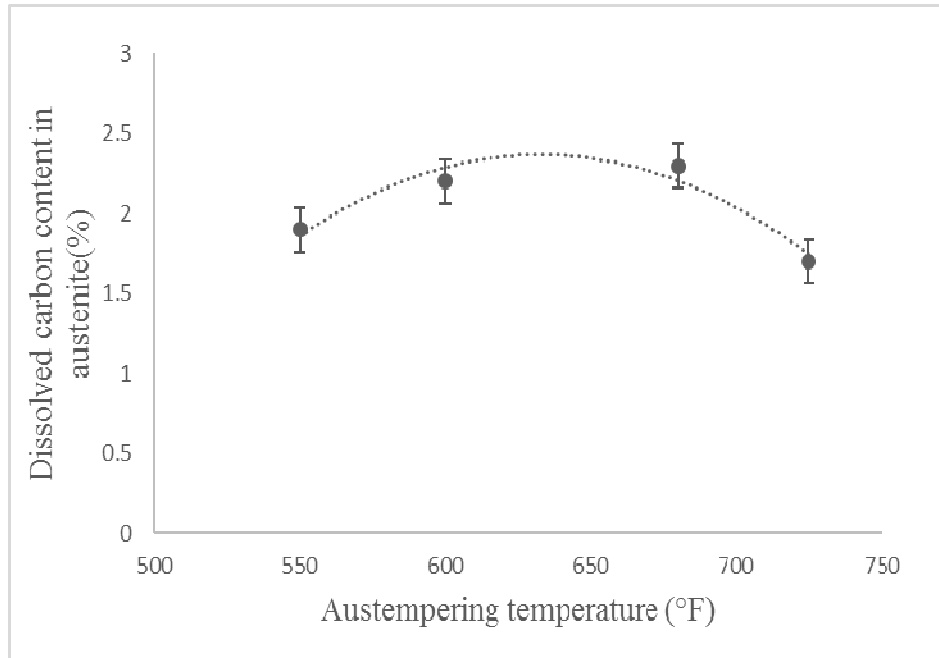


Figure.61: Influence of austempering temperatures on the carbon content austenite in the intercritical ADI ( $T_{\gamma}=1520^{\circ}\text{F}$ ,  $T_{\text{A}}$  as shown)

#### 7.1.4 Variation in the volume fraction of austenite and its carbon content in conventional ADI with respect to plastic deformation

Figure 62, shows the variation of the volume fraction of austenite in the ADI austenitized at 1700°F, plastically deformed at 1700°F followed by austempering for the temperatures shown. Statistically, plastic deformation did not affect the volume fraction of austenite in the conventional ADI. The presence of islands of retained austenite in the ADI samples austempered at higher austempering temperatures resulted in the higher volume fraction of austenite at higher austempering temperatures. The retained austenite content was low at the lower austempering temperatures of 550°F and 600°F.

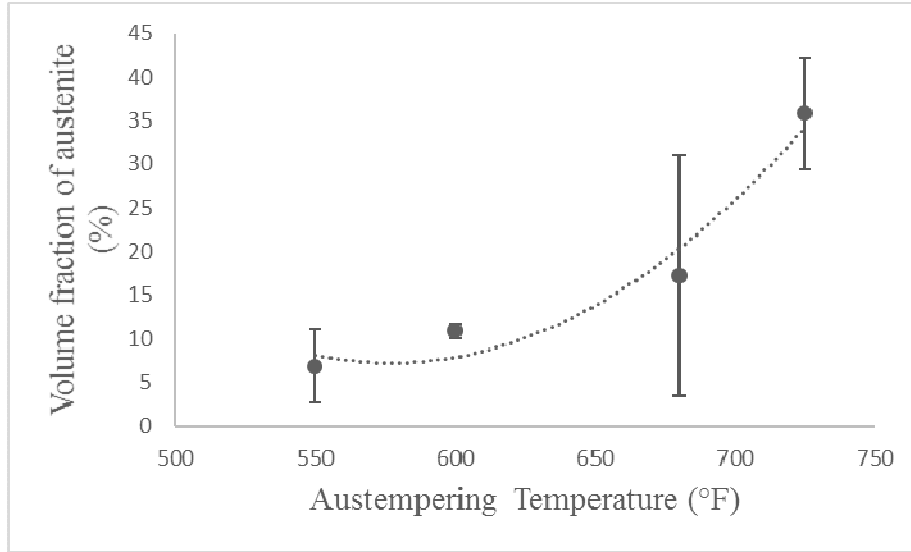


Figure.62: Influence of austempering temperatures on the volume fraction of austenite in the plastically deformed ADI ( $T_{\gamma}=1700^{\circ}\text{F}$ ,  $T_A$  as shown)

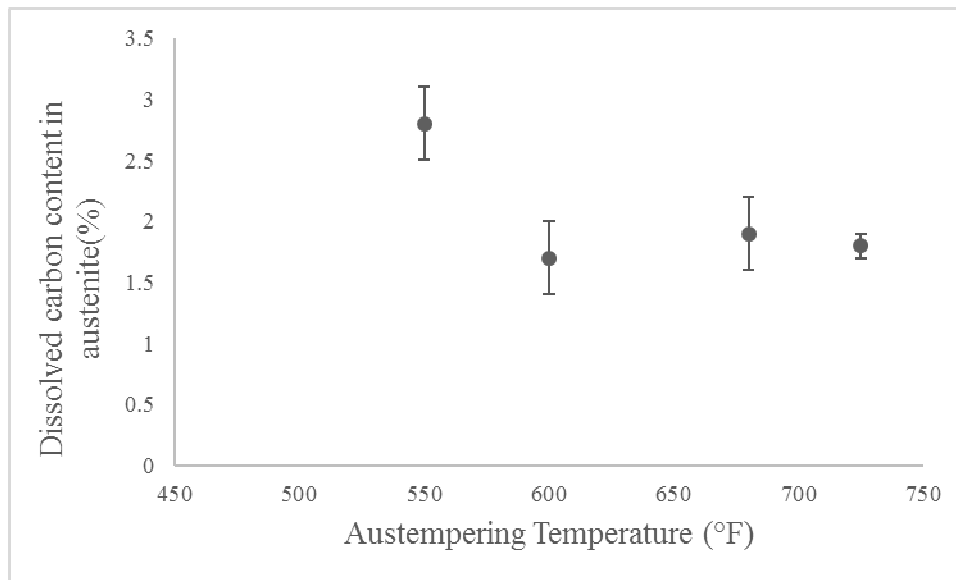


Figure.63: Influence of austempering temperatures on the volume fraction of austenitic carbon in the plastically deformed ADI ( $T_{\gamma}=1700^{\circ}\text{F}$ ,  $T_A$  as shown)

The corresponding carbon content of the austenite is shown in the Figure 63. In contrast to the conventional austempering, the plastically deformed ADI samples had higher percentage of austenitic carbon at lower austempering temperature of 550°F with lesser austenite content.

### 7.1.5 Variation in the volume fraction of austenite and its carbon content in intercritical ADI with respect to plastic deformation

Figure 64 shows the variation of the volume fraction of austenite in the ADI intercritically austenitized at 1520°F, plastically deformed at 1520°F followed by austempering for the temperatures shown. Plastic deformation in the intercritically austempered ADI resulted in significant decrease in the volume fraction of austenite in the range of about 21% to 36% when compared to the intercritical ADI without plastic deformation. The influence of austempering temperature on the volume fraction of austenite was also observed in these samples.

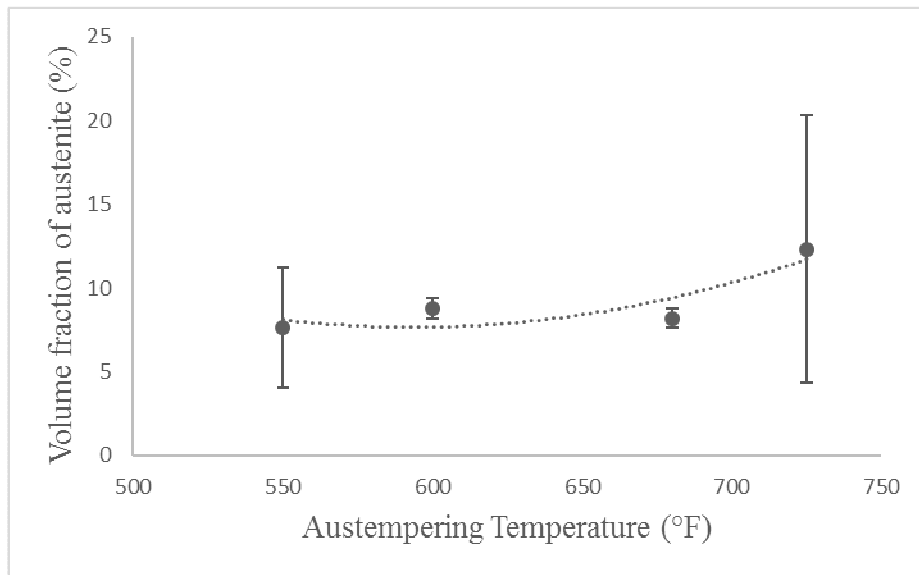


Figure.64: Influence of intercritical austenitization on the volume fraction of austenite in the plastically deformed ADI ( $T_{\gamma}=1520^{\circ}\text{F}$ ,  $T_A$  as shown)

The corresponding carbon content of the austenite for the plastically deformed ADI is represented in the Figure 65. The carbon content of the austenite is unchanged and existed in the range of approximately 2%.

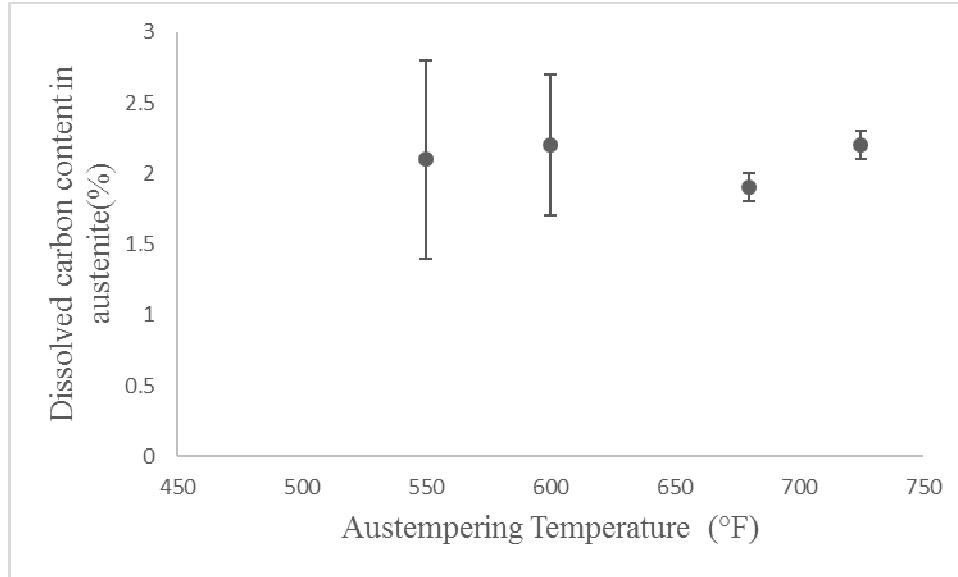


Figure.65: Influence of intercritical austenitization on the volume fraction of austenitic carbon in the plastically deformed ADI ( $T_{\gamma}=1520^{\circ}\text{F}$ ,  $T_A$  as shown)

The volume fraction of austenite for the intercritically austenitized, two step austempered ADI with respect to the plastic deformation is shown in the Figure 66. At conventional austenitizing temperature of  $1700^{\circ}\text{F}$ , the volume fraction of austenite is higher irrespective of the austempering temperatures. The volume fraction of austenite varied with respect to the austenitization as well as the austempering temperatures. Upper intercritical austenitization temperatures of  $1520^{\circ}\text{F}$  and  $1472^{\circ}\text{F}$  has higher volume fraction of austenite than the lower intercritical temperature of  $1436^{\circ}\text{F}$ . At higher austempering temperatures, the volume fraction of austenite is higher as the ausferritic structures form at upper bainitic temperatures. At lower temperatures, predominantly bainitic ferrite and retained austenite exists leading to the lower austenitic content in the ADI. The carbon content of the austenite remained with a range of 1.5 to 2.5% in this ADI samples

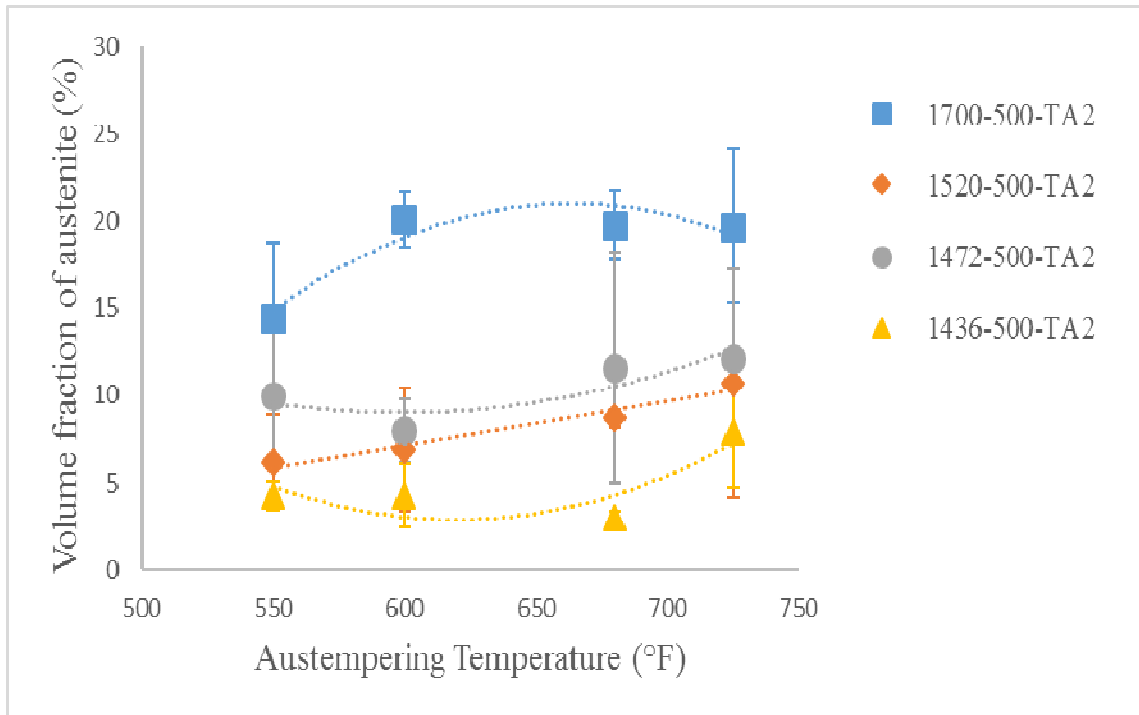


Figure.66: Influence of intercritical austenitization on the volume fraction of austenite with respect to plastically deformation and two step austempering

## 7.2 Stability of austenite

Cryogenic treatment allowed for the investigation of the thermal and mechanical stability of austenite in ADI

### 7.2.1 Thermal Stability of austenite

Table 23 shows the volume fraction of austenite with respect to the cryogenic treatment in the austempered ductile iron samples. Cryogenic treatment significantly reduced the volume fraction of austenite in the ADI samples for all the austempering temperatures and it is significantly stronger for the samples austempered at 725°F or lower temperatures. During cryogenic treatment, some of the high carbon retained austenite transformed into tempered martensite structures and hence the volume fraction of austenite decrease



Table 23: The Volume Fraction of Austenite in the ADI as a Function of Cryogenic Treatment

Austempering Temperature (°F)	Cryogenic Treatment?	Volume Fraction of Austenite in the Untested Samples (%)	Volume fraction of Austenitic Carbon content ( $X_{\gamma}C_{\gamma}$ )
500°F	No	$7.8 \pm 4.2$	0.143
	Yes	$0.0 \pm 0.0$	0.000
550°F	No	$8.3 \pm 3.1$	0.130
	Yes	$0.0 \pm 0.0$	0.000
700°F	No	$31.1 \pm 5.8$	0.506
	Yes	$25.3 \pm 1.8$	0.430
725°F	No	$32.7 \pm 2.8$	0.503
	Yes	$24.4 \pm 0.9$	0.463
750°F	No	$23.3 \pm 3.5$	0.372
	Yes	$21.2 \pm 1.0$	0.275

Generally, it is known that the high carbon austenite is thermally unstable and transform into martensite. Because of this thermal instability, the high carbon austenite is prone to transfer to tempered martensite upon cryogenic processing. However, the degree of transformation of austenite to tempered martensite depend on the austempering temperature. The volume fraction of the austenite after cryogenic treatment in the ADI samples austempered at lower bainitic temperatures austempering were thermally unstable and transformed into tempered martensite.

However, cryogenic treatment of the samples austempered at upper bainitic temperatures resulted in thermally stable austenite which did not completely transform to tempered martensite when subjected to cryogenic processing. Apparently, the degree of transformation of austenite into tempered martensite depends on the carbon content of the austenite.

Table 23 also shows the austenitic carbon content as a function of austempering temperatures in the cryogenically treated ADI samples. The cryogenic treatment of ADI samples austempered at lower bainitic temperatures of 500°F and 550°F resulted in complete transformation of austenite into tempered martensite. This is due to the lower austenitic carbon present in these ADI samples prior to the cryogenic treatment. Lower austenitic carbon is prone to increase the martensitic start temperatures. It is evident that higher carbon content lowers the martensitic start temperatures ( $M_s$ ) in steels [128], this in turn increases the stability of the austenite. At higher austempering temperatures, the austenitic carbon content is increased and thus the degree of transformation of austenite to tempered martensite is reduced.

### **7.2.2 Influence of cryogenic treatment on the mechanical stability of austenite**

The mechanical stability of the austenite was determined by a series of tensile and fracture toughness tests. Tensile test allows for the free flow of the material allowing the strain induced transformation of austenite to martensite. In the fracture toughness tests, the material is subjected to mostly elastic deformation due to the very limited plasticity at the crack tip as well as the high constraint in the specimen geometry. Thus, in fracture toughness tests, the transformation of austenite to martensite occur by stress induced transformation process. The deformation mechanism associated with cryogenic treatment of ADI can be analyzed by the tensile and fracture toughness tests.

### 7.2.2.1 Strain induced transformation

Table 24 shows the volume fractions of austenite for the tensile tests performed on the conventionally austempered as well as cryogenically treated ADI samples. After tensile tests, the volume fraction of the austenite was calculated and significant reduction in the volume fraction of the austenite was observed in the conventional ADI. Thus, tensile test resulted in the strain induced transformation of austenite to martensite.

Table 24: The Volume Fraction of Austenite in the ADI as a Function of Cryogenic Treatment and Testing

Austempering Temperature (°F)	Cryogenic Treatment?	Volume Fraction of Austenite (%) in	
		Pre-test (untested samples)	Post-Test (tensile tested samples)
500°F	No	$7.8 \pm 4.2$	$0.0 \pm 0.0$
	Yes	$0.0 \pm 0.0$	$0.0 \pm 0.0$
550°F	No	$8.3 \pm 3.1$	$0.0 \pm 0.0$
	Yes	$0.0 \pm 0.0$	$0.0 \pm 0.0$
700°F	No	$31.1 \pm 5.8$	$24.4 \pm 4.6$
	Yes	$25.3 \pm 1.8$	$12.5 \pm 2.9$
725°F	No	$32.7 \pm 2.8$	$22.8 \pm 3.8$
	Yes	$24.4 \pm 0.9$	$12.1 \pm 4.2$
750°F	No	$23.3 \pm 3.5$	$23.5 \pm 6.3$
	Yes	$21.2 \pm 1.0$	$16.3 \pm 10.5$

The magnitude of the transformation of austenite to martensite in the mechanically tested (tensile test) ADI samples accounts to approximately 8% for samples austempered between 500°F and 725°F.

As illustrated in the Table 24, during cryogenic treatment, the retained austenite is transformed to martensite and the degree of transformation is dependent on the austempering temperature. At lower bainitic temperatures of 500°F and 550°F, the cryogenic treatment resulted in the complete transformation of retained austenite to martensite prior to tensile testing. Therefore, no strain induced transformation of austenite to martensite is expected in these samples. In the samples austempered in the upper bainitic temperature and cryogenic treatment resulted in the partial transformation of austenite to martensite due to the thermal instability of retained austenite.

At the austempering temperature of 700°F, approximately 18% of the austenite was transformed into martensite during cryogenic processing. In the samples austempered at 725°F, approximately 25% of austenite to martensite transformation occurred during cryogenic processing prior to tensile testing. Upon tensile testing the cryogenically treated ADI samples, the mechanical instability was obvious as the transformation of the retained austenite to martensite accounted for approximately 50%. The magnitude of transformation of austenite to martensite is greater for the cryogenically treated and tensile tested samples as opposed to the ADI that underwent either cryogenic treatment or tensile testing. Thus, cryogenically treated ADI samples follow the same trend as the conventional ADI with lower amount of austenite present.

#### **7.2.2.2 Stress-induced deformation**

Table 25 shows the volume fraction of austenite in the conventional ADI as well as cryogenic ADI both before and after the fracture toughness test. As detailed in the Table 25, the

stress induced transformation resulted in complete transformation of retained austenite to martensite in the conventional ADI austempered at lower bainitic temperatures of 500°F and 550°F. However, in the upper bainitic temperature range, only partial transformation of austenite to martensite occurred.

Table 25: The Volume Fraction of Austenite in the ADI as a Function of Cryogenic Treatment and Testing

Austempering Temperature (°F)	Cryogenic Treatment?	Volume Fraction of Austenite (%)		Average Volume Fraction of Austenite Transformed to Martensite (%)
		Pre-test (Untested Samples)	Post test (Tested Fracture Toughness Samples)	
500°F	No	7.8 ± 4.2	0.0 ± 0.0	7.8
	Yes	0.0 ± 0.0	0.0 ± 0.0	0.0
550°F	No	8.3 ± 3.1	0.0 ± 0.0	8.3
	Yes	0.0 ± 0.0	0.0 ± 0.0	0.0
700°F	No	31.1 ± 5.8	25.9 ± 5.2	5.2
	Yes	25.3 ± 1.8	21.2 ± 1.9	4.1
725°F	No	32.7 ± 2.8	19.8 ± 2.1	12.
	Yes	24.4 ± 0.9	18.5 ± 1.5	5.9
750°F	No	23.3 ± 3.5	17.6 ± 2.4	5.7
	Yes	21.2 ± 1.0	16.8 ± 4.3	4.4

In the samples, conventionally austempered at 700°F, stress induced transformation resulted in approximately 17% transformation of austenite to martensite. In the ADI, conventionally austempered at 725°F, fracture toughness test resulted in approximately 40% of the austenite to martensite conversion by stress induced transformation process.

In the ADI samples austempered in the lower bainitic temperature range and cryogenically treated, the retained austenite has been completely transformed to martensite prior to fracture toughness testing. Thus, there is no retained austenite to undergo stress induced transformation during fracture toughness tests. However, in the upper bainitic temperature range, only a partial transformation of austenite to martensite was observed due to the thermal instability of austenite that underwent cryogenic treatment. Greater magnitude of the austenite to martensite transformation by stress induced transformation was observed for the samples with both cryogenic processing and fracture toughness tests than those with either cryogenic processing or fracture toughness test.

### **7.2.2.3 Analytical Model for the Crack Growth Process**

The analysis of the volume fraction of austenite in ADI subjected to cryogenic treatment, tensile test and the fracture toughness tests show that the austenite is neither thermally nor mechanically stable. This instability of austenite led to the transformation of the high carbon retained austenite to martensite either thermally or by stress/strain induced transformation. This transformation of austenite to martensite would be expected to deteriorate the fracture toughness of ADI. However, the cryogenic treatment did not significantly deteriorate the fracture toughness of the ADI. An analytical model has been developed to detail the phenomena occurring at the crack tip of the ADI.

It is generally known that the stress concentration ahead of the advancing crack can lead to the transformation of austenite to martensite in iron alloys. Consider a compact tension sample used for the fracture toughness tests. As the crack propagates, the stress concentration ahead of the advancing crack tip induce the austenite to martensite transformation. Thus, a portion of the energy supplied to the sample is used up for this  $\gamma_{\text{HC}} \rightarrow \text{M}$  transformation. This stress induced transformation of austenite to martensite produces compressive stresses on the crack tip. This compressive stress on the crack tip must be overcome to propagate the crack further. This process lowers the energy available to continue the fracture the material. Thus, the dissipative process, occurring ahead of the crack tip should increase the fracture resistance of the material.

Statistically, there is no significant difference in the fracture toughness of the ADI with and without cryogenic treatment. While an austenite to martensite transformation is expected to increase the fracture resistance or the crack propagation, the martensite phase is more susceptible to the crack growth than the austenite phase. Thus, the magnitude of change in the propagation of the crack will depend on the newly formed microstructure. In other words, the fracture resistance is dependent up on the volume fractions of the austenite and the martensite phases.

A schematic model for the crack growth mechanism in ADI is proposed. Consider a compact tension sample with the crack tip consisting of ferrite and austenite as shown in the Figure 67.

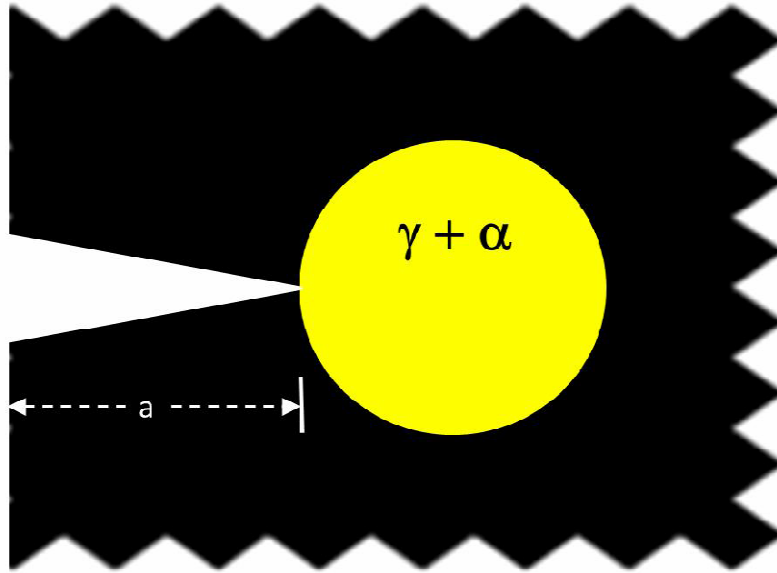


Figure.67: Area ahead of the Crack Tip

Let the stress concentration act on this compact tension sample containing a crack of length 'a' that is subjected to tensile load.

The stress intensity factor for a loaded specimen with a crack is given by

$$K = \sigma * (\Pi * a)^{1/2} * \alpha \quad (7.3)$$

where  $\sigma$  is the stress,  $a$  is the crack length, and  $\alpha$  is the geometry factor.

The force for the crack extension (or the strain energy release rate) is given by

$$G = K^2 / E. \quad (7.4)$$

Substituting (7.3) in (7.4), yields the crack growth energy  $G_{prop}$

$$G_{prop} = \frac{\sigma^2 * \Pi * a * \alpha^2}{E} \quad (7.5)$$

Now let  $V_\alpha$  and  $V_\gamma$  be the volume fractions of ferrite and austenite respectively. Thus, the total volume of the phases ahead of the crack tip is given by

$$V = V_\alpha + V_\gamma \quad (7.6)$$



Up on application of load or force, a portion of austenite is transformed to martensite by stress induced transformation process. Thus, the total volume of the phases ahead of the crack tip is given by

$$V = V_{\alpha} + V_M + V_{\gamma} \quad (7.7)$$

where  $V_M$  is the volume fraction of the transformed martensite.

The transformation of austenite to martensite utilize a part of the energy supplied by the force. Thus, since a part of the energy is dissipated in transformation austenite to martensite, only the part of the energy is used for the crack propagation.

Therefore, the energy for the crack propagation can be represented as

$$G_{\text{prop}} = G_{\text{total}} - G_{\text{trans}} \quad (7.8)$$

After the transformation, the new microstructure consists of ferrite, austenite and martensite. Martensite has low resistance to the propagation of the crack than ferrite and austenite. Thus, the crack propagated by a distance 'da' ahead of the crack tip as shown in the Figure 68.

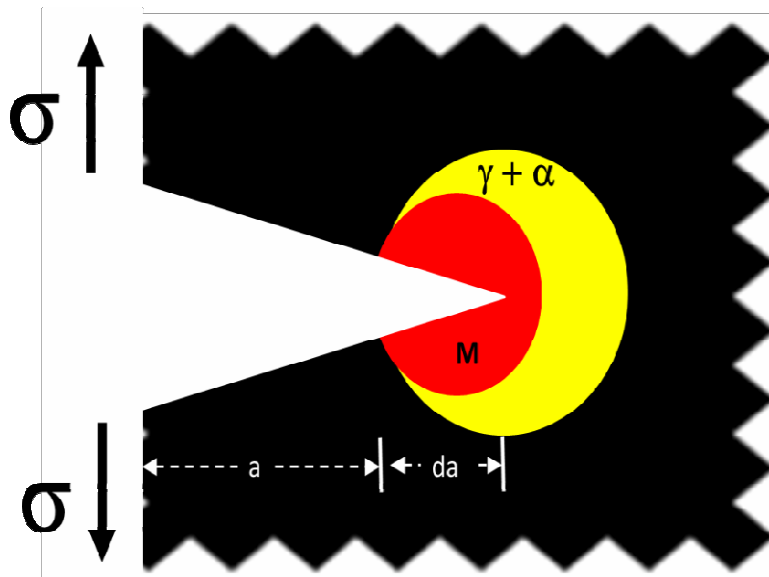


Figure.68: Area ahead of the Crack Tip during loading

The transformation of austenite to martensite produces a volume expansion of about 3%. This in turn lead to the compressive residual stress in the material.

With the application of load, when the crack tip opens to propagate the crack, the surrounding material will resist the expansion or opening, resulting in a partial closure of the crack tip as well as reducing the effective crack length by a length  $\Delta a$  as shown in the Figure 69.

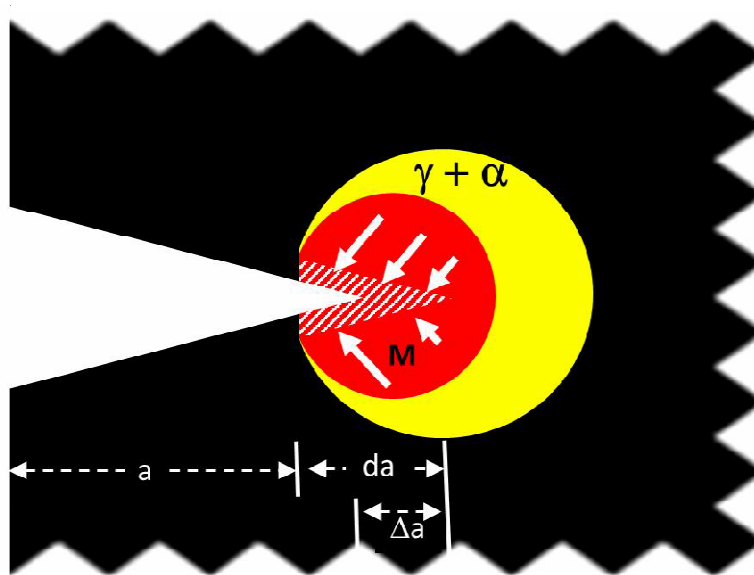


Figure.69: Effective crack length

Therefore, the crack length 'a' can be replaced by an effective crack length 'a<sub>eff</sub>' and can be represented as

$$a_{\text{eff}} = a + da - \Delta a \quad (7.9)$$

The crack growth energy is directly proportional to the crack length 'a'. The crack driving force will be reduced according to equation (7.9), thus the material should have higher resistance to the crack growth, despite the formation of martensite in the material. Similarly, the effective stress acting on the material to propagate the crack will also be reduced due to the compressive residual stress acting on the crack tip of the material.

Therefore, the stress “ $\sigma$ ” in the equation (3) can be replaced by

$$\sigma_{\text{net}} = \sigma - \sigma_{\text{residual}} \quad (7.10)$$

The combination of the crack closure and lower effective stress should significantly improve the fracture toughness of the material. But there is no significant improvement in the fracture toughness of the cryogenically treated ADI. This can be explained as follows.

Case 1: Consider a material with higher volume fraction of austenite. This will lead to transformation of more austenite to martensite by the stress induced transformation process. Thus, the value of  $\Delta a$  and  $\sigma_{\text{residual}}$  will be higher resulting in lower  $a_{\text{eff}}$  and  $\sigma_{\text{net}}$ . Substituting these values in equations (7.3) and (7.5), results in significant decrease in both  $K$  and  $G_{\text{prop}}$ , indicating a higher resistance to crack growth and hence higher fracture toughness.

Case 2: Consider a material with lower volume fraction of austenite value. Lower volume fraction of austenite means a lesser volume fraction of transformed martensite. In this case, the value of  $\Delta a$  and  $\sigma_{\text{residual}}$  will be smaller, and hence minor degree of decrease in the value of both  $K$  and  $G_{\text{prop}}$ . This indicates that there is only a minor change in the crack growth rate. Resulting in no significant improvement in the fracture toughness of the material. Case 2 was observed in the ADI used in this study. There is no significant improvement in the fracture toughness of the cryogenically processed ADI. An examination of the volume fraction of austenite before and after the test was observed to be less than 13%. This indicates that the transformation of austenite to martensite was not high enough to improve the fracture toughness of the material. Thus, there exists a threshold value, above which enough transformation of austenite to martensite occur to produce an observable effect on the fracture toughness of ADI.

## CHAPTER 8. MICROSTRUCTURE-PROPERTY RELATIONSHIP

### 8.1 Mechanical properties and fracture toughness of conventional and cryogenically treated ADI

The mechanical properties of ADI with respect to the conventional austempering and cryogenic treatment is reported in Table 26. The fracture toughness and hardness of ADI with respect to cryogenic treatment are reported in Table 27.

Table 26: Mechanical Properties of ADI with respect to cryogenic treatment

<b>Austempering Temperature</b>	<b>Cryogenic Treatment?</b>	<b>Yield Strength (MPa)</b>	<b>Ultimate Tensile Strength (MPa)</b>	<b>% Elongation</b>
500°F	No	1390 ± 28	1594 ± 21	1.4 ± 0.1
	Yes	1359 ± 18	1569 ± 29	1.2 ± 0.1
550°F	No	1199 ± 5	1329 ± 5	1.9 ± 0.1
	Yes	1303 ± 30	1466 ± 81	1.4 ± 0.2
700°F	No	898 ± 28	1078 ± 34	2.8 ± 1.3
	Yes	901 ± 15	1100 ± 53	2.8 ± 0.3
725°F	No	819 ± 19	1013 ± 30	3.2 ± 1.1
	Yes	903 ± 13	1148 ± 42	1.8 ± 0.7
750°F	No	779 ± 38	1008 ± 11	4.2 ± 0.2
	Yes	887 ± 4	1096 ± 98	1.6 ± 0.4

At higher austempering temperatures, the hardness and strength of the ADI samples are generally lower than the ADI samples austempered at lower austempering temperatures. This is due to the coarseness of bainitic ferrite structures at higher austempering temperatures. However, improvement in ductility is observed with the increase in austempering temperature. The fracture toughness of the conventionally austempered ADI increases to a maximum at 700°F, before decreasing.

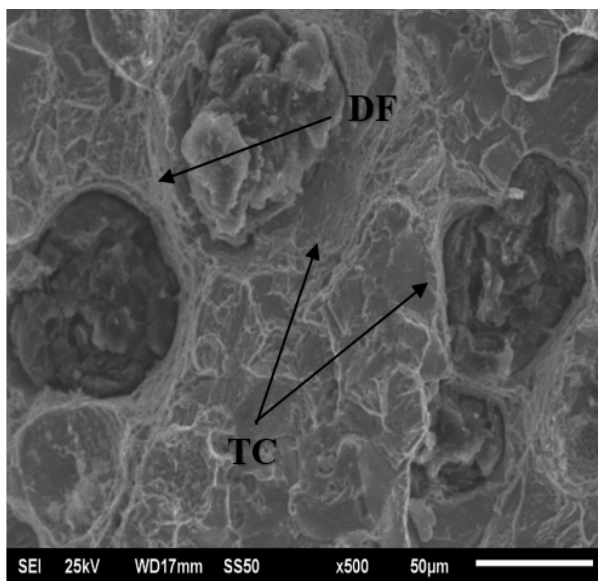
Table 27: Fracture toughness and Hardness of ADI with respect to cryogenic treatment

<b>Austempering Temperature</b>	<b>Cryogenic Treatment?</b>	<b>Fracture Toughness (MPa√m)</b>	<b>Hardness (Rockwell C)</b>
500°F	No	48.0 ± 0.8	48 ± 1
	Yes	48.2 ± 1.9	48 ± 1
550°F	No	59.7 ± 1.9	38 ± 1
	Yes	58.4 ± 0.3	41 ± 1
700°F	No	62.7 ± 1.8	33 ± 1
	Yes	66.3 ± 3.0	35 ± 2
725°C	No	61.3 ± 1.0	32 ± 1
	Yes	61.2 ± 2.2	37 ± 1
750°F	No	53.0 ± 2.1	29 ± 2
	Yes	49.7 ± 1.4	32 ± 1

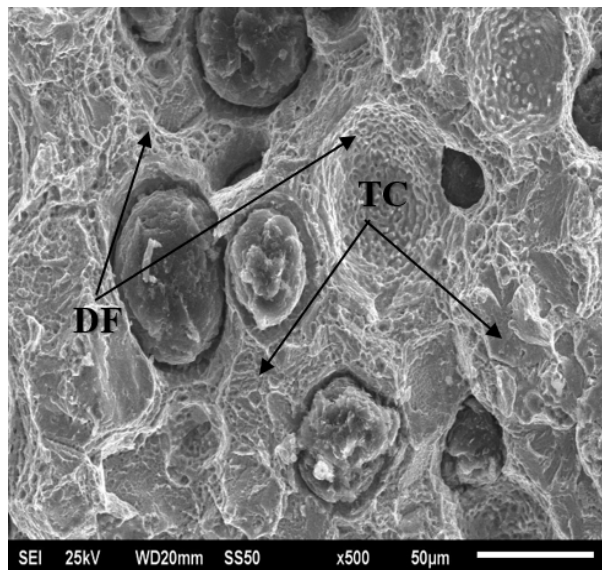
The examination of trends in the mechanical properties of the cryogenically treated ADI shows the same trend as the conventional ADI. In this case, the fracture toughness as well as ductility increases up to a maximum at 700°F, before decreasing. The comparison of the mechanical properties of the ADI with and without cryogenic treatment shows that the cryogenic treatment slightly improved the hardness, ultimate tensile strength and yield strength of the conventional ADI. However, the ductility of the ADI is reduced after cryogenic treatment. This improvement in the hardness, ultimate tensile strength and yield strength as well as the reduction in ductility can be attributed to the changes in the microstructure of the ADI after cryogenic treatment, where the retained austenite transformed to martensite. However, cryogenic treatment did not affect the fracture toughness of the ADI.

### 8.1.1 Fractographs of the conventional ADI

The mode of fracture is determined from the fractographs of the conventional and the cryogenically treated ADI. Figure 70 (a)-(e) shows the fractographs of the conventional ADI under different austempering temperatures.



(a)  $T_{\gamma}=1700^{\circ}\text{F}$ ,  $T_A=500^{\circ}\text{F}$



(b)  $T_{\gamma}=1700^{\circ}\text{F}$ ,  $T_A=550^{\circ}\text{F}$

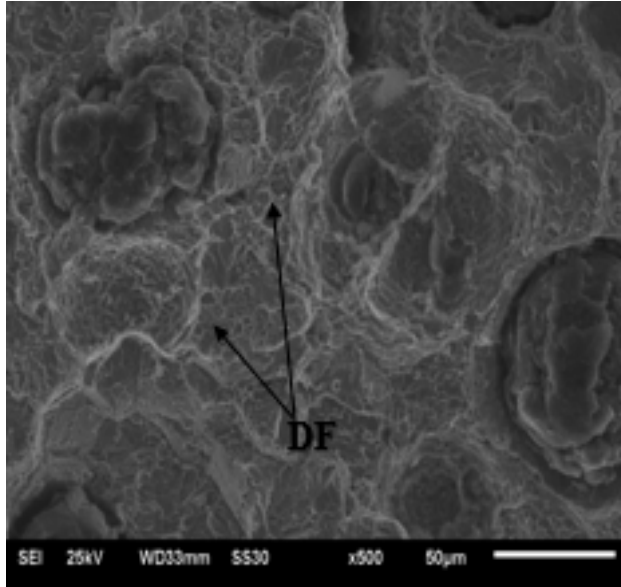
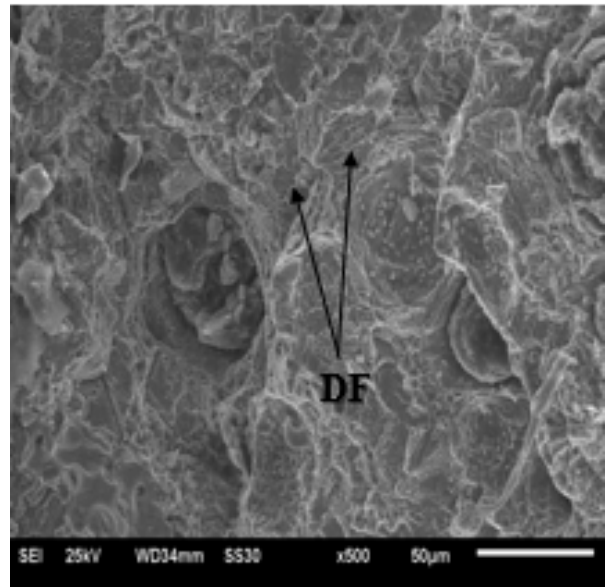
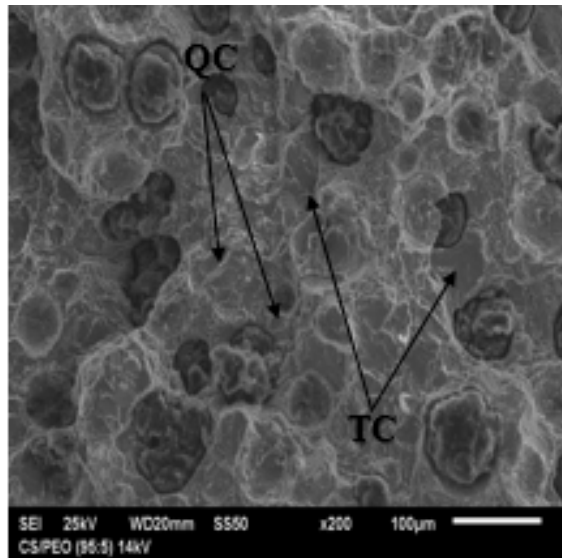
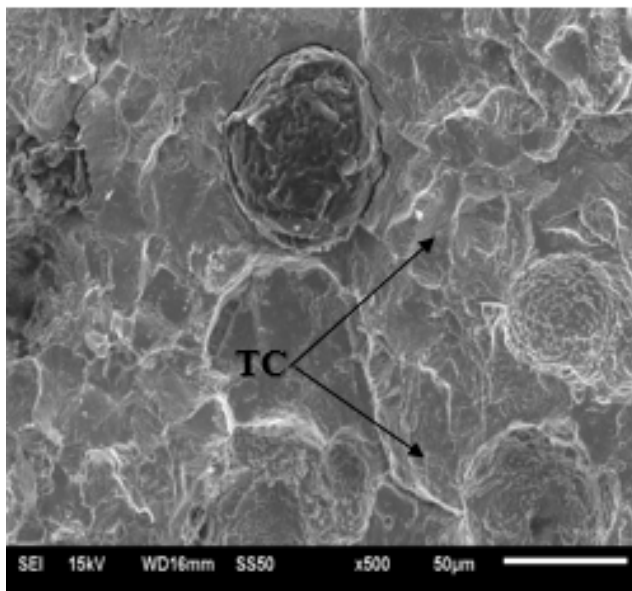
(c)  $T_{\gamma}=1700^{\circ}\text{F}$ ,  $T_A=700^{\circ}\text{F}$ (d)  $T_{\gamma}=1700^{\circ}\text{F}$ ,  $T_A=725^{\circ}\text{F}$ (e)  $T_{\gamma}=1700^{\circ}\text{F}$ ,  $T_A=750^{\circ}\text{F}$ 

Figure.70: SEM fractographs of conventional ADI (CT) specimen, (a)  $T_{\gamma}=1700^{\circ}\text{F}$ ,  $T_A=500^{\circ}\text{F}$ , (b)  $T_{\gamma}=1700^{\circ}\text{F}$ ,  $T_A=550^{\circ}\text{F}$  (c)  $T_{\gamma}=1700^{\circ}\text{F}$ ,  $T_A=700^{\circ}\text{F}$ , (d)  $T_{\gamma}=1700^{\circ}\text{F}$ ,  $T_A=725^{\circ}\text{F}$ , (e)  $T_{\gamma}=1700^{\circ}\text{F}$ ,  $T_A=750^{\circ}\text{F}$ , DF- Dimpled ductile fracture, TC- Transgranular cleavage fracture, QC-Quasi cleavage

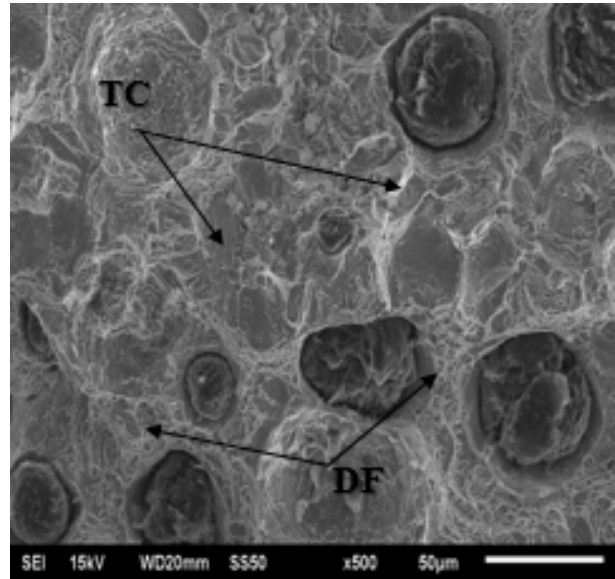
The ADI austempered at lower austempering temperatures of 500°F and 550°F showed a mixture of predominantly transgranular cleavage type of fracture reflecting low ductility resulting in brittle failure in this material. The ADI austempered to 700°F and 725°F showed predominantly dimple ductile fracture where the dimple depressions in the fracture surface is evident along with quasi cleavage pattern, reflecting the moderate ductility in the ausferritic structures. The ADI austempered at higher austempering temperature of 750°F resulted in transgranular and quasi cleavage type of fractures and hence the lower fracture toughness. This variation in the fracture mode with respect to the austempering temperature corresponds to the fracture toughness of ADI. Dimple ductile fracture produced highest fracture toughness greater than 60 MPa√m.

### 8.1.2 Fractographs of the cryogenically treated ADI

The fractographs of the cryogenically treated ADI are shown in the Figure 71 (a)-(e).



(a)  $T_{\gamma}=1700^{\circ}\text{F}$ ,  $T_A=500^{\circ}\text{F}$



(b)  $T_{\gamma}=1700^{\circ}\text{F}$ ,  $T_A=550^{\circ}\text{F}$



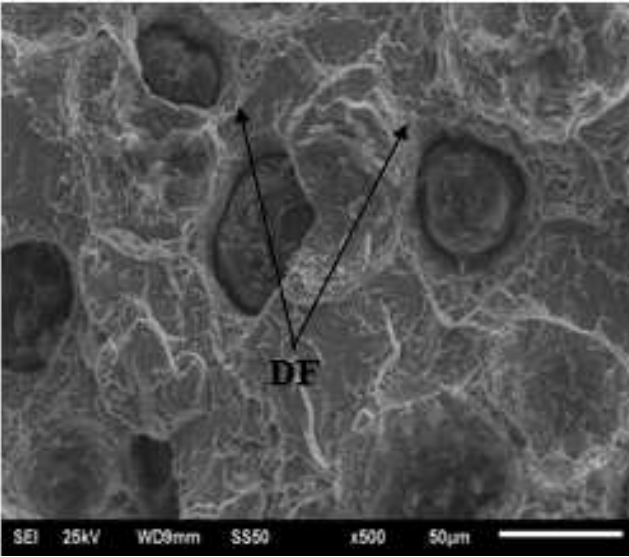
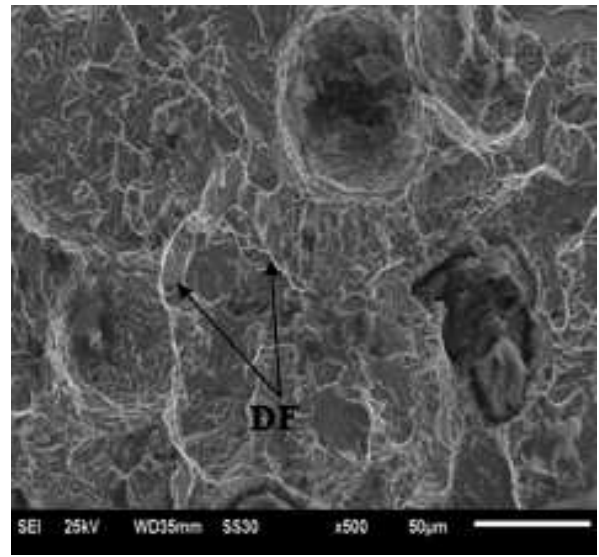
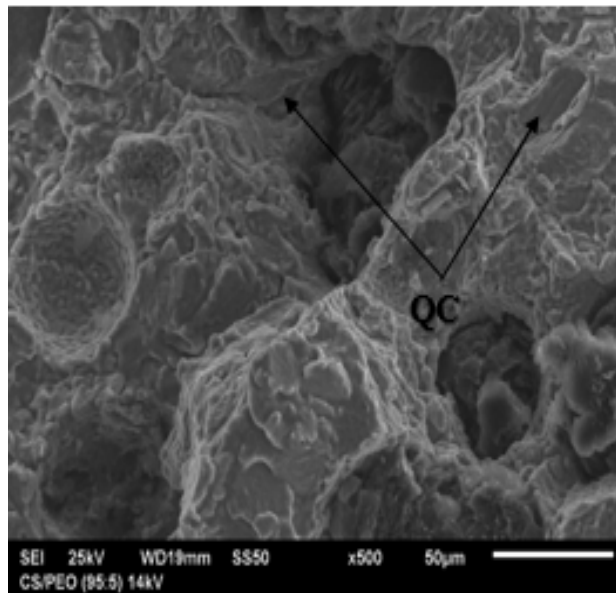
(c)  $T_{\gamma}=1700^{\circ}\text{F}$ ,  $T_A=700^{\circ}\text{F}$ (d)  $T_{\gamma}=1700^{\circ}\text{F}$ ,  $T_A=725^{\circ}\text{F}$ (e)  $T_{\gamma}=1700^{\circ}\text{F}$ ,  $T_A=750^{\circ}\text{F}$ 

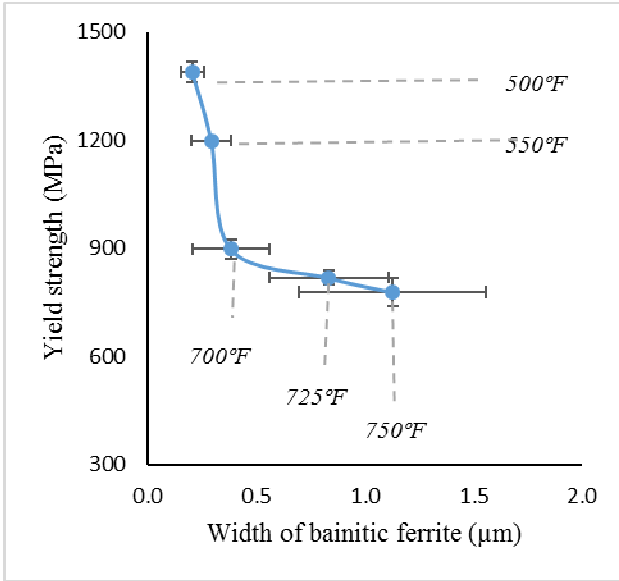
Figure.71: SEM fractographs of cryogenically treated ADI (CT Specimen) (a)  $T_{\gamma}=1700^{\circ}\text{F}$ ,  $T_A=500^{\circ}\text{F}$ , (b)  $T_{\gamma}=1700^{\circ}\text{F}$ ,  $T_A=550^{\circ}\text{F}$  (c)  $T_{\gamma}=1700^{\circ}\text{F}$ ,  $T_A=700^{\circ}\text{F}$ , (d)  $T_{\gamma}=1700^{\circ}\text{F}$ ,  $T_A=725^{\circ}\text{F}$ , (e)  $T_{\gamma}=1700^{\circ}\text{F}$ ,  $T_A=750^{\circ}\text{F}$ , DF- Dimpled ductile fracture, TC- Transgranular cleavage fracture, QC- Quasi cleavage fracture

Cryogenic treatment did not significantly alter the mode of fracture in the previously austempered ADI samples. From this experimental data, it is clear that the cryogenic treatment significantly improves the mechanical properties of ADI without compromising the fracture toughness of ADI.

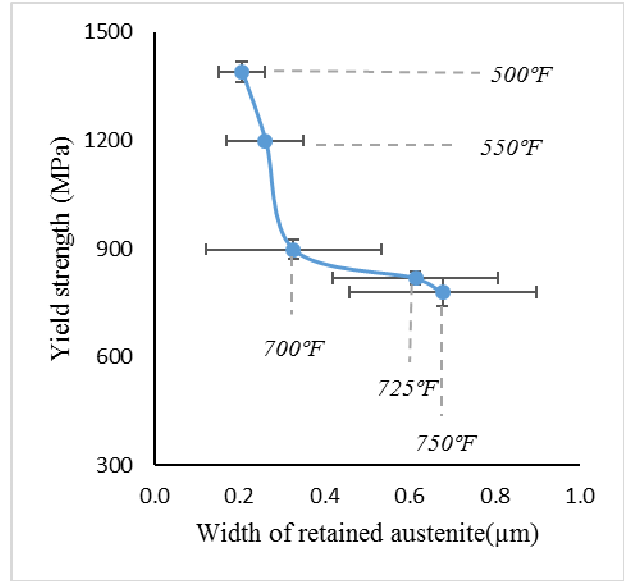
### **8.1.3 Influence of width of different phases on the yield strength of conventional ADI**

Figure 72 (a),(b) and (c) represents the influence of the width of bainitic ferrite, films of retained austenite and the islands of retained austenite respectively on the yield strength of the conventional ADI. Significant reduction in the width of the bainitic ferrite and austenite is observed as the austempering temperature decreases from 750°F to 500°F. Lower the width of bainitic ferrite and retained austenite, higher the strength of ADI. The width of the bainitic ferrite and the austenite is statistically similar at the lower austempering temperatures ranging from 500°F to 700°F.

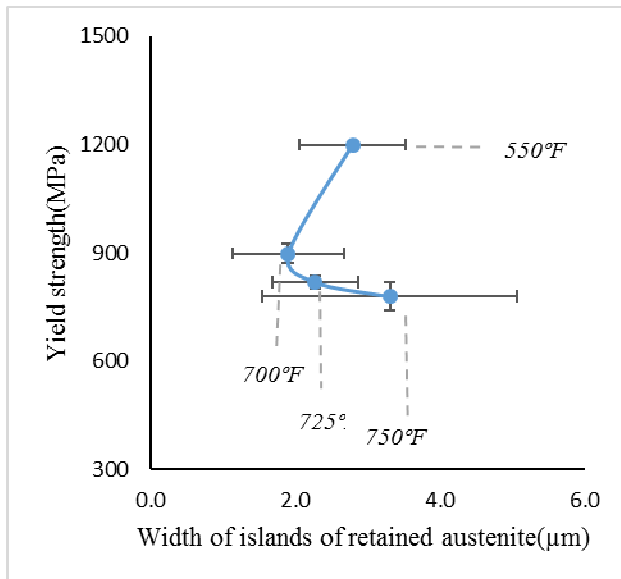
At higher austempering temperature of 725°F and 750°F, the width of the bainitic ferrite is less than the width of the films of retained austenite by approximately 33 and 48% respectively. The islands of the retained austenite are present in the samples austempered in the range of 550°F to 750°F. The presence of islands of retained austenite is detrimental to the mechanical properties of the ADI. The islands of the retained austenite are not sufficiently enriched with carbon when compared to the films of retained austenite, resulting in its instability, leading to the transformation of austenite to martensite by either stress or strain induced transformation process.



(a)



(b)

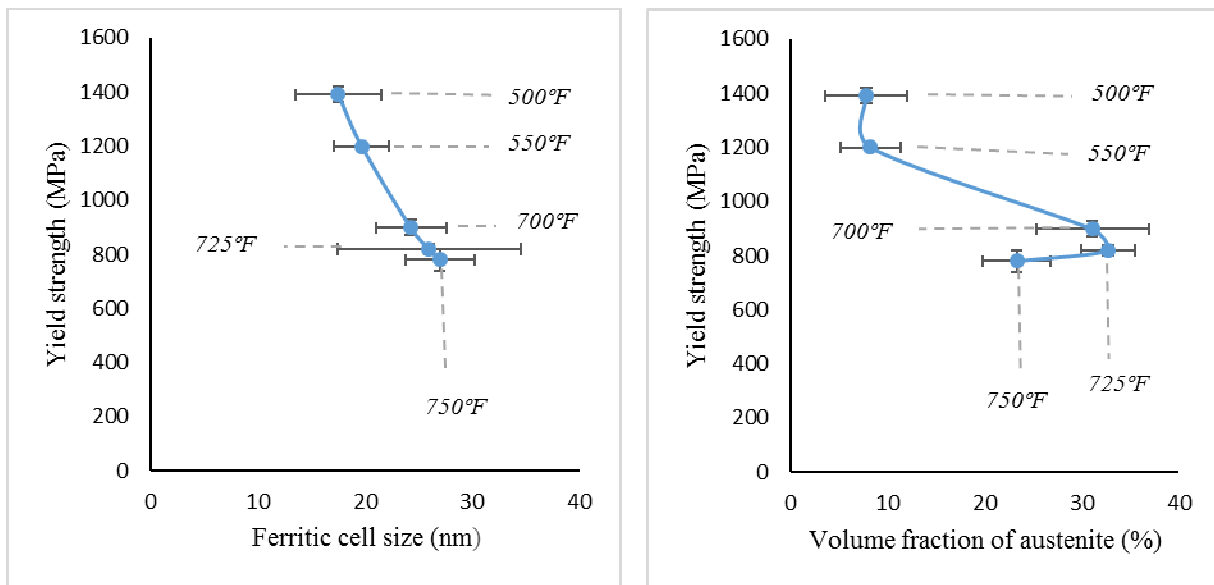


(c)

Figure.72: Influence of the width of (a) bainitic ferrite lath, (b) films of retained austenite and (c) islands of retained austenite on the yield strength of conventional ADI(  $T_{\gamma} = 1700^{\circ}\text{F}$ ,  $T_A$  as shown)

### 8.1.4 Influence of ferritic cell size and austenite volume fraction on the yield strength of conventional ADI

Figure 73 shows the influence of ferritic cell size and the volume fraction of austenite on the yield strength of the conventional ADI. The average ferritic cell size of the samples at lower bainitic austempering temperature is slightly lower than those of the upper bainitic austempering temperature. Statistically, no significant variation in the ferritic cell size of the samples have been observed with respect to the austempering temperature as shown in Figure 73 (a). Lower volume fraction of austenite at the lower bainitic austempering temperature range of 500°F and 550°F resulted in higher strength in ADI.



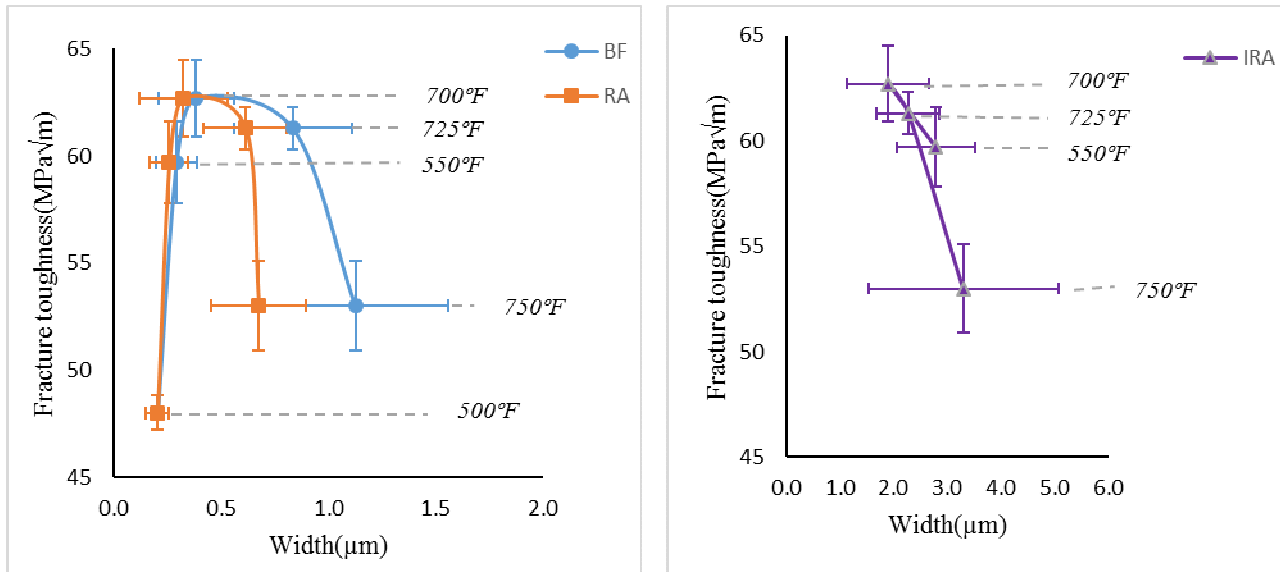
(a)

(b)

Figure.73: Influence of the width of (a)ferritic cell size, (b)volume fraction of austenite on the yield strength of conventional ADI (  $T_{\gamma}= 1700^{\circ}\text{F}$ ,  $T_A$  as shown)

### 8.1.5 Influence of width of different phases on the fracture toughness of conventional ADI

Figure 74 show sthe influence of the width of the bainitic ferrite lath, films of retained austenite and islands of retained austenite on the fracture toughness of conventional ADI with respect to the austempering temperature.



(a)

(b)

Figure.74: Influence of the width of (a) BF-bainitic ferrite lath, RA-films of retained austenite and (b) IRA- islands of retained austenite on the fracture toughness of conventional ADI(  $T_{\gamma} = 1700^{\circ}\text{F}$ ,  $T_A$  as shown)

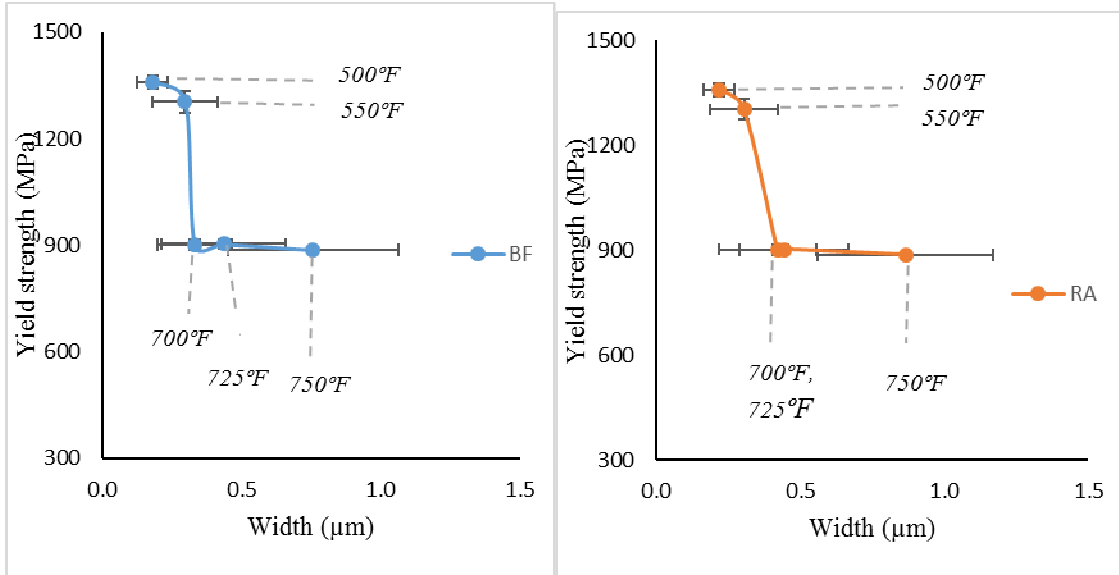
The lath sizes of the retained austenite and bainitic ferrite is statistically similar at austempering temperatures up to 700°F. The fracture toughness increases as the austempering temperature is increases from 500°F to a maximum at 700°F before decreasing. At higher austempering temperatures of 725°F and 750°F, the width of the retained austenite is larger than the width of bainitic ferrite. This resulted in increased strength but lower fracture toughness in ADI. There exists a optimum temperature for austempering for tuning the fracture toughness of ADI. Presence of islands of retained austenite causes adverse effect on the fracture toughness of

the material. During crack propagation, the large stresses at the crack tip, transforms the unstable islands of retained austenite to martensite resulting in reduced fracture toughness value.

### **8.1.6 Influence of width of different phases on the yield strength of cryogenically treated ADI**

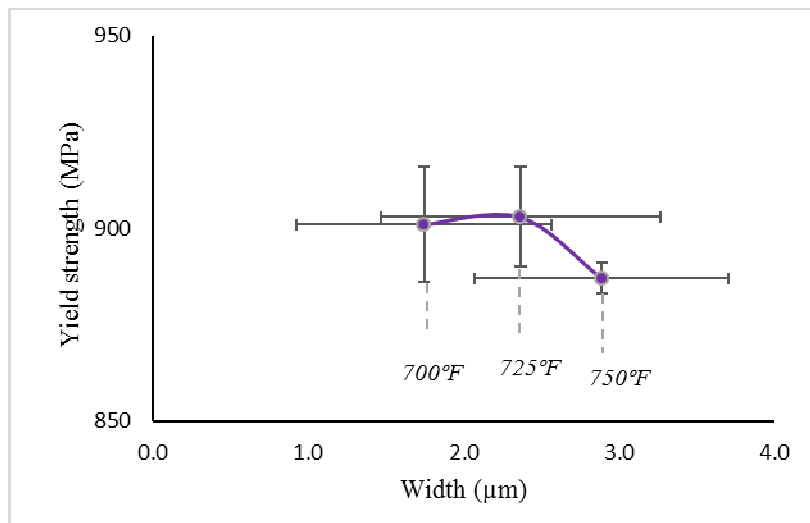
Figure 75 (a), (b) and (c) shows the influence of the width of bainitic ferrite laths, films of retained austenite and the islands of retained austenite respectively, on the yield strength of the cryogenically treated ADI. The average width of the bainitic ferrite is significantly reduced by the cryogenic processing. Statistically, there is no significant difference in the width of the films of retained austenite in ADI before and after the cryogenic processing. The influence of the austempering temperature on the strength of the ADI still exists after cryogenic processing. The average width of the bainitic ferrite and retained austenite reduces with the increase in austempering temperature. Lower the width of bainitic ferrite and retained austenite, higher the strength in cryogenically treated ADI. Cryogenic processing significantly increased the strength of the prior conventionally austempered ADI. This can be attributed to the presence of appreciable amount of martensite laths along with the bainitic ferrite laths in the cryogenically treated ADI.

The islands of retained austenite were present only in the cryogenically treated ADI, austempered in the upper bainitic temperature range of 700°F to 750°F in which the yield strength is lower than the samples austempered at higher temperatures. Thus, the presence of islands of the retained austenite is detrimental to the strength of the ADI.



(a)

(b)



(c)

Figure.75: Influence of the width of (a)bainitic ferrite, (b) films of retained austenite and (c)

islands of retained austenite on the yield strength of the cryogenically treated ADI

( $T_{\gamma}=1700^{\circ}\text{F}$ ,  $T_A$  as shown)

### 8.1.7 Influence of ferritic cell size and austenite volume fraction on the yield strength of cryogenically treated ADI

Figure 76 (a) and (b) shows the effect of ferritic cell size and the volume fraction of austenite respectively, on the yield strength of cryogenically treated ADI. Cryogenic treatment resulted in decrease in average ferritic cell size of ADI. As expected, the samples with lower bainitic ferrite width had lower ferritic cell size and higher strength than those with higher ferritic cell sizes.

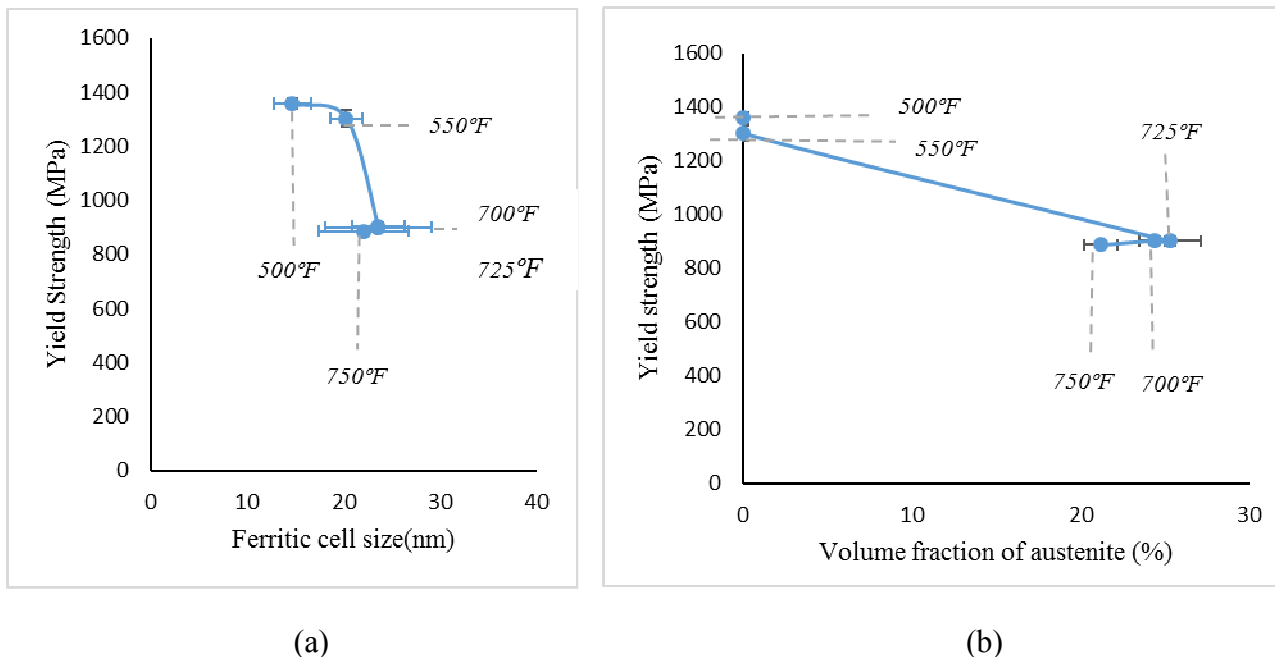


Figure.76: Influence of the width of (a)ferritic cell size, (b)volume fraction of austenite on the yield strength of the cryogenically treated ADI (  $T_{\gamma}= 1700^{\circ}\text{F}$ ,  $T_A$  as shown)

The average volume fraction of retained austenite reduced significantly after cryogenic treatment in ADI. The reduction in the volume fraction of austenite at higher austempering temperatures from  $700^{\circ}$  to  $750^{\circ}\text{F}$  resulted a increase in yield strength of the cryogenically treated ADI. No retained asutenite was observed in the cryogenically treated ADI, austempered at lower bainitic austempering temperatures of  $500^{\circ}\text{F}$  and  $550^{\circ}\text{F}$  resulting in higher yield strength.



### 8.1.8 Influence of width of different phases on the fracture toughness of cryogenically treated ADI

The influence of width of the bainitic ferrite lath, retained austenite lath and the width of islands of retained austenite on the fracture toughness of the cryogenically treated ADI as shown in the Figure 77 (a) and (b) respectively.

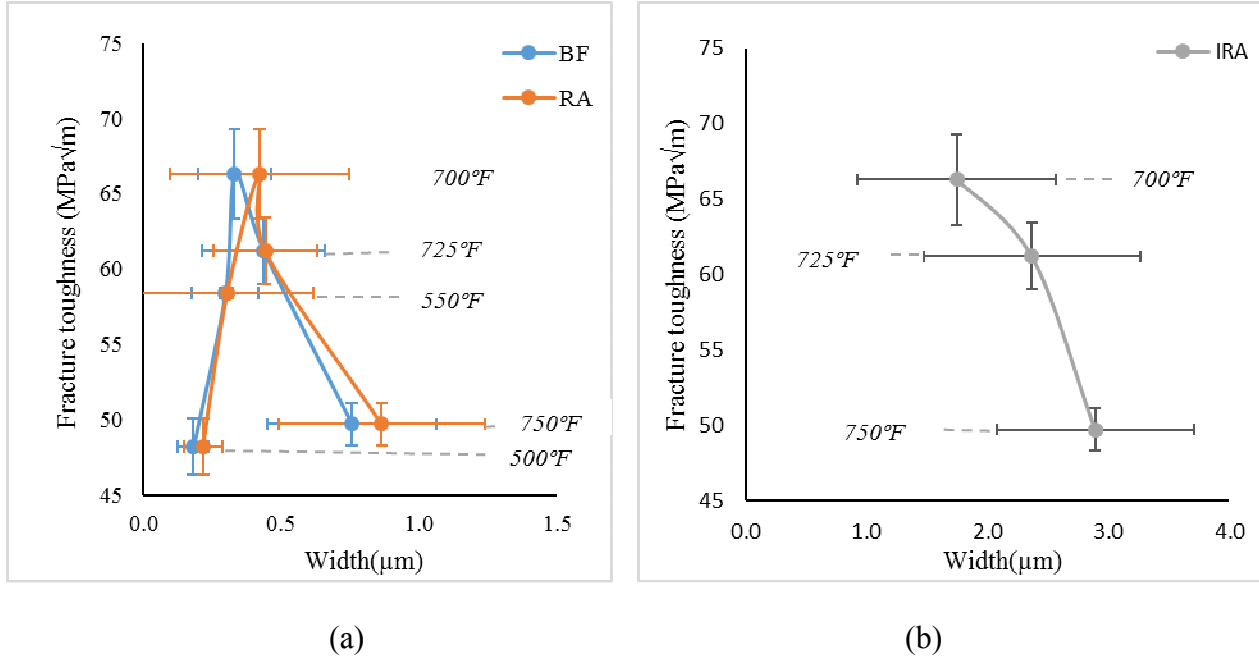


Figure.77: Influence of the width of (a) BF-bainitic ferrite lath, RA-films of retained austenite and (b) IRA- islands of retained austenite on the fracture toughness of cryogenically treated ADI

( $T_{\gamma} = 1700^{\circ}\text{F}$ ,  $T_A$  as shown)

Statistically there is no significant difference in the lath sizes of the austenite and bainitic ferrite laths, therefore, no conclusion could be drawn regarding the higher fracture toughness with respect to the lath sizes. There exists an optimum combination of lath size and temperature of  $700^{\circ}\text{F}$  at which fracture toughness is higher. Islands of retained austenite were present only in the cryogenically treated samples austempered at higher austempering temperatures from  $700^{\circ}\text{F}$  to  $750^{\circ}\text{F}$ . This has resulted in higher fracture toughness in these ADI samples.

## 8.2 Mechanical properties and fracture toughness of intercritically austenitized ADI

Table 28 compares the mechanical properties of ADI with respect to the intercritical austempering. Table 28 also reports the mechanical properties of ADI intercritically austenitized at 1520°F with respect to the austempering temperature.

Table 28: The Mechanical Properties of the ADI as a Function of intercritical austenitizing and Austempering Temperature.

Austenitizing Temperature (°F)	Austempering Temperature (°F)	Yield Strength (MPa)	Ultimate Tensile Strength (MPa)	% Elongation
1535°F	680°F	722.3 ± 163.8	919.1 ± 127.5	5.9 ± 0.9
1520°F	725°F	887.9 ± 34.4	1052.3 ± 6.2	6.0 ± 1.1
	680°F	634.4 ± 124.8	813.6 ± 120.2	5.3 ± 2.2
	600°F	1228.8 ± 14.6	1384.8 ± 33.8	3.1 ± 0.3
	550°F	1225.4 ± 10	1381 ± 31	2.0 ± 0.5
1472°F	680°F	604.6 ± 95.2	823.1 ± 86.8	8.2 ± 0.5
1436°F	680°F	380 ± 0.9	490.3 ± 6.2	12.3 ± 0.2
1418°F	680°F	374 ± 39.3	497.7 ± 17.9	12.6 ± 0.1

The yield strength and ultimate tensile strength of the intercritically austempered ADI increases with the increase in austenitization temperature. As the intercritical austenitization

temperature is lowered from 1520°F to 1418°F, the strength of the ADI decreases while the ductility increases. This can be attributed to the increase in volume fraction of proeutectoid ferrite with the decrease in intercritical austenitization temperature.

The influence of austempering temperature was observed for the samples austenitized at a constant intercritical austenitization temperature of 1520°F. The yield strength and ultimate tensile strength was higher whereas the ductility is lower for the samples austempered at lower austempering temperatures of 550°F and 600°F. This is due to the presence of very fine ausferritic structure present at lower austempering temperatures. As predicted by the Hall-Petch equation [25,26], the finer ausferritic structure contributed higher strength in the ADI austempered at low austempering temperatures. The coarse ausferritic microstructure in the ADI samples austempered in the upper bainitic region resulted in lower strength but increased ductility.

Table 29 compares the fracture toughness and hardness of the ADI with respect to the intercritical austenitization temperature. The hardness of the ADI samples decreased with the decrease in intercritical austenitization temperatures.

Table 29 also details the hardness and fracture toughness of ADI with respect to austempering temperature for a constant intercritical austenitization temperature of 1520°F. The Rockwell C hardness of the ADI is higher for the samples austempered at lower austempering temperatures. The fracture toughness of the intercritical austenitized ADI increases with the increase in austempering temperature from 550°F to 680°F before decreasing. This represents that there exists an optimum austempering temperature for tuning the fracture toughness of ADI with respect to intercritical austenitization.

Table 29: The Fracture toughness and Hardness of the ADI as a Function of Intercritical austenitizing and Austempering Temperature.

Austenitizing Temperature	Austempering Temperature	Fracture toughness(KQ) (MPa)	Hardness (Rockwell C)
1535°F	680°F	66.0 ± 2.7	34 ± 1
1520°F	725°F	56.6 ± 1.5	32 ± 1
	680°F	62.2 ± 2.0	32 ± 3
	600°F	59.0 ± 1.2	40 ± 1
	550°F	53.3 ± 2.0	46 ± 1
1472°F	680°F	54.4 ± 4.1	22 ± 1
1436°F	680°F	46.4 ± 0.3	11 ± 1
1418°F	680°F	42.7 ± 2.0	7 ± 1

### 8.2.1 Fractographs of the intercritical ADI

The change in fracture toughness value of the ADI with respect to intercritical austenitization can be associated with the variation of the fractured surface of the samples. The SEM fractographs of the intercritical austenitized samples are shown in the Figure78 (a)-(d). The fractured sequence of the intercritical austempered samples is similar to the fracture sequence obtained for the ductile iron with uniform matrix structure. The sample austenitized at 1535°F, at a temperature just above the upper intercritical temperature, shows dimple ductile fracture

throughout the fractured surface. Dimple ductile fracture produces a fracture toughness of  $60 \pm 5$   $\text{MPa}\sqrt{\text{m}}$  in ADI [129].

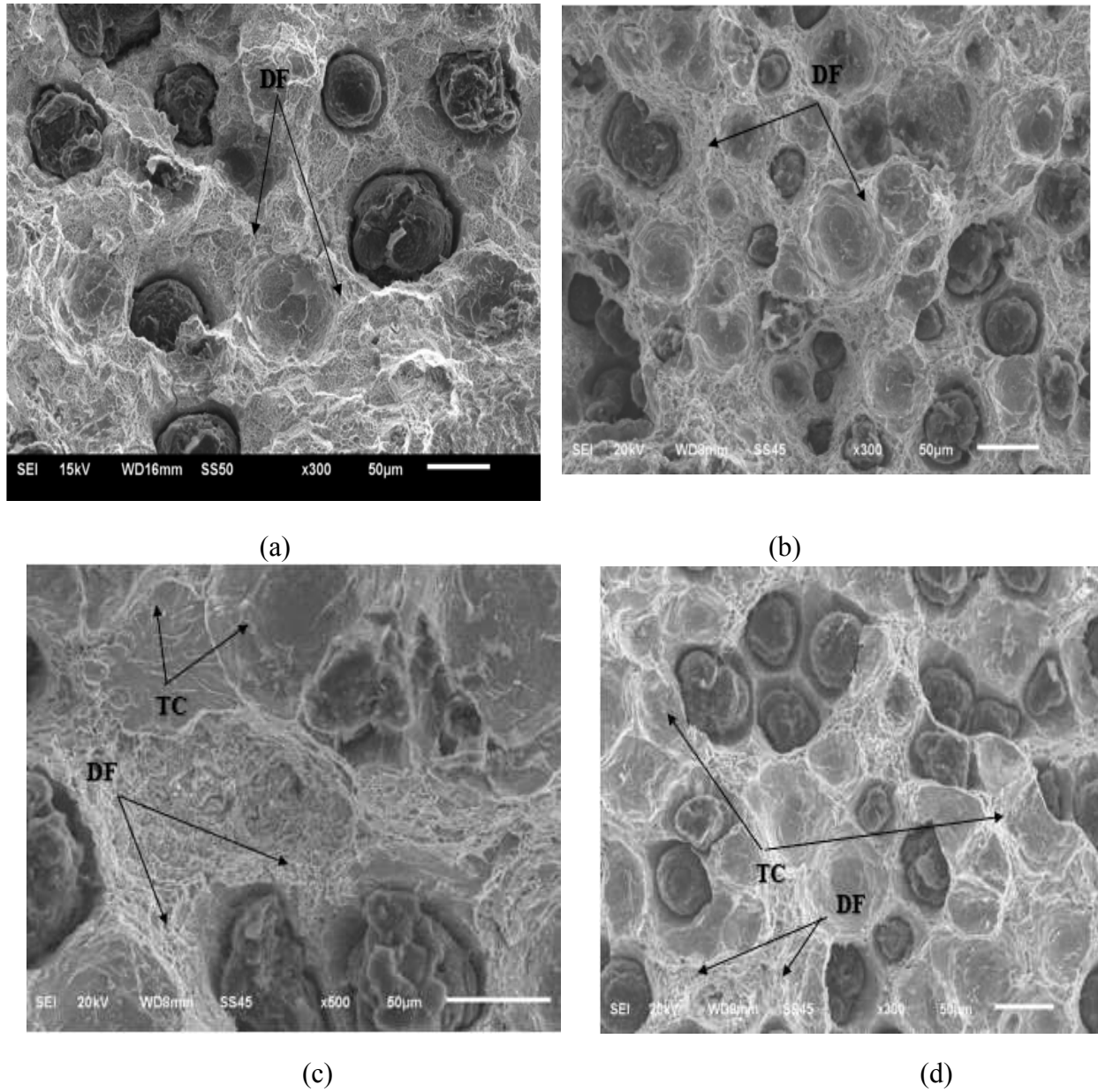
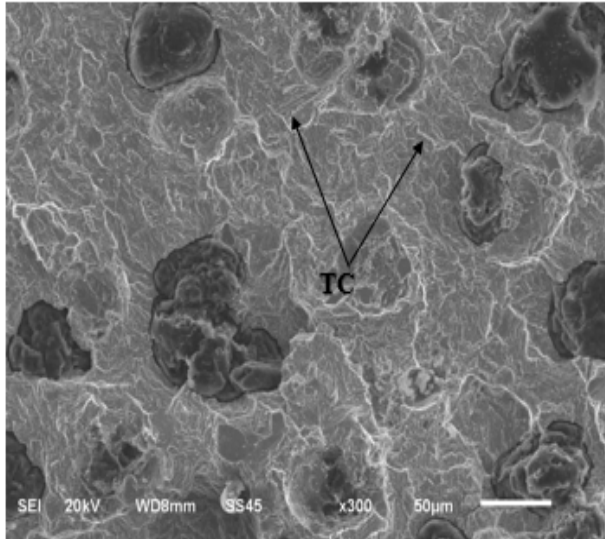


Figure.78: SEM fractographs of intercritical ADI (CT) specimen (a) 1535°F -680°F, (b) 1472°F - 680°F, (c)  $T_\gamma=1436^\circ\text{F}$ ,  $T_A=680^\circ\text{F}$ , (d)  $T_\gamma=1418^\circ\text{F}$ ,  $T_A=680^\circ\text{F}$ , DF- Dimpled ductile fracture, TC- Transgranular cleavage fracture

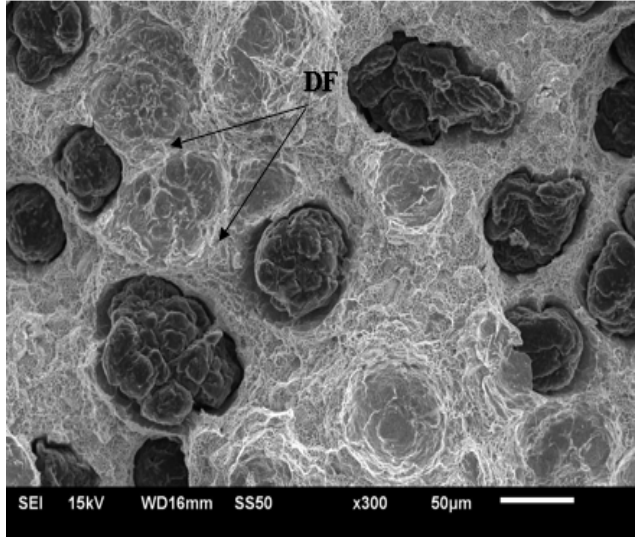
The 1535°F austenitized sample produced a fracture toughness of 66 MPa√m. This result is in favor to the literature data, where in, the conventional single step austempering process produced ADI with a maximum fracture toughness value between 60 and 66 MPa√m [1,130,131].

As the austenitizing temperature is reduced from the upper critical austenitization temperature of 1520°F to the lower intercritical austenitization temperature of 1418°F, the variation of the fractured surface occurs. The fractured surface is predominantly dimple ductile type, along with some transgranular pattern in the ADI austenitized at 1436°F and 1418°F, this has caused lower fracture toughness in these samples. Figure 79 (a)-(d) shows the fractographs of the ADI intercritically austenitized at 1520°F with respect to the austempering temperature. The fracture toughness of the ADI increases with the increase in austempering temperature for the ADI intercritically austenitized at 1520°F up to a maximum at 680°F before decreasing. This is due to the fineness of the ferritic structure with the decrease in austempering temperature as well the variations in the volume fraction of austenite [2,62,131].

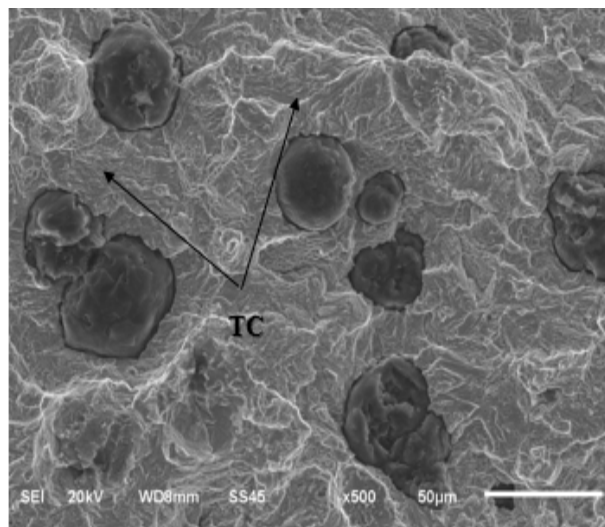
In this intercritically austenitized ADI, the sample austempered at 680°F showed dimple ductile fracture and therefore resulted in higher fracture toughness of 62.25 MPa√m. It is evident from the literature that higher strength at low austempering temperature as well as coarse ausferritic structure favor transgranular cleavage fracture. The samples austempered at 725°F, 600 °F and 550 °F had transgranular predominantly transgranular cleavage fracture rather than the dimple ductile fracture and that appears to be the reason for the lower fracture toughness in these samples.



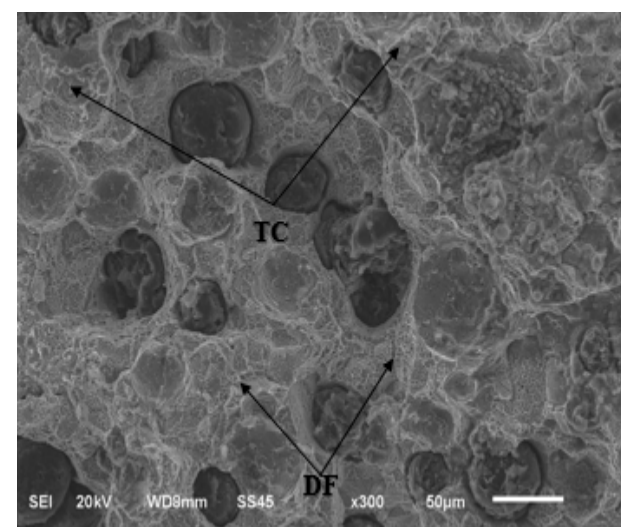
(a)



(b)



(c)



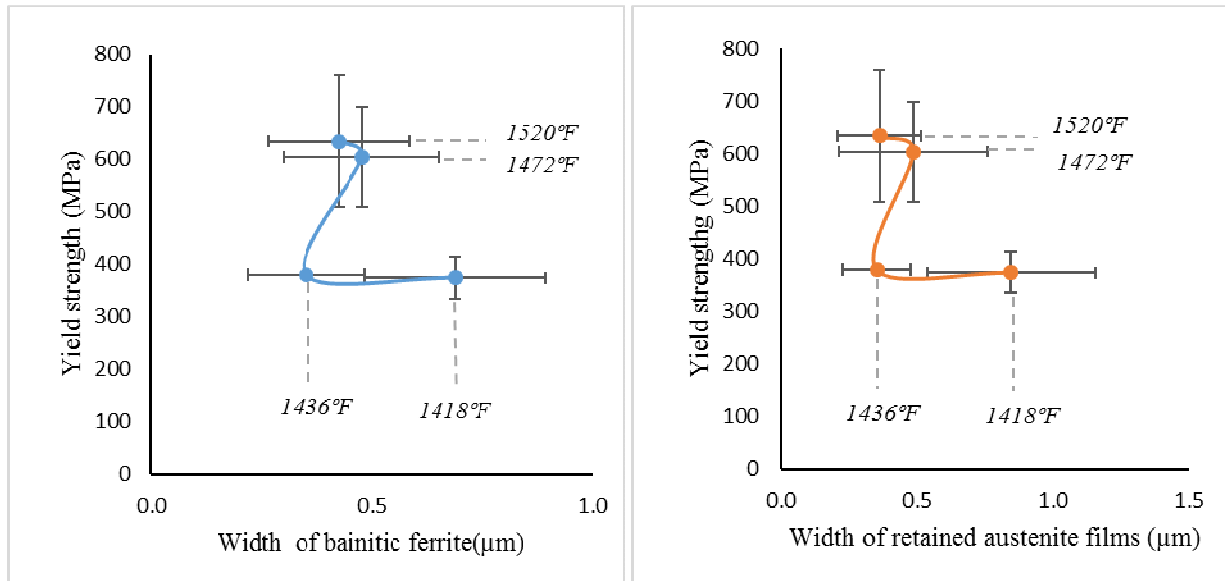
(d)

Figure.79: SEM fractographs of intercritical ADI (CT) °F, (a)  $T_{\gamma}=1520^{\circ}\text{F}$ ,  $T_{\text{A}}=725^{\circ}\text{F}$  and (b)  $T_{\gamma}=1520^{\circ}\text{F}$ ,  $T_{\text{A}}=680^{\circ}\text{F}$ , (c)  $T_{\gamma}=1520^{\circ}\text{F}$ ,  $T_{\text{A}}=600^{\circ}\text{F}$ , (d)  $T_{\gamma}=1520^{\circ}\text{F}$ ,  $T_{\text{A}}=550^{\circ}\text{F}$ , respectively, DF-

Dimpled ductile fracture, TC- Transgranular cleavage fracture

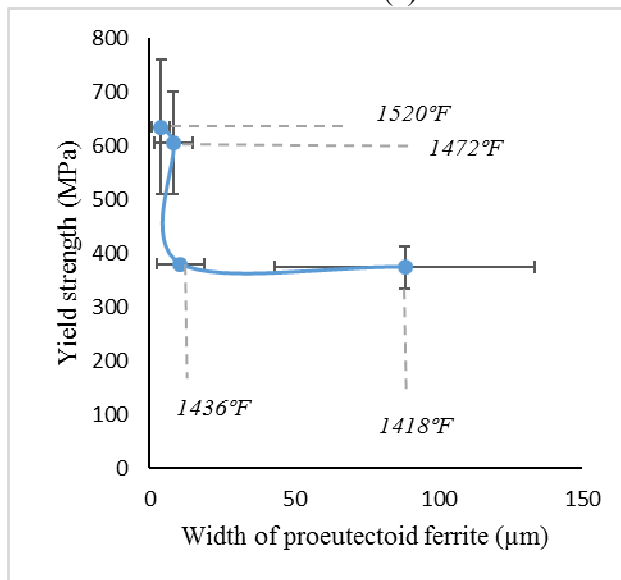
## 8.2.2 Influence of width of different phases on the yield strength of intercritical ADI

(constant  $T_A$ )



(a)

(b)



(c)

Figure.80: Influence of the width of (a)bainitic ferrite, (b) films of retained austenite and (c) islands of retained austenite on the yield strength of intercritical ADI ( $T_\gamma$  as shown, constant

$T_A=680^\circ\text{F}$ )



Figure 80 shows the effect of the width of different phases on the strength of the ADI austempered at 680°F with respect to the intercritical austenitizing temperature. Statistically, there is no significant difference in the lath sizes of bainitic ferrite and retained austenite with respect to austenitization temperature. Generally, the strength of the material increases as the lath sizes is reduced. The ADI intercritically austenitized at 1520°F with the bainitic lath size of 0.360 $\mu\text{m}$ , had the maximum strength of 634 MPa, while the sample austenitized at lower intercritical temperature of 1418°F with the bainitic ferrite lath size of 0.844  $\mu\text{m}$  resulted in yield strength of only 374 MPa.

The lower yield strength in the intercritically austenitized ADI can be attributed to the presence of proeutectoid ferrite in the microstructure matrix. Figure 80(c) shows the variation in the width of proeutectoid ferrite with respect to the intercritical austenitization temperature. The width of the proeutectoid ferrite increases as the intercritical austenitization temperature decreases from 1520°F to 1418°F. The percentage difference of approximately 95% is observed in the width of the proeutectoid ferrite as the austenitization temperature reduced from 1520°F to 1418°F.

### **8.2.3 Influence of ferritic cell size and austenite volume fraction on the yield strength of cryogenically treated ADI (contant $T_A$ )**

Figure 81 (a) shows the variation of the ferritic cell size on the yield strength of the of the intercritically austenitized ADI. Statistically, there is no significant difference between the ferritic cell size of the intercritically austenitized samples and the ferritic cell size lie within a range of approximately 23 to 27nm.

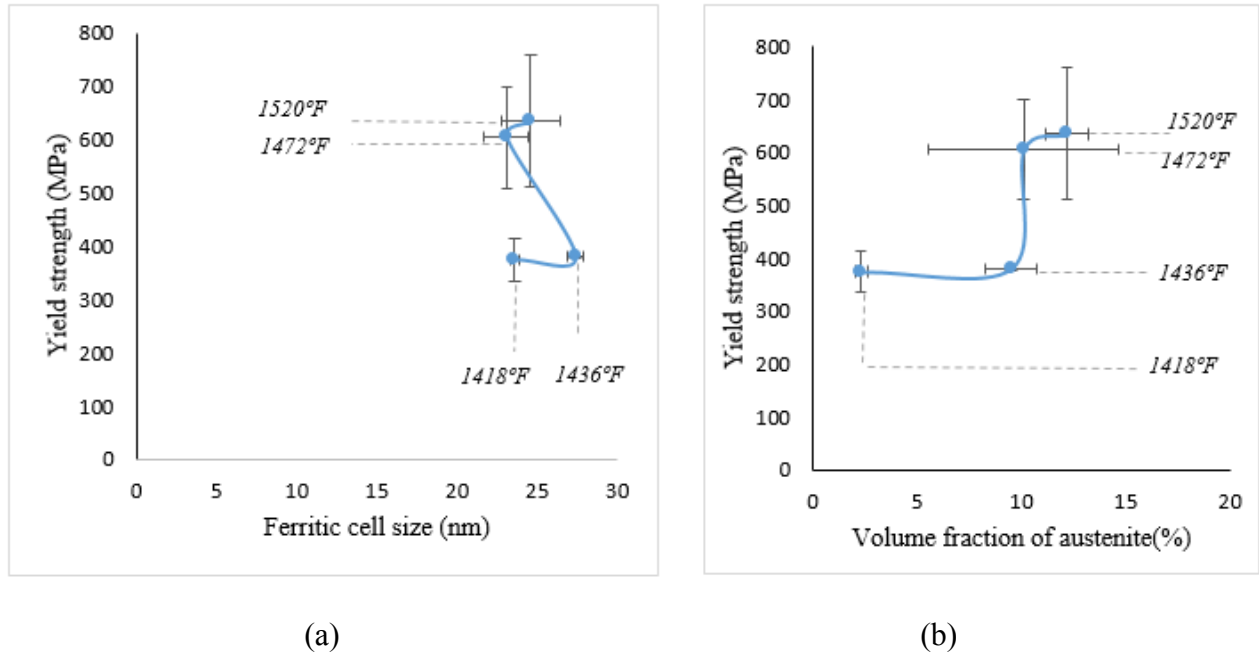


Figure.81 : Influence of the width of (a) ferritic cell size, (b) volume fraction of austenite on the yield strength of intercritical ADI ( $T_\gamma$  as shown, constant  $T_A=680^\circ\text{F}$ )

Figure 81(b) shows the influence of the volume fraction of austenite on the yield strength of the ADI with respect to the intercritical austenitization temperatures. In this case, relatively higher volume fraction of approximately 12% resulted in higher yield strength in the 1520°F austenitized ADI. The average volume fraction of retained austenite significantly decrease as the austenitizing temperature is decreased from 1520°F to 1418°F.

#### 8.2.4 Influence of width of different phases on the fracture toughness of intercritical ADI (constant $T_A$ )

Figure 82 shows the influence of the width of different phases on the fracture toughness of intercritically austenitized ADI. Statistically, there is no significant difference in the width of bainitic ferrite and austenite in the ADI austenitized in the intercritical austenitization temperature range. It is generally known that the increase in strength will decrease the fracture toughness of ADI. However, in the intercritically austenitized ADI, the sample austenitized at

upper intercritical austenitizing temperature of 1520°F had relatively higher strength as well the higher fracture toughness value. Width of the proeutectoid ferrite had a significant effect in determining the fracture toughness of intercritically austenitized ADI. Higher the width of the proeutectoid ferrite, lower the fracture toughness of ADI.

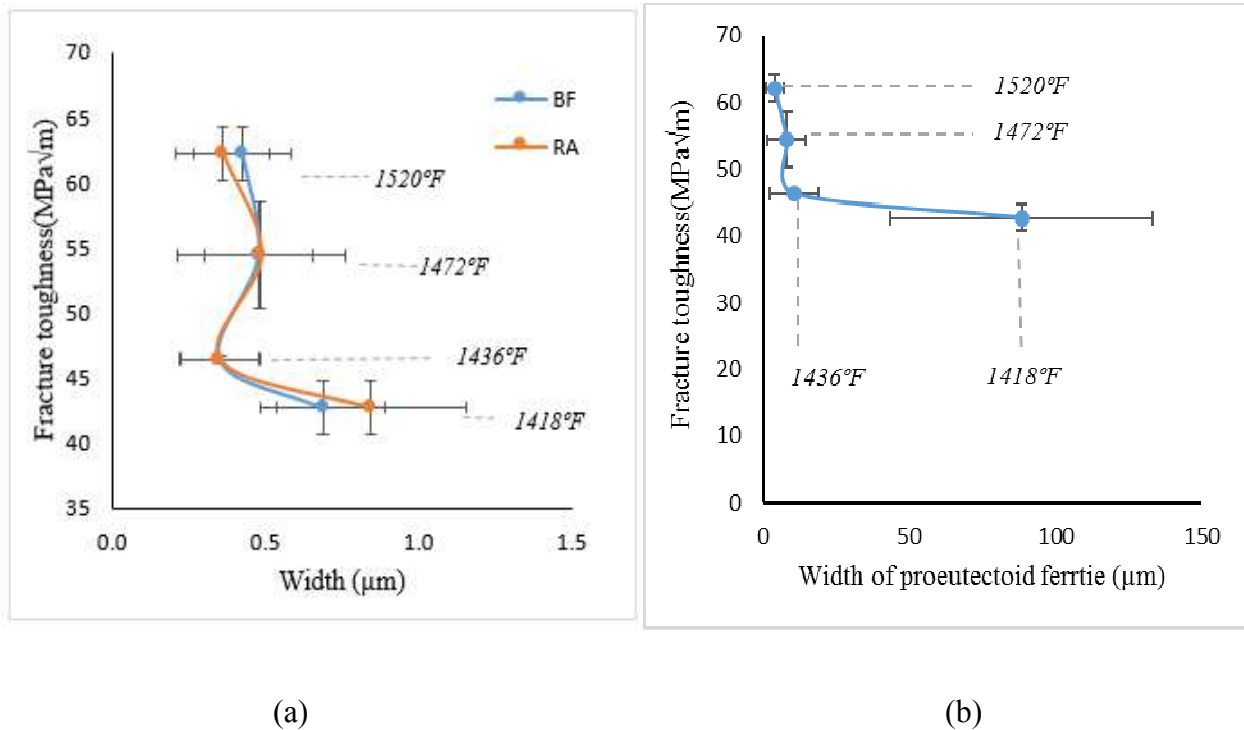


Figure.82: Influence of the width of (a)ferritic cell size, (b)volume fraction of austenite on the yield strength of intercritical ADI ( $T_\gamma$  as shown, constant  $T_A=680^\circ\text{F}$ )

### 8.2.5 Influence of width of different phases on the yield strength of intercritical ADI

(constant  $T_\gamma$ )

The influence of the lath sizes of the different phases on the yield strength of the ADI intercritically austenitized at 1520°F with respect to the austempering temperatures is shown in the Figure 83.

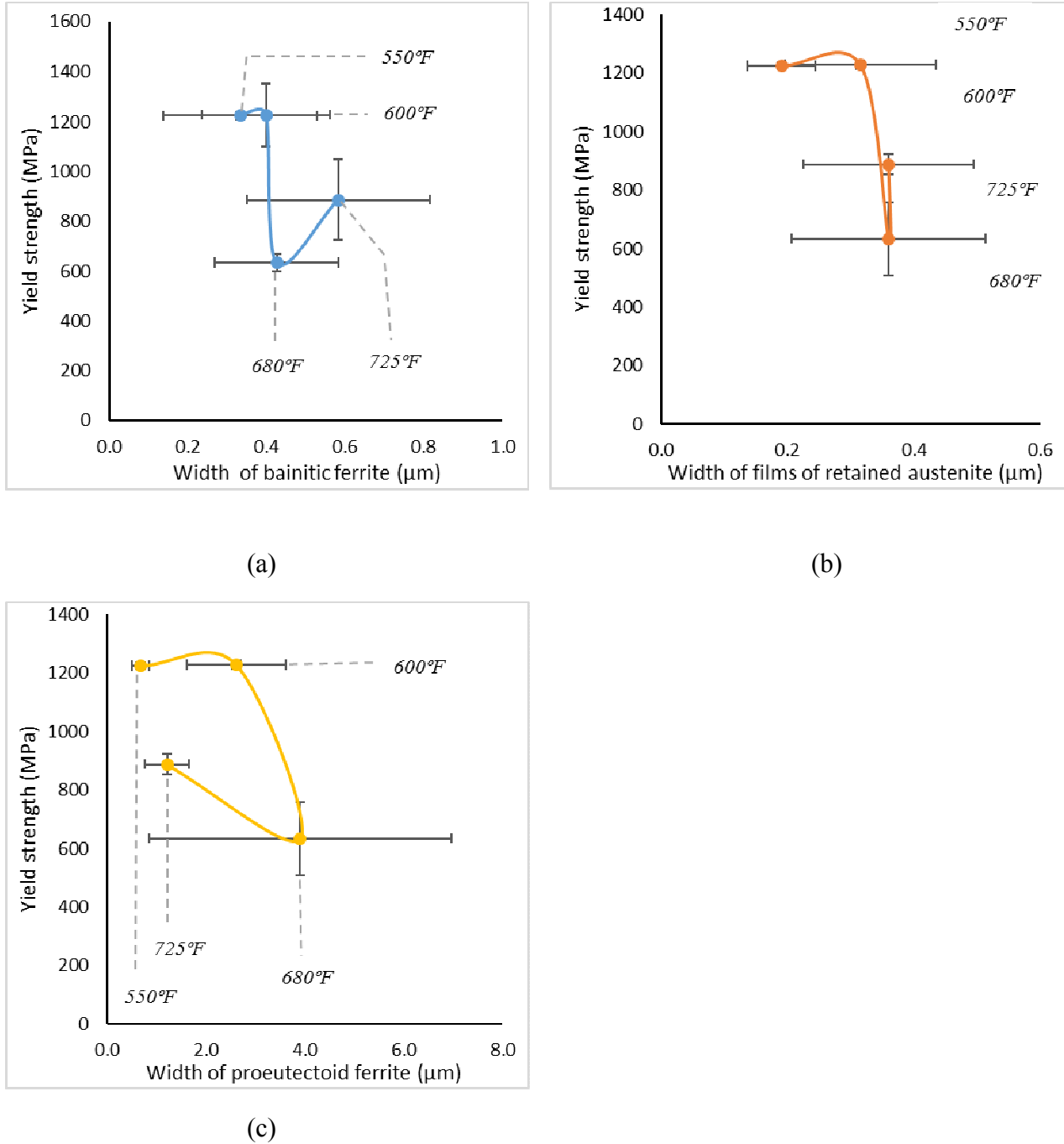


Figure.83: Influence of the width of (a)bainitic ferrite, (b) films of retained austenite and (c) islands of retained austenite on the yield strength of intercritical ADI ( $T_{\gamma}= 1520^{\circ}\text{F}$ ,  $T_A$  as shown)

The width of the retained austenite is finer than the width of bainitic ferrite in these samples. The width of the bainitic ferrite lath as well as the width of films of retained austenite reduces as the austempering temperature is decreased from 725°F to 550°F. Finer width of bainitic

ferrite and retained austenite resulted in higher yield strength in the ADI austempered at lower bainitic austempering temperature ranges. Statistically, no significant difference was observed in the width of the proeutectoid ferrite of the ADI with respect to austempering temperatures.

### 8.2.6 Influence of austenite volume fraction and ferritic cell size on the yield strength of intercritical ADI (contant $T_\gamma$ )

The effect of austenite volume fraction on the variation of the yield strength of the intercritically austenitized ADI is shown in the Figure 84.

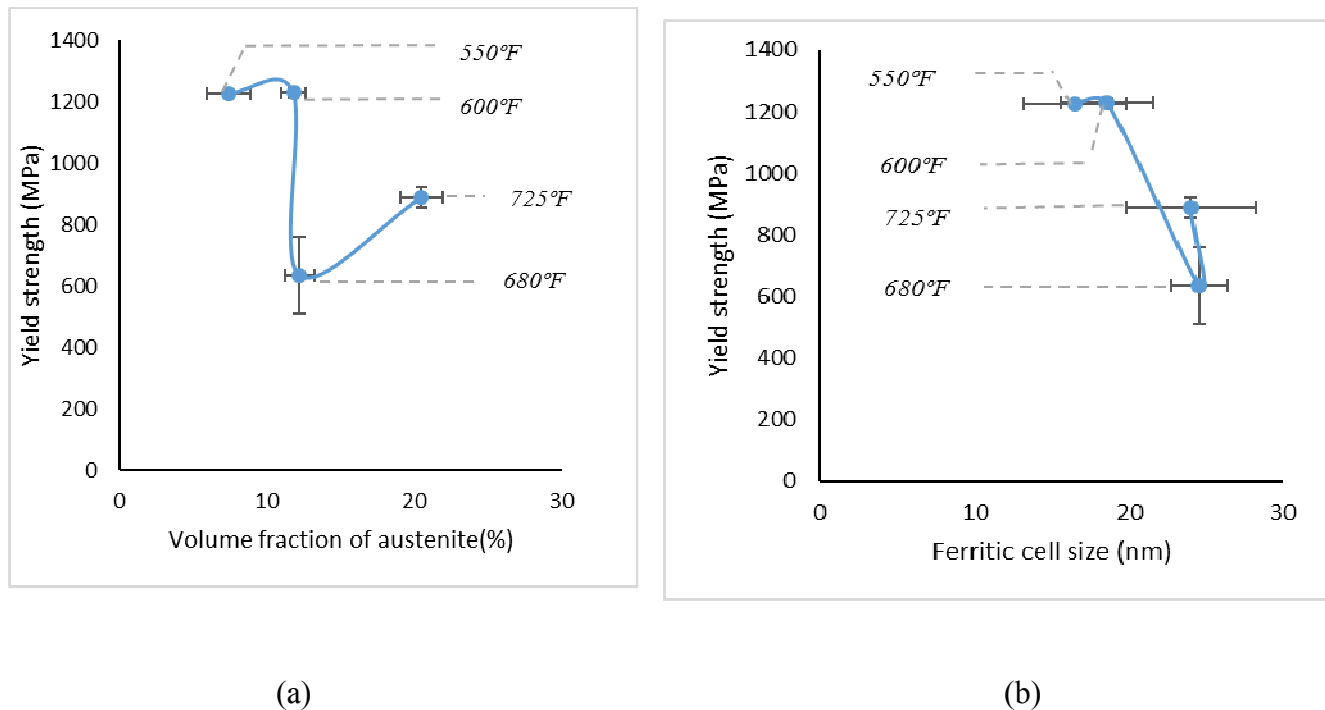
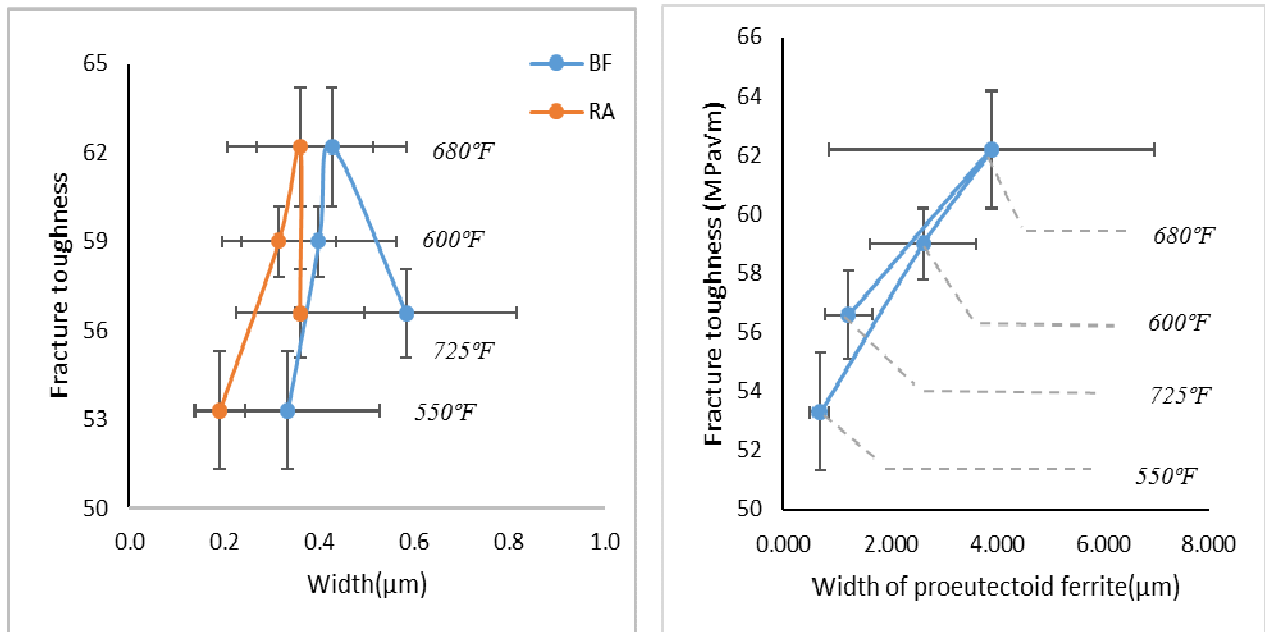


Figure.84: Influence of the (a) volume fraction of austenite, (b) ferritic cell size on the yield strength of intercritical ADI ( $T_\gamma=1520^\circ\text{F}$ ,  $T_A$  as shown)

Lower volume fraction of austenite resulted in higher yield strength. Ferritic cell size of the intercritically austempered ADI decreases with the decrease in austempering temperature. Higher yield strength is obtained at lower austempering temperature of 550°F and 600°F where the ferritic cell size is in the range of approximately 16 to 18 nm.

### 8.2.7 Influence of width of different phases on the fracture toughness of intercritical ADI (contant $T_\gamma$ )

In general, as the strength increases, the fracture toughness of ADI decreases. As the width of the bainitic ferrite and austenite laths increases, the fracture toughness of the intercritically austempered ADI increases to a maximum and then decreases as shown in the Figure 85. Statistically, there is no significant difference in the width of the proeutectoid ferrite and hence definitive conclusion regarding its effect on the fracture toughness cannot be drawn.



(a)

(b)

Figure.85: Influence of the width of (a)BF-bainitic ferrite, RA-films of retained austenite, (b) proeutectoid ferrite on the fracture toughness of intercritical ADI ( $T_\gamma= 1520^\circ\text{F}$ ,  $T_A$  as shown)

### 8.3 Mechanical properties of plastically deformed ADI- single step austempering

In Table 30, the trends observed in the mechanical properties of the plastically deformed samples with respect to austenitizing and austempering temperatures.

Table 30: The Mechanical Properties of the ADI as a Function of austenitization temperature, plastic deformation and Austempering Temperature.

$T_Y$	$T_A$	Yield Strength (MPa)	Ultimate Tensile Strength (MPa)	Hardness
1700°F	725°F	708.6 ± 14	969.6 ± 24	35 ± 3
	680°F	750.4 ± 30	1109.3 ± 67	37 ± 3
	600°F	896.3 ± 6	971.0 ± 18	48 ± 8
	550°F	1158.7 ± 35	1243.9 ± 42	49 ± 5
1520°F	725°F	783.1 ± 29	929.9 ± 18	44 ± 2
	680°F	829.9 ± 18	1062.3 ± 23	47 ± 2
	600°F	1069.6 ± 36	1349.3 ± 28	49 ± 5
	550°F	1164.5 ± 42	1488.0 ± 37	50 ± 3

Plastic deformation was performed at the strain rate of 5mm/min. The samples underwent plastic strain between 3% and 8% at the austenitizing temperature prior to austempering. The lower austempering temperature of 550°F and 600°F promoted the hardness, yield and ultimate tensile strength of the plastically deformed ADI irrespective of the austenitization temperature. The upper austempering temperature of 680°F and 725°F produced coarser and feathery ferrite and more austenite. This structural features are responsible for the lower strength in this ADI samples. It is also interesting to note that the samples austenitized in the upper intercritical

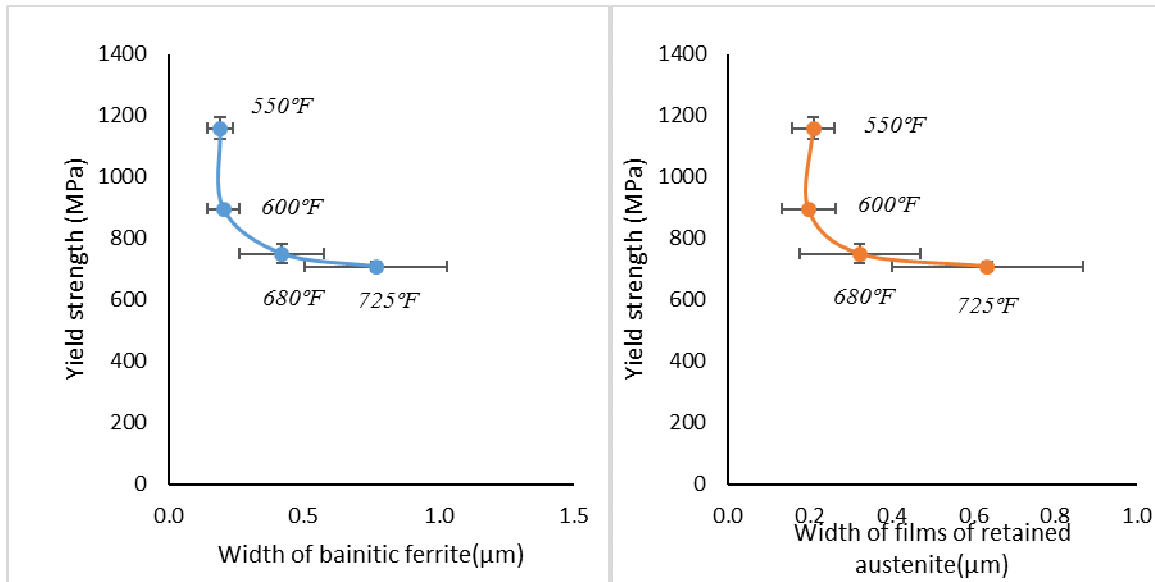
temperature of 1520°F yielded higher hardness, yield strength and ultimate tensile strength than those ADI samples austenitized at conventional austenitizing temperature of 1700°F. This can be attributed to the fact that the ADI austenitized in the upper intercritical austenitization temperature of 1520°F resulted in lesser volume fraction of austenite leading to the higher strength than the ADI austenitized at higher conventional austenitization temperature of 1700°F.

### **8.3.1 Influence of width of different phases on the yield strength of plastically deformed**

#### **ADI- single step austempering**

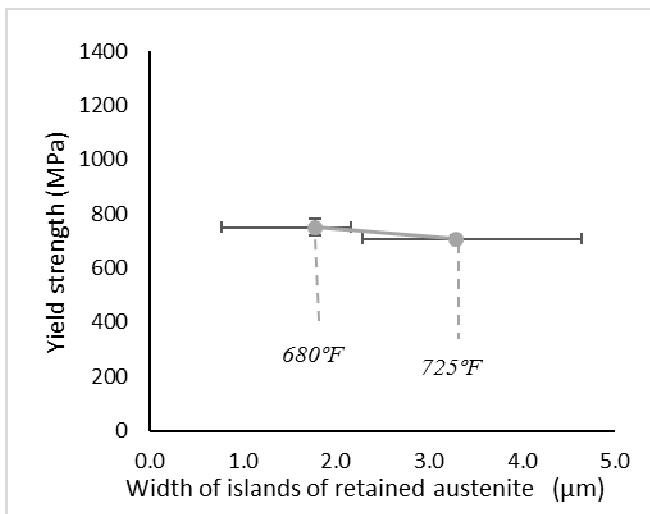
Figure 86 shows the effect of the different phases on the ADI conventionally austenitized at 1700°F, subjected to plastic deformation and single step austempering. The yield strength of the plastically deformed ADI increases with the reduction in the width of bainitic ferrite lath and films of retained austenite as the austempering temperature is decreased from 725°F to 550° F. Highest strength of 1158 MPa was obtained in the ADI austempered at 550°F which had bainitic ferrite width of 0.192  $\mu\text{m}$  and retained austenite width was 0.209  $\mu\text{m}$ . Islands of retained austenite was present in the samples austempered at upper bainitic temperature range of 700°F and 725°F. As mentioned earlier, the presence of islands of retained austenite results in detrimental effects on the mechanical properties of ADI.





(a)

(b)



(c)

Figure.86: Influence of the width of (a)bainitic ferrite, (b) films of retained austenite and (c) islands of retained austenite on the yield strength of plastically deformed ADI, ( $T_{\gamma}=1700^{\circ}\text{F}$ ,

$T_D=1700^{\circ}\text{F}$ ,  $T_A$  as shown)

### 8.3.2 Influence of ferritic cell size and austenite volume fraction on the yield strength of plastically deformed ADI: $T_{\gamma}=1700^{\circ}\text{F}$ and single step austempering

The influence of the of ferritic cell size on the yield strength shown in the Figure 87 (a).

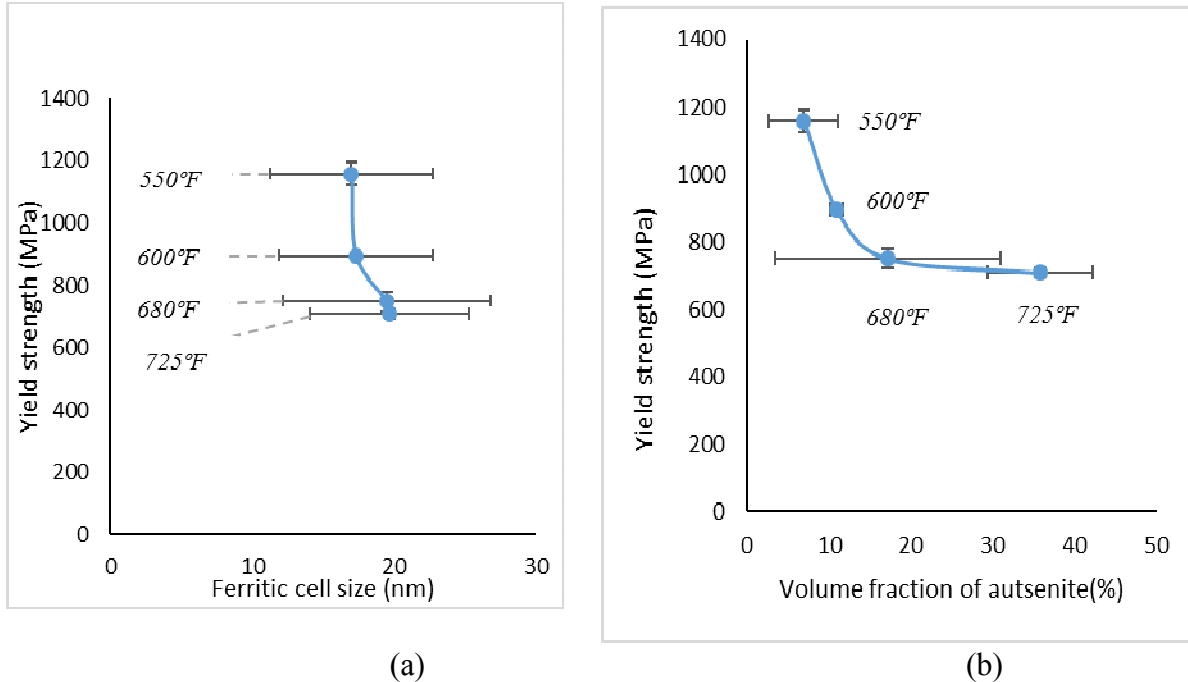


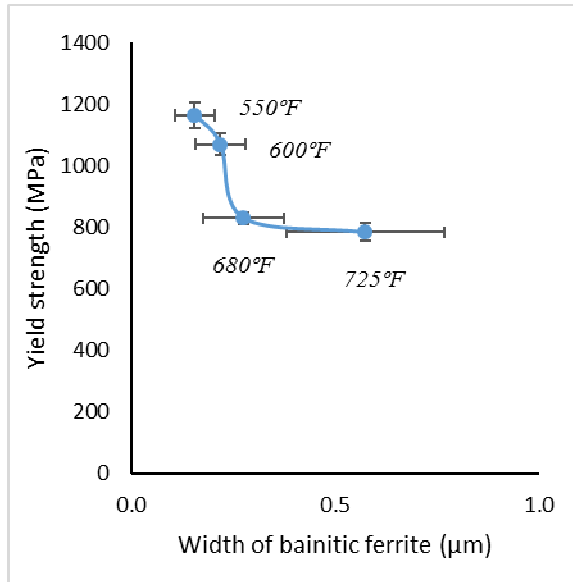
Figure.87: Influence of (a) ferritic cell size, (b) volume fraction of austenite on the yield strength of plastically deformed ADI, ( $T_{\gamma}=1700^{\circ}\text{F}$ ,  $T_D=1700^{\circ}\text{F}$ ,  $T_A$  as shown)

Statistically, there is no significant difference in the ferritic cell size of the plastically deformed ADI with respect to austempering temperatures. However, plastic deformation reduced the ferritic cell size compared to conventional ADI samples. For instance, the ferritic cell size of the plastically deformed ADI is reduced by approximately 24% for the ADI samples austempered at upper bainitic temperature range of 725°F. The average ferritic cell size of the samples slightly decreases as the austempering temperature is decreased from 725°F to 550°F.

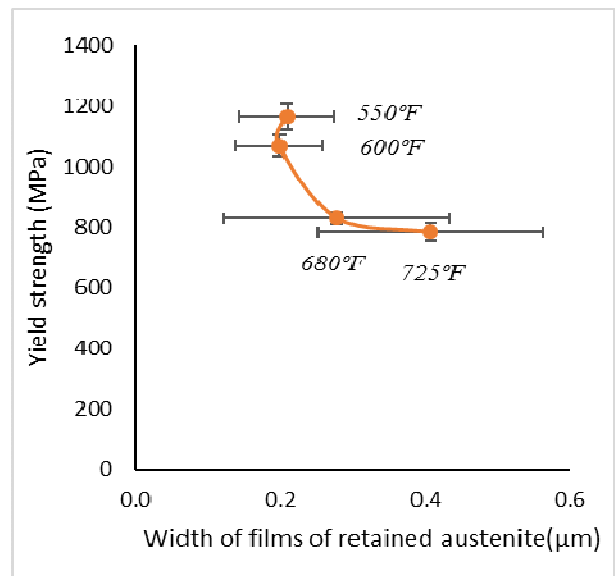
Figure 87 (b) shows the variation of yield strength with respect to the volume fraction of austenite. The volume fraction of austenite decreases as the austempering temperature decreases. Lower volume fraction of austenite promoted higher yield strength in plastically deformed ADI.

### 8.3.3 Influence of width of different phases on the yield strength of plastically deformed

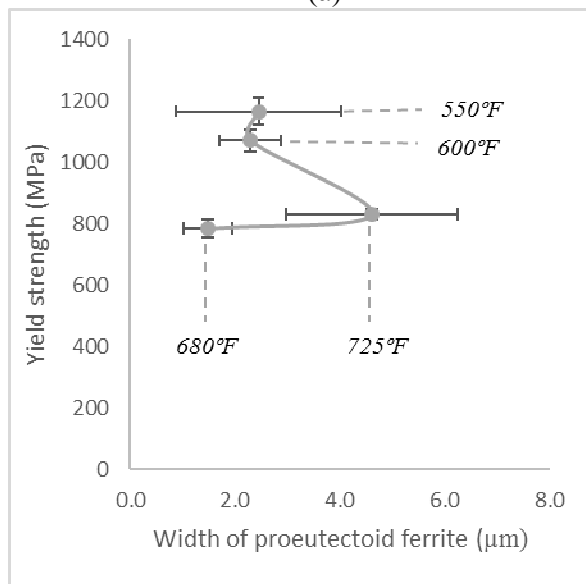
ADI-:  $T_{\gamma}=1520^{\circ}\text{F}$  and single step austempering



(a)



(b)



(c)

Figure.88: Influence of the width of (a)bainitic ferrite, (b) films of retained austenite and (c) islands of retained austenite on the yield strength of plastically deformed ADI, ( $T_{\gamma}=1520^{\circ}\text{F}$ ,

$T_D=1520^{\circ}\text{F}$ ,  $T_A$  as shown)

The effect of the width of different phases on the yield strength of the ADI intercritically austenitized at 1520°F, subjected to plastic deformation and single step austempering is shown in the Figure 88. The intercritically austenitized, plastically deformed ADI followed the same trend as the conventionally austenitized, plastically deformed ADI. The yield strength of the plastically deformed ADI is higher when the width of the bainitic ferrite lath and the width of the films of retained austenite are lower. Statistically, no significant variation in the width of the proeutectoid ferrite is observed with respect to the austempering temperature.

### 8.3.4 Influence of ferritic cell size and austenite volume fraction on the yield strength of plastically deformed ADI:- $T_{\gamma}=1520^{\circ}\text{F}$ and single step austempering

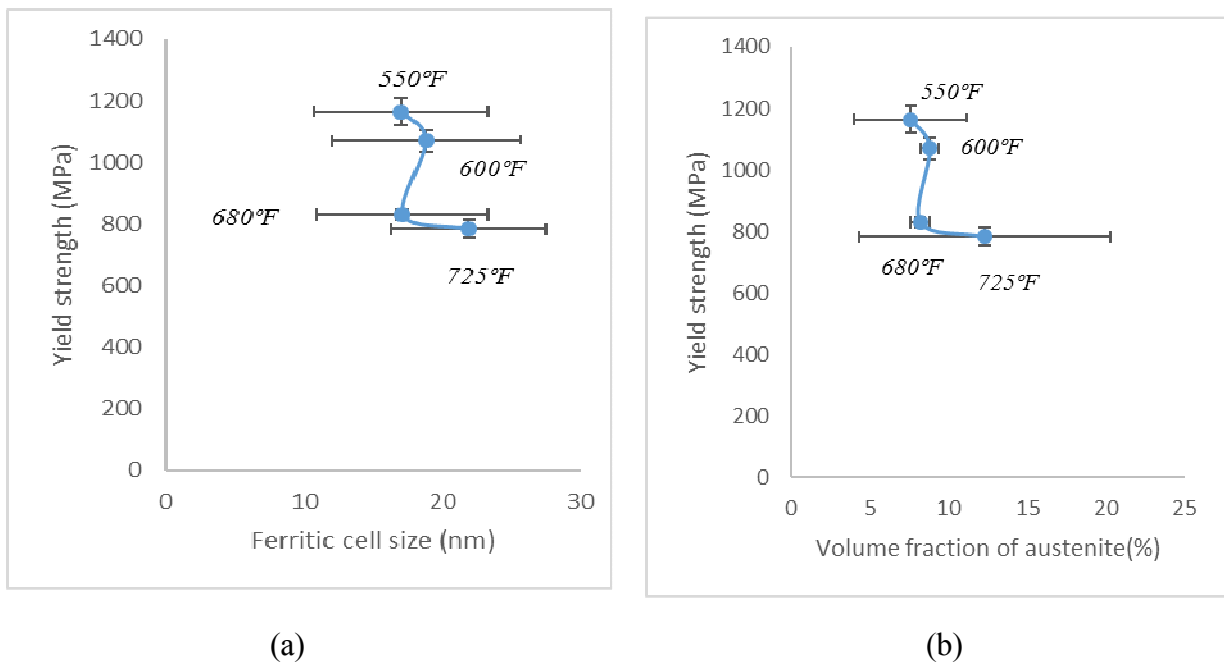


Figure.89: Influence of (a) ferritic cell size, (b) volume fraction of austenite on the yield strength of plastically deformed ADI, ( $T_{\gamma}=1520^{\circ}\text{F}$ ,  $T_{D}=1520^{\circ}\text{F}$ ,  $T_{A}$  as shown)

The ferritic cell size of the intercritical austenitized plastically deformed ADI as shown in the Figure 89(a) is slightly higher than the conventional austenitized, plastically deformed ADI.

As shown in the Figure 89 (b), lower volume fraction of austenite resulted in higher yield strength of the plastically deformed ADI.

#### **8.4 Mechanical properties of plastically deformed ADI- two-step austempering**

Mechanical properties of the ADI that underwent plastic deformation and two step austempering is reported in Table 31. Given that only one sample per condition was tested, definitive conclusions cannot be drawn; however, the results allow for an examination of trends in the ADI mechanical properties. Plastic deformation of the samples were performed at the rate of 5mm/min. Each sample underwent a maximum plastic strain up to 5.5% beyond its yield strength.

The yield strength and ultimate tensile strength of the samples austenitized at 1520°F had higher strength when compared to those austenitized at 1700°F. At lower austenitization temperature of 1472°F and 1418°F, the yield strength and tensile strength remain significantly low. This is due to the differences in the microstructures and volume fraction of phases obtained in these samples. At higher austenitization temperature, the microstructure is composed of mostly ausferritic structure in the matrix yielding higher strength. As the austenitization temperature is lowered, the presence of more proeutectoid ferrite in the matrix reduces the strength of the ADI. Moreover, there is also a variation in the strength with respect to the austempering temperature of the ADI. Higher austempering temperatures of 725°F and 680°F produced coarser ausferrite resulting in slightly lower strength than those fine ausferritic structures produced at lower austempering temperatures. This trend is not observed in the samples austenitized at lower austenitizing temperature of 1436°F indicating the requirement of statistical analysis.

Table 31: The Mechanical Properties of the ADI as a Function of austenitization temperature, plastic deformation and two- step austempering.

$T_{\gamma}$	$T_{A1}$	$T_{A2}$	Yield Strength (MPa)	Ultimate Tensile Strength (MPa)	Hardness (HRC)
1700°F	500°F	725°F	953	1065	34±2
	500°F	680°F	963	1093	37 ±2
	500°F	600°F	1199	1334	41 ± 2
	500°F	550°F	1208	1304	42 ± 2
1520°F	500°F	725°F	986	1097	36 ± 4
	500°F	680°F	1155	1227	33 ±7
	500°F	600°F	1168	1214	37± 5
	500°F	550°F	1313	1469	40±2
1472°F	500°F	725°F	453	622	19±1
	500°F	680°F	453	657	21±2
	500°F	600°F	600	685	20±1
	500°F	550°F	654	862	31±3
1436°F	500°F	725°F	343	523	16±3
	500°F	680°F	343	500	10±2
	500°F	600°F	366	644	15±2
	500°F	550°F	401	622	18±1

### 8.4.1 Influence of width of bainitic ferrite on the yield strength of plastically deformed ADI:- two step austempering

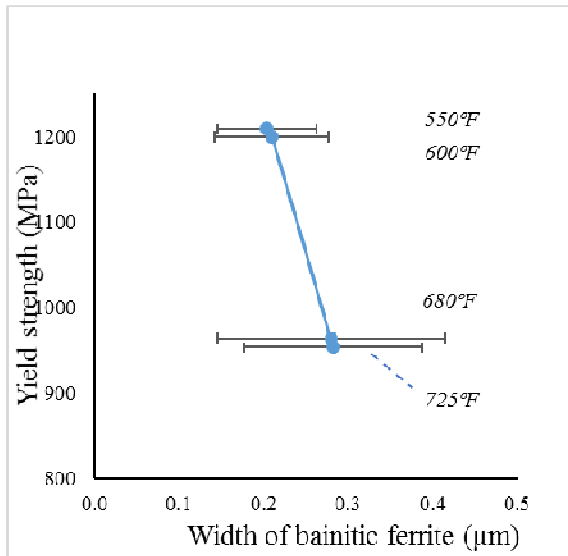
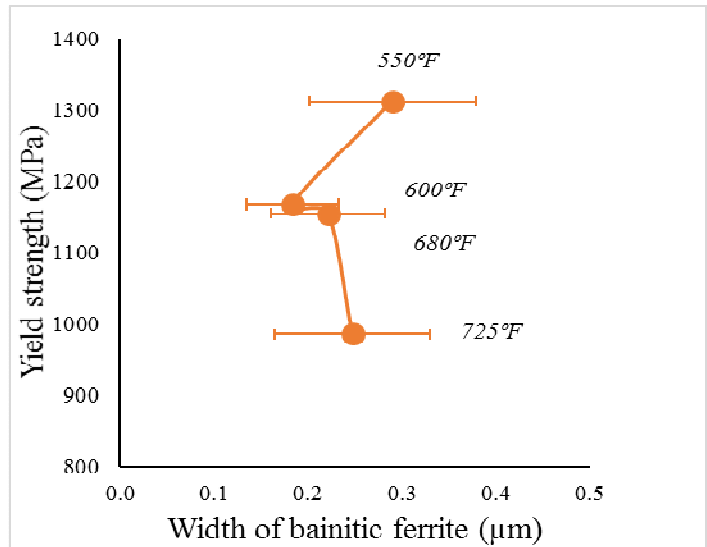
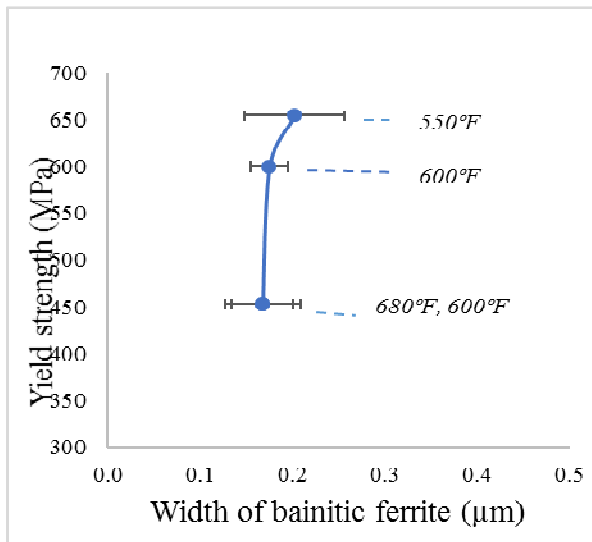
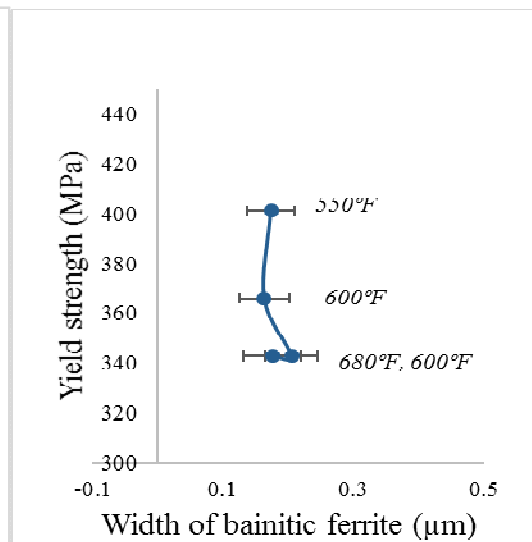
(a)  $T_{\gamma}=1700^{\circ}\text{F}$ ,  $T_{A1}=500^{\circ}\text{F}$ ,  $T_{A2}$  as shown(b)  $T_{\gamma}=1520^{\circ}\text{F}$ ,  $T_{A1}=500^{\circ}\text{F}$ ,  $T_{A2}$  as shown(c)  $T_{\gamma}=1472^{\circ}\text{F}$ ,  $T_{A1}=500^{\circ}\text{F}$ ,  $T_{A2}$  as shown(d)  $T_{\gamma}=1436^{\circ}\text{F}$ ,  $T_{A1}=500^{\circ}\text{F}$ ,  $T_{A2}$  as shown

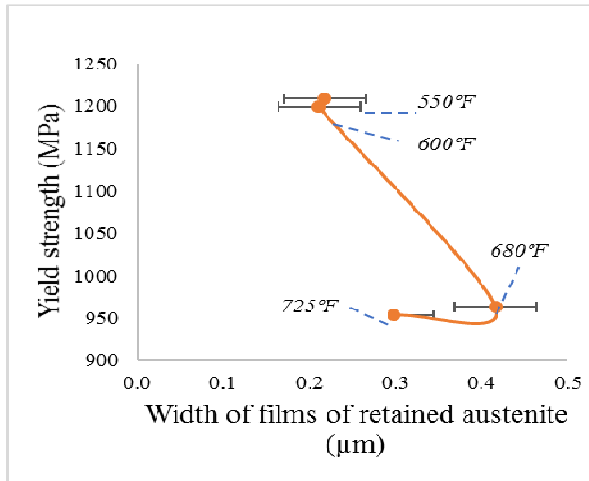
Figure.90: Comparison of the effect of width of the bainitic ferrite on the yield strength of the plastically deformed, two-step austempered ADI with respect to the austenitization temperature.

Figure 90 compares the effect width of the bainitic ferrite on the yield strength in the plastically deformed, two-step austempered ADI, austenitized at different austenitizing

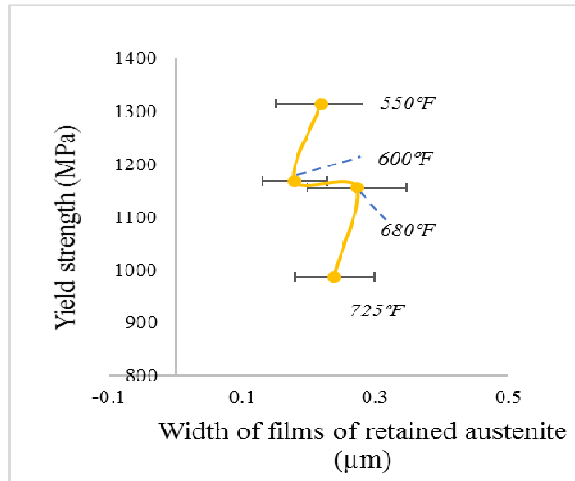
temperatures. The width of the bainitic ferrite lath slightly decrease as the austenitizing temperature decreases from 1700°F to 1436°F.

**8.4.2 Influence of width of retained austenite on the yield strength of plastically deformed**

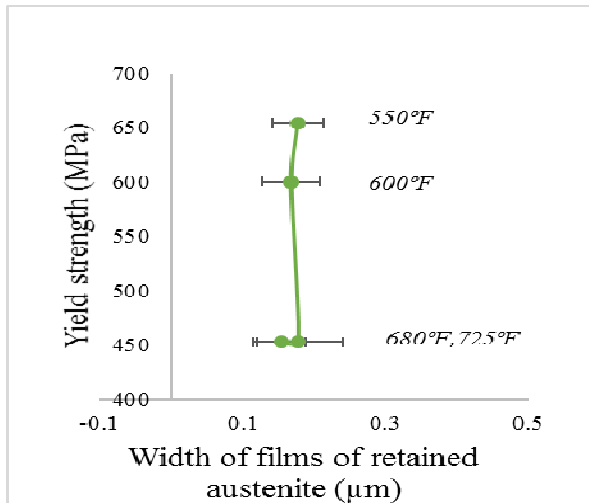
**ADI:- two step austempering**



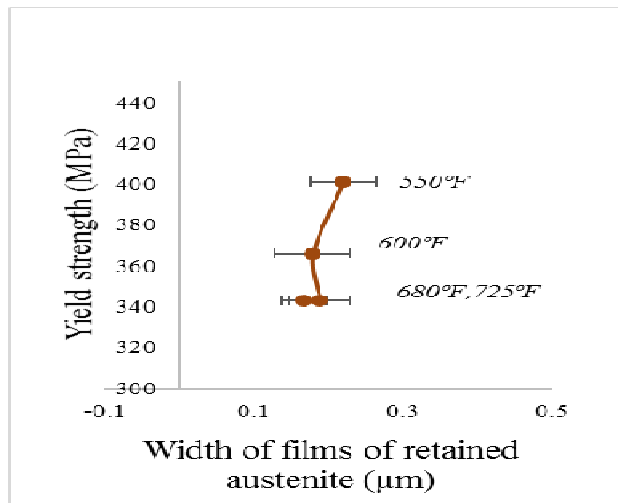
(a)  $T_{\gamma}=1700^{\circ}\text{F}$ ,  $T_{A1}=500^{\circ}\text{F}$ ,  $T_{A2}$  as shown



(b)  $T_{\gamma}=1520^{\circ}\text{F}$ ,  $T_{A1}=500^{\circ}\text{F}$ ,  $T_{A2}$  as shown



(c)  $T_{\gamma}=1472^{\circ}\text{F}$ ,  $T_{A1}=500^{\circ}\text{F}$ ,  $T_{A2}$  as shown



(d)  $T_{\gamma}=1436^{\circ}\text{F}$ ,  $T_{A1}=500^{\circ}\text{F}$ ,  $T_{A2}$  as shown

Figure 91: Comparison of the effect of width of films of retained austenite on the yield strength of the plastically deformed, two-step austempered ADI with respect to  $T_{\gamma}$



Figure 91 compares the width of the films of retained austenite to the yield strength of the plastically deformed, two-step austempered ADI samples. Higher yield strength is obtained in the samples austenitized at 1520°F with plastic deformation and two-step austempering. The samples austenitized in the lower intercritical austenitizing temperature region of 1472°F and 1436°F had lower retained austenite lath size.

### 8.4.3 Influence of width of proeutectoid ferrite on the yield strength of plastically deformed ADI-: two step austempering

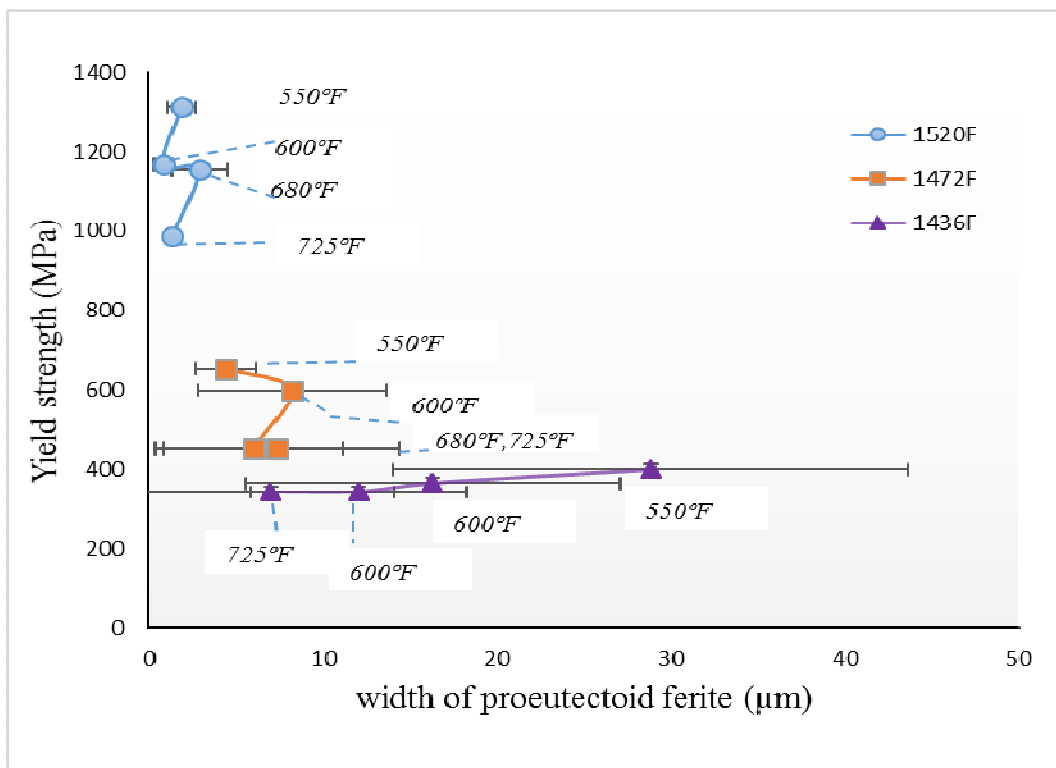


Figure.92: Comparison of the effect of width of the proeutectoid ferrite on the yield strength of the plastically deformed, two-step austempered ADI with respect to the austenitization temperature.

The larger width of the proeutectoid ferrite at the lower intercritical austenitizing temperature of 1472°F and 1436°F as shown in the Figure 92 was detrimental to the mechanical properties of the ADI.

#### 8.4.4 Influence of ferritic cell size on the yield strength of plastically deformed ADI:- two step austempering

Figure 93 compares the effect of ferritic cell size on the yield strength of the plastically deformed, two-step austempered ADI with respect to the austenitization temperature.

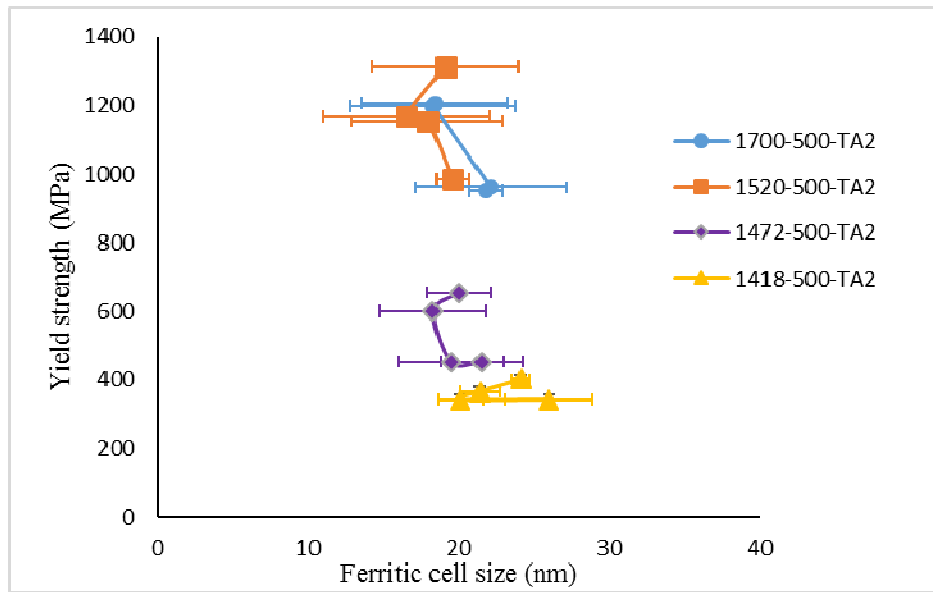
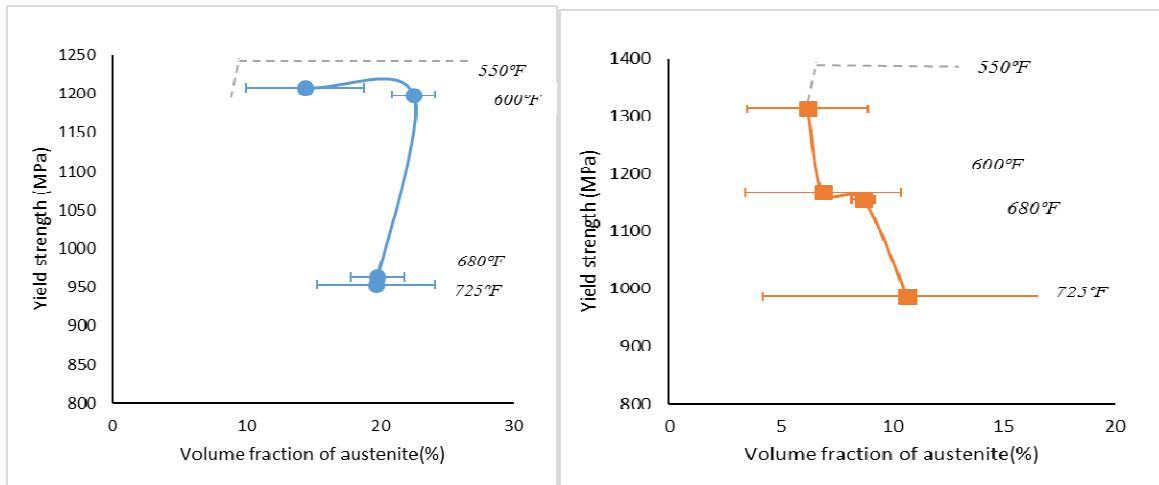


Figure.93: Comparison of the ferritic cell size to the yield strength of plastically deformed, two-step austempered ADI with respect to the austenitization temperature

The ferritic cell size of the ADI austenitized at intercritical austenitization of 1520°F had finer ferritic cell size than the ADI austenitized at 1700°F. At lower austenitization temperature of 1436°F, the ferrite cell size of the ADI increased. Combined effect of the width of the bainitic ferrite lath, retained austenite lath, width of proeutectoid ferrite, volume fraction of austenite and the ferritic cell size determines the mechanical properties of the ADI.

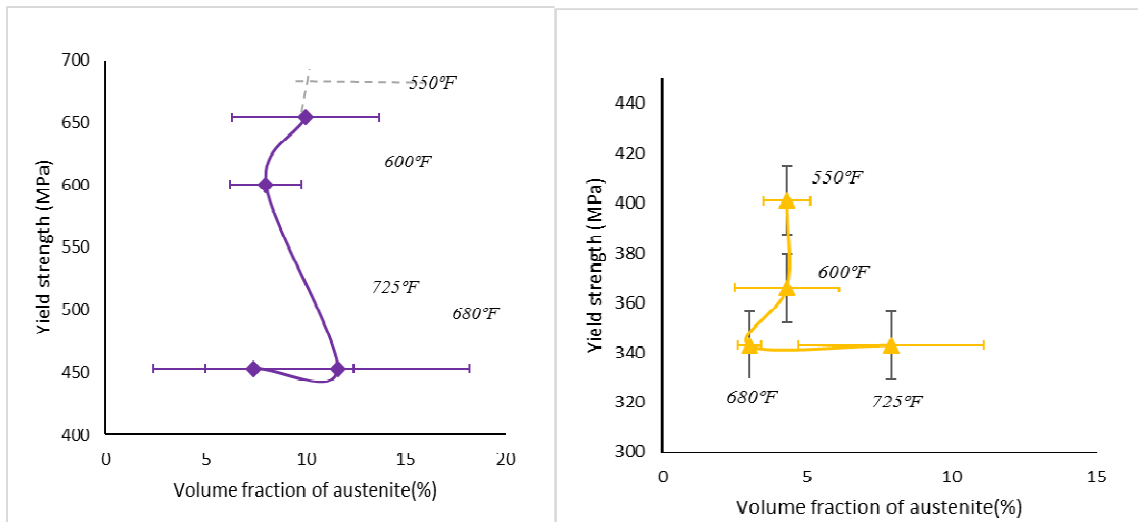
### 8.4.5 Influence of austenite volume fraction on the yield strength of plastically deformed

#### ADI: two step austempering



(a)  $T_{\gamma}=1700^{\circ}\text{F}$ ,  $T_{A1}=500^{\circ}\text{F}$ ,  $T_{A2}$  as shown

(a)  $T_{\gamma}=1500^{\circ}\text{F}$ ,  $T_{A1}=500^{\circ}\text{F}$ ,  $T_{A2}$  as shown



(c)  $T_{\gamma}=1472^{\circ}\text{F}$ ,  $T_{A1}=500^{\circ}\text{F}$ ,  $T_{A2}$  as shown

(d)  $T_{\gamma}=1436^{\circ}\text{F}$ ,  $T_{A1}=500^{\circ}\text{F}$ ,  $T_{A2}$  as shown

Figure.94: Comparison of the volume fraction of austenite to the yield strength of plastically deformed, two-step austempered ADI with respect to the austenitization temperature.

Figure 94 compares the volume fraction of the retained austenite to the yield strength of the plastically deformed, two-step austempered ADI with respect to the austenitization temperature. Lower volume fraction of austenite resulted in higher yield strength in the ADI

irrespective of the austenitization temperature. The volume fraction of the austenite decreased as the austenitization temperature is decreased from 1700 °F to 1436°F.

### 8.5 Comparison of yield strength with respect to the heat treatment

Figure 95 compares the yield strength of the conventional, cryogenically treated, intercritically austempered as well as the plastically deformed ADI with respect to austempering temperature.

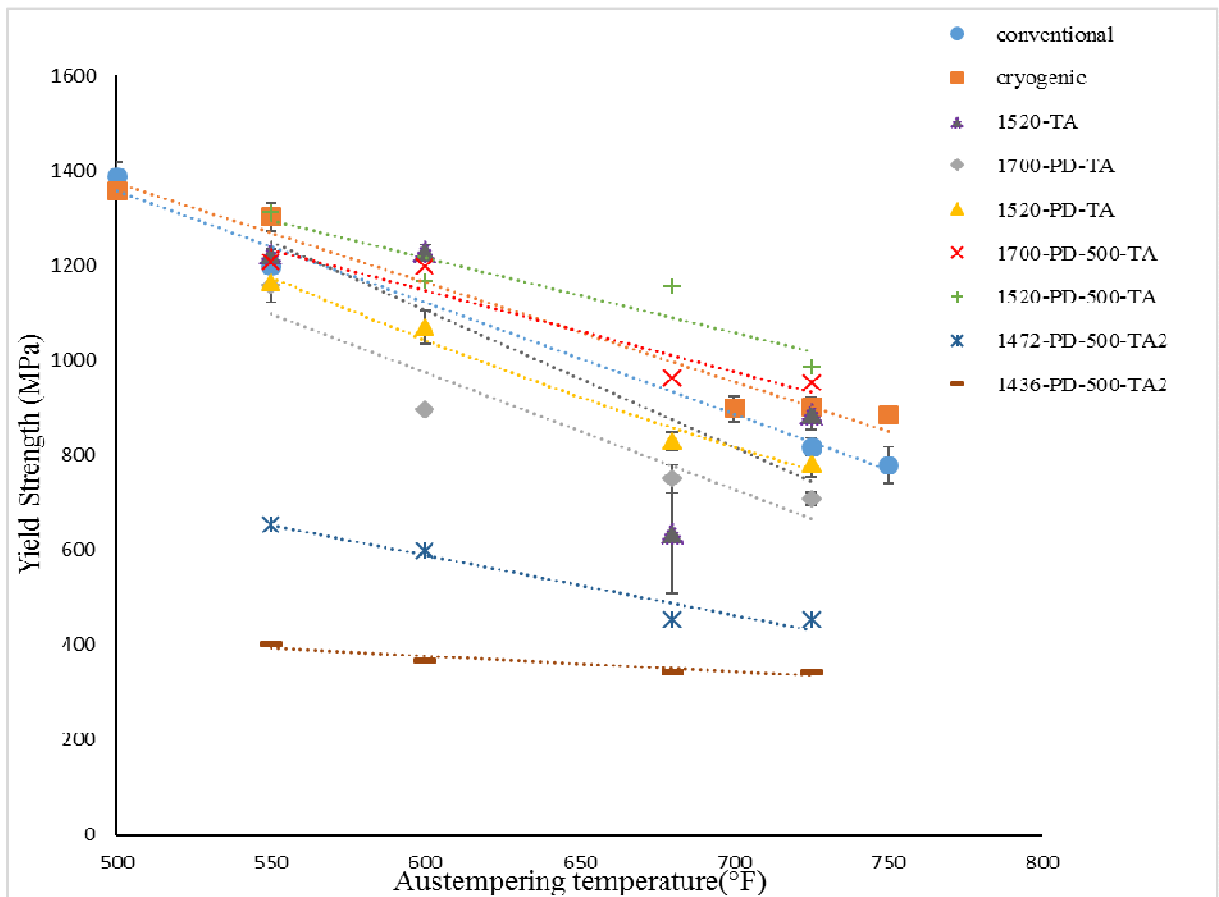


Figure.95: Comparison of yield strength of ADI with respect to the heat treatment

From the graph, it is evident that the yield strength of the ADI is significantly higher when austempered in the lower bainitic temperature ranges. In general, as the austempering temperature increases, strength decreases. Cryogenic treatment resulted in significant improvement in the

yield strength of the ADI. Intercritical austenitizing at 1520°F followed by plastic deformation and austempering had higher yield strength than the ADI intercritically austenitized at 1700°F followed by plastic deformation and austempering. However, the yield strength of either of the ADI is not significantly higher than the conventional ADI. Plastic deformation followed by two step austempering in the ADI austenitized at the conventional austenitizing temperature of 1700°F as well as in the upper intercritical temperature of 1520°F enhanced the yield strength slightly higher than the conventional ADI. Even though the samples austenitized at lower intercritical temperature of 1472°F and 1436°F subjected to plastic deformation and two-step austempering had finer lath size of bainitic ferrite and austenite, the presence of higher volume fraction of proeutectoid ferrite deteriorated its yield strength.

#### **8.6 Comparison of ultimate tensile strength with respect to the heat treatment**

Figure 96 compares the ultimate tensile strength of the conventional austempered, cryogenically treated, intercritically austempered as well as the plastically deformed ADI with respect to the austempering temperature. Cryogenic treatment of the ADI resulted in improvement in the ultimate tensile strength for all the austempering temperatures. This change in strength can be attributed to the transformation of austenite to martensite during cryogenic treatment. The ultimate tensile strength of the intercritically austempered ADI is lower at 680°F corresponding to the higher volume fraction and width of proeutectoid ferrite. Austenitizing at either 1700°F or 1520°F followed by plastic deformation and austempering did not contribute to the increase in the strength of ADI at upper bainitic temperature ranges. Austenitizing at either 1700°F or 1520°F followed by plastic deformation and two-step austempering slightly improve the ultimate tensile strength of the ADI. The influence of higher volume fraction of proeutectoid ferrite deteriorated the strength of ADI austenitized in the lower intercritical temperatures of 1472°F and 1436°F

regardless of the finer lath sizes of bainitic ferrite and austenite in these plastically deformed, two-step austempered samples.

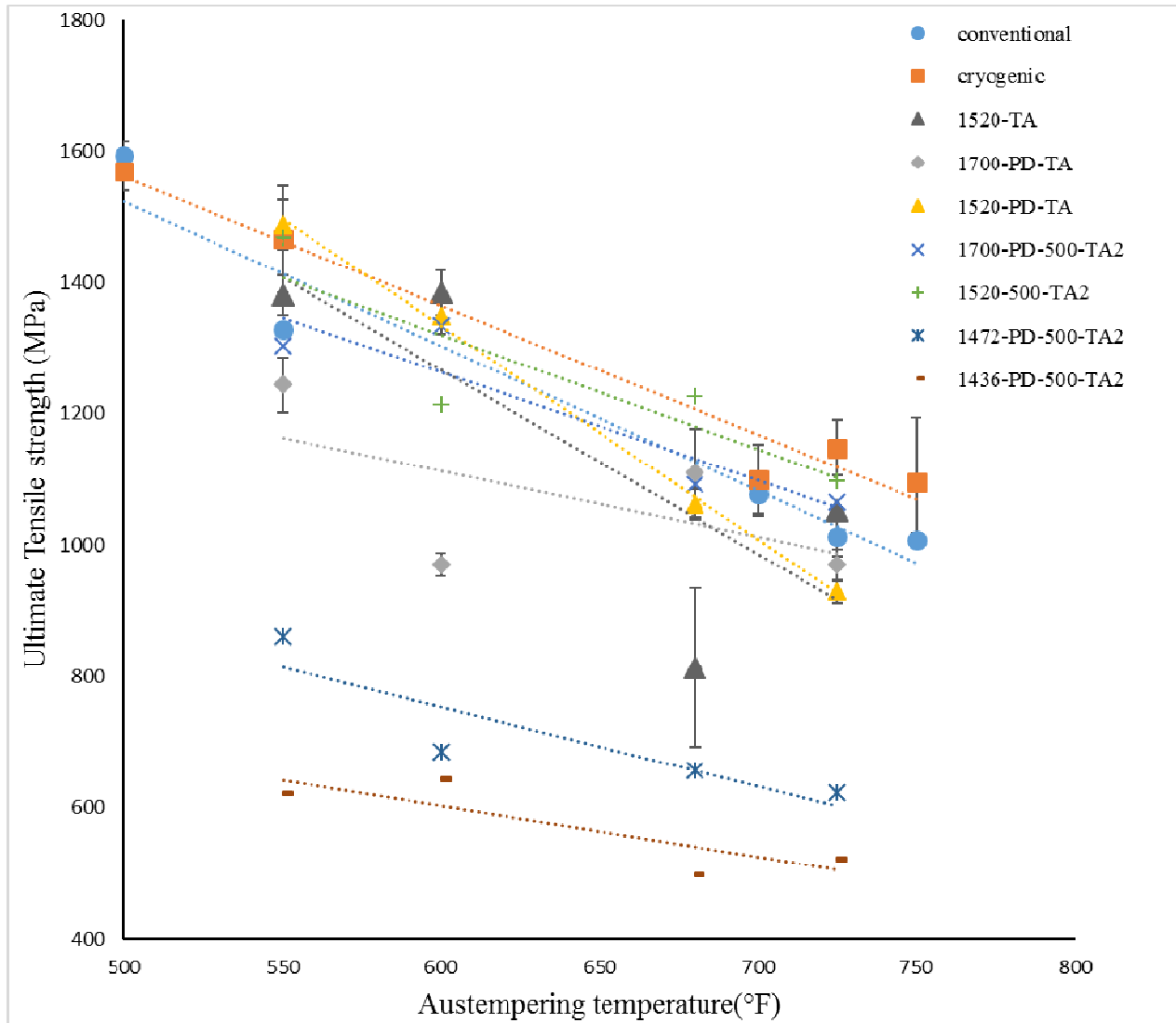


Figure.96: Comparison of ultimate tensile strength of ADI with respect to the heat treatment

## CHAPTER 9. OBSERVATIONS

- Conventional austempering produced austferritic microstructure consisting of bainitic ferrite and high carbon austenite. Feathery ausferritic structure observed in the upper bainitic austempering temperature resulted in decrease of the strengths of ADI.
- Cryogenic treatment has been observed to improve the tensile strength and hardness of the prior austempered ductile iron samples, the elongation was observed to decrease, and fracture toughness was unaffected. Cryogenic treatment can be used to create ADI with improved strength properties without compromising the fracture resistance of the material.
- The intercritical austempering of ductile cast iron produced a unique microstructure consisting of pro-eutectoid ferrite, bainitic ferrite and high carbon austenite in ADI. The small amount of proeutectoid ferrite present in the microstructure is beneficial to improve the ductility of the ADI.
- The mechanical properties including the yield strength, ultimate tensile strength of ADI gradually reduced with the decrease in austenitizing temperature due to an increase in proeutectoid ferrite content.
- A progressive increase in the ductility (% elongation) of the ADI samples was observed with the decrease in austenitizing temperature due to the larger volume fraction of pro-eutectoid ferrite in the microstructure of ADI austenitized at lower intercritical temperatures.
- Fracture toughness of the intercritically austenitized ADI was observed to decrease with the decrease in austenitization temperature. This can also be attributed to the presence of increasing amount of proeutectoid (polygonal) ferrite in the matrix microstructure.
- Intercritical austempering close to the upper critical temperature (1520°F) resulted in improved mechanical properties (high yield strength, high ultimate tensile strength and ductility) with good

fracture toughness. Thus, austenitizing in the upper intercritical temperature of ADI resulted in the optimum combination of strength of toughness of ADI.

- Intercritical austenitizing well below upper critical did not result in exceptional properties. The reason for this appears to be the coarse grained proeutectoid ferrite in the matrix microstructure of the intercritically austempered ductile iron.
- The austempering at lower temperature (550°F) appear to produce lower bainite combined with low retained austenite content. It appears that low carbon austenite produced by austenitizing near the upper critical temperature produced fine ferrite cell size.
- The presence of large volume fraction of islands of retained austenite has been observed to cause detrimental effects to the mechanical properties of the ADI.
- The austenite formed at the lower austempering temperatures of 500°F and 550°F was thermally unstable in ADI and transformed into martensitic under cryogenic treatment.
- The austenite formed at upper austempering temperatures between 700 - 750°C had more thermal stability and was only partially transformed into martensite under cryogenic treatment.
- Strain-induced transformation of austenite to martensite was observed in samples both with and without cryogenic treatment. The amount of transformation depended upon the austempering temperature.
- Stress-induced transformation of austenite to martensite also occurred in samples with and without cryogenic treatment. Again, the degree of transformation depended upon the temperature at which austempering was performed.
- Thus, it appears that adding suitable alloying elements can improve the thermal and mechanical stability of austenite by promoting more carbon partitioning into austenite.



- The width of the bainitic ferrite generally decreased with the decrease in austempering temperature. High temperature plastic deformation greatly reduced the width of bainitic ferrite in the ADI samples austempered in the upper bainitic temperatures.
- High temperature plastic deformation and austempering in the lower bainitic temperature range resulted in ultra fine or nano sized laths of bainitic ferrite and retained austenite in ADI.
- High temperature plastic deformation resulted in finer ferritic cell sizes in the nanometer scale in the ADI samples.
- Plastic deformation resulted in the grain refinement in the nanoscale range which is evident from the ring SAED pattern obtained from the plastically deformed ADI samples.

## CHAPTER 10. CONCLUSIONS

- A unique heat treatment process consisting of austenitization and plastic deformation followed by austempering has been proposed and its microstructure and mechanical properties were analyzed.
- High temperature plastic deformation and austempering in the lower bainitic temperature range resulted in ultra fine laths of bainitic ferrite and retained austenite in ADI.
- It was confirmed that the plastic deformation resulted in the grain refinement from the observation of the ring shaped SAED pattern.
- The ADI processed by austenitizing at 1520°F followed by plastic deformation at a strain rate  $\leq 10$  mm/min and given an austempering treatment of either a single step/two-step resulted in an optimum combination of strength and toughness.
- The selection of appropriate heat treatment parameters including the austenitization temperature, austempering temperature and time, for the given chemical composition of the ductile cast iron, enables the production of nanostructured ductile cast iron with excellent mechanical properties and improved ductility than conventional ADI.
- The proposed unique heat treatment process involving a combination of high temperature plastic deformation and subsequent austempering has resulted in a robust process window that makes nano ADI with better mechanical properties, practically possible from production standpoint.

## **CHAPTER 11. FUTURE WORK**

Further research can be carried out on this low alloyed ductile cast iron to determine the vital material properties such as the fatigue strength, wear resistance, bending strength, and machinability. In this study, austenitizing and austempering time of 3 hours each is used for all the plastically deformed samples, which may not be an attractive feature from industrial point of view. Therefore, research can be carried out to optimize the heat treatment parameters including the austenitizing and austempering temperature and time. The research can also be extended to study the effect of variation in the strain% on the microstructure and mechanical properties of the unalloyed ductile iron used in this study.

## APPENDIX -MICROSTRUCTURES OF ADI

### Microstructures of conventionally austempered ductile cast iron samples

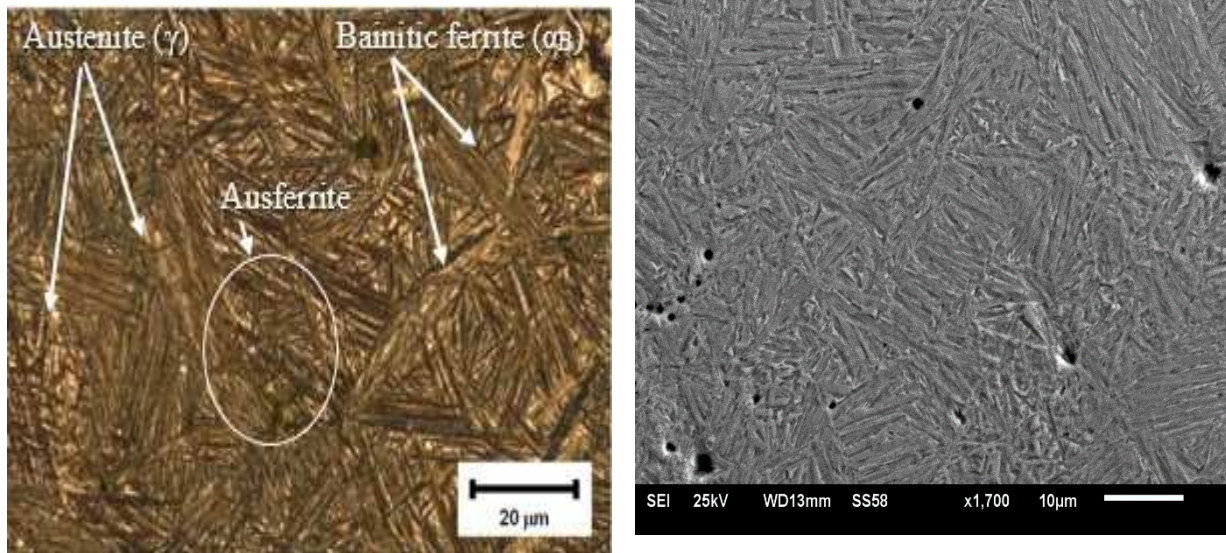


Figure.A.1: Optical and SEM micrograph of ADI,  $T_\gamma=1700^\circ\text{F}$ ,  $T_A=550^\circ\text{F}$

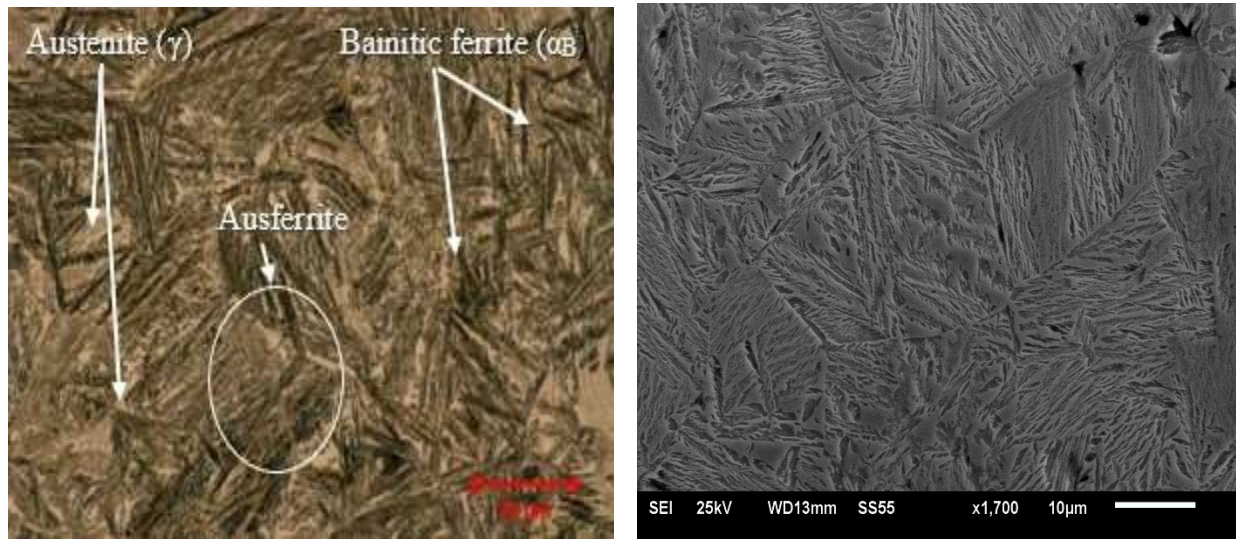


Figure.A.2: Optical and SEM micrograph of ADI,  $T_\gamma=1700^\circ\text{F}$ ,  $T_A=700^\circ\text{F}$

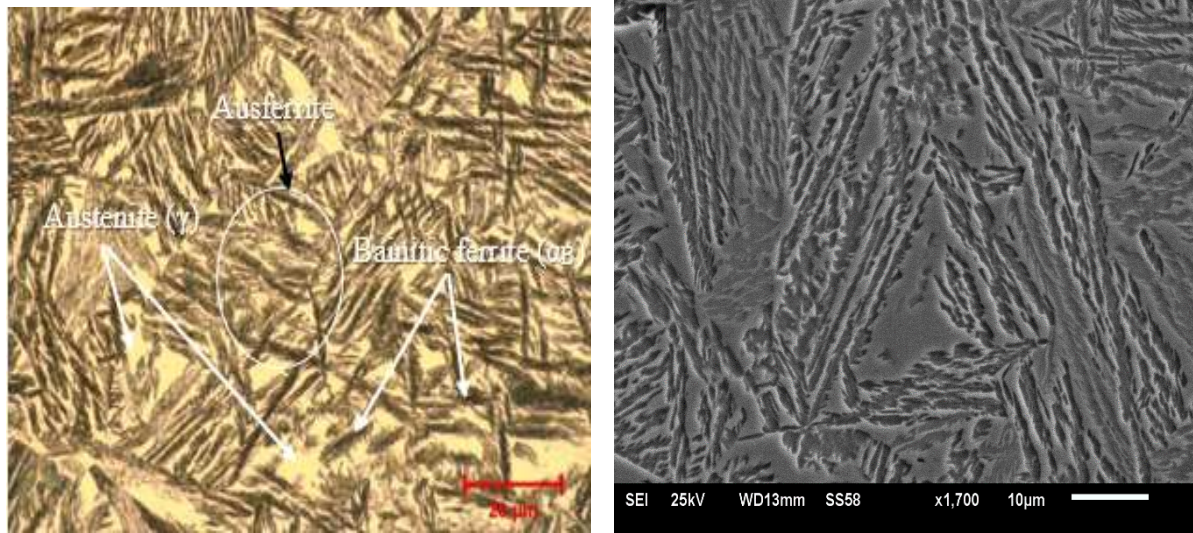


Figure.A.3: Optical and SEM micrograph of ADI,  $T_{\gamma}=1700^{\circ}\text{F}$ ,  $T_A=750^{\circ}\text{F}$

#### Microstructures of cryogenically treated ADI

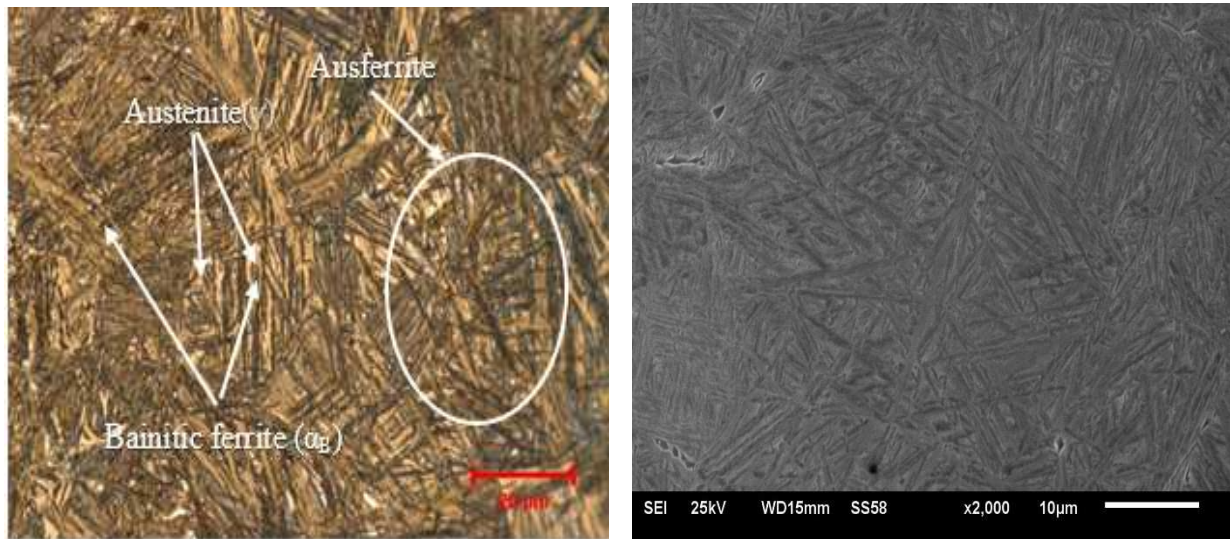


Figure.A.4: Optical and SEM micrograph of cryogenically treated ADI,  $T_{\gamma}=1700^{\circ}\text{F}$ ,  $T_A=550^{\circ}\text{F}$

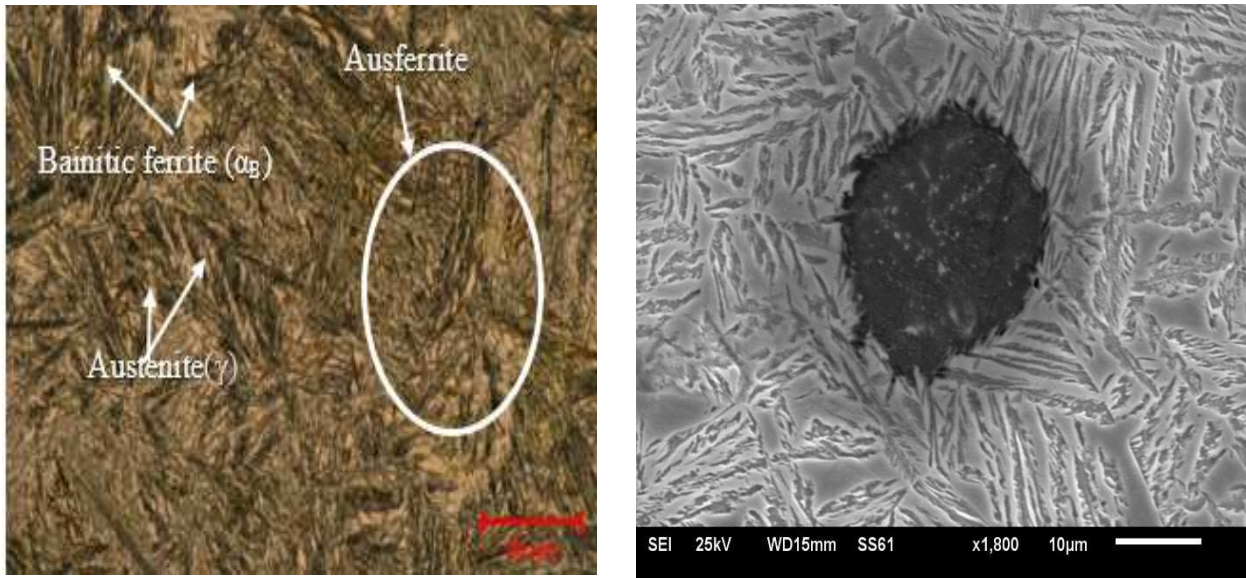


Figure.A.5: Optical and SEM micrograph of cryogenically treated ADI,  $T_\gamma=1700^\circ\text{F}$ ,  $T_A=700^\circ\text{F}$

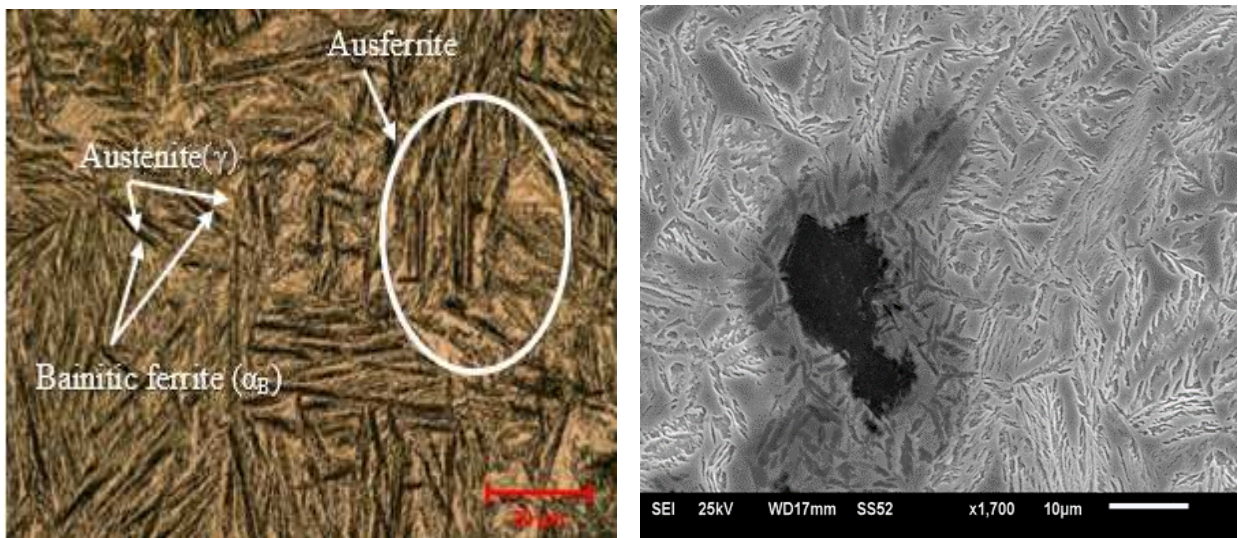


Figure.A.6: Optical and SEM micrograph of cryogenically treated ADI,  $T_\gamma=1700^\circ\text{F}$ ,  $T_A=750^\circ\text{F}$

### Microstructures of intercritically austempered ADI samples( $T_{\gamma}=1700^{\circ}\text{F}$ )

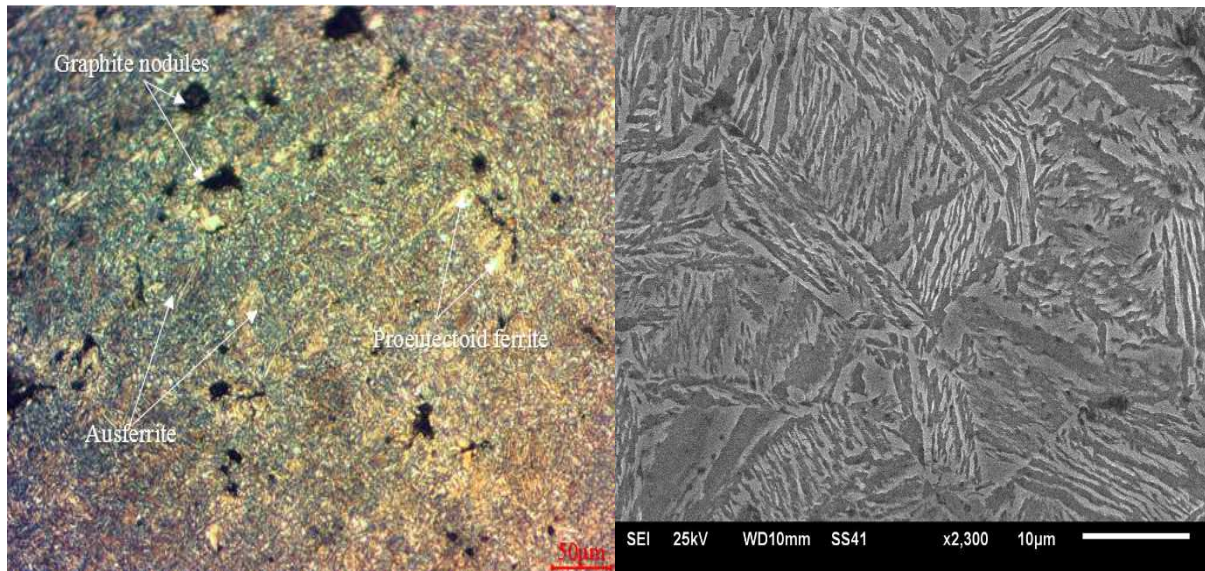


Figure.A.7: Optical and SEM micrograph of intercritically austempered ductile cast iron,

$T_{\gamma}=1520^{\circ}\text{F}$ ,  $T_A=680^{\circ}\text{F}$

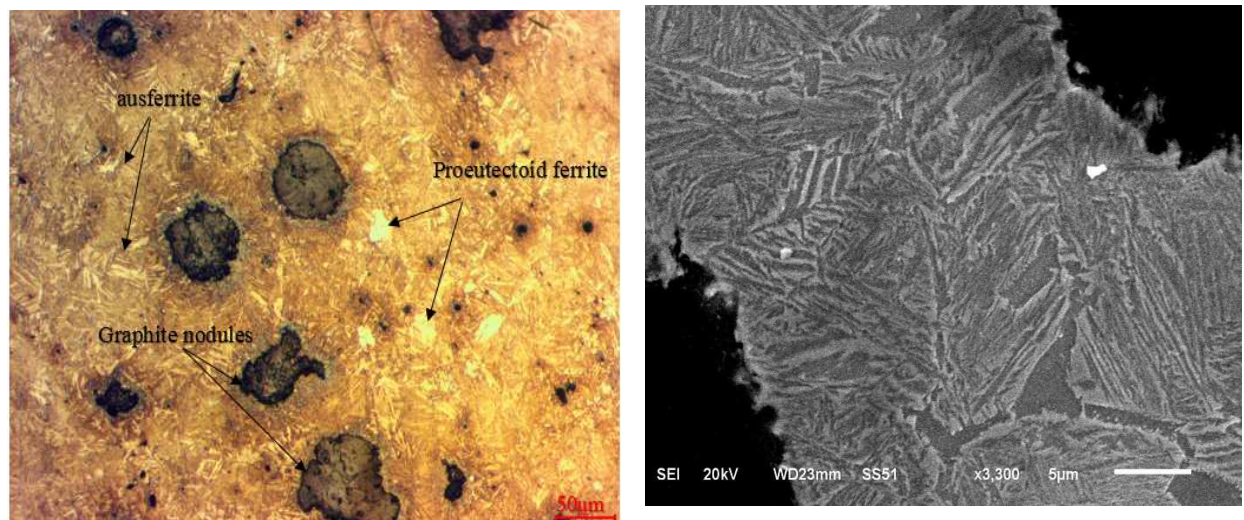


Figure.A.8: Optical and SEM micrograph of intercritically austempered ductile cast iron,

$T_{\gamma}=1520^{\circ}\text{F}$ ,  $T_A=600^{\circ}\text{F}$

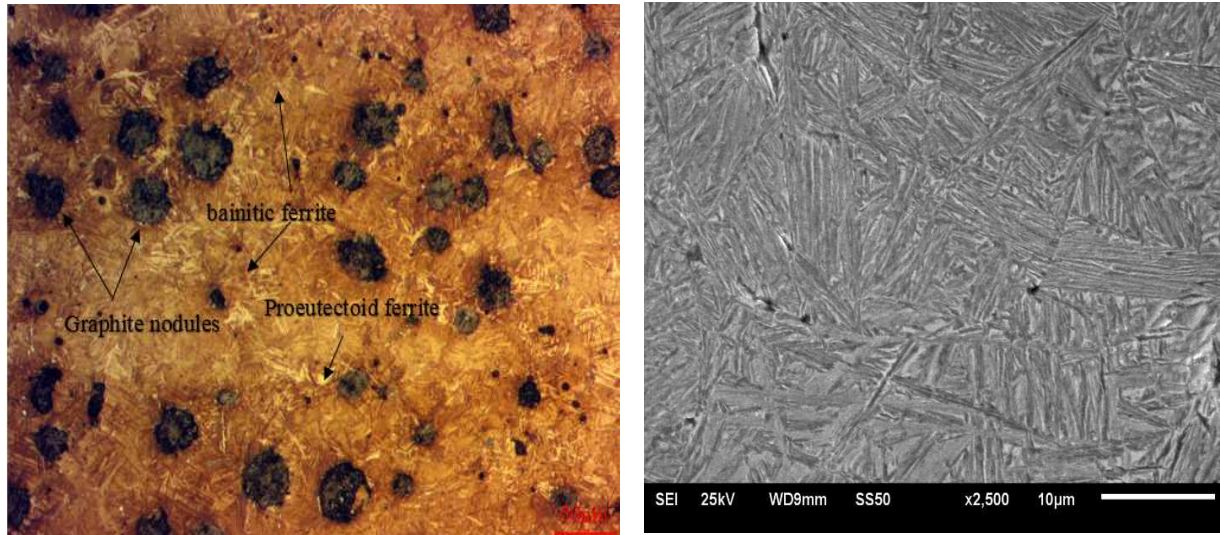


Figure.A.9: Optical and SEM micrograph of intercritically austempered ductile cast iron,

$T_{\gamma}=1520^{\circ}\text{F}$ ,  $T_{\text{A}}=550^{\circ}\text{F}$

#### Microstructure of plastically deformed, conventionally austempered ductile cast iron

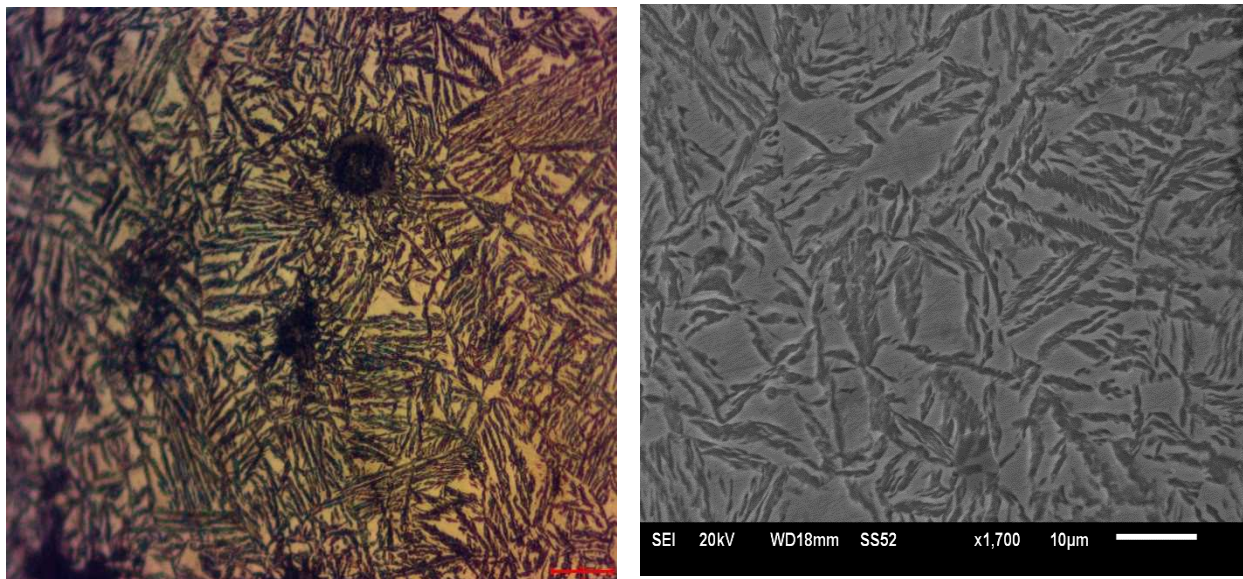


Figure.A.10: Optical and SEM micrograph of plastically deformed ADI,  $T_{\gamma}=1700^{\circ}\text{F}$ ,  $T_{\text{D}}=1700^{\circ}\text{F}$ ,

$T_{\text{A}}=680^{\circ}\text{F}$



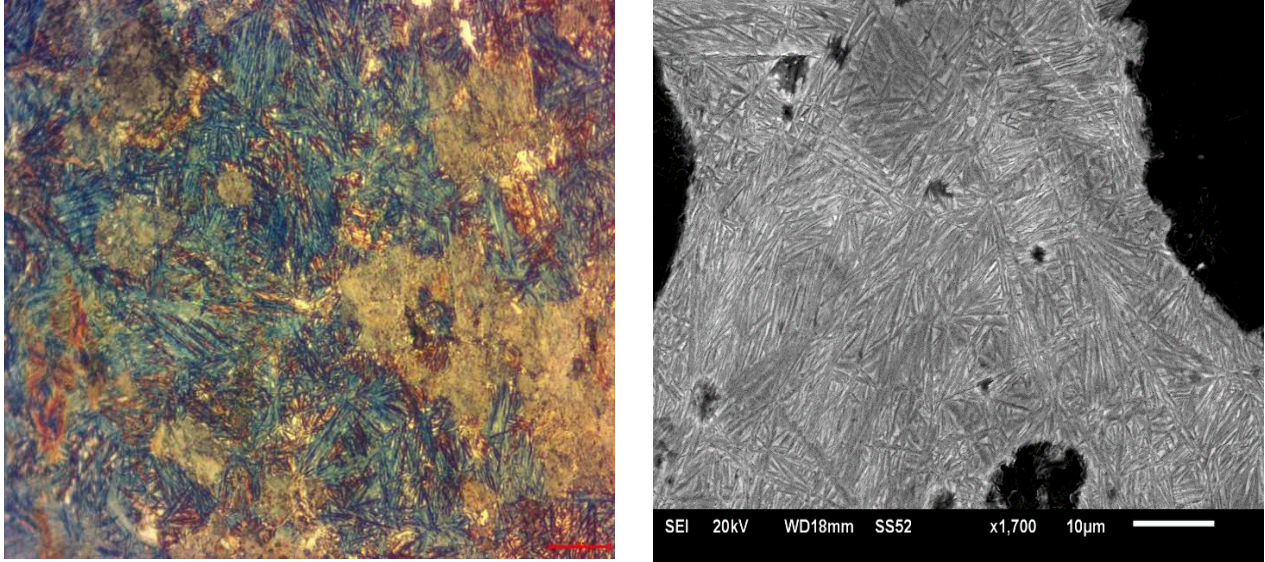


Figure.A.11: Optical and SEM micrograph of plastically deformed ADI,  $T_{\gamma}=1700^{\circ}\text{F}$ ,  $T_{\text{D}}=1700^{\circ}\text{F}$ ,  
 $T_{\text{A}}=600^{\circ}\text{F}$

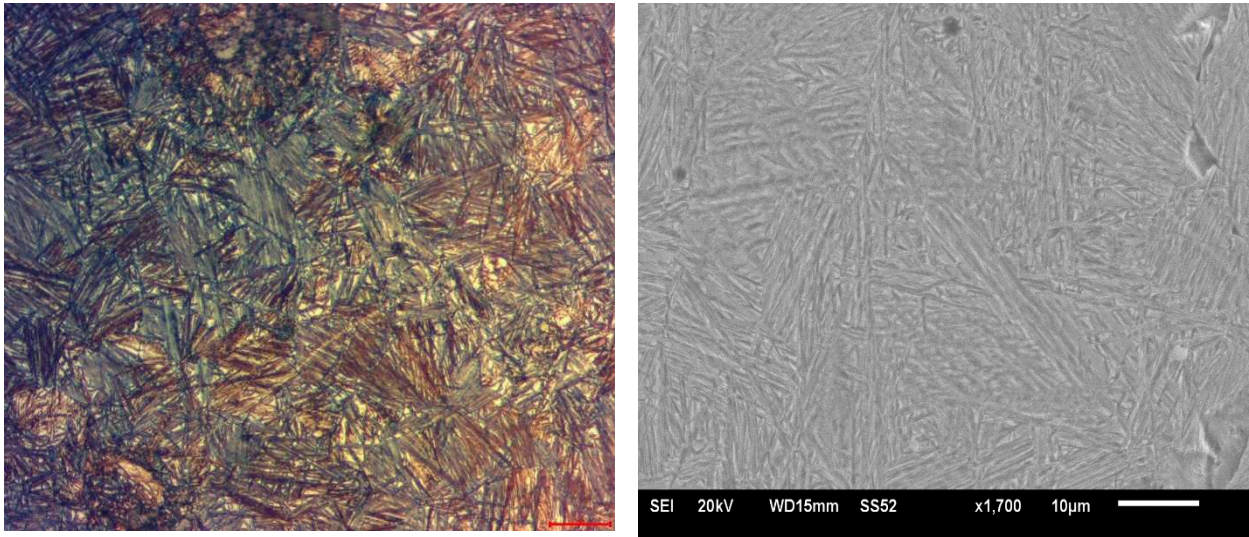


Figure.A.12: Optical and SEM micrograph of plastically deformed ADI,  $T_{\gamma}=1700^{\circ}\text{F}$ ,  $T_{\text{D}}=1700^{\circ}\text{F}$ ,  
 $T_{\text{A}}=550^{\circ}\text{F}$

**Microstructure of plastically deformed, conventionally austempered ductile cast iron( $T_{\gamma}=1520^{\circ}\text{F}$ )**

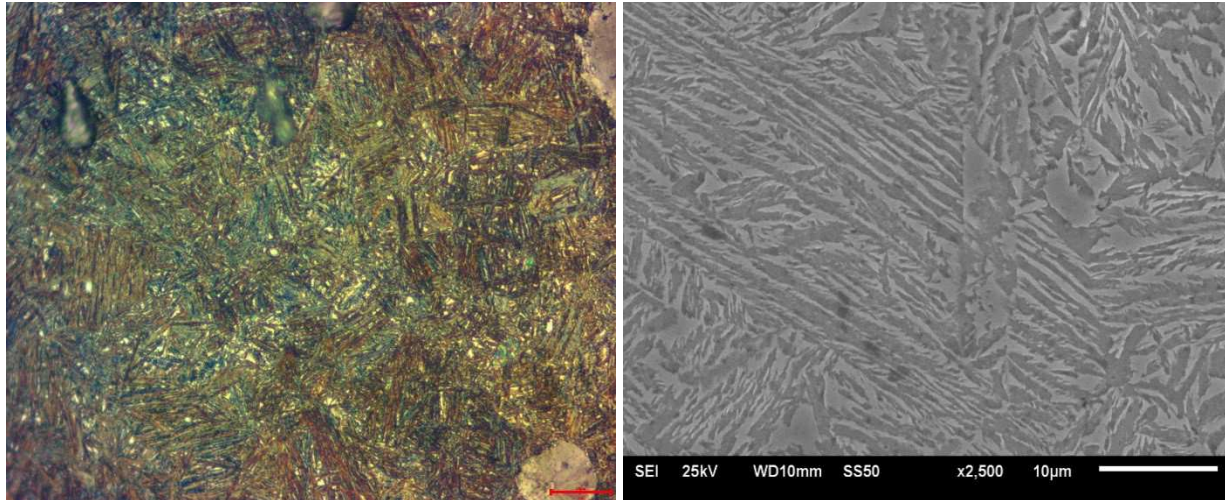


Figure.A.13: Optical and SEM micrograph of plastically deformed ADI,  $T_{\gamma}=1520^{\circ}\text{F}$ ,  $T_{D}=1520^{\circ}\text{F}$ ,  
 $T_{A}=680^{\circ}\text{F}$

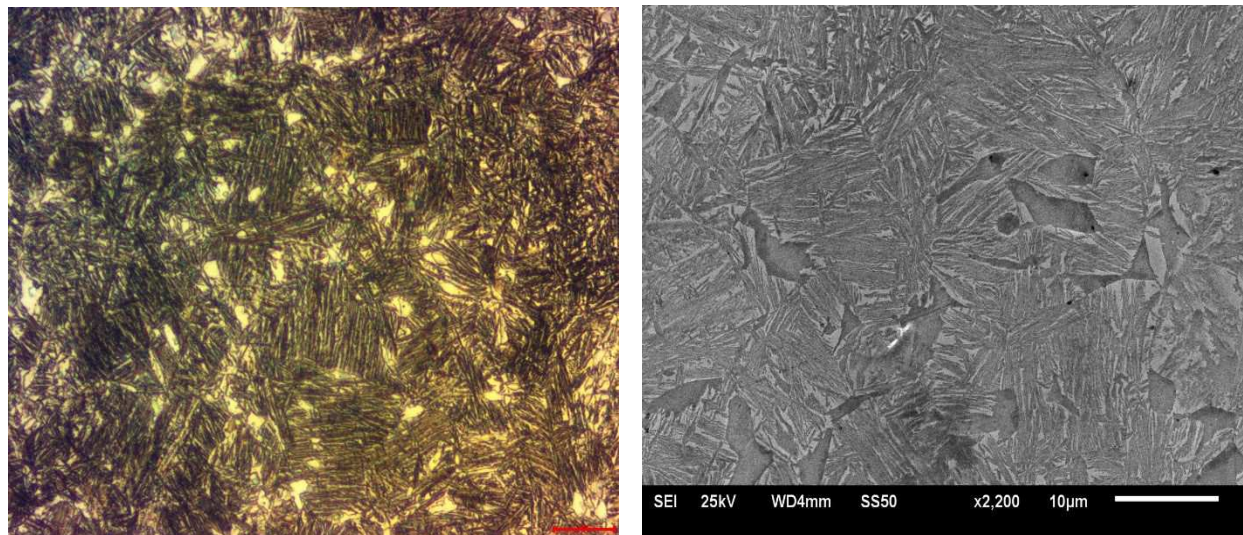


Figure.A.14: Optical and SEM micrograph of plastically deformed ADI,  $T_{\gamma}=1520^{\circ}\text{F}$ ,  
 $T_{D}=1520^{\circ}\text{F}$ ,  $T_{A}=600^{\circ}\text{F}$

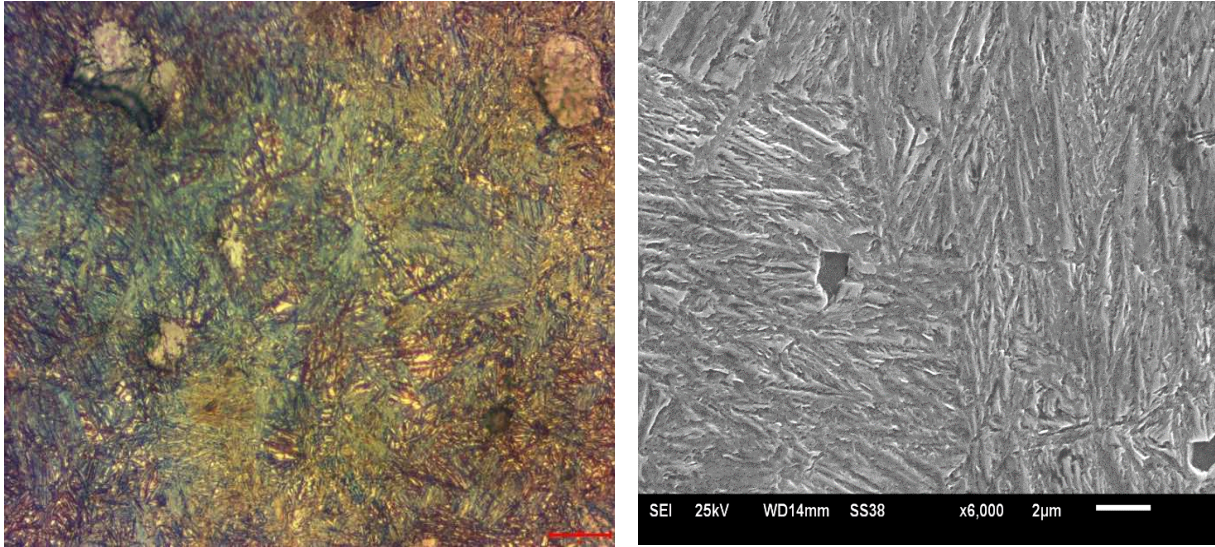


Figure.A.15: Optical and SEM micrograph of plastically deformed ADI,  $T_{\gamma}=1520^{\circ}\text{F}$ ,  $T_{D}=1700^{\circ}\text{F}$ ,  
 $T_{A}=550^{\circ}\text{F}$

#### Microstructures of the plastic deformed, two- step austempered ductile cast iron

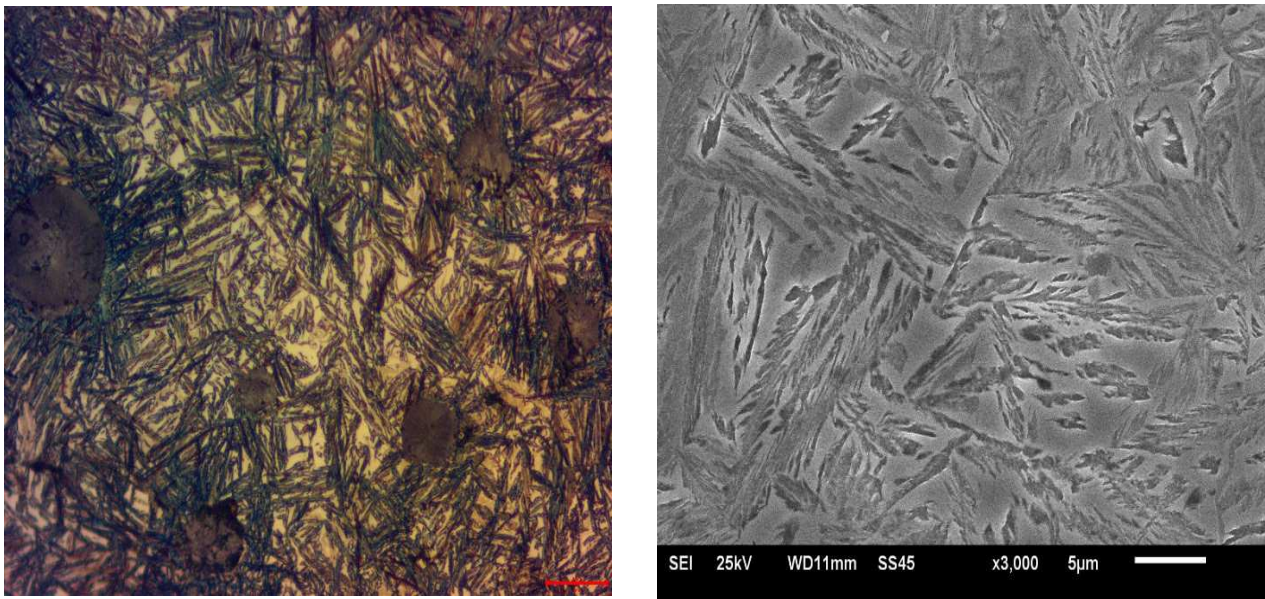


Figure.A.16: Optical and SEM micrograph of plastically deformed, two step austempered ADI,  
 $T_{\gamma}=1700^{\circ}\text{F}$ ,  $T_{D}=1700^{\circ}\text{F}$ ,  $T_{A1}=500^{\circ}\text{F}$ ,  $T_{A2}=725^{\circ}\text{F}$

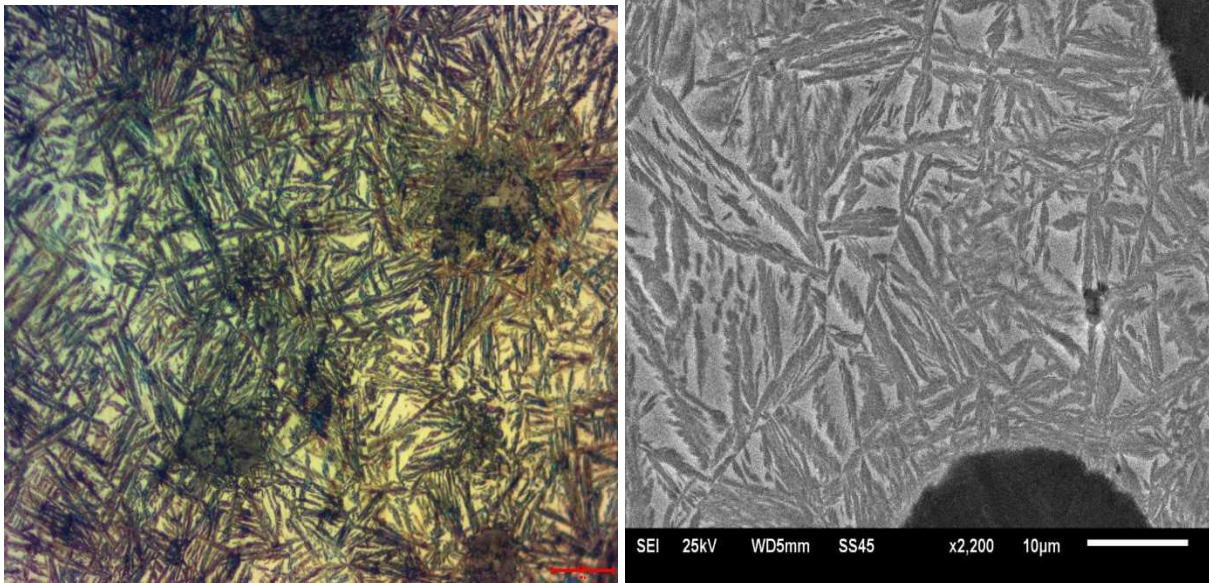


Figure.A.17: Optical and SEM micrograph of plastically deformed, two step austempered ADI,  
 $T_{\gamma}=1700^{\circ}\text{F}$ ,  $T_D=1700^{\circ}\text{F}$ ,  $T_{A1}=500^{\circ}\text{F}$ ,  $T_{A2}=680^{\circ}\text{F}$

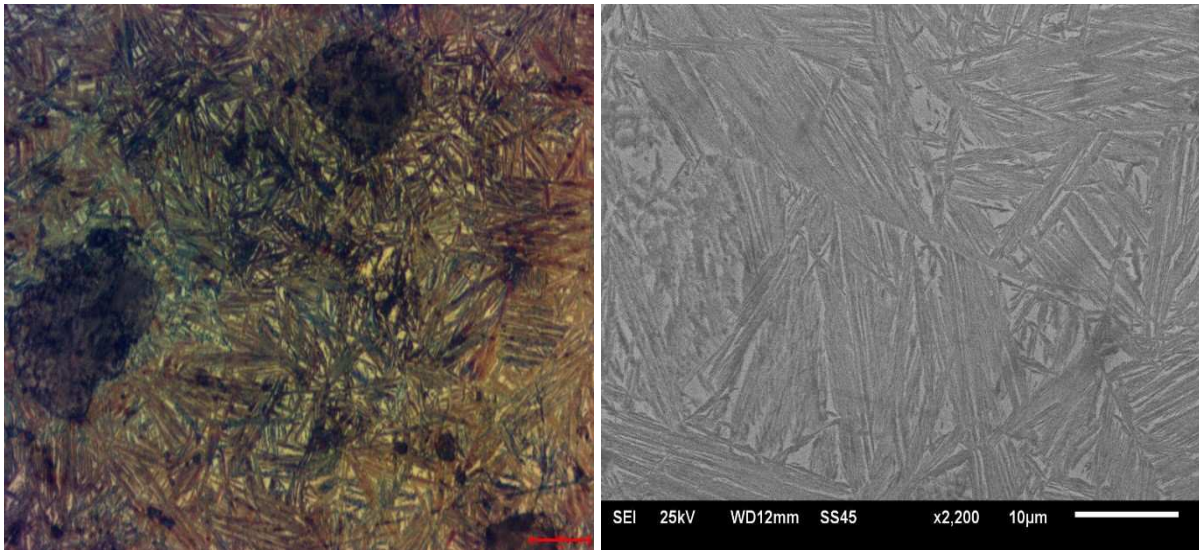


Figure.A.18: Optical and SEM micrograph of plastically deformed, two step austempered ADI,  
 $T_{\gamma}=1700^{\circ}\text{F}$ ,  $T_D=1700^{\circ}\text{F}$ ,  $T_{A1}=500^{\circ}\text{F}$ ,  $T_{A2}=600^{\circ}\text{F}$

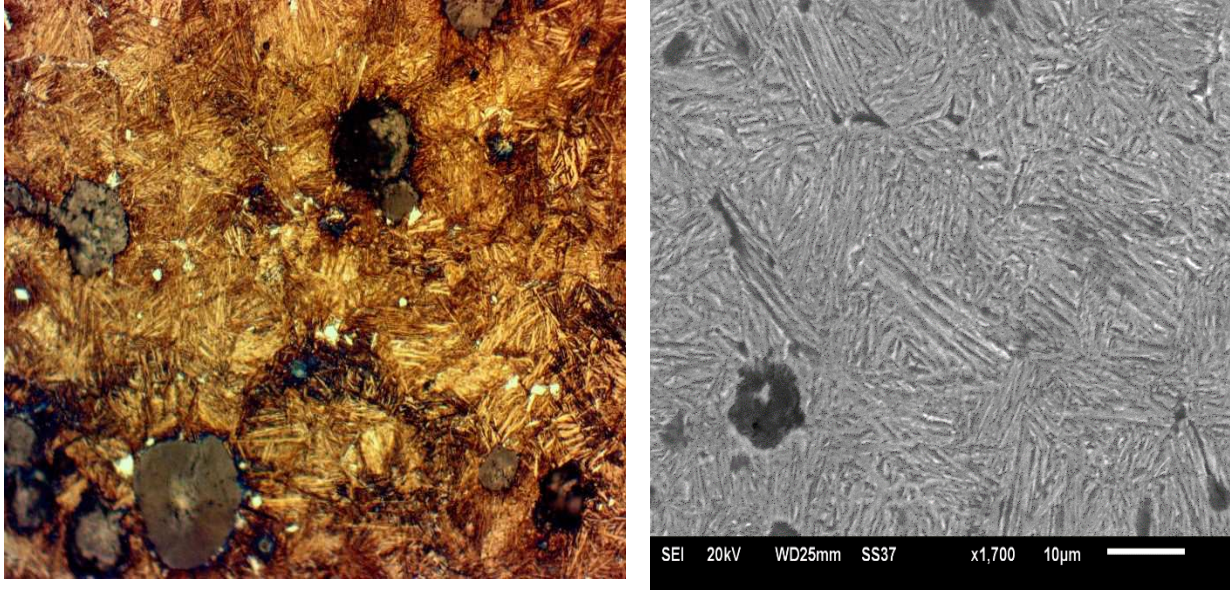


Figure.A.19: Optical and SEM micrograph of plastically deformed, two step austempered ADI,  
 $T_{\gamma}=1520^{\circ}\text{F}$ ,  $T_{D}=1520^{\circ}\text{F}$ ,  $T_{A1}=500^{\circ}\text{F}$ ,  $T_{A2}=725^{\circ}\text{F}$

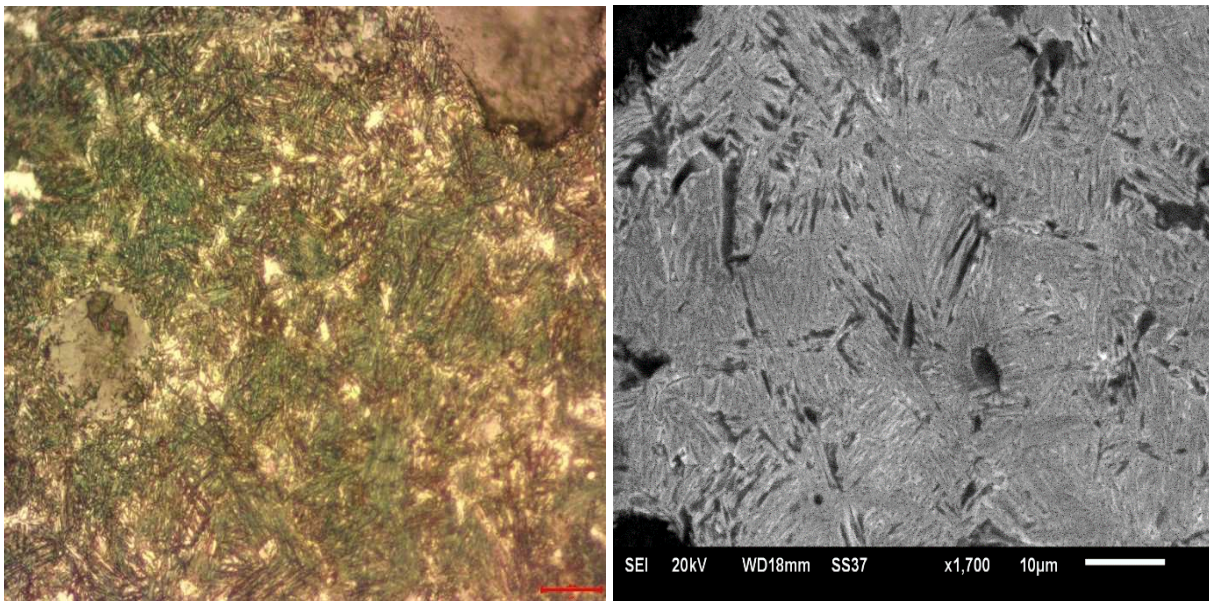


Figure.A.20: Optical and SEM micrograph of plastically deformed, two step austempered  
 ADI,  $T_{\gamma}=1520^{\circ}\text{F}$ ,  $T_{D}=1520^{\circ}\text{F}$ ,  $T_{A1}=500^{\circ}\text{F}$ ,  $T_{A2}=680^{\circ}\text{F}$

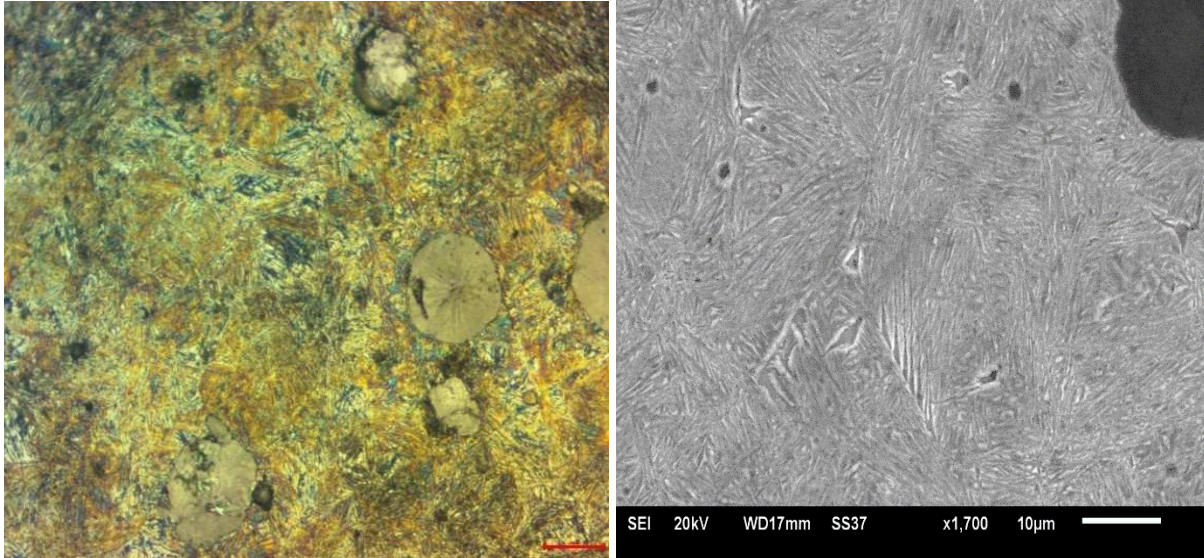


Figure.A.21: Optical and SEM micrograph of plastically deformed, two step austempered ADI,  
 $T_{\gamma}=1520^{\circ}\text{F}$ ,  $T_{D}=1520^{\circ}\text{F}$ ,  $T_{A1}=500^{\circ}\text{F}$ ,  $T_{A2}=600^{\circ}\text{F}$

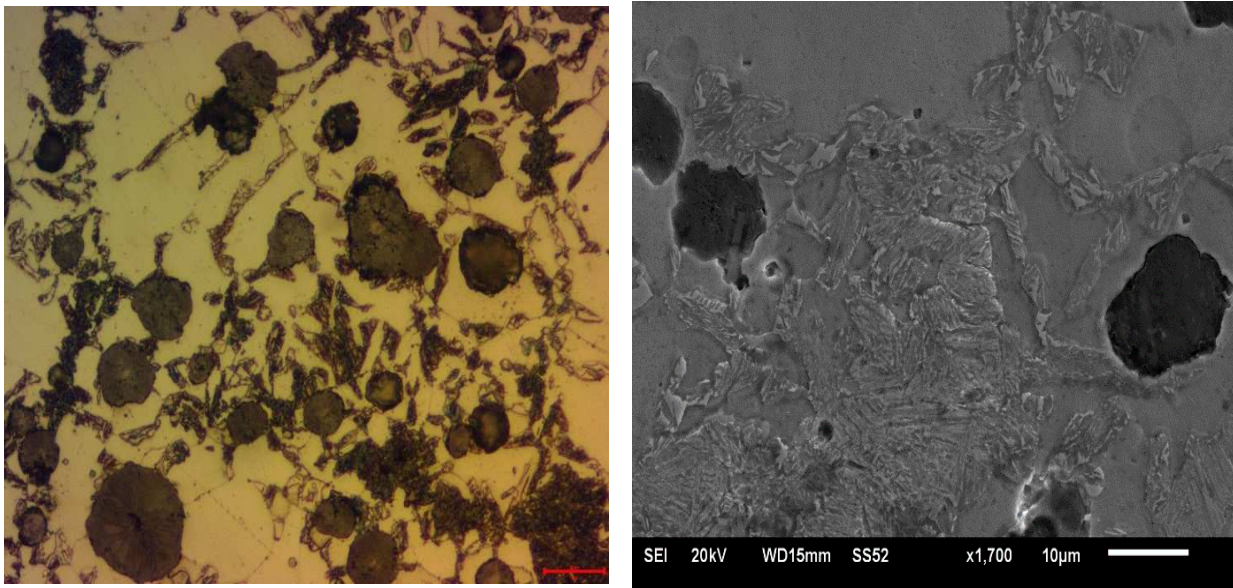


Figure.A.22: Optical and SEM micrograph of plastically deformed, two step austempered ADI,  
 $T_{\gamma}=1472^{\circ}\text{F}$ ,  $T_{D}=1472^{\circ}\text{F}$ ,  $T_{A1}=500^{\circ}\text{F}$ ,  $T_{A2}=725^{\circ}\text{F}$

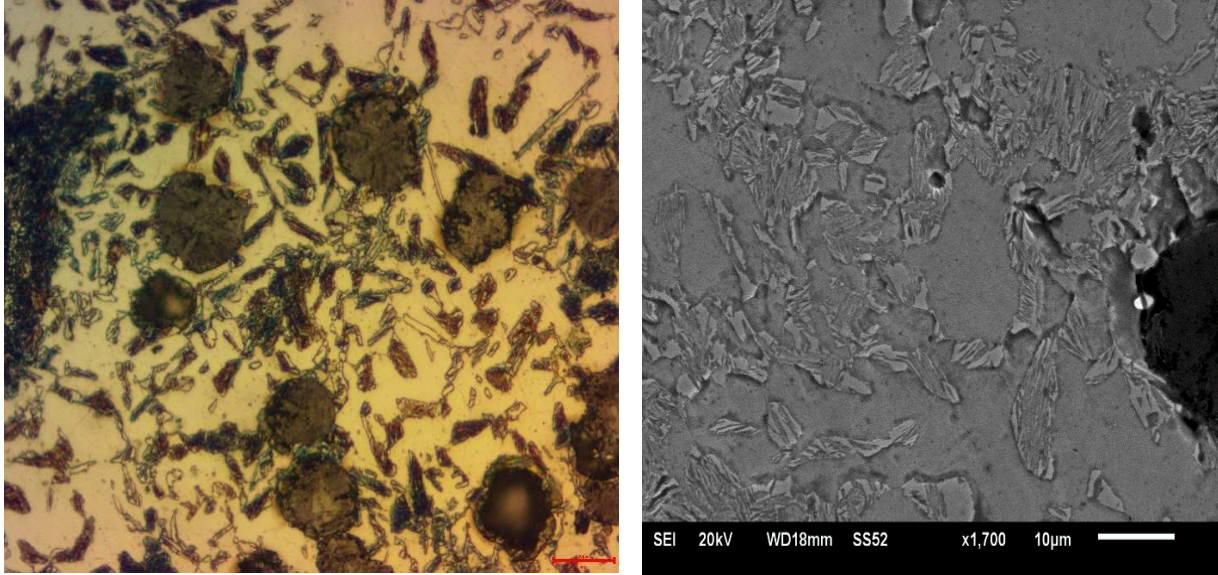


Figure.A.23: Optical and SEM micrograph of plastically deformed, two step austempered ADI,  
 $T_{\gamma}=1472^{\circ}\text{F}$ ,  $T_{D}=1472^{\circ}\text{F}$ ,  $T_{A1}=500^{\circ}\text{F}$ ,  $T_{A2}=680^{\circ}\text{F}$

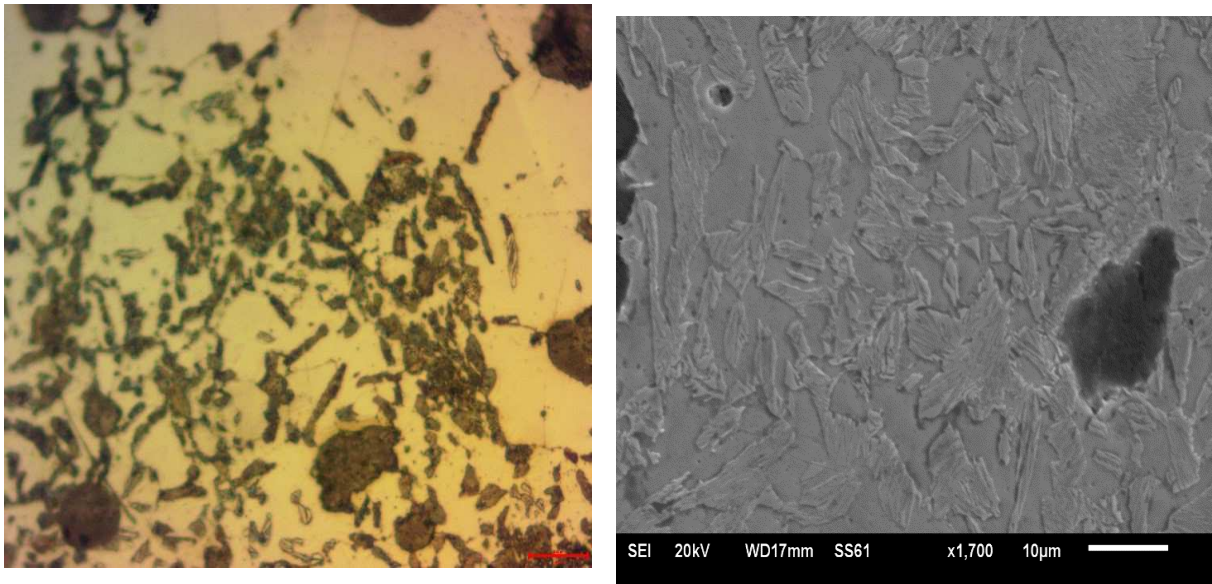


Figure.A.24: Optical and SEM micrograph of plastically deformed, two step austempered ADI,  
 $T_{\gamma}=1472^{\circ}\text{F}$ ,  $T_{D}=1472^{\circ}\text{F}$ ,  $T_{A1}=500^{\circ}\text{F}$ ,  $T_{A2}=600^{\circ}\text{F}$

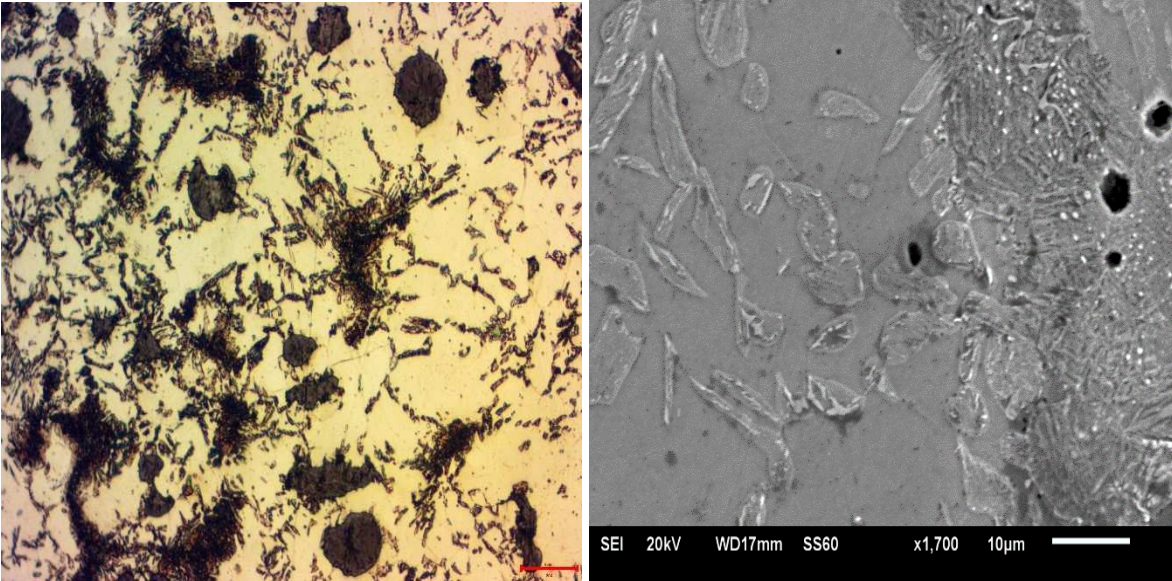


Figure.A.25: Optical and SEM micrograph of plastically deformed, two step austempered ADI,

$T_{\gamma}=1436^{\circ}\text{F}$ ,  $T_{D}=1436^{\circ}\text{F}$ ,  $T_{A1}=500^{\circ}\text{F}$ ,  $T_{A2}=725^{\circ}\text{F}$

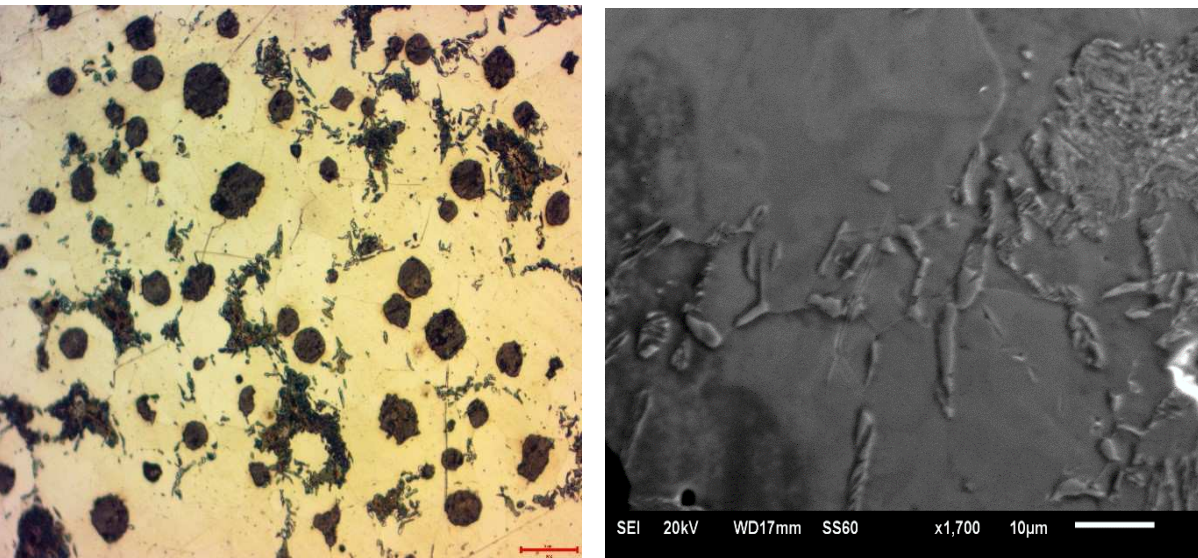


Figure.A.26: Optical and SEM micrograph of plastically deformed, two step austempered ADI,

$T_{\gamma}=1436^{\circ}\text{F}$ ,  $T_{D}=1436^{\circ}\text{F}$ ,  $T_{A1}=500^{\circ}\text{F}$ ,  $T_{A2}=680^{\circ}\text{F}$



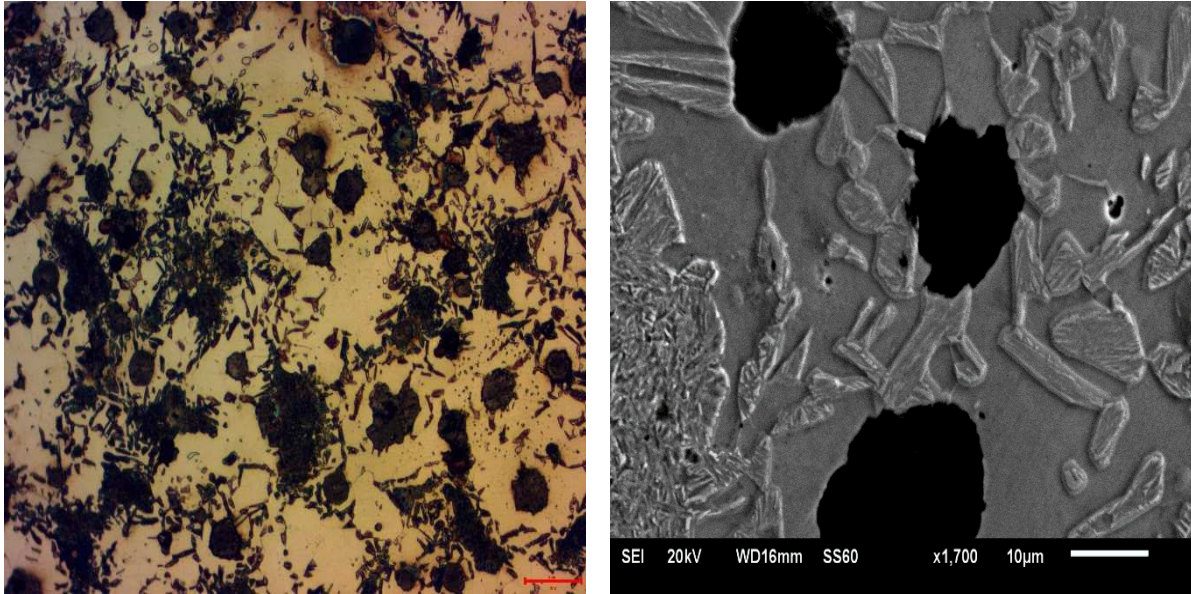


Figure.A.27: Optical and SEM micrograph of plastically deformed, two step austempered ADI,

$T_{\gamma}=1436^{\circ}\text{F}$ ,  $T_D=1436^{\circ}\text{F}$ ,  $T_{A1}=500^{\circ}\text{F}$ ,  $T_{A2}=600^{\circ}\text{F}$

#### Microstructure of ductile iron plastically deformed at different strain rate

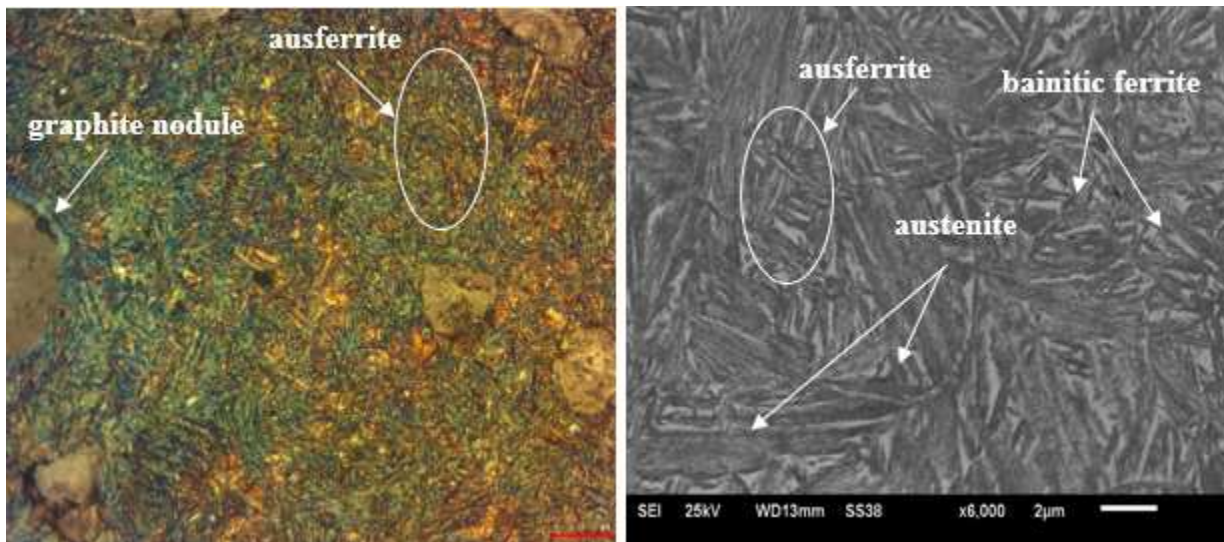


Figure.A.28: Optical and SEM micrograph of plastically deformed, two step austempered ADI,

$T_{\gamma}=1520^{\circ}\text{F}$ ,  $T_D=1520^{\circ}\text{F}$ , strain rate = 10mm/min,  $T_A=550^{\circ}\text{F}$

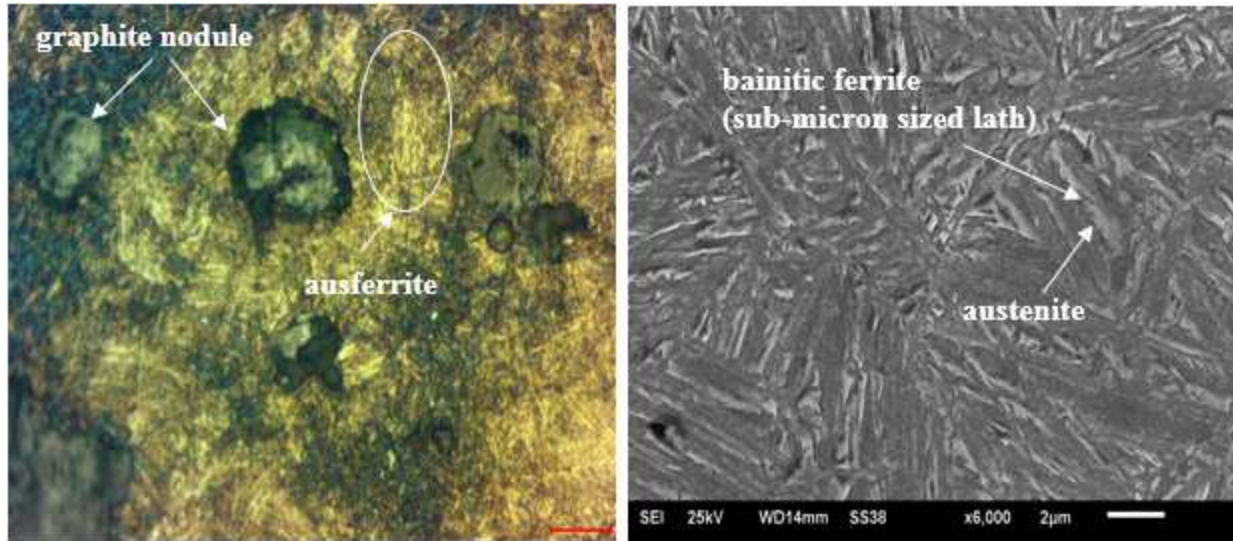


Figure.A.29: Optical and SEM micrograph of plastically deformed, two step austempered ADI,  
 $T_{\gamma}=1520^{\circ}\text{F}$ ,  $T_D=1520^{\circ}\text{F}$ , strain rate = 0.5mm/min,  $T_{A1}=500^{\circ}\text{F}$ ,  $T_{A2}=550^{\circ}\text{F}$

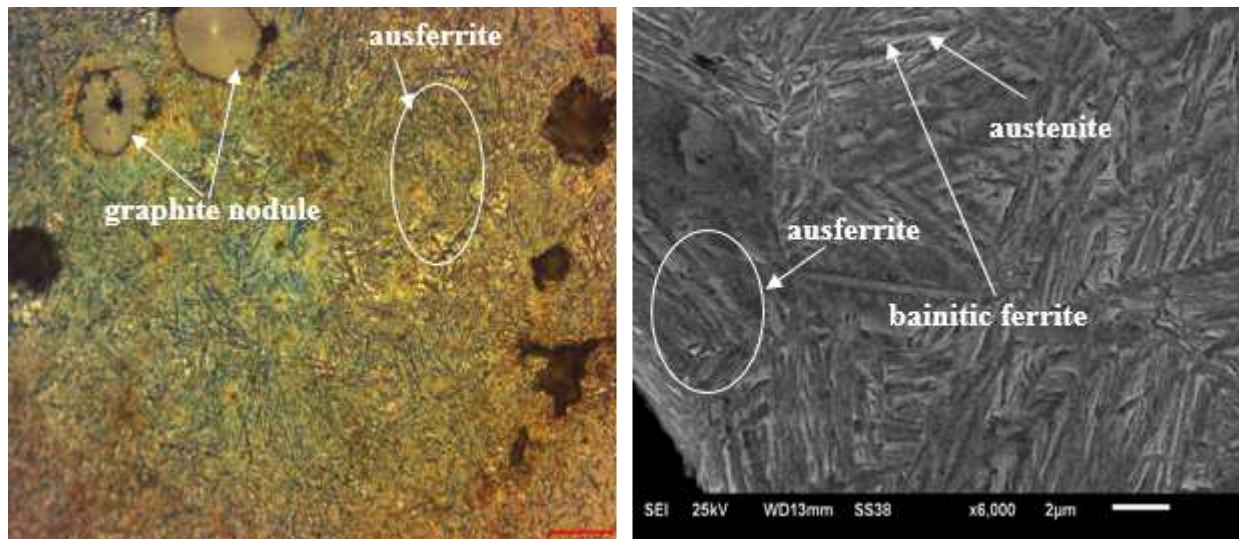


Figure.A.30: Optical and SEM micrograph of plastically deformed, two step austempered ADI,  
 $T_{\gamma}=1520^{\circ}\text{F}$ ,  $T_D=1520^{\circ}\text{F}$ , strain rate = 10mm/min,  $T_{A1}=500^{\circ}\text{F}$ ,  $T_{A2}=550^{\circ}\text{F}$

**REFERENCES**

1. P.P. Rao and S.K. Putatunda, "Influence of microstructure on fracture toughness of austempered ductile iron" Metallurgical and Materials Transactions A, Vol 28A, pp. 1457–1470, (1997).
2. P.P. Rao and S.K. Putatunda, "Comparative study of fracture toughness of austempered ductile irons with upper and lower ausferrite microstructures", Material Science and Technology, Vol 14, pp.1257– 1265, (1998).
3. J.L. Doong, F.C. Ju, H.S. Chen and L.W. Chen, "Influence of Austempering on Fracture Toughness in Bainitic Nodular Cast Iron", Journal of Materials Science Letters, pp. 555–558, (1986).
4. I. Schmidt, Z. Metallkd. Vol.75, pp.747–751, (1984).
5. S.M. Shah and J.D. Verhoeven, "Erosion Behaviour of High Silicon Bainitic Structures Austempered Ductile Cast Iron," Wear, Vol 113, pp.267–273, (1986).
6. R.B. Gundlach and J.F. Janowak, "Austempered ductile irons combine strength with toughness and ductility", Metal Progress, Vol.128 (2), pp. 19–26, (1985).
7. R.B. Gundlach and J.F. Janowak, "Development of Ductile Iron for Commercial Asutempering" AFS Transactions, Vol 91, pp. 377–388, (1983).
8. A. Trudel and M. Gagne, "Effect of composition and Heat treatment parameters on the characteristics of Austempered Ductile Irons", Canadian Metallurgical Quarterly, Vol 36, No.5, pp.289-298, (1997).
9. J. R. Keough and K. L. Hayrynen, "Designing with Austempered Ductile Iron (ADI)", Paper 10-129.pdf, Page 1 of 15, AFS Proceedings 2010 © American Foundry Society, Schaumburg, IL USA, (2010).

10. M. Yamanaka, R. Tamura, K. Inoue and Y. Narita, "Bending fatigue strength of austempered ductile iron spur gears", *Journal of Advanced Mechanical Design, Systems and Manufacturing*, Vol 3, pp.203-211 (2009).
11. C Suryanarayana, D Mukhopadhyay, SN Patankar and FH Froes, "Grain size effects in nanocrystalline materials" *Journal of Materials Research*, Vol 7, pp.2114-2118, (1992).
12. GE Fougere, JR Weertman and RW Siegel, "Processing and mechanical behavior of nanocrystalline Fe", *Nanostructured Materials*, Vol 5, pp.127-134, (1993).
13. RW Siegel, GE Fougere, "Mechanical properties of nanophase metals", *Nanostructured Materials*, Vol 6, pp. 205, (1995).
14. P. D. Hodgson, M. R. Hickson and R. K. Gibbs, "Ultrafine ferrite in low carbon steel", *Scripta Materialia*, Vol 40, No.10, pp.1179-1184. (1999).
15. P. J. Hurley, P. D. Hodgson and B. C. Muddle, "Analysis and characterization of ultra-fine ferrite produced during a new steel strip rolling process", *Scripta Materialia*, Vol 40, No.4, pp.433-438, (1999).
16. R. Z Valiev, A. V. Korznikov and R. R. Mulyukov, "Structure and properties of ultrafine-grained materials produced by severe plastic deformation", *Materials Science & Engineering, A: Structural Materials Properties, Microstructure and Processing*, Vol A168, No.2), pp.141-148, (1993).
17. V. Y. Gertsman, R. Birringer, R. Z. Valiev and H. Gleiter, "On the structure and strength of ultrafinegrained copper produced by severe plastic deformation", *Scripta Metallurgica et Materialia*, Vol 30, No.2, pp. 229-234, (1994).
18. A. V. Korznikov, G. Tram, O. Dimitrov, G. F. Korznikova, S. R. Idrisova and Z. Pakiela, "The mechanism of nanocrystalline structure formation in Ni<sub>3</sub>Al during severe plastic

- deformation”. *Acta Materialia*, Vol 49, No.4, pp. 663-671, (2001).
19. F. G. Caballero, H. K. D. H. Bhadeshia, K. J. A. Mawella, D. G. Jones and P. Brown, “Very Strong Low Temperature Bainite”, *Materials Science and Technology*, Vol. 18, No.3, pp. 279-284, (2002).
  20. H. K. D. H. Bhadeshia, “The first bulk nanostructured metal”, *Science and Technology of Advanced Materials*, Vol 14, pp.1-7, (2013).
  21. H.P. Karnthaler, T. Waitz, C. Rentenberger and B. Mingler, “TEM of nanostructured metals and alloys”, *Materials Science and Engineering A*, Vol. 387–389, pp. 777–782, (2004).
  22. Kaijian Chen, Ke Cao, Chengcheng Xing, Yongping Hu, Jiabin Liu and Yan He, “In situ TEM study of the lithiation and delithiation of FeS nanosheets”, *Journal of alloys and compounds*” Volume 688, pp.946-952, (2016).
  23. D. Myszka, E. Skolek and A. Wiczorek, “Manufacture of toothed elements in nanoausferritic ductile iron”, *Archives of Metallurgy and Materials*, Vol. 59, pp. 1217-1221, (2014).
  24. Cast Metals Development Ltd, “Austempered ductile-iron castings-advantages, production, properties and specifications”, *Materials and Design*, Vol.13, pp.285-297, (1992).
  25. EO Hall, “Deformation and aging of mild steel”, *Proceedings of the Physics Society*, Vol. B64, pp.747-753, (1951)
  26. N J Petch, “The cleavage strength of polycrystals”, *Journal of Iron and Steel Institute*, Vol.174, pp.25-28, (1953).
  27. R. Elliot, *Cast Iron Technology*, Butterworth & Co (publishers) Ltd., 1988.
  28. W.D. Callister, *Materials Science and Engineering an Introduction*, 7<sup>th</sup> edition, John wiley and Sons Inc.,2007.

29. Sorelmetal, "A Design Engineer's digest of ductile iron", RTZ Iron & Titanium America, 8<sup>th</sup> edition.
30. A.G. Guy, Elements of physical Metallurgy, Addison-Wesley Publishing company Inc. 2<sup>nd</sup> edition, (1960).
31. J.R. Davis, "Classifications and basic metallurgy of cast irons", ASM Specialty Handbook Cast Irons, pp.3-12, (1996).
32. ASTM E2567, "Standard test method for determining nodularity and nodule count in ductile iron using image analysis", ASTM International, West Conshohocken, PA, (2016).
33. S.K. Putatunda and P.K. Gadicherla, "Influence of austenitizing temperature on fracture toughness of a low manganese austempered ductile iron (ADI) with ferritic as cast structure", Materials Science and Engineering A, Vol 268, pp. 15-31, (1997).
34. J. Dodd, "High strength, high ductility, ductile irons", Modern casting, Vol 68, Issue 5, pp.60-66, (1978).
35. B.Y.Lin, E.T. Chen and T.S.Lei, "The effect of alloy elements on the microstructure and properties of austempered ductile irons" Scripta Metallurgica et Materialia, Vol 32, No.9, pp.1363-1367, (1995).
36. L.Guerin and M Gagne "Effect of Mn, Cu and Sn on the Microstructure and Properties of Ductile Iron Castings", The Foundryman, Vol. 80, part 7, pp. 336-344, (1987).
37. B. Kovacs, "Heat Treating of Austempered ductile Iron", AFS Transactions, Vol 75, pp.281-286, (1991).
38. J.F. Janowak, R.B. Gundlach, G.T. Eldis and K. Rohrting, "Technical Advances in Cast Iron Metallurgy," AFS International Cast Metal Journal, Vol.6, pp.28-42, (1982).

39. J.F. Janowak and P.A. Norton, "A Guide to Mechanical Properties Possible by Austempering, 1 S percent Ni, 0.3 percent Mo Iron," AFS Transaction, Vol.88, pp.123-135, (1985).
40. M.Bahmani, R. Elliot, "Effects of pearlite formation on mechanical properties of austempered ductile iron", Materials Science and Technology, Vol 10, pp.1068-72, (1994)
41. H.K.D.H. Bhadeshia, "Bainite in steels", Journal of the Institute of Metals, (1992).
42. H.K.D.H. Bhadeshia and D.V. Edmonds, "The mechanism of bainite formation in steels", Acta Metallurgica., Vol 28(9): pp. 1265-73, (1980).
43. J. Aranzabal and I. Gutierrez "Influence of Heat Treatment on the Microstructure of an Austempered Ductile Iron," Materials Science and Technology, Vol 20, pp. 36-46, (1994).
44. S. K. Putatunda and P.P. Rao, "Influence of Microstructure on Fracture Toughness Austempered Ductile Cast Iron," Metallurgical and Materials Transaction, Vol 28A. No.7, pp.1457-1470, (1997).
45. B.V. Kovacs, "Austempered Ductile Iron, Fact and Fiction", Modern Casting, pp.38-41, (1990).
46. G.I. Rees and H.K.D.H. Bhadeshia, "Bainite transformation kinetics- Part 1" Materials Science and Technology, Vol 8 (11), pp.985-993, (1992).
47. C. Zener, "Kinetics of the decomposition of austenite", Transactions of the American Institute of Mining and Metallurgical Engineers, Vol 167, pp. 550–595, (1946).
48. T. Kobayashi, "Effect of holding time in the ( $\alpha+\gamma$ ) temperature range on toughness of specially austempered ductile iron", Metallurgical and Materials Transactions A, Physical Metallurgy and Materials Science, Vol 27, No.7, pp.1961-1971, (1996).

49. Adel Nofal, "Advances in the Metallurgy and Applications of ADI", Journal of Metallurgical Engineering, Vol 2 Issue 1, (2013).
50. D.J. Moore, T.B. Noun and K.B. Rundman, "Structure and mechanical properties of Austempered Ductile Cast Iron," AFS Transactions, Vol.103, pp. 705- 718, (1985).
51. H. K. D. H. Bhadeshia, "Hard bainite", Solid-Solid Phase Transformations in Inorganic Materials 2005, Proceeding of the International Conference, Phoenix, AZ, United States, May 29-June 3, Vol. 1, pp. 469-484, (2005).
52. F. G. Caballero and H. K. D. H. Bhadeshia, "Very Strong Bainite", Current Opinoin in Solid State and Materials Science, Vol. 8, pp. 251-257, (2004).
53. M. Cerah, K. Kocatepe, and M. Erdogan, "Influence of Martensite Volume Fraction and Tempering Time on Tensile Properties of Partially Austenitized in the ( $\alpha + \gamma$ ) Temperature Range and Quenched + Tempered Ferritic Ductile Iron", Journal of Material Science, Vol 40, No.13, pp. 3453-3459, (2005).
54. M. Erdogan, V Kilicli and B Demir, "The Influence of Austenite Dispersion on Phase Transformation During Austempering in Ductile Cast Iron with Dual Matrix Structure", Research in Materials Science, Vol 99, No.7, pp. 751-760, (2008).
55. K Kocatepe, K Cerah and M Erdogan, "The Tensile Fracture Behaviour of Intercritically Annealed and Quenched+Tempered Ferritic Ductile Iron with Dual Matrix Structure", Materials & Design Vol 28, No.1, pp. 172-181, (2007).
56. M Erdogan V Kilicli and B Demir, "Transformation Characteristics of Ductile Iron Austempered From Intercritically Annealing Temperature Ranges", Journal of Materials Science Vol 44, No.5, pp. 1394-1403, (2009).



57. P.P. Rao and S.K. Putatunda "Dependence of Fracture Toughness of Austempered Ductile Cast Iron on Austempering Temperature" Metallurgical and Materials Transaction, Vol 29A, pp. 3005-3016, December (1998).
58. P. Shanmugam, P.P. Rao, K.R. Udupa, N. Venkataraman, "Effect of microstructure on the fatigue strength of austempered ductile iron, Journal of Materilas Science, Vol.29, pp.4933-4940, (1994).
59. P.P. Rao and S.K. Putatunda "Investigations on Fracture Toughness of Austempered Ductile Iron Alloyed with Chromium", Materials science and Engineering, Vol A346, pp. 254-265, (2003).
60. A.S.H. Ali, K.I. Uzlov, N. Darwish and R. Elliot "Austempering of a Low Manganese Ductile Iron, Part 4 Relationship between Mechanical Properties and Microstructure", Materials Science and Technology, Vol 70, pp. 35-48, (1994).
61. K.L. Harynen, D.J. Moore and K.B. Rundman, "Tensile Properties and Microstructure of a Clean Austempered Ductile Iron", AFS Transaction, Vol 98, pp. 471, (1990).
62. J.L. Doong and C. Chen, "Fracture Toughness of Bainitic-Nodular Cast iron," Fatigue Fracture of Engineering Material and Structure, Vol.12, pp.155-165, (1989).
63. M. Grech, P. Bowen and J.M. Young, "Effect of austempering temperature on the fracture toughness and tensile properties of an ADI alloyed with copper and nickel", Proceedings of the World Conference on Austempered Ductile Iron, Bloomingdale, IL, pp.338-374, (1991).
64. G.E. Dieter, "Mechanical Metallurgy", McGraw Hill, 3rd Edition, (1986).
65. C. C. Koch, D. G. Morris, K Lu and A Inoue, "Ductility of Nanostructured Materials", MRS Bulletin, Vol 24, No.2, pp.54-8, (1999).

66. A. Karimpoor, U. Erb, K. T. Aust and G. Palumbo, "High strength nanocrystalline cobalt with high tensile ductility", *Scripta Materialia*, Vol 49, No.7, pp.651-656, (2003).
67. Y. M. Wang and E Ma, "Temperature and strain rate effects on the strength and ductility of nanostructured Copper", *Applied Physics Letters*, Vol 83, No.15, pp.3165-7, (2003).
68. V.Kilicli and M. Erdogan, "Effect of ausferrite volume fraction and morphology on tensile properties of partially austenitized and austempered ductile irons with dual matrix structures", *International Journal of Cast Metals Research*, Vol.20, pp.202-214, (2007).
69. V Kilicli and M Erdogan, "Tensile Properties of Partially Austenitized and Austempered Ductile Irons with Dual Matrix Structures", *Materials Science and Technology*, Vol 22, No.8, pp. 919-928 (2006).
70. Z.R. He, G.X. Lin, and S. Ji, "Deformation and Fracture Behaviour of Cast Iron with Optimized Microstructure", *Materials Characterization*, 38(4-5), p 251-258, (1997).
71. W.F. Smith and J Hashemi, *Foundations of Materials Science and Engineering*, 4<sup>th</sup> edition, McGraw-Hill, pp. 318–320., (2006). R.W. Hertzberg, "Deformation and Fracture Mechanics of Engineering Materials", John Wiley and Sons, Third Edition, (1986).
72. R.W. Hertzberg, "Deformation and Fracture Mechanics of Engineering Materials", John Wiley and Sons, Third Edition, (1986).
73. K. Okabayashi, M. Kawamoto, A. Ikenaga and M. Tsujikawa, "Impact characteristics and fractography of spheroidal graphite cast iron and graphite steel with hard eye structure", *Transactions of the Japan Foundrymen's Society*, Vol 1, pp. 37–41, (1982).
74. T. Kobayashi and H. Yamamoto, "Transformation induced plasticity in austempered low alloyed ductile iron", *Transactions of the Japan Foundrymen's Society*, pp. 30–34. (1989).

75. R. Kazerooni, A. Nazarboland and R. Elliot, "Use of austenitizing temperature in control of austempering of an Mn-Mo-Cu alloyed ductile iron", *Materials Science and Technology*, Vol.13, pp.1007-1015, (1997).
76. A.S. Hamid and R. Elliot, "Influence of austenitizing temperature on austempering of an Mn-Mo-Cu alloyed ductile iron Part-2- Mechanical properties", *Materials Science and Technology*, Vol. 13, pp.24-30, (1997).
77. A.S. Hamid and R. Elliot, "Influence of austenitizing temperature on austempering of an Mn-Mo-Cu alloyed ductile iron Part-1-Austempering kinetics and the processing window", *Materials Science and Technology*, Vol.12, pp.1021-1031, (1996).
78. M.Grech and J.M. Young, "Effect of austenitizing temperature on tensile properties of Cu-Ni Austempered ductile iron", *Materials Science and Technology*, Vol. 6, pp.415-421, (1990).
79. T. Rouns, K.B. Rundman and D. Moore, "On the structure and properties of Austempered ductile cast iron", *AFS Transactions*, Vol. 92, pp. 815-840, (1984).
80. R.C. Voigt, L.M. Eldoky and H.S. Chiou, "Fracture of ductile cast irons with dual matrix structures", *AFS Transactions*, Vol 94, pp.645-656, (1986).
81. V.Kilicli and M. Erdogan, "The nature of the tensile fracture in austempered ductile iron with dual matrix microstructure", *Journal of Materials Engineering and Performance* Vol 19, Issue 1, pp.142-149, (2010).
82. T. Kobayashi and H. Yamamoto, "Development of high toughness in Austempered ductile cast iron and evaluation of its properties", *Metallurgical Transactions A*, Vol 19A, pp.319-327, (1988).

83. A. Basso, R. Martinez and J. Sikora, "Influence of austenitizing and austempering temperatures on dual phase ADI", *Materials Science and Technology*, Vol.23, pp.1321–1326, (2007).
84. M.Erdogan, M. Cerah and K. Kocatepe, "Influence of intercritical austenitizing, tempering time and martensite volume fraction on the tensile properties of ferritic ductile iron with dual matrix microstructure", *International Journal of Cast Metals Research*, Vol 19, Issue 4, pp. 248–253, (2006).
85. K. Kocatepe, M. Cerah and M. Erdogan, "Effect of martensite volume fraction and its morphology on the tensile properties of ferritic ductile iron with dual matrix structures", *Journal of Materials Processing Technology*, Vol 178, pp.44-51, (2006).
86. A. Basso and J. Sikora, "Review on production processes and mechanical properties of dual phase austempered ductile iron" *International Journal of Metal Casting*, Vol.6, pp.7-14, (2012).
87. J. Aranzabal, G. Serramoglia, and D. Rousiere, "Development of a New Mixed (Ferritic-Ausferritic) Ductile Iron for Automotive Suspension Parts", *International Journal of Cast Metals Research*, Vol 16, No.1-3 pp. 185-190, (2003).
88. Bartosiewicz, S. Duraiswamy, A. Sengupta, S.K. Putatunda, "Near threshold fatigue crack growth behavior of austempered ductile cast iron", *Morris Fine Symposium, TMS, Detroit*, pp. 135–138, (1991).
89. L. Bartosiewicz, A.R. Krause, A. Sengupta, S.K. Putatunda, "Relationship between fatigue threshold and fatigue strength in austempered ductile cast iron", *International Symposium for Testing and Failure Analysis, ISTFA, ASM Vol.16*, pp.323–336, (1990).

90. J.F. Janowak, P.A. Norton, "A guide to mechanical properties possible by austempering, 1.5% Ni, 0.3% Mo iron, AFS Transactions, Vol. 88, pp. 123–135, (1985).
91. S.K. Putatunda, "Development of austempered ductile cast iron (ADI) with simultaneous high yield strength and fracture toughness by a novel two-step austempering process", Materials Science and Engineering. A, Vol 315, pp.70-80, (2001).
92. J Yang, & SK Putatunda, "Improvement in strength and toughness of austempered ductile cast iron by a novel two-step austempering process", Materials and Design, Vol. 25, pp. 219-230, (2004).
93. S.K. Putatunda "Influence of Two-step Austempering on Mechanical Properties of ADI", Proceeding of the Conference, Heat Treatment Congress, ASM International, Gothenburg, Sweden, pp. 345-360, (2000).
94. Andoko and P. Puspitasari, "Effect of temperature and time of two-step austempering method on mechanical properties for nodular cast iron", ARPN Journal of Engineering and Applied Sciences, Vol 11, pp.863-866, (2016).
95. S.K. Putatunda, C. Martis, F. Diekman and R. Papp, "Effect of cryogenic processing on the mechanical properties of austempered ductile cast iron" Proceedings of the 26<sup>th</sup> ASM Heat Treating Society Conference, pp.44-49, (2011).
96. H. Bayati and R. Elliot, "Thermal and Mechanical Stability of Austenite in High Mn ADI", Proceedings of the 20<sup>th</sup> Heat Treating Conference (ASM International), pp. 578-585, (2000).
97. D.Myszka, T. Borowski and T. Babul," Influence of cryogenic treatment on microstructure and hardness of austempered ductile iron", Proceedings of the 5<sup>th</sup> IASME/WSEAS International Conference on Heat Transfer, pp.123-128, (2007).

98. Agus Suprpto, Agus Iswantoko<sup>2</sup>, Ike Widyastuti, “Impact Evaluation of Cryogenic Treatment to Wear Characteristics of ADI Cutting Tool”, *International Journal of Applied Engineering Research*, Vol 11, pp.7691-7697, (2016).
99. U.R. Kumari and P.P. Rao, “Study of wear behavior of austempered ductile iron”, *Journal of Materials Science*, Vol. 44, pp. 1082-1093, (2009).
100. M.Naili Ahmadabadi, “Bainitic transformations in Austempered ductile iron with reference to untransformed austenite volume phenomenon”, *Metallurgical and Materials Transactions A*, Vol. 28A, pp.2159-2162, (2007).
101. J. Vuorinen, *AFS Transactions*, Vol.86, (1983), pp.577-588
102. P. Mayr, H. Vethers and J. Walla, *Proceedings of the 2nd International Conference on austempered Ductile Iron*, Ann Arbor, MI, (1986), pp.171-178.
103. J. Dan, W.G. Zhang, S.H. Li and Z.Q. Lin “A model for strain-induced martensitic transformation of TRIP steel with strain rate” *Computational Materials Science*, Vol.40, pp. 101–107, (2007).
104. I.B. Timokhina, P.D. Hodgson and E.V. Pereloma, “Effect of microstructure on the stability of retained austenite in transformation-induced-plasticity steels”, *Metall Mater Trans A*, 35A (2004), pp. 2331–2341104
105. L.Sidjanin, R. E Smallman and S.M. Boutorabi, *Materials Science Technology* Vol.8 (1992), pp.1095-2006.
106. L.Sidjanin, R. E Smallman and S.M. Boutorabi, “Microstructure and fracture of aluminium austempered ductile iron investigated using scanning electron microscopy”, *Materials Science Technology*, Vol.10, pp.711-720, (2013).

107. M. Ramadan, A. A. Nofal, I. Elmahalawi and R. Abdel-Karim: “Influence of graphite nodularity on microstructure and processing window of 1.5% Ni–0.3% Mo austempered cast iron”, *Materials Science and Engineering A*, Vol.435–436, pp.564–572, (2006).
108. D. Myszka, K. Wasiluk, E. Skoek and W. Swiatnicki, “Nanoausferritic matrix of ductile iron”, *Materials Science and Technology*, Vol. 31, pp.829-834, (2015).
109. R.Z. Valiev, R.K. Islamgaliev and I.V. Alexandrov, “Bulk Nanostructured Materials from Severe Plastic Deformation”, *Progress in Materials Science*, Vol.45, pp.103-189, (2000).
110. W.B. Morrison, “The effect of grain size on the stress-strain relationship in low-carbon steel”, *ASM Transactions*, Vol 59, pp.824-846, (1966).
111. J.G. Sevillano and J. Aldazabal, “Ductilization of nanocrystalline materials for structural applications”, *Scripta Materiali*, Vol 51, pp.795-800, (2004).
112. G.W. Nieman, JR Weertman, and R W Siegel, “Mechanical Behavior of Nanocrystalline Metals”, *Scripta metallurgica et Materialia*, Vol 24, pp.145, (1990)
113. F.B. Pickering and T. Gladman, “Metallurgical developments in carbon steels”, Special report 81, Iron and Steel Institute, 1963.
114. R. Biernacki, J. Kozłowski, D. Myszka and M. Perzyk, “Prediction of properties of ductile iron assisted by artificial neural networks”, *Material Science – Medziagotyra*, Vol. 12, pp. 11-15 (2006).
115. R.Z. Valiev and T.G. Langdon, “Principles of equal-channel angular pressing as a processing tool for grain refinement”, *Progress in Materials Science*, Vol. 51, pp. 881-981, (2006).
116. X.Zhang, H. Wang, R.O. Scattergood, J. Naryan, C.C. Koch, A.V. Sergueeva and A.K. Mukherjee, “Studies of deformation mechanisms in ultra-fine-grained and nanostructured Zn”, *Acta materialia*, Vol. 50, pp. 4823-4830, (2002).

117. F.B. Pickering and T. Gladman, "Metallurgical developments in carbon steels", Special report 81, Iron and Steel Institute, (1963).
118. C.R.F. Azevedo, A.A. Garboggini and A.P. Tschipitschin, "Effect of austenite grain refinement on morphology of product of bainitic reaction in austempered ductile iron" Materials Science and Technology, Vol.9, pp.705-710, (1993).
119. A. International, ASTM A536, "Standard specifications for ductile iron castings" West Conshohocken, PA, (2014).
120. A. International, ASTM E8 / E8M-13a, "Standard Test Methods for Tension Testing of Metallic Materials". West Conshohocken, PA, (2013).
121. A. International, ASTM E399-12e3, "Standard Test Method for Linear-Elastic Plane-Strain Fracture Toughness  $K_{Ic}$  of Metallic Materials". West Conshohocken, PA, (2012).
122. ASTM E-562, Standard Test Method for determining volume fraction by systemic manual point count, ASTM International, West Conshohocken, PA, 2011.
123. K.B. Rundman, R.C. Klug, An x-ray and metallographic study of austempered ductile cast iron, American Foundry Society Transactions, Vol. 90, pp. 499-508, (1982).
124. B.D. Cullity and S.R. Stock, Elements of X-Ray Diffraction, 3rd Edition.: Prentice Hall, (2001).
125. C.S. Roberts, Effect of carbon on the volume fractions and lattice parameters of retained austenite and martensite. Journal of Metals, Vol.5, (1953).
126. ASTM E-18, "Test Methods for Rockwell hardness and Rockwell superficial hardness for metallic materials, Annual Book of ASTM Standards, ASTM Philadelphia, Vol.03, No.01, pp. 175-199, (1984).
127. E. Dorazil, "Mechanical properties of Austempered ductile iron", Foundry Management and



- Technology, pp.36-45, (1986).
128. C.Capdevila, F.G. Caballero and C. Garcia de Andres, “Analysis of effect of alloying elements on martensite start temperature of steels”, *Materials Science and Technology*, Volume 19, pp.581-586, (2003).
129. P.P. Rao and S.K. Putatunda, “Investigations on the Fracture Toughness of austempered ductile irons austenitized at different temperatures”, *Materials Science and Engineering A*, 349, pp.136-149, (2003).
130. J.L. Doong and C. Chen, “Fracture toughness of bainitic nodular cast iron” *Fatigue and Fracture of Engineering Material Structure*, Vol. 12, pp. 155–165, (1989).
131. E. Dorazil and M. Holzman, “Fracture behavior of austempered ductile iron *Proceedings of the World Conference on Austempered Ductile Iron*”, Bloomingdale, IL, pp. ,32–66, (1991).

**ABSTRACT****DEVELOPMENT OF NANOSTRUCTURED AUSTEMPERED DUCTILE CAST IRON**

by

**SARANYA PANNEERSELVAM****August 2017****Advisor:** Dr. Susil K. Putatunda**Major:** Materials Science and Engineering**Degree:** Doctor of Philosophy

Austempered Ductile Cast Iron is emerging as an important engineering materials in recent years because of its excellent combination of mechanical properties such as high strength with good ductility, good fatigue strength and fracture toughness together with excellent wear resistance. These combinations of properties are achieved by the microstructure consisting of acicular ferrite and high carbon austenite. Refining of the ausferritic microstructure will further enhance the mechanical properties of ADI and the presence of proeutectoid ferrite in the microstructure will considerably improve the ductility of the material.

Thus, the focus of this investigation was to develop nanostructured austempered ductile cast iron (ADI) consisting of proeutectoid ferrite, bainitic ferrite and high carbon austenite and to determine its microstructure-property relationships. Compact tension and cylindrical tensile test samples were prepared as per ASTM standards, subjected to various heat treatments and the mechanical tests including the tensile tests, plane strain fracture toughness tests, hardness tests were performed as per ASTM standards. Microstructures were characterized by optical metallography, X-ray diffraction, SEM and TEM.

Nanostructured ADI was achieved by a unique heat treatment consisting of

austenitization at a high temperature and subsequent plastic deformation at the same austenitizing temperature followed by austempering. The investigation also examined the effect of cryogenic treatment, effect of intercritical austenitizing followed by single and two step austempering, effect of high temperature plastic deformation on the microstructure and mechanical properties of the low alloyed ductile cast iron. The mechanical and thermal stability of the austenite was also investigated. An analytical model has been developed to understand the crack growth process associated with the stress induced transformation of retained austenite to martensite.

## AUTOBIOGRAPHICAL STATEMENT

**Name:** Saranya Panneerselvam

**Date of Birth:** October 31, 1987

**Education:**

2011 - M. Tech Nanotechnology, Anna University, India.

2009 - B.E. Biomedical Instrumentation Engineering, Avinashilingam University, India.

**Publications:**

1. Saranya Panneerselvam, Susil. K. Putatunda, Richard Gundlach and James Boileau, "Influence of intercritical austempering on the microstructure and mechanical properties of austempered ductile cast iron (ADI), Materials Science and Engineering A, Vol.694, pp72-80, 2017.
2. Saranya Panneerselvam and Codrick J. Martis, S. K. Putatunda and James Boileau, "An Investigation on the Stability of Austenite in Austempered Ductile Cast Iron (ADI)", Materials Science and Engineering A, Vol.626, pp.237-246, 2015.
3. S. K. Putatunda, Saranya Panneerselvam and M. Alshwigi, "Development of Nanostructured Austempered Ductile Cast Iron (ADI)", Proceedings of the 28th ASM Heat Treating Society Conference, pp.71-75, 2015.
4. S. K. Putatunda, Saranya Panneerselvam, Codrick.J. Martis, Frederick Diekman and Rozalia Papp, "Improvement in Mechanical Properties of Austempered ductile Iron (ADI) by Cryogenic Treatment", Proceedings of the 27<sup>th</sup> ASM Heat Treating Society Conference, pp.189-192, 2013

**Selected Presentations:**

1. Saranya Panneerselvam, "Processing of nanostructured Austempered Ductile Cast Iron", American Advanced Materials Congress, December 4-9, 2016, Miami, USA.
2. Saranya Panneerselvam, "Intercritical Austempering of Austempered Ductile Iron (ADI)", Materials Science & Technology 2014, October 12-16, Pittsburgh, PA, USA.